Characterization of Chloride-Induced Corrosion Products that form in Steel-Reinforced Cementitious Materials

by

Tracy Dawn Marcotte

.

A thesis
presented to the University of Waterloo
in fulfilment of the
thesis requirement for the degree of
Doctor of Philosophy
in
Mechanical Engineering

Waterloo, Ontario, Canada, 2001
© Tracy Dawn Marcotte 2001

0-612-65251-3

Canada

The University of Waterloo requires the signatures of all persons using or photocopying this thesis. Please sign below, and give address and date.

ABSTRACT

The goals of this investigation were to identify the chloride-induced corrosion products that form from steel reinforcement in concrete, determine where they form, the corresponding corrosion rate, and relate these observations to the performance of steel-reinforced concrete in the field. This information is intended to be incorporated into structural service life models such that more accurate predictions of the remaining lifetime of a structure can be made. To accomplish these goals, experiments were conducted on various cementitious materials that ranged from steel in simulated pore solution to concrete of various types.

In situ electrochemical and Raman spectroscopy observations were performed on steel immersed in either a Type 10 or Type 50 white cement simulated pore solution that contained varying levels of chlorides up to 1 M NaCl. The composition of these pore solutions was developed from pore solutions expressed from 6 month old cement paste cylinders. The surface of the steel was either ground with 240 grit SiC paper or left in the as-received condition with a mill scale predominately composed of magnetite (Fe_3O_4). The effects of the type of pore solution, surface condition of the steel, and varying chloride exposure on the type and distribution of corrosion products were studied. The results indicated that the critical chloride/hydroxide ratios at which corrosion initiates depend upon the pH of the simulated pore solution, even within the narrow range of 12.9 to 13.4. Corrosion initiated with lower chloride levels and at lower applied potentials in the lower pH level of the white cement simulated pore solution than in the relatively higher pH Type 10 cement simulated pore solution. In addition, mill scale was observed to provide some enhanced corrosion protection by delaying the onset of corrosion. Once corrosion initiated, however, the corrosion rates of the as-received steel were similar to the ground steel surfaces. The corrosion products observed included magnetite, maghemite, Green Rust I, and hæmatite.

To coordinate with the aforementioned simulated pore solution-steel experiments, steel plates were cast into a 0.45 w/c cement paste which had been stabilized with 10% by mass of silica sand (henceforth referred to as modified cement paste). As before, both Type 10 and white cement pastes were studied as well as the effect of the surface finish of the steel, either ground or as-received. These steel-reinforced cement paste prisms were cured in their moulds for 3 months and then partially immersed in a their respective simulated pore solutions with sufficient chlorides, added as NaCl, to make a 1 M solution. Potential mapping in a manner similar to ASTM C876 and linear polarization resistance measurements were performed regularly to determine the corrosion state of the prisms. Once corrosion was considered to be initiated, the prisms were sectioned and examined *ex situ* using chemical, macro- and microstructural techniques to determine the influence of cement type, surface finish of the steel, surface cracks, and the confinement of the modified cement paste cover on the formation of corrosion products. A range of corrosion products was observed to form primarily within shrinkage cracks: magnetite, goethite, hæmatite, and

possibly Green Rust I. The formation of these products could not be correlated to the measured corrosion rates because the area of steel actually corroding could not be determined non-destructively. Furthermore, some corrosion products such as magnetite, haematite, and goethite were observed to form within the Type 10 modified cement paste cover but not within the white modified cement paste because of the relatively more open pore structure in the former.

The final experimental program involved the study of four different types of concrete: a low quality concrete (0.54 w/cm), an industrial standard concrete (0.41 w/cm), a high performance concrete (0.27 w/cm), and a high performance concrete with 10% by mass of cement of silica fume (0.25 w/cm). Concrete prisms (500 x 100 x 100 mm) had been cast commercially from these four mix designs with an embedded five element corrosion probe. Channels had been sawn into half of the prisms to position ~0.3 mm cracks subsequently induced by three-point bending. The prisms were exposed to simulated sea water (ASTM D1141) for up to four years. During this time, the corrosion state of the prisms was regularly assessed using open circuit potential and linear polarization resistance measurements. After at least three years exposure, the average corrosion rates (i.e., not corrected for area of steel actually corroding) indicated that the cracked low quality prisms had the highest corrosion rate (~0.04 A/m^2) while the steel in the industrial standard and high performance concretes were corroding at lower rates (~0.01 A/m^2). The same trends were noted in the uncracked specimens except that the rates were approximately one order of magnitude lower for only the high performance concretes (~0.002 A/m^2). Those prisms with the highest corrosion rates were then sectioned and studied in a manner similar to the modified cement paste prisms with particular attention paid to the effect of concrete type and position of the induced crack, on the type and location of any corrosion products that formed. Within the industrial standard and high performance concrete with silica fume, a dense layer of magnetite formed at the steel/concrete interface and within the induced crack. Magnetite also formed in the other two concretes but additional corrosion products such as akaganeite, goethite, and haematite were also observed within the concrete cover and were attributed to the higher connectivity of their pore networks from a higher w/cm ratio or microcracks. The removal of the corrosion products from the steel permitted the area of the steel that actually corroded to be estimated. Corrected corrosion rates indicated that the steel in the cracked high performance concretes was corroding at a rate almost an order of magnitude higher than the steel in either the industrial standard or low quality concretes with the higher electrical resistivity of the former concretes confining corrosion to a localized area at the root of the crack.

Overall, all experiments indicated that there is not any correlation between the corrosion rate measurements, steel surface finish, or chloride ion source on the types or location of corrosion products. Products which, in their pure state, have specific volumes not more than 3.5 were observed within the concrete specimens which suggests that the typically assumed range of 6 to 7 must be revised to reflect the service environment when used in theoretical service life models.

ACKNOWLEDGEMENTS

.

TABLE OF CONTENTS

LIST OF TABLES

LIST OF FIGURES

xvii

xxiii

CHAPTER ONE

INTRODUCTION

Steel-reinforced concrete is an extensively used structural material because of its low cost, ease of construction, and durability. With the ingress of chlorides into the concrete, however, the embedded steel may corrode and form expansive corrosion products at the steel/concrete interface which crack and spall the concrete cover. This allows more chlorides to ingress more easily and eventually the structure may be unable to safely perform the service for which it was designed because the load bearing capacity of the steel is reduced. In Ontario, the use of de-icing salts during the winter months causes the deterioration of an increasing number of bridges, support columns, parking garages, and other steel-reinforced concrete structures.

Canada's infrastructure is estimated to have a yearly cost of $3 billion to taxpayers but surveys of Canadian municipalities have indicated a financial shortfall in the rehabilitation of their infrastructure in the order of $20 billion (Concrete Canada 1997). This value is increasing and will soon represent $1000 per Canadian. It is, therefore, important to develop more accurate estimates of the remaining service life of steel-reinforced concrete structures such that economically efficient financial plans can be implemented for new construction and rehabilitation.

Typically, structural service life estimates are based upon empirical information collected from older structures that were likely composed of different concrete mix designs and situated within potentially dissimilar environments (i.e., the structural design affects the severity of seemingly similar environmental exposures). This potential for inaccuracy has led to increased attention towards developing theoretical models of corrosion that can be appropriately tailored for different materials and environments. Current theoretical service models represent corrosion as a two stage phenomenon: the time period prior to the initiation of corrosion, and the period thereafter while the damage accumulates to failure. Until recently it has been assumed that once corrosion initiates, the structural service life is

1

over because the damage accumulation phase was comparatively smaller, and therefore, insignificant. This is now acknowledged not to be the case but modelling the damage accumulation phase is complex because of a lack of important information concerning the variation in corrosion rates during that period and the corrosion products that form.

It is the objective of this work to identify the physical and chemical characteristics, and spatial distribution of corrosion products resulting from chloride-induced corrosion based upon different types of concrete and the presence of cracks. The correlation of these analyses with the corrosion rate will provide insight into the volume of corrosion products that can be accumulated before the concrete is damaged and the consequential impact on the remaining lifetime of a structure such that more accurate service life predictions may be calculated.

This thesis is structured such that the current understanding of chloride-induced corrosion is presented in Chapter 2 while the research programme is detailed in Chapter 3. Studies of the corrosion products that form in simulated pore solution, modified cement paste, and different types of concrete are presented in Chapters 4, 5, and 6, respectively. The results of these Chapters are discussed in Chapter 7 and is followed by Conclusions and Recommendations in Chapter 8.

CHAPTER TWO

THEORETICAL CONSIDERATIONS

2.1 CHARACTERIZATION OF CEMENTITIOUS SYSTEMS

Cement, when mixed with water, forms cement paste. Mortar is composed of cement, sand, and water, while concrete is prepared from cement, sand, water, and coarse aggregate (stones).

2.1.1 Portland Cement

2.1.1.1 Manufacture

Portland cement is manufactured from an adaptable range of raw materials, usually limestone (predominantly $CaCO_3$), and shale or clay (predominantly aluminum silicates with some magnesium and iron) (Taylor 1990). If a whiter cement is desired, the proportion of iron minerals added to the mix is reduced. The components are mixed and ground in an approximate 3:1 proportion of Ca:Si equivalents, and are fed into the top of a rotating kiln that is inclined to the horizontal by a few degrees. As the components move down the kiln, their temperature becomes progressively higher, in the range of 1400° to 1500°C, and liquid phases are formed that fuse the remaining solid phases together into balls known as clinker. After cooling, a small amount, 3 to 6% by mass, of either gypsum ($CaSO_4 \cdot 2H_2O$) or anhydrite ($CaSO_4$) is added to the clinker to "control" the hydration process of the tricalcium aluminate, described in Section 2.1.1.2. Gypsum is added to ordinary Portland cement clinker while anhydrite is added to white Portland cement in accordance with their respective aluminate contents. The clinker is ground into a powder with particle sizes, ranging approximately from 2 μm to 90 μm (Taylor 1990). Table 2.1

3

lists the four major compounds and their chemical formulae[1], comprising Portland cement powder. Minor phases consist of alkali sulphates and calcium oxides and constitute only a few mass percent of the cement powder.

Table 2.1 The major compounds and their approximate amounts in ordinary Portland cement (OPC) (Taylor 1990).

Major Compound	Chemical Formula	Chemical Notation[1]	Mass Percentage in OPC
Tricalcium Silicate	$3\,CaO \cdot SiO_2$	C_3S	50 - 70
Dicalcium Silicate	$2\,CaO \cdot SiO_2$	C_2S	15 - 30
Tricalcium Aluminate	$3\,CaO \cdot Al_2O_3$	C_3A	5 - 10
Tetracalcium Aluminoferrite	$4\,CaO \cdot Al_2O_3 \cdot Fe_2O_3$	C_4AF	5 - 15

2.1.1.2 Hydration of Cement Powder

Cement clinker powder is hydraulic, that is, it reacts spontaneously with water. Its hydration reaction processes have been the subject of a considerable amount of research but are still not fully understood. The complex hydration process begins immediately with the

---

1   Chemical formulae are often simplified in cement chemistry using a notation based upon the sums of oxides present in the cement compounds. The oxides are described by the first letter of their compound where C represents CaO. S represents SiO_2. A represents Al_2O_3. F represents Fe_2O_3, and H represents H_2O. In the case of SO_3 and CO_2. $\bar{S}$ and $\bar{C}$ are used to distinguish them from SiO_2 and CaO, respectively.

mixing of cement powder with water and continues at a decreasing rate for months or years. Cement paste consists of the hydrated compounds of the cement powder, any unhydrated cement powder, and any water not consumed in the hydration reaction. This water remains as water-filled pores, known as capillary pores, in the solid network of phases and as gel pores or interlayer water, described below. During the first 24 hours, the anhydrous cement grains in the presence of sufficient water will have reacted between 30 to 50%, after which time hydration is significantly slower. After one year with sufficient water present, typically 80 to 90% hydration of the anhydrous cement grains has occurred to form hydration products (Crumbie 1994). It is important to recognize, however, that this hydration reaction rarely reaches completion, and as a result, many of the properties of cement-based materials constantly improve with age, albeit at an ever decreasing rate.

During the hydration process, the calcium silicates react to form calcium silicate hydrate (C-S-H), and calcium hydroxide (CH). The composition of C-S-H varies with C:S ratios of about 1.7 to 2.0, hence the dashes in its abbreviation (Scrivener 1989). The aluminates and ferrites react with the added gypsum or anhydrite to initially form metastable ettringite, $C_6 A \overline{S}_3 H_{32}$, a member of the AFt family, which often reacts further forming monosulphate, $C_4 A \overline{S} H_{18}$, a member of the AFm family. Ettringite gradually converts to monosulphate depending upon the aluminate/sulphate ratio in solution. If there is insufficient gypsum, and consequently sulphate, for the hydration of C_3A, the ettringite already formed decomposes to monosulphate to provide it.

C-S-H is the most important of all the hydrated solid phases primarily because it constitutes approximately 50-60% of the volume of the cement paste and is responsible for the structural rigidity and inherent strength of hydrated cement paste (Mehta 1993). It is predominantly a poorly crystalline product with a range of morphologies. Within this product there exist interlayer solution-filled spaces, on the order of nanometres, known as gel pores. These very fine pores do not limit the strength, permeability or durability of

cement and concrete materials–these characteristics are controlled by the comparatively larger capillary pore network, air voids, and cracks.

In contrast to C-S-H, calcium hydroxide (CH) is likely to contribute to the strength limitations of hydrating cement paste because of its high crystallinity. Its structure consists of hexagonal plates which preferentially cleave along the (0001) plane. CH forms "through solution" in the interstices between the clinker grains which become capillary pores. The CH can, therefore, grow to fill relatively large regions (up to 10 μm diameter) depending on the pore space and Ca^{2-} ions available. CH masses also are generally isolated from each other and the total volume percentage of CH in fully hydrated paste is only 10 to 15% of the cement paste or 20-25% of the ignited mass (Taylor 1990). It has been observed that in the early stages of hydration (especially the first few hours) Ca^{2-} ions will diffuse over large distances (approximately 20 to 40 μm) to precipitate preferentially in larger pore spaces rather than those closer to the hydrating anhydrous grain (Crumbie 1994). Therefore, it is not homogeneously distributed and prefers interfacial regions, discussed in greater detail in Section 2.1.2. Calcium hydroxide is the solid phase primarily responsible for buffering the pH of the pore solution to approximately 12.5 although both the carbonate (CO_3^{2-}) and bicarbonate (HCO_3^{-}) species, if present, would also contribute to the alkalinity of the pore solution.

The calcium aluminate phases also do not contribute significantly to the strength of cement paste, again because of their high crystallinity but also because they are only minor compounds in the hydrated cement paste. They are, however, responsible for the initial set of the cement within the first few hours of the hydration process (Taylor 1990).

2.1.1.3 Porosity

Total porosity is the combination of the capillary and gel pores within the network of solid phases formed during hydration. These pores contain a solution based on the water

remaining from the mixing of the cement or from ingressed water from the environment. The solid phases have varying degrees of solubility and their dissolved ions transform the water into a highly concentrated solution predominantly composed of NaOH, KOH, and to a lesser extent, $Ca(OH)_2$. Because of the small dimensions of the gel pores (about 0.5 to 3.0 nm) and the polar nature of water molecules, interlayer water behaves differently from both the water of hydration (which is bound by primary chemical bonds) and the water in the capillary pores (which can flow freely). Interlayer water is chemisorbed onto the gel and can be thought of as a structural component of the C-S-H.

It is predominantly through the capillary pore network that aggressive species ingress into the cement paste from the environment. Thus, it is not the total porosity that determines the permeability of cement paste but the volume, size, and interconnectivity of capillary pores. Pore size distribution measurements of hardened cement pastes have shown that a greater volume of capillary pores corresponds directly with increased permeability to water (Mehta and Manmohan 1980). Moreover, a high w/c ratio results in a greater pore volume and interconnectivity of the pores (Mehta and Manmohan 1980). Thus, it is desirable to minimize the w/c ratio to reduce the permeability of the concrete while still adding sufficient water to ensure that the concrete can be properly mixed and placed.

2.1.1.4 Effect of Chlorides on the Microstructure of Cement

Chlorides in cement paste are considered to exist in three states: (i) chemically bound as reaction products of hydrating C_3A and to a lesser extent, C_4AF; (ii) adsorbed within the structure of C-S-H; and (iii) freely available within the pore solution. It is generally thought that more chlorides will be chemically bound or adsorbed if added at the time of mixing of the cement than if introduced later from the environment. This is due to the rapid hydration of C_3A and the calcium silicates within the first few days of hydration, described

in Section 2.1.1.2.

Many investigations have been performed to study the chloride-binding capacity of C_3A (Ramachandran 1976; Conjeaud 1982; Suryavanshi, Scantlebury et al. 1996). The only form of calcium monochloroaluminate hydrate ($C_3A \cdot CaCl_2 \cdot 10\ H_2O$) produced in the environmental conditions usually existing in cementitious materials is known as Friedel's salt, Equation 2-1.

$$CaCl_{2(aq)} + C_3A_{(s)} + 10\ H_2O_{(l)} - C_3A \cdot CaCl_2 \cdot 10\ H_2O_{(s)} \qquad (2\text{-}1)$$
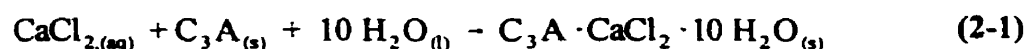
It has been shown that the amount of calcium monochloroaluminate hydrate increased with increasing C_3A content and $w_{/c}$ ratio, and depended on the chloride cation type (Arya, Buenfeld et al. 1990; Suryavanshi, Scantlebury et al. 1996). In general, calcium chloride produces a greater proportion of calcium monochloroaluminate hydrate than does sodium chloride.

In addition to this product, Conjeaud observed that chlorides may be incorporated into ettringite to form a chloro-ettringite of an unspecified composition as well as incorporated into the C-S-H (Conjeaud 1982). However, chloride binding may still occur at later ages during the hydration of aluminoferrites within the remaining anhydrous portions of cement grains (Csizmadia, Balázs et al. 2001). Additionally, free chlorides in pore solution may become incorporated into solid phases such as C-S-H to maintain the equilibrium between the solid phases and the pore solution (Leek 1997).

2.1.2 Mortar, Concrete, and Steel-Reinforced Concrete

Cement paste alone is an impractical structural material because it shrinks as it hydrates and its dimensions change with the ambient temperature and humidity. Therefore, a major role of the aggregate in concrete is to provide dimensional stability, reducing the overall shrinkage to less than 1%. The addition of aggregate also reduces the cost per volume of

material since the cement is significantly more expensive than aggregate. Fine aggregate (sand) is typically composed of particles with diameters that range from 75 μm to 5 mm, while coarse aggregate (stones) has particles with diameters greater than 5 mm to approximately 50 mm (Mehta 1993). Steel reinforcing bars and other reinforcing materials are often added to concrete to provide tensile strength and toughness.

All these inclusions, however, introduce interfacial regions within the concrete and complicate the already complex microstructure of the cement. This results primarily from the increased particle size range. Instead of particle sizes that range from 2 to 90 μm (mostly 5 to 20 μm) within the cement, the upper limit is expanded to approximately 50 mm (Mehta 1993). The microstructure of the cement paste within mortar, concrete, and reinforced concrete is affected in the interfacial regions by the larger particles for two main reasons: (a) the inefficient packing of cement particles during casting as a result of the "wall effect", and (b) settlement during the placement and compaction of the concrete.

The "wall effect" results from the inability of the cement powder particles to pack efficiently against the much larger surfaces of the inclusions, schematically illustrated in Figure 2.1.2(a) (Johansen and Andersen 1991). Interfaces are considered to be formed surfaces, aggregate, and by extension, embedded steel. This packing "wall" effect lowers the amount of anhydrous cement within the closest 20 μm of the interface. Correspondingly, this results in a significant higher porosity within this region of about 20-30 μm.
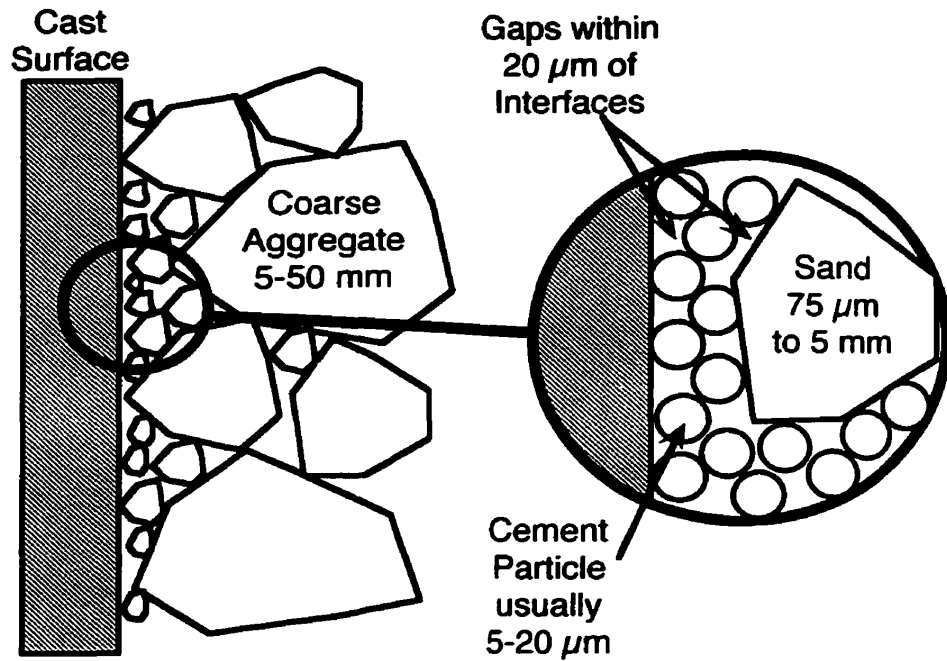
Figure 2.1.2(a) Schematic illustration of the "wall effect" present at cast surfaces and interfacial regions (modified from Johansen and Andersen (1991)).

Another mechanism which involves the casting process can also contribute to the significantly higher porosity in interfacial regions. The solid particles settle during placement and compaction and this causes pockets of air and water to form under the particles, a process known as bleeding, shown schematically in Figure 2.1.2(b) (Chatterji and Jensen 1992). These pockets are correspondingly deficient in cement paste and this influences the final microstructure of the concrete.
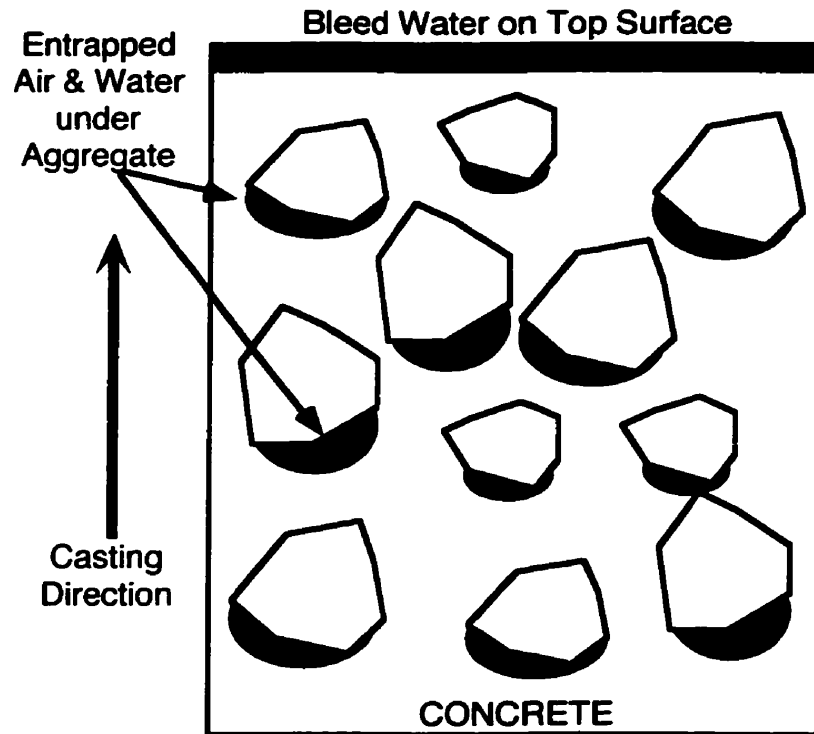
Figure 2.1.2(b) Schematic illustration of the segregation of a cement/concrete mix during placement and compaction, known as bleeding (modified from Mehta (1993)).

Overall, the end result of either the "wall effect" or bleeding is the same: the lower amount of anhydrous cement in interfacial regions affects the development of the microstructure as hydration proceeds. Thus, less C-S-H forms in this region than further away in the 'bulk' microstructural regions and a locally higher porosity results. CH and AFt form preferentially in these regions because of the easy migration of ions. However, the relative amounts of the CH and AFt hydration products are low and the higher porosity in the interfacial regions persists throughout hydration (Crumbie 1994). If this higher porosity results in a continuous path from one side of a cementitious pore network to the other, this is known as percolation. Work by Winslow and Lui (Winslow and Liu (1990) as reviewed by Taylor (1990)) concluded that percolation occurs in most normal quality

11

concretes and this effect accounts for the higher permeability of concrete with respect to comparable cement pastes.

2.1.3 Supplementary Cementitious Materials

Certain minerals are known to have cementing properties and are classified either as pozzolans or latent hydraulic materials. Pozzolans are materials which when mixed with cement and water form C-S-H whereas latent hydraulic materials require a catalyst to produce C-S-H. The addition of these products to a concrete mix reduces the cement requirement for strength, the heat of curing during early hydration, and enhances its durability over time. The most prevalent additions are ground granulated blast furnace slag, fly ash, and silica fume. Ground granulated blast furnace slag and fly ash are waste products of steel production and coal-burning power stations, respectively, and incorporating them into concrete mixes reduces energy consumption by reducing the cement requirement of the mix as well as recycling waste. Silica fume is also a waste product of the silicon industry but because of the excellent benefits it offers concrete mixes, it now commands a price higher than that of cement powder. Since only fly ash and silica fume were used in this research, these are the only products described in greater detail in the next paragraphs.

Fly ash is used both as a separate ingredient in concrete mix designs as well as a component of blended cement powders. It is catagorized according to the proportion of CaO in its chemistry: Class F fly ash is more than 70% composed of SiO_2, Al_2O_3, and Fe_2O_3 with only a small amount of CaO while Class C fly ash contains less than 70% of SiO_2, Al_2O_3, and Fe_2O_3 with a correspondingly larger amount of CaO. This higher proportion of calcium compounds (reported as CaO) in Class C fly ashes allows this fly ash to be also cementitious as well as pozzolanic.

Both fly ashes are predominantly composed of fine, spherical particles that can range

from 1 μm to 1 mm. However, to be suitable for use in concrete mixes, most fly ash particles should pass a 45 μm sieve. The individual particles can be glassy or crystalline, solid or hollow. Higher proportions of glassy particles result in higher pozzolanic or cementitious reactivity and are, therefore, more desirable. In addition, hollow spheres are known as cenospheres while spheres that contain smaller particles are known as pleurospheres. These qualities, in combination with the aforementioned compositional variations affect the properties of fresh and hardened concrete. The presence of fly ash reduces the heat of hydration as well as the mixing water required for a particular slump. The reduction of the water requirement is extremely important for achieving low w/cm mixes (i.e., high performance concretes). The presence of carbon in the fly ash can interfere with air-entraining admixtures and detrain air. In addition, carbon retards setting and strength development at very early ages (i.e., up to 21 days). After approximately 28 days, however, concrete mixes that contain fly ash can have strengths that are equivalent or exceed non-fly ash concrete mixes. This is a result of the fly ash reacting with the CH that may accumulate at interfaces and depositing C-S-H thus improving the interface bond and the bulk strength of the overall concrete.

Similarly, silica fume reacts with CH to form C-S-H at interfaces and densifies concrete. Silica fume is composed of predominantly silica, glassy spheres (usually 86-90% (Taylor 1990), approximately 100 nm in diameter (about two orders of magnitude smaller than cement particles) and as such, it reacts much earlier, approximately 7 to14 days after mixing. Its fine surface area also reduces bleeding and the water demand of a particular mix to the point finishing operations can be difficult. This effect can be offset by the use of a superplasticizer (described in Section 2.1.4). Overall, silica fume increases strength, reduces permeability, and can dramatically increase electrical resistivity.

2.1.4 Chemical Admixtures

Chemical admixtures, like the supplementary cementitious materials described in Section 2.1.3, are added to fresh concrete mixes to improve either the constructability of the fresh concrete or the durability of the hardened concrete, or both. Although there are a wide range of admixtures used in general practice, only superplasticizers and air-entrainers were used in this work, and therefore, are the only admixtures described.

Superplasticizers (also known as high-range water reducers) reduce the amount of water necessary for workability of the fresh concrete to produce higher strength concretes. This admixture is a necessary component of high performance concrete for the reasons described in Section 2.1.5. It is essentially an anionic addition to a linear polymer with regular sulphonate groups.

Air-entraining agents add a fine dispersion of air voids, preferably 10-250 μm in diameter, spaced approximately 200 μm apart to allow a concrete to resist freeze/thaw damage (Powers 1949). This admixture is a surfactant with long chains that have a polar group at one end. It increases workability in a manner similar to superplactizers but to a lesser extent. However, the presence of a superplasticizer can interfere with entrained air because of the higher fluidity of the mix. As previously mentioned, carbon in fly ash also detrains air.

2.1.5 High Performance Concrete

The development of high performance concrete (HPC) was initially aimed at providing significantly higher strengths and its secondary goal has been to provide greater durability through a reduction in the interconnected porosity of the concrete. The hypothesis has been that, by reducing the water/cementitious materials ratio (w/c) and providing adequate workability, compaction, and curing by the addition of appropriate chemical admixtures (e.g., air-entraining agents and superplasticizers) and procedures, the interconnected

porosity is greatly reduced, thereby limiting the ingress of deleterious species such as chlorides or CO_2. The addition of silica fume to the mix has been shown to be able to virtually eliminate capillary porosity in a manner shown by Sellevold et al. (Sellevold, Bager et al. 1982). Other properties that enhance durability include: increased electrical resistivity, increased strength if strong aggregates are used, increased freeze/thaw resistance, and decreased scaling.

A compromise to these enhanced properties is an increase in the brittleness of HPC (John and Shah 1989). This could decrease its capacity to accommodate any corrosion products if their formation exerts pressures which exceed the critical tensile stresses of the concrete. In consideration of all these factors, it is anticipated that only cracked concrete would allow the ingress of sufficient chlorides to initiate and sustain the corrosion of embedded reinforcing steel, as described in Section 2.3.2. However, it is also thought that cracks can be autogenously healed by the exposure of unhydrated cement grains to water, as reviewed in detail by Jacobsen et al. (Jacobsen, Marchand et al. 1998).

2.2 TECHNIQUES FOR MICROSTRUCTURAL CHARACTERIZATION

2.2.1 Scanning Electron Microscopy (SEM) Techniques

These techniques have been extensively reviewed by Diamond as they apply to the study of the microstructure of cement and concrete and he detailed the important contributions of various researchers such as Moranville-Regourd, Homain, and Aïtcin (Diamond 1994). Electron microscopy enables the direct observation of cement and concrete microstructures, and both the morphology and spatial distribution of the individual constituents to be addressed (Crumbie 1994). While other microstructural characterization techniques are more suited to bulk investigations (e.g., thermogravimetric analysis, differential scanning calorimetry, mercury intrusion porosimetry, solvent exchange, etc.), electron microscopy

permits local areas to be studied.

The high vacuum used in scanning electron microscopy requires that samples must first be dried to remove the evaporable water. For investigations of morphology and chemical composition of phases, freeze drying is presently the most suitable technique used to remove the water from the samples (Crumbie 1994). Moreover, since the dry cement-based materials are non-conductive, the samples must be coated with carbon or gold to eliminate electron charging. Two imaging modes are utilized in scanning electron microscopy: backscattered electron imaging and secondary electron imaging.

2.2.1.1 Backscattered Electron Imaging (BEI)

Backscattered electron imaging (BEI) requires flat, polished specimens whose microstructures are revealed by compositional contrast. Different phases are distinguished by the intensity of electrons backscattered from each phase which is determined by the average atomic number of the phase. The contrast appears as differences in grey level. Anhydrous particles, hydration products, porosity, and aggregate particles can be discriminated. In addition, the spatial distribution of the phases in two dimensions can be assessed. Parameters such as area and the diameters of microstructural constituents can be measured by quantitative analysis of the images produced.

2.2.1.2 Secondary Electron Imaging (SEI)

Secondary electron imaging (SEI) gives topographical contrast and is, therefore, suited for investigating the morphology of phases which is often studied using surfaces exposed by fracture. A disadvantage of this technique is that the fracture path often occurs through the weaker phases and may not be representative of the 'bulk' microstructure. In addition, the resolution of the SEM limits the observation of small phases within the cement microstructure (< 1 μm).

2.2.1.3 Energy Dispersive X-ray Spectroscopy (EDS)

EDS enables the elemental composition of components to be assessed. For quantitative elemental analyses, this technique requires flat, polished surfaces and standards of similar compounds to the materials to be analysed. It is for this reason that quantitative analyses must be made in conjunction with flat surfaces, such as those used for BEI. Major constituent elements, greater than 10% by mass, can be measured with a high degree of confidence but there are larger errors associated with minor analyses (1 - 10% by mass), and trace elemental analyses (< 1% by mass) are not possible (Goldstein 1981). EDS is often used with fracture surfaces using SEI, but this is not suitable and is considered to be a dubious practice for quantitative analysis (Scrivener 1984). However, measurements made within the SEI mode on fracture surfaces can be considered qualitatively to help assess which elements compose a phase. When considered with the morphology, intelligent deductions can be made as to the exact composition and the type of compound observed (Crumbie 1996).

2.2.1.4 Environmental Scanning Electron Microscopy (ESEM) with EDS

The ESEM is designed to permit the introduction of a gaseous environment into the specimen chamber (Danilatos 1991). This microscope, coupled with EDS, is capable of imaging and analyzing specimens in virtually any environment at a relatively high pressure, up to approximately 6.7 kPa (50 Torr). The most common environment is water vapour and with the control of the pressure inside the chamber and temperature of the specimen, 100% relative humidity is possible. This is very suitable for *in situ* cement and concrete studies as specimens do not need to be dried or coated with gold or carbon for imaging. This is a significant advantage over conventional SEM studies since drying and coating can distort the fragile microstructure (Jennings, Dalgleish et al. 1981). In addition, dynamic

17

hydration studies can be performed within the ESEM as the presence of water allows the hydration to proceed during observations. Another advantage is that the preparation time of samples studied with the ESEM is dramatically reduced compared to that of the SEM. The major disadvantage is the image resolution which is slightly lower.

2.2.2 X-ray Diffraction (XRD) Techniques

While EDS is limited to elemental analyses, XRD assesses the organization of these elements and is used to identify the chemical compounds within cement pastes from their crystallographic forms. There are limitations to the application of XRD techniques to cementitious materials: (i) the major phase, C-S-H, cannot be thoroughly assessed by XRD due to its inherent poorly crystalline structure; (ii) many constituents of cement paste have peaks which overlap others (Taylor 1990); or (iii) only a trace amount of the phase is present and is, therefore, below the resolution limit of this technique, about 5%. Analyses of mortar or concrete are further complicated due to the presence of aggregate within the analysed sample. Since aggregate often constitutes a large proportion of the material (typically 3-6 times the volume of cement), XRD peaks from the cementitious phases are minimized and obscured by the aggregate peaks. These factors have been overcome, in part, by isolating the desired phases either through the deliberate destruction of non-desired phases (Gutteridge 1979), or the careful manufacture of the chosen phase in a controlled laboratory atmosphere (Crammond 1985; Guirado, Galí et al. 1994). In fact, there has not been any work to date which has used XRD as its primary tool to analyze concrete or mortar. It is always used in combination with other techniques such as electron microscopy and thermal analysis. XRD is more often used with cement paste for preferred orientation work (Grandet and Ollivier 1980; Grandet and Ollivier 1980) or to confirm the significant presence of one phase or another (Rasheeduzzafar, Al-Saadoun et al. 1990).

2.2.3 Porosity Measurements

2.2.3.1 Total Porosity Measurements

The simplest of total porosity measurements is based upon the Archimedes' Principle which states a body wholly or partially immersed in a fluid is buoyed by a force equal to the mass of the fluid displaced (Lide 1999). The total porosity (P) of cement-based materials can then be calculated from their water saturated surface dry mass (m_{sat}), their mass suspended in water (m_{water}), and their oven dry mass[2] (m_{dry}), Equation 2-2.

$$P\ (\%)\ =\ \frac{m_{sat}\ -\ m_{dry}}{m_{sat}\ -\ m_{water}}\ *\ 100 \qquad\qquad (2\text{-}2)$$

These moisture states are schematically illustrated in Figure 2.2.3.1. Equation 2-2 applies to systems in which all pores within the sample are water saturated which may not be the case, especially if discontinuous pores are present. Unfilled pores cause the specimen to be lighter in water thus underestimating the total porosity. However, this is not a major problem for comparisons between samples. This technique is not suitable for early hydration studies within the first day because exposure to water to saturate the sample would alter the degree of hydration. In older cement and concrete samples, the time taken to saturate the samples, typically 24 to 48 hours, is insignificant with regard to the state of hydration.

---

2   Mass after drying at 105°C until all evaporable water is removed.
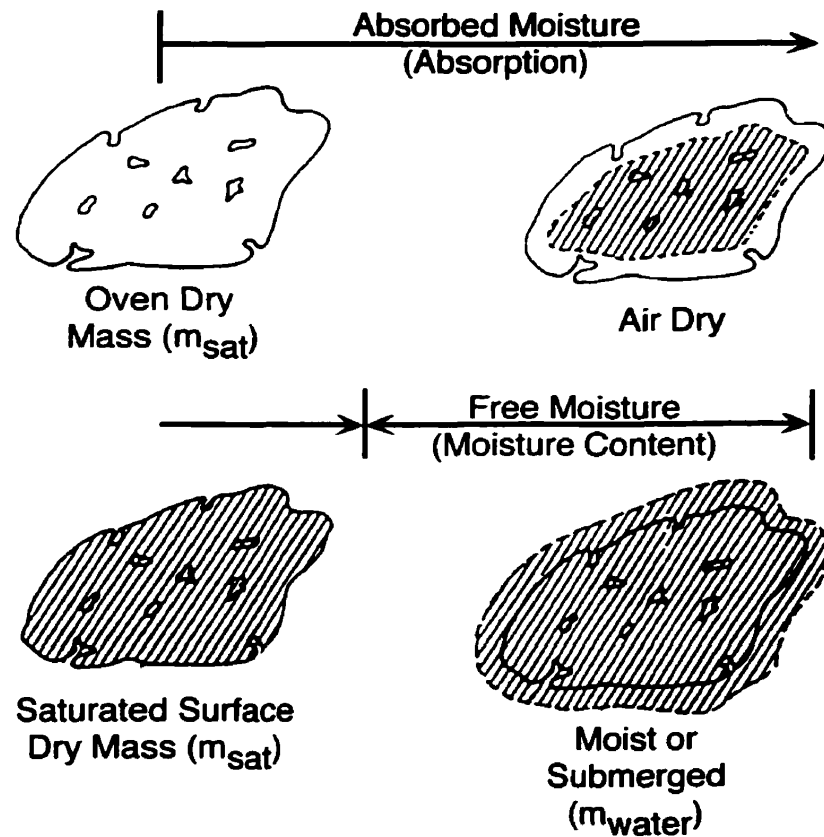
Figure 2.2.3.1 Schematic illustration of moisture states of cement-based materials (Neville 1973).

2.2.3.2 Pore Size Distribution Measurements

Mercury intrusion porosimetry (MIP) is the most commonly used method for determining pore size distributions because of its ability to measure an extensive range of pore sizes (i.e., from approx. 4 nm up to 1 mm) (Diamond 1989; Winslow 1989). The technique is based upon the principle that a non-wetting liquid (e.g., mercury) will not enter a porous solid except under pressure (Taylor 1990). A number of researchers have reviewed this technique and described its limitations (Diamond 1989; Winslow 1989; Cook and Hover 1993). The latter two studies further examined the impact of various assumptions used

with cement-based materials. These assumptions include: (i) the pores are cylindrical; (ii) the pore network contains its coarsest pores at the exterior and that finer pores always branch from larger pores; and (iii) the pore network is continuous. In reality, pores have varying diameters that can branch to both larger and smaller pores (bottlenecks) or end altogether to make the network locally discontinuous. The presence of cracks within a sample complicates analyses further. The end result of these assumptions suggests that pore size distributions measured with MIP are best used for comparative analyses and that replicate samples must be analyzed. If the pores are assumed to be cylindrical and have a constant contact angle (q), and surface energy of the liquid (g), the pressure required (p), to force the liquid in a pore of radius (r), is given by the Washburn equation, Equation 2-3.

$$p = \frac{-2\gamma \cos \theta}{r} \qquad (2\text{-}3)$$

For the mercury to intrude, however, the free water must be removed. Marsh et al. concluded that solvent replacement methods were preferable to oven drying since the latter significantly alters and coarsens the pore structures within cementitious materials (Marsh, Day et al. 1985). Although the high pressures used in the MIP technique may disrupt the fine pores, and the mercury may not enter discontinuous pores or the interlayer space present in the microstructure, MIP is the only currently available technique to date that encompasses the extensive pore size range within cements for relative comparisons (Taylor 1990).

2.2.4 Thermal Analysis

Thermal analyses measure the dynamic relationship between temperature and the mass or enthalpy of a material. The most common techniques are thermogravimetric analysis (TG), differential thermal analysis (DTA), and differential scanning calorimetry (DSC). Since only TG and DTA were used in this work, they are the only two methods described

hereafter.

TG is used to measure changes in the mass of a sample over a given temperature range while DTA is used to measure enthalpy changes. Both techniques can provide valuable information about the constituents of cementitious materials (e.g., CH, $CaCO_3$, calcium monochloroaluminate hydrate). TG is a more quantitative technique than DTA and both provide information on the composition by measuring the onset and duration of phase changes such as dehydration and decomposition. For example, quantifying the amount of CH using TG can indicate the progress of hydration, especially if pozzolanic materials are a part of the mix. In addition, using DTA, minerals can be identified by the phase changes that occur over certain temperature ranges. Overall these techniques are more precise with simpler systems that contain only a few compounds because interpreting results with overlapping peaks can be difficult. Concrete samples are especially difficult to study because they contain a large volume of aggregate, the constituents of which also changes over the same temperature range as the cementitious minerals under investigation. For example, common aggregates include those predominantly composed of $CaCO_3$ which directly interferes with carbonation studies in cement paste. Interpretations of results are aided by examining the derivative of the curves which helps identify any changes in slopes of the curves corresponding to mass or enthalpy changes, referred to as differential thermogravimetric analysis (DTG).

2.3 CORROSION OF STEEL-REINFORCED CONCRETE

2.3.1 The Passivation of Steel in Concrete

Concrete provides more than a protective cover to guard against corrosion: it also offers a passivating environment because of the high pH of the pore solution (approximately 12.5-13.8). Iron passivity results from the formation of an ultra-thin (< 10 nm), protective oxide or hydroxide film that slows down the rate of anodic dissolution to negligible levels

(Shreir, Jarman et al. 1994). The formation of a passive film begins with the dissolution of the metal and the corresponding oxygen reduction which uses the electrons generated by the metal dissolution in its reaction, represented by Equations 2-4 and 2-5, respectively.

$$2 \, Fe_{(s)} \rightarrow 2 \, Fe^{2+}_{(aq)} + 4 \, e^- \qquad (2\text{-}4)$$

$$O_{2.(g)} + 2 \, H_2O_{(l)} + 4 \, e^- \rightarrow 4 \, OH^-_{(aq)} \qquad (2\text{-}5)$$
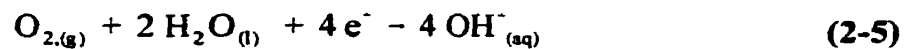
The resulting ferrous ions are attracted to the cathodic portions of the steel. The closest cathodic site is where the iron ions combine with hydroxide ions from the cathodic reaction to form the solid product of ferrous hydroxide, Equation 2-6. It is also possible that hydroxide ions may travel to the anodic regions.

$$2 \, Fe^{2-}_{(aq)} + 4 \, OH^-_{(aq)} \rightarrow 2 \, Fe(OH)_{2. (s)} \qquad (2\text{-}6)$$
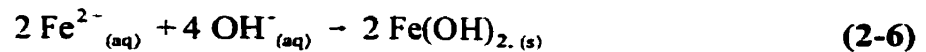
Upon exposure of this film to oxygen, other passivating oxides may form (e.g., Fe_3O_4, and Fe_2O_3) on the outer surface of the film. As a result, these passive films can consist of layers of iron hydroxides or oxides in different states of oxidation (Uhlig and Revie 1985).

The work of Pourbaix defined the range of pH and electrochemical potentials where insoluble and thermodynamically stable films of $Fe(OH)_2$, Fe_3O_4, and Fe_2O_3 form in water (Pourbaix 1966). Figure 2.3 presents a redox potential-pH diagram that combines all species calculated by Pourbaix (i.e., the formation of hydroxides and oxides) with additional species, $FeOH^-$ and FeO_2^{2-}, that were not considered in his original work resulting from the hydrolysis of the ferrous ions in solution. The one obvious drawback with the presentation of this thermodynamic data is that it does not consider kinetics or the effect of other species other than water. Although the information presented does concur with the observed behaviour of iron at various potentials and pH values, kinetic considerations would possibly include metastable and other stable compounds and complexes that may result from the ionic species present within the pore solution of concrete.

Generally, the study of these films *ex situ* is challenging. For example, it has been observed that the passive film formed on iron in a borate buffer solution (deaerated 0.3 M

H_3BO_3 + 0.075 M $Na_2B_4O_7$, pH about 9.2) further oxidizes and can possibly dehydrate upon exposure to air (Goetz, Mitchell et al. 1987; Eldridge and Hoffman 1989). This suggests that all observations of the passive film should be performed *in situ*.

Other contributing factors to the protective environment present in concrete include: the electrical resistivity of concrete which can slow the corrosion rate by impeding the movement of ions between anodic and cathodic sites; it limits the access of oxygen to the steel; and the possible preferential formation of CH at the steel/concrete interface which provides a physical barrier to aggressive species, described in Section 2.1.2.
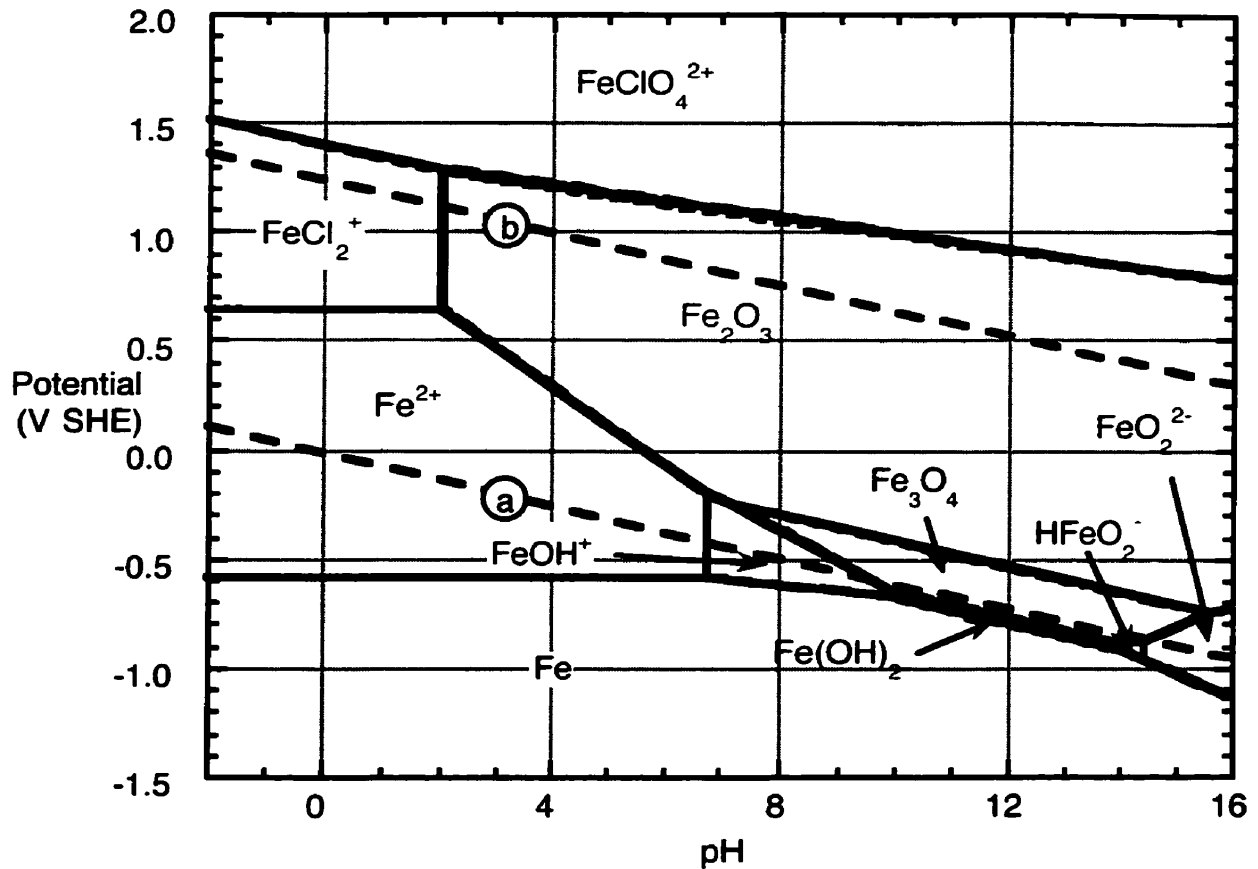
Figure 2.3 Calculated $Fe-H_2O$ redox potential-pH diagram (25°C and 101.3 kPa) that assumes the molality of iron is 10^{-6} (Bale, Pelton et al. 1995).

2.3.2 The Active Corrosion of Steel in Concrete

The passivity of steel embedded in good quality concrete can be compromised in a number of environmental situations: aggressive ions (e.g., Cl- ions) are introduced into the concrete that attack the steel; the pH of the concrete is lowered (e.g., by carbonation); or insufficient oxygen is present at the steel to maintain the passive film. Other causes of active

reinforcing steel corrosion include: galvanic cell formation from the contact of dissimilar metals (e.g., stainless steel fittings, galvanized rebar, bronze hangers for precast sections of concrete), and stray currents (e.g., from DC high-tension power lines, impressed current cathodic protection systems, or electric railway lines). Only chloride-induced corrosion is considered in this literature review.

2.3.2.1 Chloride-Induced Corrosion

Chloride ions locally destroy the passive film on steel in concrete. The sources of these ions include: any chlorides originally present within the cement powder, calcium chloride added at the time of mixing as a set-accelerator, contaminated aggregate or mixing water, or those introduced over the service life of the reinforced concrete structure from marine exposure or the use of de-icing salts. In Ontario, the largest source of chlorides is from the use of de-icing salts during the winter months.

Sufficient chlorides present in the pore solution adjacent to the steel reinforcement can initiate active metal dissolution at local sites, known as pitting corrosion, provided the supply of oxygen and water is also high enough to ensure that the cathodic reactions can take place over the remaining surface of the steel. The presence of millscale typically observed on the surface of reinforcing steel restricts the attack of the chloride ions to those areas of the steel where the scale is broken.

The exact mechanism of chloride-induced pitting in concrete is not known but it is thought that the overall process is that schematically illustrated in Figure 2.4. This diagram was developed assuming a neutral aqueous solution but a similar process can be assumed for steel in concrete albeit at a lower rate and without the evolution of hydrogen gas for the conditions typically encountered in concrete. In addition, the resulting corrosion products could be different than that shown.

Chloride-induced corrosion initiates similarly to the passivation process represented

by Equations 2-4 and 2-5. Chloride ions are then attracted to the metal dissolution sites to maintain electro-neutrality and generate soluble iron chlorides. These chloride products can have a range of compositions which are often simplified and reported as ferrous chloride, the thermodynamically favoured product, Equation 2-6.

$$2 \, Fe^{2+}_{(aq)} + 4 \, Cl^{-}_{(aq)} \rightarrow 2 \, FeCl_2 \cdot 4 \, H_2O_{(s)} \qquad (2\text{-}7)$$
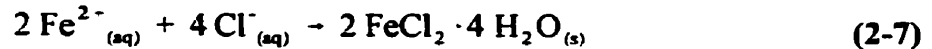
The increased localized dissolution of the metal generates pits because the surrounding steel remains passive and acts as a cathode. The ferrous chloride compound formed in the pits is stable at the low pH present in the pit but diffuses out of the pit because of the locally high concentration present within the pit. At the higher pH outside of the pit, the ferrous chloride compounds are no longer stable and dissociate. The chloride ions are then released into the pit for further chloride attack while the ferrous ions are attracted to the cathodic portions of the steel. The closest cathodic site is at the mouth of the corrosion pit and here the iron ions combine with hydroxide ions from the cathodic reaction to form the solid corrosion product of ferrous hydroxide according to Equation 2-6.

The formation of this product during pitting does not passivate the anodic site because chlorides become incorporated into the product thus reducing its electrical resistivity and increasing the possibility of further corrosion at this site. The corrosion products that form during this process are described in the next Section. In addition, the presence of chloride ions increases the conductivity of the pore solution such that the distance between anodic and cathodic sites can be larger (Uhlig and Revie 1985). This allows more of the cathodic surface of the steel to drive the anodic reactions occurring within significantly smaller corrosion pit. Consequently, these corrosion pits are self-sustaining and the rate of corrosion is determined by chloride ion mobility, oxygen availability, and the electrical resistivity of the concrete. As the corrosion rate increases, the pH of the pore solution in the pit decreases, thus accelerating the rate of iron dissolution and deepening the pit.

This presence of millscale on the surface of the steel has been studied by several researchers (Addleson and Rice 1995; Mammoliti, Brown et al. 1996; Li and Sagüés 2001). The work of Addleson and Rice concluded that mill scale contributes to this attack of the steel when the steel is exposed to sea water. They postulated that this mill scale forms a physical barrier but once it is penetrated, the corrosion pits can be four times deeper than bare steel within the first year but this effect will lessen with time (Addleson and Rice 1995). These results were not observed by the latter researchers in alkaline solutions who noted that ground steel, presumably similar to the bare steel of the Addleson and Rice study, increased the chloride threshold for corrosion initiation over the mill scale but once corrosion initiated, the corrosion rates were higher for the ground steel. This discrepancy may result from the different types of immersion solutions (i.e., sea water versus alkaline solutions intended to simulated pore solution) used in the research. In a similar manner, it is likely that the presence of a cementitious cover would affect the initiation of corrosion and the subsequent corrosion rate but no known research of this type has been published.
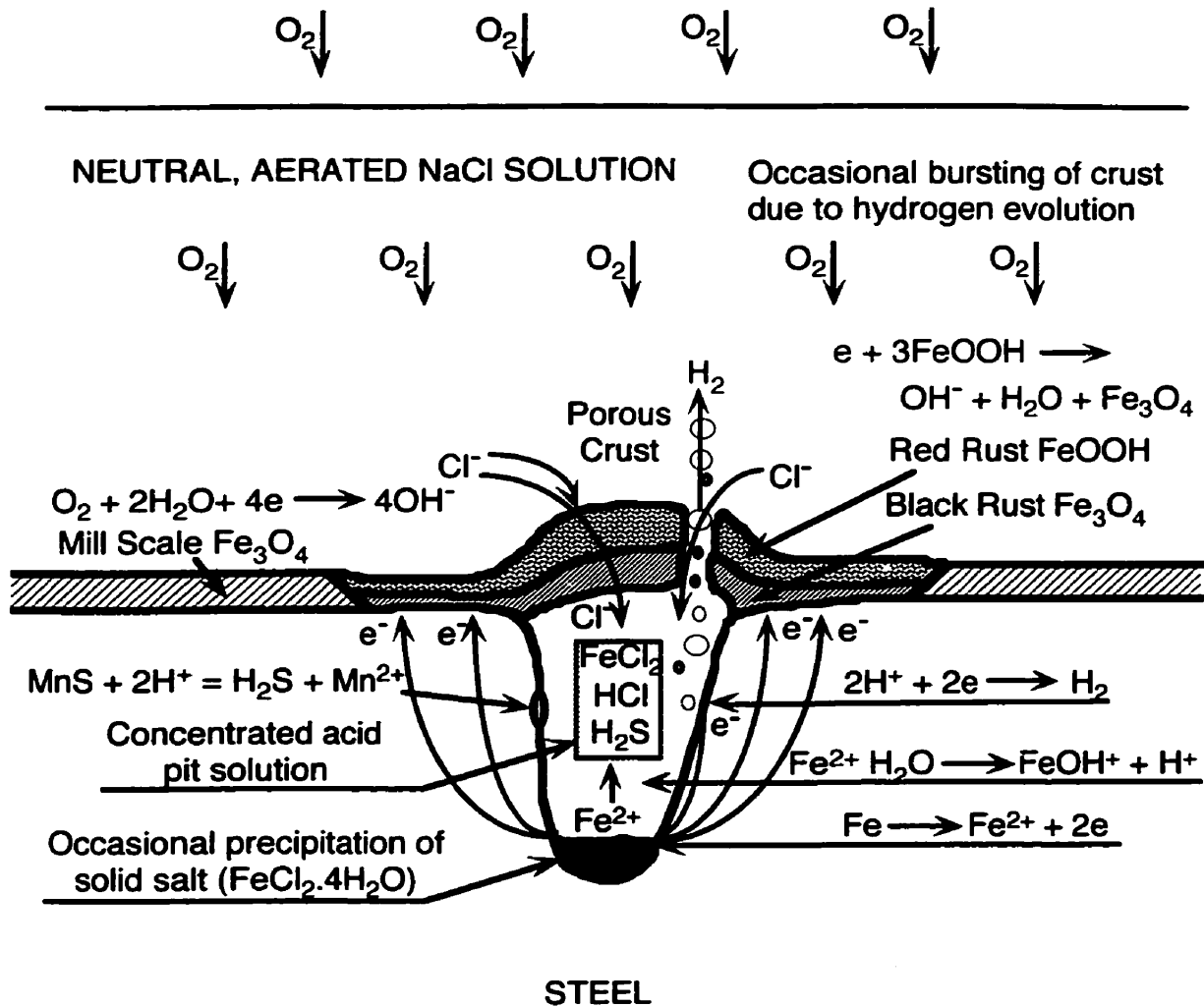
Figure 2.4 Schematic illustration of the chloride-induced corrosion of steel in a neutral, aerated solution (Wranglén 1985).

2.3.2.2 Chloride-Induced Corrosion Products

Herholdt et al. presented the sequence of corrosion products that form on steel according to the availability of water and oxygen present in the system, shown in Figure 2.5 (Herholdt,

Justesen et al. 1985). The corresponding specific volume of these products related to the parent iron metal, shown in Figure 2.6, was estimated using crystallographic data and clearly shows why the formation of corrosion products within concrete is generally thought to cause the cracking and spalling of the concrete cover. Figure 2.5 is oversimplified, however, in four areas: (i) FeO (wüstite) is not considered stable under 843 K and ambient atmospheric conditions (Simmons and Leidheiser 1976); (ii) the green intermediate product does not specify the required presence of either chlorides or other anions such as sulphates; and (iii) the specified end products of magnetite (Fe_3O_4) and "rust" ($Fe(OH)_3 \cdot nH_2O$) do not entirely represent experimentally observed products, a range of ferric oxyhydroxides (α, β, γ and δ-FeOOH) as well as magnetite (Fe_3O_4), hæmatite (α-Fe_2O_3), maghemite (γ-Fe_2O_3), and Green Rust I ($3Fe^{(II)}(OH)_2 \cdot Fe^{(III)}(OH)_2Cl \cdot nH_2O$) (Misawa, Hashimoto et al. 1974; Génin, Rezel et al. 1986; Wolski 1990; Boucherit, Hugot-Le Goff et al. 1991; Refait and Génin 1993). Similarly, the main limitation of Figure 2.6 is that the comparison of the layered structure of iron corrosion products to bulk iron hydroxides and oxides is potentially questionable and must be validated (Shreir, Jarman et al. 1994).

Oxygen Deficiency

Excess of Oxygen

| Iron | Oxygen | Water |

| Iron | Oxygen | Water |

Iron (II) Hydroxide $Fe(OH)_2$
WHITE

Rust $Fe(OH)_3.nH_2O$
BROWNISH YELLOW

Water

Iron (II) oxide   FeO
BLACK

Oxygen

Intermediate product
GREEN

Oxygen

Magnetite Fe_3O_4
BLACK

Water

Iron (III) Hydroxide $Fe(OH)_3$
BROWN

Water

Rust $Fe(OH)_3.nH_2O$
BROWNISH YELLOW
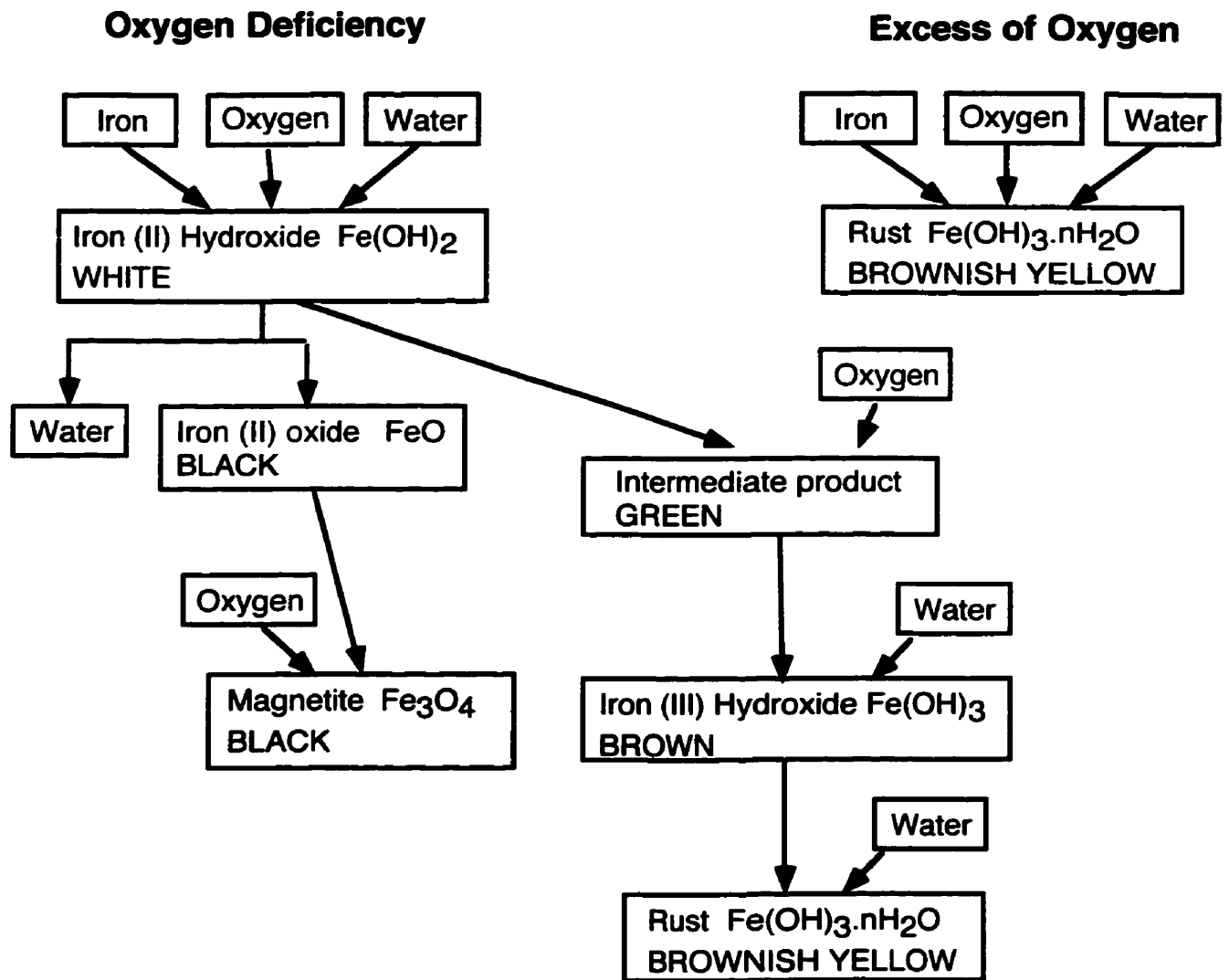
Figure 2.5 Flowchart of Product formed during the Corrosion Process depending upon the Availability of Water and Oxygen (Herholdt, Justesen et al. 1985).
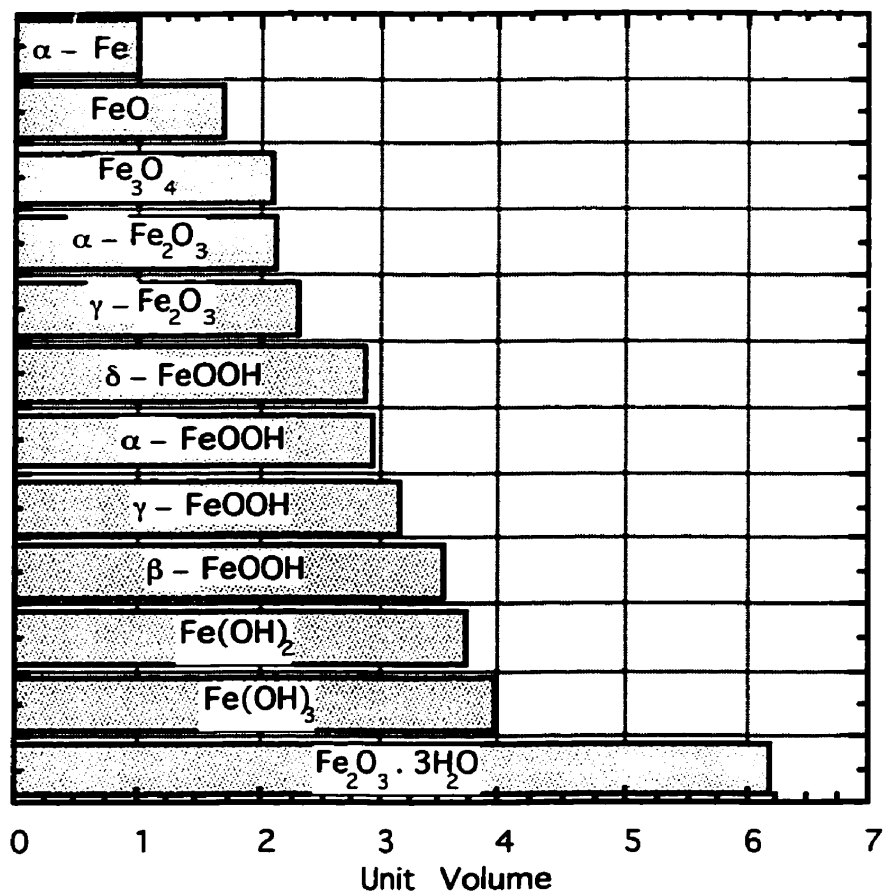
Figure 2.6 The relative volumes of iron corrosion products with all values from the Joint Committee on Powder Diffraction Standards except for $Fe(OH)_3$ and $Fe(OH)_2$ which were estimated from data presented in the CRC Handbook of Chemistry and Physics (Lide 1999).

Experimental work in aqueous solutions has observed that the corrosion products that form on steel depend on the $[Cl^-]/[OH^-]$ ratio in solution in addition to water and oxygen

availability (Misawa, Hashimoto et al. 1974; Génin, Rezel et al. 1986; Refait and Génin 1993). Génin et al. suggested that if $[Cl^-]/[OH^-] \leq 1$, then $Fe(OH)_2$ would form initially but would later oxidize to goethite (α-FeOOH) and magnetite (Fe_3O_4) (Génin, Rezel et al. 1986). Refait and Génin more recently reanalysed the influence of $[Cl^-]/[OH^-]$ ratios on the formation of Green Rust I (GR1) and its corresponding end products as outlined in Table 2.3 (Refait and Génin 1993). This work was summarized as a redox potential-pH diagram, shown as Figure 2.7. A similar product known as Green Rust II (GR2) has a similar structure to GR1 but the chloride ions are replaced with three-dimensional ions such as sulphate or selenate (Legrand, Sagon, et al. 2001).

Table 2.3 Summary of the Corrosion Products Observed for Varying $[Cl^-]/[OH^-]$ Ratios including Green Rust I (GRI) (Génin, Rezel et al. 1986; Refait and Génin 1993).

Ratio of Chloride and Hydroxide Ions in Solution	Initial Product	Intermediate Product	End Product(s)
$[Cl^-]/[OH^-] \leq 1$	$Fe(OH)_2$	-	goethite (α-FeOOH) magnetite (Fe_3O_4)
$1 \leq [Cl^-]/[OH^-] \leq 1.025$	$Fe(OH)_2$	-	hydrated magnetite ($Fe(OH)_2 \cdot 2FeOOH$)
$1.025 < [Cl^-]/[OH^-] < 1.11$	$Fe(OH)_2$	some GRI	hydrated magnetite ($Fe(OH)_2 \cdot 2FeOOH$) oxidized to non-stoichiometric magnetite ($Fe_{3-x}O_4$, $x = 0$ to $1/3$)
$1.11 \leq [Cl^-]/[OH^-] \leq 1.75$	$2Fe(OH)_2$	GRI	lepidocrocite (γ-FeOOH)
$[Cl^-]/[OH^-] > 1.75$	$2Fe(OH)_2$ $\cdot$ FeOHCl	GRI	lepidocrocite (γ-FeOOH) goethite (α-FeOOH) akaganeite (β-FeOOH)
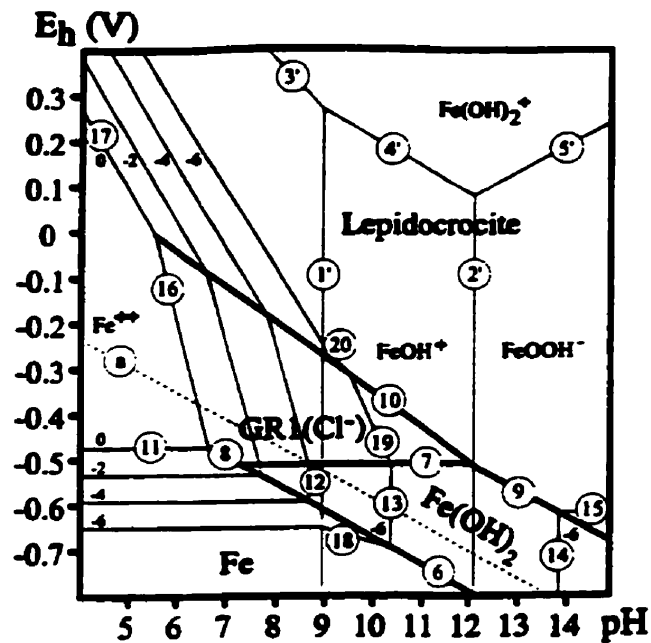
Figure 2.7 Experimentally derived $Fe-H_2O-Cl^-$ redox potential-pH diagram that assumes the molality of iron is 10^{-6} (Génin, Refait et al. 1997).

It is uncertain whether these chloride/hydroxide ratios are accurate for concrete given the inhomogeneous chemistry and the physical constraints of the concrete cover (i.e., species must diffuse through a tortuous pore network). The work reported to date on the corrosion products that form in steel-reinforced concrete has been performed *ex situ* (Suda, Misra et al. 1993; Wang and Monteiro 1996; Leek 1997). Suda et al. identified magnetite (Fe_3O_4), goethite ($\alpha-FeOOH$), and lepidocrocite ($\gamma-FeOOH$) along with unidentified amorphous content in their X-ray diffraction samples (Suda, Misra et al. 1993) while Wang and Monteiro identified goethite ($\alpha-FeOOH$), magnetite (Fe_3O_4), and haematite ($\alpha-Fe_2O_3$) (Wang and Monteiro 1996). These X-ray diffraction results may be unreliable because the *in situ* compounds may have oxidized during the sample preparation process in a manner

similar to the passive film as reported in Section 2.3.1 thus distorting the composition of the original corrosion products observed. The investigation by Leek did not suffer from this disadvantage as SEM and EDS were used to analyze elemental ratios and distributions within cementitious cover and, therefore, oxidation could be excluded from any analyses (Leek 1997). This work focussed more upon the structure of the corrosion products at the steel/mortar interface and within the mortar cover than on the exact composition of the products themselves. However, the drying atmosphere of the SEM might have dehydrated the observed morphologies of the corrosion products. Clearly, there is a significant need for *in situ* observations of the corrosion products that form in concrete along with their spatial distribution, rate of formation, and material properties.

In addition, the effect of the formation of corrosion products on the corrosion rate requires further investigation. Ashworth et al. suggested that the breakdown of passivity followed by corrosion was stifled by the formation of corrosion products that would cover corrosion pits (Ashworth, Boden et al. 1970). Leek illustrated this relationship between corrosion rate and product formation graphically and is shown as Figure 2.8 (Leek 1997). It is likely that the type of corrosion products formed would affect the final corrosion rate as denser products such as magnetite (Fe_3O_4) might offer increased resistance to further chloride ingress and dissolved oxygen than a product like hæmatite (α-Fe_2O_3).
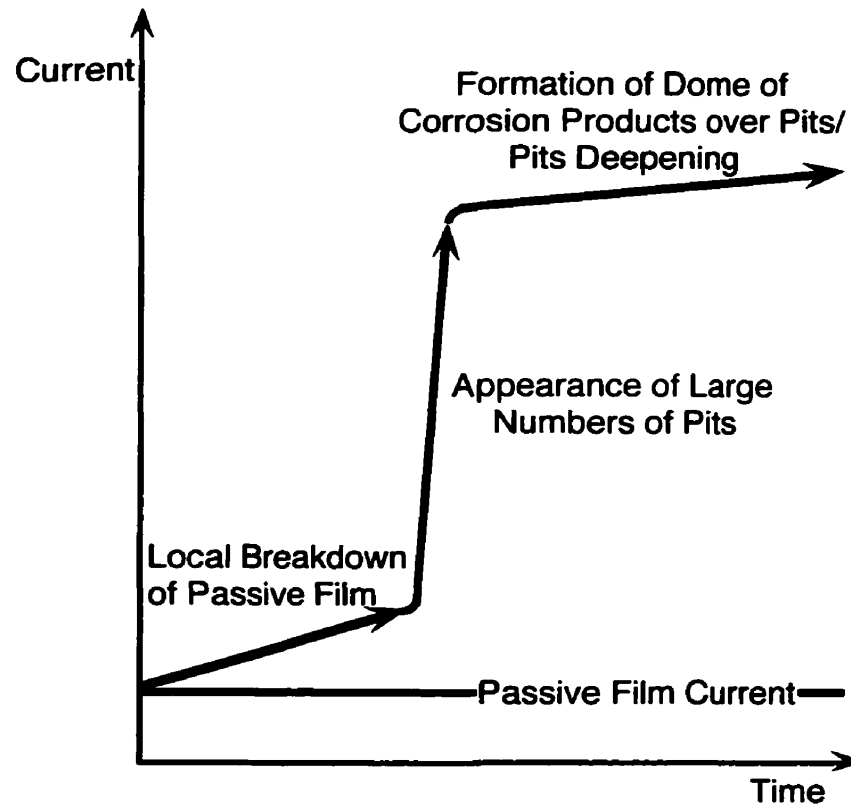
Figure 2.8 Idealized current versus time relationship for the chloride initiated breakdown of the passive film on mild steel in concrete. The work of Ashworth et al. as interpreted by Leek (Ashworth, Boden et al. 1970; Leek 1997).

2.3.3 Effect of Chloride-Induced Corrosion on the Microstructure of Concrete

Little attention has been given to microstructural characterization of concrete during chloride-induced corrosion. It is thought that the impact of chloride-induced corrosion on concrete is confined to cracking of the concrete due to the stresses imposed by the generation of expansive corrosion products at the interface. Monteiro et al. examined the

36

steel/cement interface *ex situ* after corrosion had initiated (Monteiro, Gjørv et al. 1985). They concluded that the formation of dendritic corrosion products spalled the cementitious interfacial products from the surface of the steel that were previously adherent. Whether corrosion products formed away from the steel interface within the cement paste was not reported nor were the composition of the corrosion products and the surrounding cement paste.

In later work, Wang and Monteiro observed corrosion products forming at the steel/concrete interface and within the concrete cover (Wang and Monteiro 1996). The authors suggested that corrosion products shrink and swell under drying and wetting cycles which causes the surrounding cement paste to crack. This conclusion is unlikely because a typical drying cycle would not be able to dry the concrete to the level of the reinforcement (Bakker 1988). Leek observed essentially the same damage but concluded that calcium hydroxide dissolved to counteract the acidification of the pore solution at anodic sites. These formerly occupied spaces could then accommodate corrosion products. Once this volume is exceeded, the corrosion products would begin to exert expansive forces on the cementitious cover. This is the most plausible explanation for the observed behaviour and is consistent with the observations of Allan, described in the next Section (Allan 1995).

More recently, Aligizaki et al. identified corrosion products away from the steel/concrete interface and along the aggregate/concrete interface (Aligizaki, de Rooij et al. 2000). The researchers clearly established the presence of corrosion products with the interface transition zone (ITZ) surrounding the aggregate without any observed cracking using EDS but did not did not perform any compositional analysis. Thus, it is clear that corrosion products can form away from the steel/concrete interface but what remains unknown is to what which corrosion products form and to what extent the ionic species generated by the corrosion process become incorporated into the chemistry and distribution of the cementitious phases.

2.3.4   Effect of Cracks, Microcracks, and Other Defects in Concrete on the Chloride-Induced Corrosion Rates of Steel in Concrete

It is generally accepted that cracks, microcracks (of the order of micrometres), and other defects (millimetres) are inevitable in concrete structures. Consequently, reinforced concrete structures are designed with the assumption that they will crack to ensure structural safety (Darwin, Manning et al. 1985). There exists a considerable debate, however, regarding the influence of existing cracks, microcracks, and other defects both on the initiation and propagation of chloride-induced corrosion. The formation of corrosion products generates internal stresses that eventually crack the concrete cover and accelerate the corrosion process, described in Section 2.2.2.2.

There have been two approaches to this problem to attempt to elucidate the factors that influence the corrosion rate: examining either the cracks that intersect the surface or internal cracks. Many researchers have observed the effect of surface cracks on the corrosion rate of steel in concrete (Dakhil, Cady et al. 1975; Nilsen and Espelid 1985; Okada, Kobayashi et al. 1988; Borgard, Warren et al. 1989; Rasheeduzzafar, Al-Saadoun et al. 1992; Hwang, Chen et al. 1994; Arya and Ofori-Darko 1996). This type of work has identified a complex interaction of parameters that influence the corrosion rate: the orientation of the crack with respect to the reinforcing steel (i.e., intersecting or coincident); the ratio of reinforcement bar diameter to cover depth ratio; the relationship between the width of the crack at the surface of the concrete and its width at the level of the reinforcement; and the density of cracks. The general conclusion of several researchers (Dakhil, Cady et al. 1975; Rasheeduzzafar, Al-Saadoun et al. 1992; Arya and Ofori-Darko 1996) is that increasing the cover depth reduced cracking but Rasheeduzzafar et al. further specified that the size of the reinforcing bar must be considered as well. For corrosion-induced cracks, Nilsen and Espelid observed that once cracks had formed to the level of the reinforcement, an increased cover depth did not affect the rate of corrosion

38

(Nilsen and Espelid 1985).

Fewer researchers have studied the role of internal cracking due to corrosion products (Grimes, Hartt et al. 1979; Andrade and Alonso 1993; Molina, Alonso et al. 1993; Allan 1995; Torres-Acosta and Sagüés 2000). All research, with the exception of the work of Allan, used impressed currents to generate corrosion products that cracked the concrete cover. The application of an impressed current to steel generates a more uniform corrosion layer over the surface of the steel and, therefore, may not replicate the localized nature of chloride-inducedcorrosion.

However, the work Torres-Acosta and Sagüés counteracted this limitation by applying the impressed current to only an electrically isolated portion of a steel bar. Using this technique they observed that the amount of corrosion required to crack the cover of the concrete was approximately 49 to 137 μm but unfortunately a description of the resulting corrosion products and the porosity of the concrete cover was not presented. The conclusions of other research that used hydraulic pressurization at the surface of the steel suggested that if voids and pores were present at the steel/concrete interface, the onset of cracking was delayed (Allan 1995). Clearly research directed towards understanding the factors which influence the internal cracking of concrete is burgeoning but more work remains.

2.4 CHARACTERIZATION OF CORROSION PROCESSES

The use of electrochemical techniques to detect the corrosion of steel in concrete allows for extremely sensitive, fast, and non-destructive assessments. Although electrochemical impedance spectroscopy (EIS), electrochemical noise, and other electrochemical techniques are also used in laboratories and the field, the following techniques were the only ones used in this work.

2.4.1 Open Circuit Potential Measurements

Passivation, pitting corrosion, and general corrosion have been previously described in Sections 2.3.1, 2.3.2.1, and 2.3.2.2, respectively. Active, low potential corrosion results from the absence of oxygen in the environment and leads to the electrochemical reduction of the passive film by Equation 2-5. In this condition, the passive film is unable to sustain itself leaving the bare steel to generally corrode at a slightly higher rate than during passivation (Hansson 1984).

Because of its simplicity, the open circuit potential, also known as the corrosion potential, E_{corr}, is the most widely used electrochemical measurement (Rodríguez, Ramírez et al. 1994). In the case of steel in concrete, this is a relative measure of the ease of electron charge transfer from steel to its pore solution (Hansson 1984). It is a property of the steel/concrete interface and not of the steel itself. It cannot be measured absolutely and must be measured as a potential difference with respect to a reference electrode (e.g., saturated calomel electrode, SCE). An accurate interpretation of this measurement requires a knowledge of the moisture, oxygen availability, and the occurrence of galvanic macrocouples to generate accurate information about reinforced concrete structures (Rodríguez, Ramírez et al. 1994).

The information provided by the technique is the probability of whether corrosion is occurring but not a corrosion rate and is, therefore, limited in its use. Table 2.3 presents the interpretation of these probabilities associated with a given measurement (Arup 1983).

Table 2.4 The four states of corrosion of steel in concrete (Arup 1983).

Open Circuit Potential mV SCE	State of Corrosion of Steel in Concrete
+100 to -200 (aerated) +200 to -600 (deaerated)	Passive
-200 to -500	Pitting
-450 to -600	General
≤ -1000	Active, Low Potential Corrosion

2.4.2 Full Cyclic Potentiodynamic Polarization Measurements

Full cyclic potentiodynamic polarization curves are relatively non-destructive measurements that provide information, including the corrosion rate, about the behaviour of reinforcing steel at potentials other than the open circuit potential (Hansson 1986). This measurement is accomplished with a three electrode system where the specimen (the reinforcing steel) is held at ground and a potential difference is applied between a counter electrode and a reference electrode (Figure 2.9). The resulting potential difference between the specimen and the reference electrode is measured along with the current that flows between the steel and the counter electrode by a potentiostat.
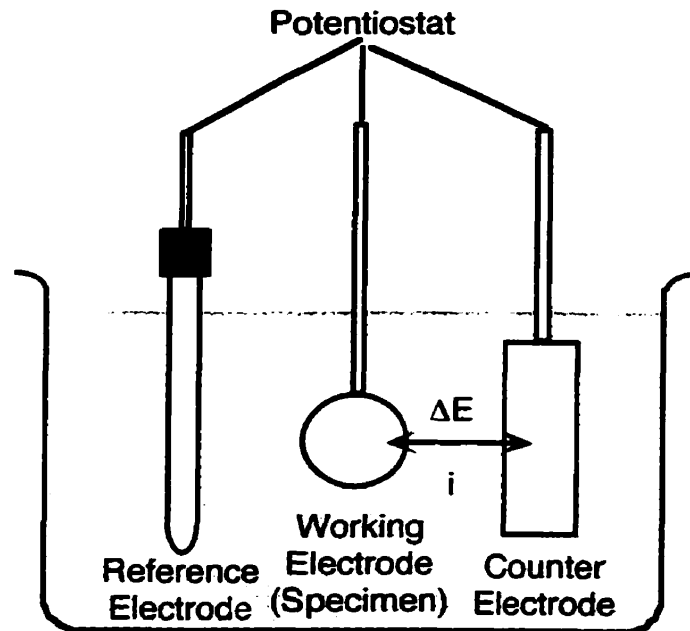
Figure 2.9 Schematic illustration of the three electrode measurement system.

For studies of steel in concrete, the applied potential is usually swept anodically and then cathodically, typically at a rate of 1 mV/s or slower. To minimize the alteration of the steel/mortar interface, the potential is kept below the oxygen evolution line but above the hydrogen evolution line, Figure 2.10. These potentials are indicated by the dashed lines (b) and (a), respectively, in Figures 2.3 and 2.7.
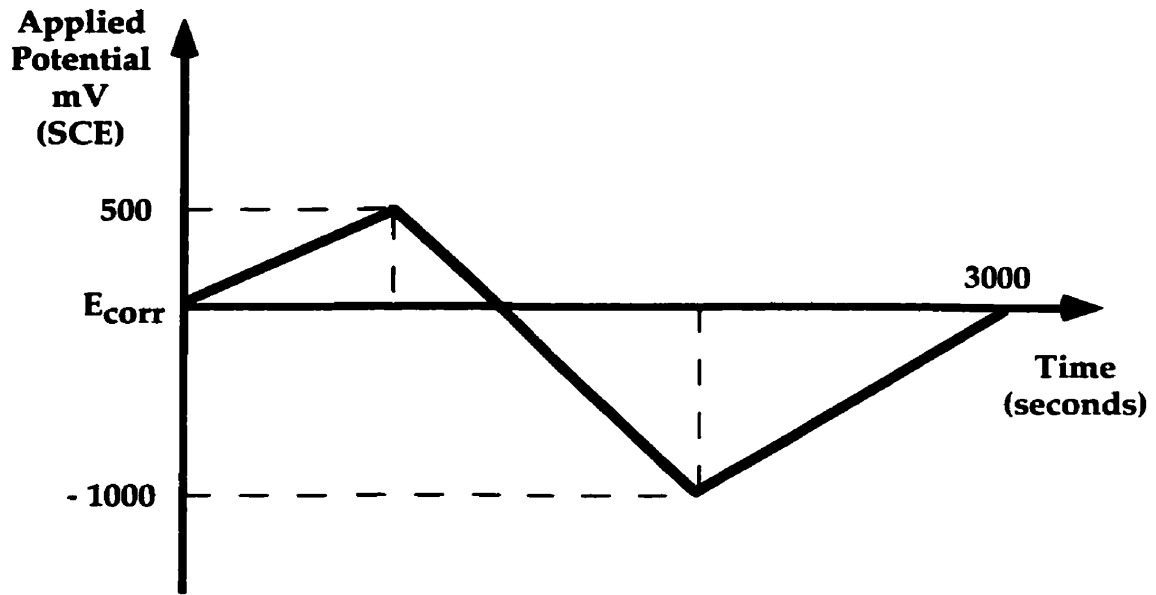
Figure 2.10 Graphical illustration of the potentials applied over time during full cyclic potentiodynamic polarization measurements.

When the applied potential is plotted versus the logarithm of the measured current density, the corrosion rate at the open circuit potential can be calculated in the manner described in Section 2.4.4. The information provided by the anodic portion of the curve includes: (i) the ability of the steel to passivate in a certain medium; (ii) the potential region where the steel remains passive; and (iii) the corrosion rate in the passive region, Figure 2.11 (EG & G 1980). If steel were to actively corrode, the magnitude of the current density and shape of the hysteresis loop would indicate the nature of the corrosion (i.e., pitting or general corrosion), Figure 2.12. The cathodic portion of the curve indicates the corrosion rate of the bare steel and any oxygen limitation during oxygen reduction, Figure 2.11. In addition, examining the slopes of these curves can emphasize changes in the surface of the steel which indicate the formation or destruction of products at different potentials. Overall, a

43

great deal of information about the electrochemical behaviour of a metal in a certain electrolyte can be collected using this technique.
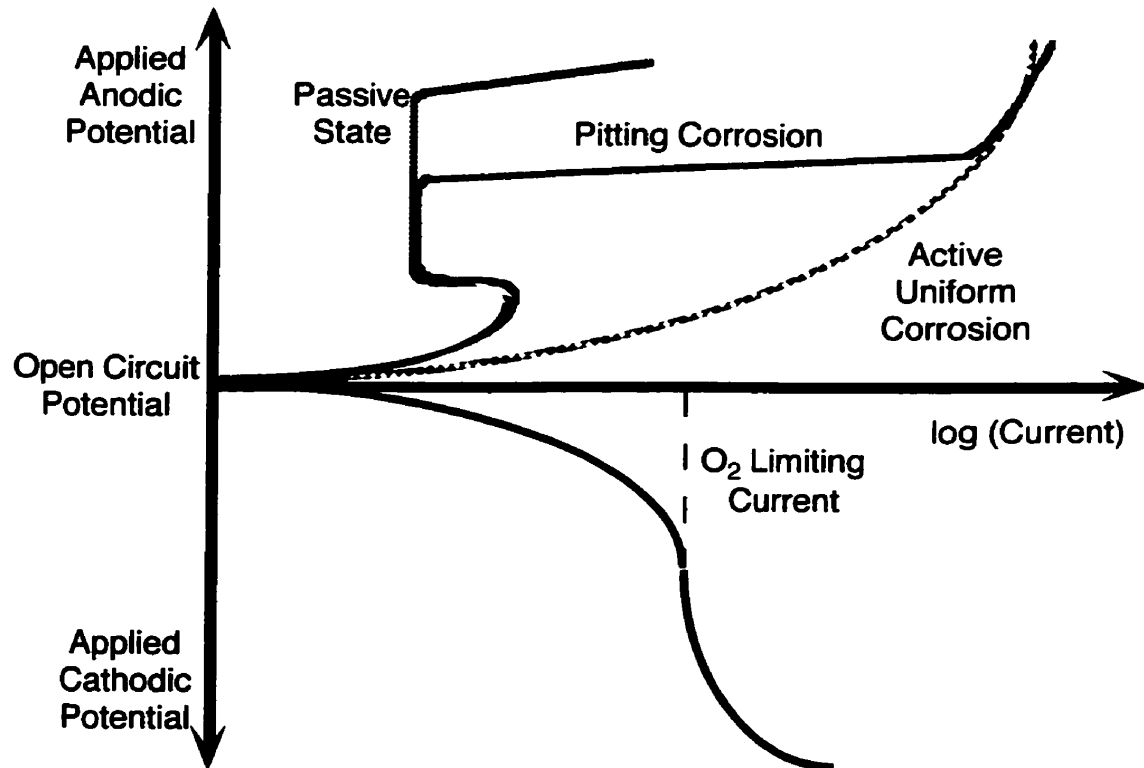
Figure 2.11 Graphical representation of the information provided by the anodic and cathodic portions of the full potentiodynamic polarization curves (modified from Enevoldsen (1993)).
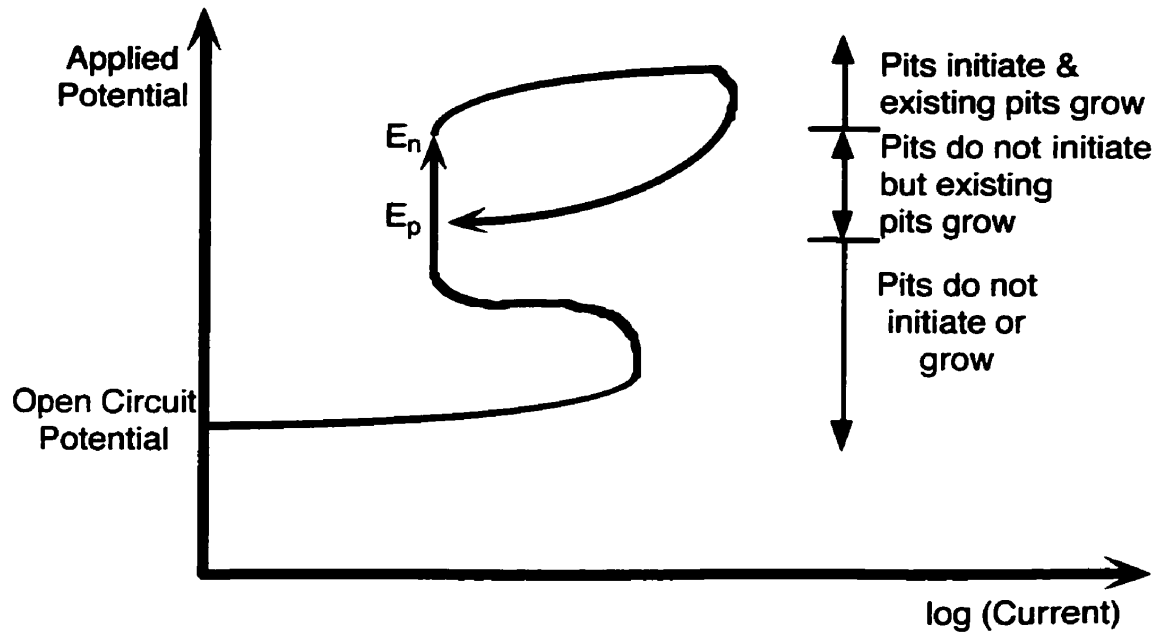
Figure 2.12 Interpretation of the anodic hysteresis loop of the full potentiodynamic polarization curve undergoing active corrosion (Mammoliti 1995). E_n represents the pitting potential while E_p represents the passivation potential.

The disadvantages of this technique include: (i) it requires hours or days to perform, and (ii) it is necessary to polarize the steel well away from the natural corrosion potential of the reinforcing steel (Hansson 1986). Also, under some circumstances, the application of potentially a few hundred millivolts can change the local environment surrounding the steel for a period of time. However, this effect is temporary and the open circuit potentials have been observed to drift back to their original value after a period of time indicating the restoration of the original conditions (Hansson 1986).

2.4.3 Linear Polarization Resistance Measurements

This is the most commonly used technique for determining corrosion rates (Rodríguez,

Ramírez et al. 1994). It is a rapid technique which determines the instantaneous corrosion rate by sweeping the potential of the steel ± 20 mV around the open circuit potential and observing the corresponding changes in the current. Similar to full potentiodynamic polarization measurements, this action biases either the anodic or cathodic reactions such that the system is shifted away from the equilibrium present at the open circuit potential and a net current can, therefore, be measured.
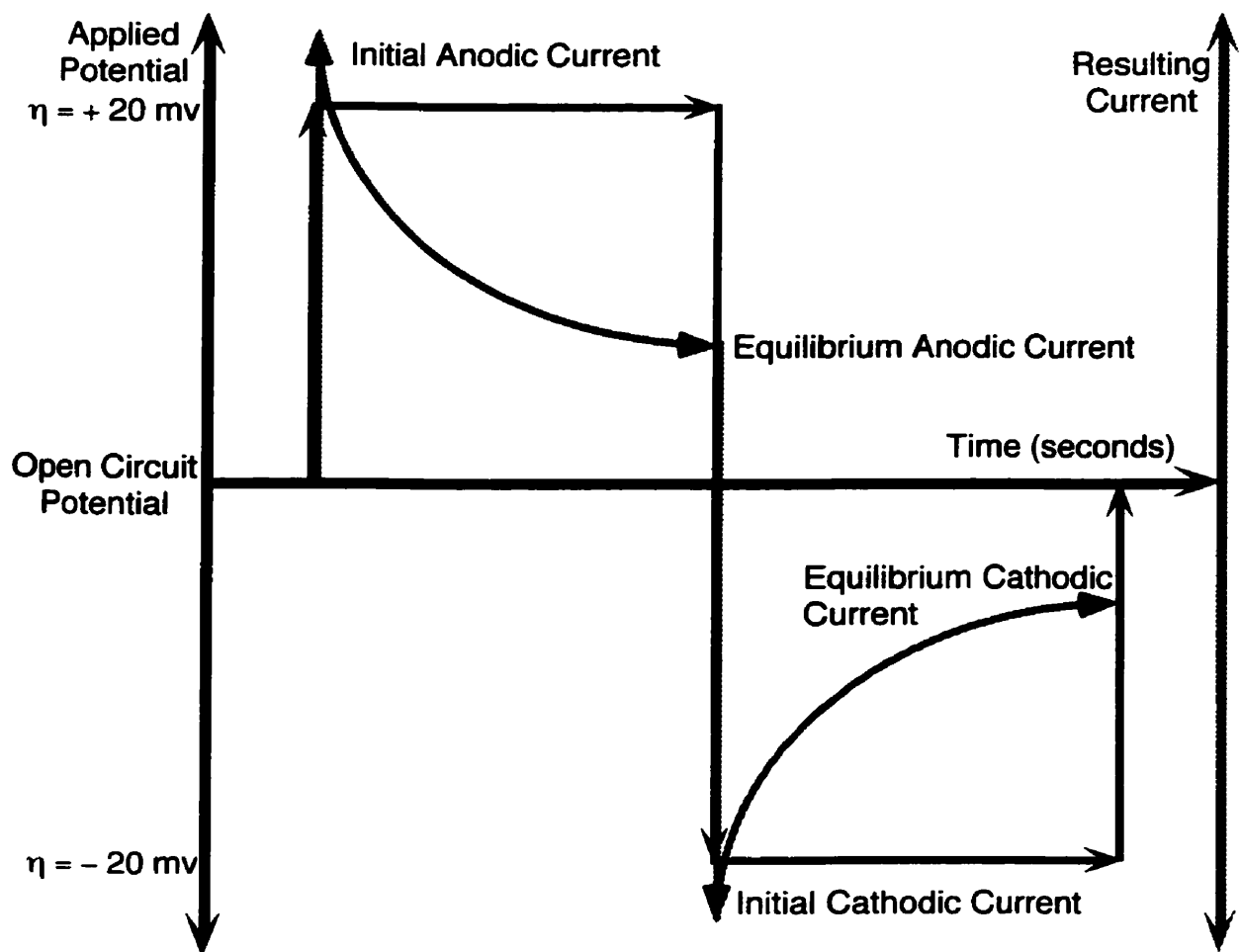
Figure 2.13 Graphical illustration of the potentials applied over time and resulting current during linear polarization resistance measurements where h represents overpotential.

This measurement is accomplished with the same three electrode system used for full potentiodynamic polarization measurements (Section 2.4.3).

In the small range of potentials studied, the slope of the applied potential, ΔE, versus the measured current, Δi, is considered to be linear as ΔE approaches zero. This slope is related to the corrosion rate, i_{corr}, by Equation 2-8, developed by Stern and Geary (Stern and Geary 1957).

$$\left(\frac{\Delta E}{\Delta i}\right)_{\Delta E - 0} = R_p = \frac{\beta_a \beta_c}{2.3 \, (i_{corr}) \, (\beta_a + \beta_c)} \qquad (2\text{-}8)$$

R_p is known as the polarization resistance, and β_a and β_c represent the Tafel constants of the anodic and cathodic currents, respectively. These constants can be experimentally determined from a full potentiodynamic polarization curve (Figure 2.8) or a simplification is often made, Equation 2-9,

$$i_{corr} = \frac{\beta_a \beta_c}{2.3 \, (\beta_a + \beta_c)} \cdot \frac{\Delta i}{\Delta E} = \frac{B}{R_p} \qquad (2\text{-}9)$$

where B represents a value ranging from 13 to 52 mV in most metal/medium systems (EG & G Research 1980). Andrade and González concluded that B = 26 mV and B = 52 mV gave sufficiently representative values for steel undergoing active microcell corrosion or passive corrosion, respectively (Andrade and González 1978).

Problems arise in interpreting this value of the corrosion current because the area actually corroding cannot be determined non-destructively for steel embedded in concrete. If the corrosion current is divided by the entire embedded portion of the steel, the corrosion current density may be underestimated, for example, where the cause of the corrosion is chloride-induced pitting. Chloride-induced pits may represent only a small portion of the entire surface of the steel but may carry almost the entire corrosion current. These measurements are, therefore, best suited for relative comparisons of specimens.

2.4.4 Raman Spectroscopy

Raman spectroscopy uses the vibrational signature of molecules within a sample to identify its constituents. Figure 2.14 illustrates the Raman effect where monochromatic incident light excites a molecule and is subsequently scattered. Most of the scattered light will have the same frequency as the incident light, known as Rayleigh scattering, while some will be scattered at a different frequency. This corresponds to changes in molecular motion (i.e., the bonds vibrate). The difference in the frequency between the incident and scattered light is known as a Raman shift. Since molecules often have multiple bonds, multiple Raman shifts that are characteristic to the molecule can be detected. These characteristic shifts can be mathematically predicted by quantum chemists but these precise computations are costly and time consuming. More commonly, experimental results are compared to reference standards.

This technique offers advantages over XRD in that its analyses are relatively fast (< 1 min.), have excellent spatial resolution (as low as 1 μm), are suitable for very small samples (e.g., 1 mm^3), and can be performed *in situ* with aqueous phases. As a result, the Raman spectroscopy technique is sensitive to changes in the molecule and the environment in which it is under investigation. This technique is typically used for structural determination measurements, multicomponent qualitative analysis, and quantitative analysis. It is, therefore, well-suited for corrosion product analyses given the instability of corrosion products under analysis, especially *ex situ*, as described in Section 2.3.1.

48
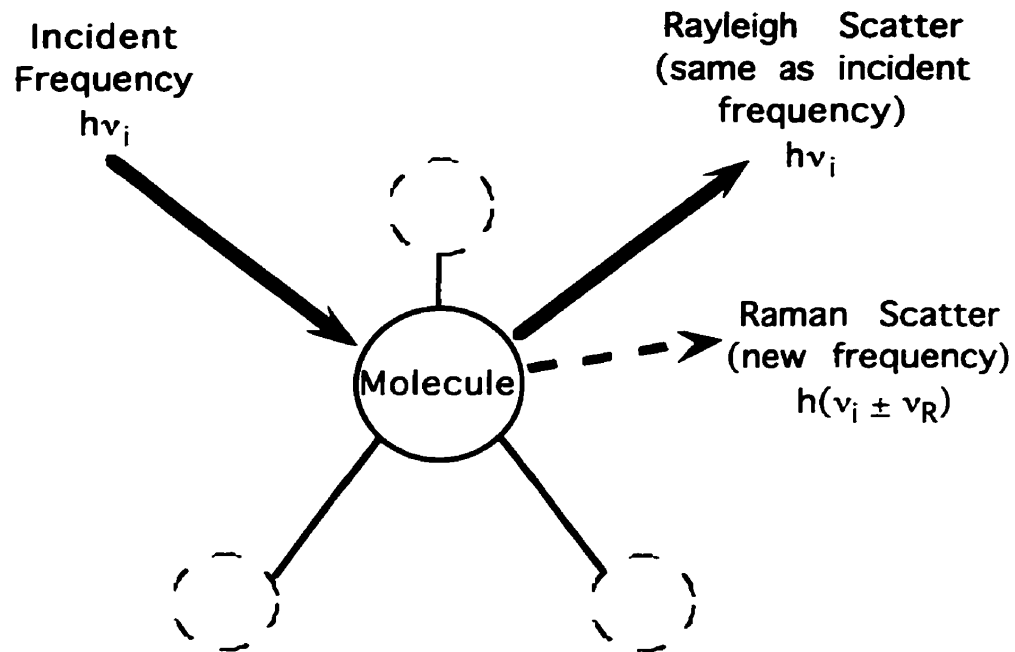
Figure 2.14 Schematic illustration of the Raman effect where h represents Planck's constant, and n_i and n_R represent the initial frequency and the scattered frequency, respectively. The new frequencies are known as Raman shifts.

Many researchers have studied the corrosion of steel (de Faria, Venâncio Silva et al. 1997; Oblonsky and Devine 1997), including those formed in alkaline solutions (Thierry, Persson et al. 1991; Simpson and Melendres 1996), and solutions containing chlorides (Raharinaivo and Génin 1986; Boucherit, Hugot-Le Goff et al. 1991; Melendres, Pankuch et al. 1992; Raharinaivo, Guilbaud et al. 1992; Refait and Génin 1993; Guilbaud, Chahbazian et al. 1994). In addition, other research has focussed upon the minerals comprising cement and cement paste (Tarrida, Madon et al. 1995; Kirkpatrick, Yarger et al. 1997) including carbonate minerals (Herman, Bogdan et al. 1987). Thus there is a considerable wealth of information for use in new research which combines corrosion studies and cementitious materials.

2.5 SERVICE LIFE PREDICTIONS OF STEEL-REINFORCED CONCRETE STRUCTURES

"Service life" of steel-reinforced concrete can have a broad range of definitions but these can be organized into three categories: technological service life, useful service life, and structural service life. Technological service life is the age at which a structure becomes obsolete because of technological improvements in the construction industry. The useful service life is the limit at which time a given structure is unable to accommodate the function for which it was designed (e.g., an overpass may be constructed to accommodate only a certain amount of traffic flow and over time, this flow may increase to the point where the overpass may be too congested for efficient travel.). Structural service life refers to the age where a structure is no longer able to fulfil its design criteria safely (e.g., from structural overload and/or deterioration caused by the service environment). For the purposes of this research, the structural service life is considered the time when repair or replacement is required as a result of chloride-induced corrosion of the steel reinforcement.

2.5.1 Structural Service Life Estimation for Chloride-Induced Corrosion Processes

Clifton identified five methods for estimating the service life of a structure: experience, deductions of performance from existing materials, accelerated testing, mathematical modelling based upon the chemistry and physics of degradation processes, and applications of reliability and stochastic concepts (Clifton 1993). Since construction materials change significantly over decades of construction, it is extremely difficult to deduce the future performance of new construction from existing materials and previous experiences. Furthermore, the use of accelerated testing by some researchers for chloride-induced corrosion is not entirely appropriate because of the localized nature of the corrosion process (Grimes, Hartt et al. 1979; Andrade and Alonso 1993; Molina, Alonso et al. 1993).

Mathematical models, and reliability and stochastic concepts are often applied in an

attempt to overcome the aforementioned limitations (Morinaga 1988; Vesikari 1988; Funahashi 1990; Cady and Weyers 1991; Fitch, Weyers et al. 1995; Bentz, Clifton et al. 1996; Poulsen 1996; Shibata 1996). However, this type of work again relies upon data provided from existing structures whose construction materials and practices may differ from new materials and current practices (e.g., curing regimes). Fagerlund added that stochastic models are valid only for the environments studied and may not be reliable for another structure in its own unique environment (Fagerlund 1982). It then becomes important to determine the processes that contribute to the deterioration of reinforcing steel in concrete due to chloride-induced corrosion such that all materials, whether new or old, can be appropriately assessed with theoretical models rather than the empirical ones currently in use. Bazant attempted to correlate corrosion processes in marine structures using mathematical formulae to develop a more accurate physical/theoretical model (Bazant 1979). This work was limited by the assumptions that were used to deduce important numerical values of certain coefficients because direct measurements were unavailable, and the types of corrosion products formed were restricted to ease the calculations process. More comprehensive information concerning the chloride-induced corrosion products that form would dramatically improve such models.

2.5.2 Theoretical Models of Chloride-Induced Corrosion on Steel in Concrete

Chloride-induced corrosion failure of the reinforcement is most often modelled as a two-stage phenomenon: initiation and propagation (Tuutti 1980), schematically illustrated in Figure 2.15. The initiation stage is the period during which chlorides ingress through the concrete cover and ends when a sufficient concentration of chlorides reach the reinforcing steel and initiate corrosion. Modelling the initiation of chloride-induced corrosion is complicated by the fact that chlorides can be incorporated into the the cement paste and

thus, the presence of high chloride concentrations in concrete does not mean that all chlorides contribute to the deterioration of the reinforcing steel. In spite of this complication, the initiation stage is generally estimated from chloride threshold values, effective diffusivities, and the ambient concentration of chlorides (Tuutti 1980).

The propagation stage (Figure 2.15) is the period during which the corrosion rate and the accumulative amount of corrosion products gradually increases until an unacceptable level of deterioration has occurred. "Significant deterioration" can be spalled concrete, a reduction in structural integrity (Browne 1986), or simply an aesthetics issue depending upon the specific structure and circumstances. The corrosion rate during this stage depends chiefly upon the availability of water and oxygen at the steel/concrete interface, the ability of the iron and hydroxide ions to migrate between the anodic and cathodic sites, the solubility of the corrosion products, and the ambient conditions. This stage is extremely difficult to model because the type of corrosion products formed, and their distribution along the reinforcing steel and within the concrete cover determines when and where the concrete will crack and spall, and these factors are not understood. It is primarily for this reason that most service life predictions are limited to determining the time required to initiate corrosion (Andrade and Alonso 1993).
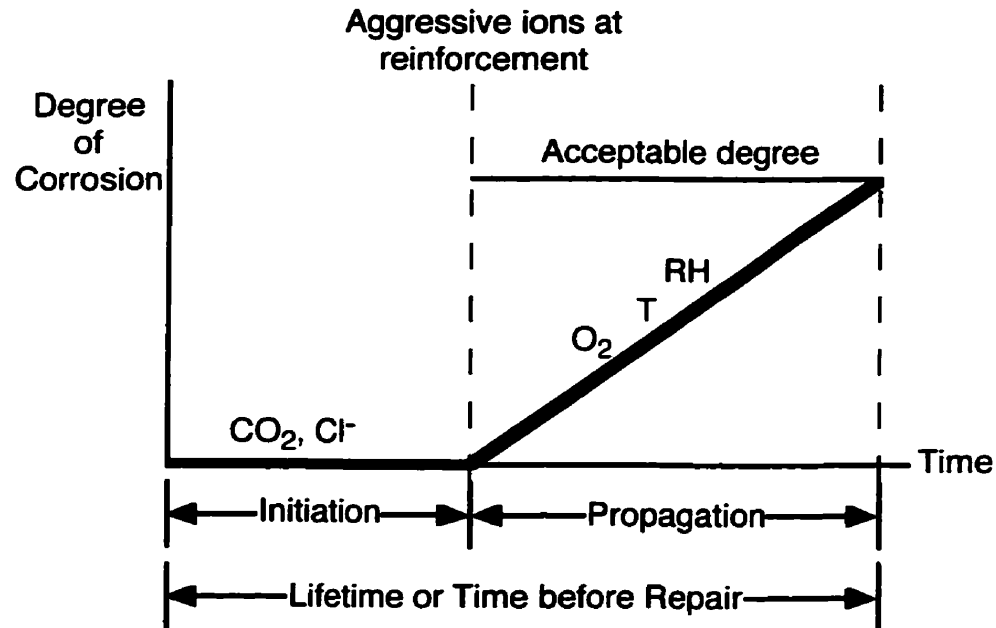
Figure 2.15 Schematic representation of the corrosion process of steel in concrete where T represents temperature and RH represents relative humidity (Tuutti 1980).

This determination is a financially impractical approximation because it is generally understood that propagation stage of corrosion may last for several years (i.e, it may take several years of active corrosion) before sufficient damage has occurred that merits repair or replacement (Browne 1986). Theories accounting for this period are described in Section 2.3.2.2. Thus, the necessary information for theoretical models includes the types of corrosion products formed, their distribution along the reinforcing steel and within the concrete cover, their rate of formation, the resulting local corrosion rate of the reinforcing steel, and the influence of the local chemistry of the concrete adjacent to the corrosion. These factors have not been addressed in literature.

CHAPTER THREE

EXPERIMENTAL PROCEDURES

To accomplish the objectives of this investigation, a range of cementitious systems was studied. The corrosion processes that occurred on steel in simulated pore solution were compared with studies of modified cement paste as well as concrete. The investigation is summarized in Figure 3.1 and Tables 4.4 (Chapter 4), 5.2 (Chapter 5), and 6.4 (Chapter 6) summarize the specimens used to study the listed parameters. This Chapter is intended to describe the experimental techniques used during this research programme.

```
CHAPTER 4
CORROSION OF STEEL IN
SIMULATED PORE SOLUTION
- effect of pore solution composition
 - effect of surface finish of steel
 - effect of chloride concentration
```

```
CHAPTER 5
CORROSION OF STEEL IN
MODIFIED CEMENT PASTE
 - effect of cement type
 - effect of surface finish of steel
  - effect of shrinkage cracks
 - effect of exposure conditions
```

```
CHAPTER 7
DISCUSSION
 - effect of a cementitious cover
 - influence of chloride ion source
  - effect of cracks
 - effect of steel surface finish
```

```
CHAPTER 6
CORROSION OF STEEL IN
CONCRETE
 - effect of concrete type
 - effect of loading cracks
  - effect of silica fume
  - effect of sea water
```

Figure 3.1 Investigation summary.

54

3.1 CHARACTERIZATION OF MATERIALS

3.1.1 Cement

In total, three cements were used for all work in this experimental programme, two ordinary Portland cements and one white Portland cement (i.e., one of the ordinary Portland cements and the white Portland cements were used exclusively in the laboratory while the second ordinary Portland cement was used only for the field concrete specimen preparation). Two types of cement were used to cast the cement paste specimens used in Chapters 4 and 5: white Portland cement similar to a sulphate resisting Type 50 and an ordinary Portland cement (Type 10). The white cement was acquired from Aarlborg Portland in Denmark while the Type 10 cement was produced by Lafarge Canada in Woodstock, Ontario. Another ordinary Portland cement was used to cast the specimens used in Chapter 6 which was manufactured by Tilbury Cement Company of Delta, British Columbia. The composition of all cements is given in Table 3.1(a). All data concerning the cements was provided by their respective manufacturers.

From the compositional analyses of the cement powders, the relative amounts of the major constituents of the cements were calculated using the Bogue method[1] and are reported in Table 3.1(b). The use of the white Portland cement was considered especially important because of its relatively low iron content. It was thought that this cement would simplify the studies of the corrosion products. The white Portland cement, however, added some complexity to the analyses as it differed chemically from the ordinary Portland cement (Type 10) and was ground considerably finer than the ordinary Portland cement (Type 10) (i.e., Blaine 410 versus 368 m^2/kg). The influence of the differing chemical composition and physical properties are noted in the relevant sections of Chapter 5.

---

[1] The potential equilibrium composition of cement is obtained from the known percentage of oxides present in the cement using equations developed by R.H. Bogue and others (Neville, 1973; Bye, 1983).

Table 3.1(a) Cement compositions (Analyses courtesy of Aalborg Portland, Lafarge Canada, Inc., and Tilbury Cement Company).

Constituent	Chap 4 & 5 White Portland	Chap. 4 & 5 Ordinary Portland	Chap. 6 Ordinary Portland
SiO_2	25.01	20.66	21.30
Al_2O_3	1.91	4.87	4.65
Fe_2O_3	0.32	2.46	3.20
CaO	69.34	65.59	65.15
MgO	0.56	1.91	0.80
SO_3	2.10	3.11	2.82
Na_2O	0.17	0.10	0.09
K_2O	0.12	0.43	0.19
TiO_2	0.09	-	-
Cl	0.008	-	-
Loss on Ignition	0.41	2.00	1.86

Table 3.1(b) Relative amounts of important cement constituents determined by the Bogue method[2] using the information provided in Table 3.1(a) and other physical properties (Courtesy of Aalborg Portland, Lafarge Canada, Inc., and Tilbury Cement Company). The balance of the cement powder is composed of free lime (CaO), excess MgO, clinker sulphates (i.e., Na_2SO_4, K_2SO_4, $CaSO_4$), insoluble residue, and residual contributions from phases not included in the calculations.

Compound	Chap. 4 & 5 White Portland	Chap. 4 & 5 Ordinary Portland	Chap. 6 Ordinary Portland
Tricalcium Silicate (C_3S)	73	64.9	60
Dicalcium Silicate (C_2S)	17	10.3	16
Tricalcium Aluminate (C_3A)	4.5	8.7	7
Tetracalcium Aluminoferrite (C_4AF)	1.0	7.5	10
Sodium Equivalent	0.25	0.38	0.19
Blaine (m^2/kg)	410	368	300-350*

* Not known but assumed range for typical Type 10 cement.

3.1.2 Supplementary Cementitious Materials

Some of the concrete cast for the work of Chapter 6 contained silica fume and Type F fly ash. The silica fume was predominately SiO_2 while the composition of the Type F fly ash (siliceous) used in Chapter 6 is listed in Table 3.2. The fly ash was acquired from Pozzolanic International and approximately 83% of the material passed through a 45 μm sieve. Although the fly ash complies with ASTM C 618, the minor presence of Fe_2O_3 complicates any corrosion product analyses. However, it was preferred to have concrete mix designs that represent common practice such that any conclusions drawn from this research could be directly applied to the construction industry.

Table 3.2 Composition of the Type F fly ash used in Chapter 6. The balance of the material is composed of Na_2O, MgO, K_2O, and C.

Constituent	Mass Percentage
SiO_2	49.45
Al_2O_3	23.50
Fe_2O_3	6.35
SO_3	0.51
CaO	7.91
Moisture Content	0.05
Loss on Ignition	0.16

3.1.3 Aggregates

The predominantly silica sand (99.60 mass% SiO_2) used in the work described in Chapter 5 was white, hard, and rounded with a fineness of 2.65. It was desired to have as homogenous a sand as possible such that it could be easily excluded from any analyses (e.g., microstructural, chemical) of the cement paste, steel, and any corrosion products. This sand conformed with the requirements of CAN/CSA-A23.1 (Canadian Standards Association 1990) and was only added to the cement pastes to reduce cracks arising from drying and chemical shrinkage. For the concrete prisms cast for the work of Chapter 6, commonly available sand and coarse aggregate, largely composed of silica, and orthoclase $(KAlSi_3O_8)$ and albite $(NaAlSi_3O_8)$, respectively, was used that also conformed with CAN/CSA-A23.1. These hard, angular aggregates are typical of those used in Vancouver,

British Columbia for concrete construction and are similar to those used in other parts of Canada.

3.1.4 Water

Distilled water was used to prepare any simulated pore solutions (Chapters 4 and 5), and also to cast the modified cement paste specimens (Chapter 5). Distilled water was used also for all titrations, and any other solutions so that measurements made concerning the corrosion products and cement paste would be as free as possible from extraneous ions. Potable water was used to cast the concrete specimens (Chapter 6).

3.1.5 Steel

The steel used for the work of Chapter 6 is a typical ribbed, reinforcing steel that is commonly used in concrete practice and conforms with CSA/CAN-G30.18 (Canadian Standards Association 1992). For the steel used in the work of Chapters 4 and 5, it was desired to simulate the commercially available reinforcing steel as closely as possible (including mill scale) without the geometric complication of the ribs. For this reason, a plain carbon steel plate was selected for use in the work of Chapters 4 and 5. Its composition, detailed in Table 3.3, and physical properties (yield strength: 310-379 MPa; ultimate tensile strength: 497-538 MPa) conform with the requirements of CSA/CAN-G30.18. In addition, the steel had been hot-rolled between 925 - 1150°C and then air-cooled such that a black-coloured mill scale covered the exposed surface of the steel bar. This mill scale was intended to match as closely as possible the mill scale that is formed on typical steel reinforcement. Raman spectroscopy of the mill scale showed that it was largely composed of magnetite (Fe_3O_4) with a surface layer of haematite (α - Fe_2O_3) and goethite (α - FeOOH), shown in Figure 3.1, which is generally accepted as the bulk

composition of mill scale.

Table 3.3 The alloying components of the steel used (Provided by Kitchener Steel).

Element	Mass Percentage
Silicon	0.300
Sulphur	0.041
Phosphorus	0.017
Manganese	0.880
Carbon	0.160
Nickel	0.100
Chromium	0.180
Molybdenum	0.056
Copper	0.290
Vanadium	0.028
Boron	0.003
Zirconium	0.002
TOTAL	2.057
Iron	Balance
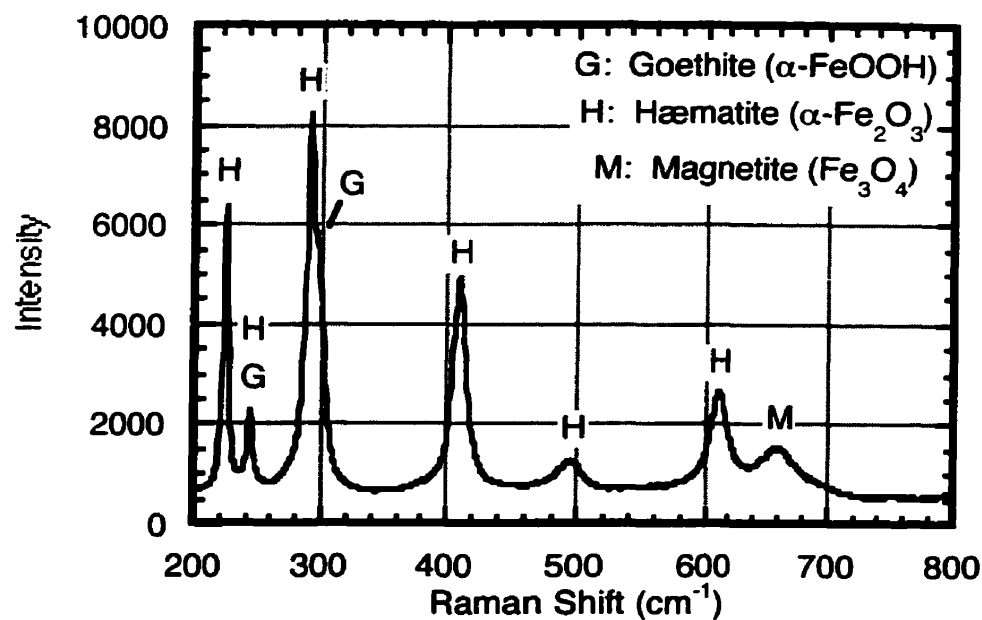
Figure 3.1.5 Composition of the bar mill scale as determined by Raman spectroscopy.

3.1.6 Chemical Reagents

All chemical reagents used were analytical grade materials. These reagents included: sodium chloride (NaCl), calcium hydroxide ($Ca(OH)_2$), sodium hydroxide (NaOH), potassium hydroxide (KOH), aluminum oxide (Al_2O_3), anhydrous isopropan-2-ol (C_3H_8O), hydrochloric acid (HCl), nitric acid (HNO_3), sulphuric acid (H_2SO_4), methyl orange indicator, and silver nitrate ($AgNO_3$).

3.2 CHARACTERIZATION TECHNIQUES

3.2.1 Pore Solution Expression and Analysis

Pore solution was extracted from hardened cementitious materials under high pressures (about 500 MPa) using a device that was based upon the unit described by Barneyback and Diamond (1981). For each pore solution analysis, a cement paste cylinder (Ø51 x 102 mm) was demoulded and immediately placed within the central chamber to prevent any evaporation of water from the cylinder. The central chamber and hardened steel plunger had been lubricated with a hydrophobic, dry carbon which was considered to not affect subsequent chemical analyses. The sample was then covered by a 6 mm thick nylon disc and covered by the plunger. The specimen was subsequently compressed to 150 MPa, followed by 345 MPa, and finally a maximum pressure of 494 MPa, holding each pressure for 10 min. The resulting fluid was passed through a 0.45 μm filter that had been pre-rinsed with about 20 mL of distilled water.

The filtered pore solution was then diluted by mass to a 1:5 ratio[2] and divided into two representative samples. One of the pair of samples was subsequently acidified to a pH less than 2 using reagent grade hydrochloric acid to stabilize it until a cation analysis could be conducted. The pair of samples was then analyzed at the Solutions Laboratory (formerly Water Quality Laboratory) at the University of Waterloo. Inductively coupled plasma (Thermo Jerrell Ash Iris Plasma Spectrometer) was used to identify the cations in the acidified sample while ion chromatography (Dionex Ion Chromatograph, 4400 Integrator, AS4A IonPac Column) was used to identify the anions. All results are considered accurate within ± 2.5% of the reported values, as determined by the Solutions

---

[2] The volume of pore solution expressed from each cylinder was typically 1-2 mL which made it difficult to accurately apportion the sample without dilution. In addition, the pH of the solution was too high without dilution for the subsequent analyses at Solutions at that time. Within the last two years, the analytical techniques have been sufficiently calibrated to permit direct analyses on undiluted samples greater than 4 mL.

Laboratory.

3.2.2 X-ray Diffraction (XRD) Analyses

Chemical compounds can be identified using X-ray diffraction (XRD) which measures crystallographic interplanar spacings (d) using X-rays of a known wavelength (λ) over a range of contact angles (θ) in accordance with Bragg's Law where n represents the interplanar spacing under consideration, Equation 3-1.

$$n\lambda = 2\ d \sin \theta \qquad\qquad (3\text{-}1)$$

The measured interplanar spacings and their corresponding intensities are unique for each compound. This technique is subject to the limitations described in Section 2.2.2 and was, therefore, used to confirm the presence of crystalline compounds in the cementitious and corrosion product samples.

X-ray diffraction analyses were performed with a Siemens Kristalloflex Diffractometer, irradiated with a nickel-filtered Cu K_α radiation (λ_1 = 0.15406 nm, λ_2 = 0.15444 nm) generated at 50 kV and 30 mA. Samples were ground in an agate mortar and pestle without lubrication. All solids were distributed on a (511) silicon wafer and sealed by a piece of X-ray transparent polyester film (Mylar$^{\circledR}$ - Dupont) to prevent any changes in the solids from occurring during the analysis. The scans covered the range from 5° to 70° with steps of 0.05, and 1 second per step.

3.2.3 Raman Spectroscopy

Raman spectra, either *in situ* or *ex situ*, were obtained with a Renishaw 1000 Raman

microscope system that consisted of an Olympus microscope, a single spectrograph fitted with holograph notch filters for spectroscopy mode, and a Peltier-cooled CCD detector. Excitation was achieved using the 632.8 nm line of a Melles Griot 35 mW HeNe laser. This power level of the laser, however, was reduced to approximately 3 mW on the surface of a sample primarily due to the focussing of the laser light by the optics system. The optics system consists of about 20 mirrors which reflect the laser light, each of which reduces the power by approximately 10%. In addition, flaws in the focussing ability of the objective lens reduce the power available for analyses. Overall, this low level of light intensity was advantageous as it was unlikely to alter the composition of any surface films, particularly *in situ* measurements because it is an insufficient amount of energy to straddle the difference between the Fermi and conductance bands. This assumption was confirmed after each spectrum was obtained by performing a visual inspection of the sample to detect any surface changes (e.g., sample colour) using white light illumination. Data analysis of the spectra was performed using the Grams386 software developed by Galactica. Reference standards of magnetite (Fe_3O_4), hematite (α-Fe_2O_3), and maghemite (γ-Fe_2O_3) of 99.5% purity or greater were obtained from Aldrich in powder form. These standards were run using the same experimental conditions as the work of Chapters 4, 5, and 6 and are presented as Figures 3.2(a), (b), and (c). A sample of ISOPAR M, the fluid used as a lubricant during sample preparation procedures, was also analyzed and is presented as Figure 3.2(d).

The advantages and limitations of the technique are described in Section 2.4.4 while the procedures used to study the different types of samples in Chapters 4 through 6 are described in their respective experimental procedures sections. In general, typically five or more scans were performed on a given area within a particular sample such that microscopic variations in corrosion products could be detected, if present. The spectra presented in the next Chapters are considered representative of all measurements taken for each aspect

studied.
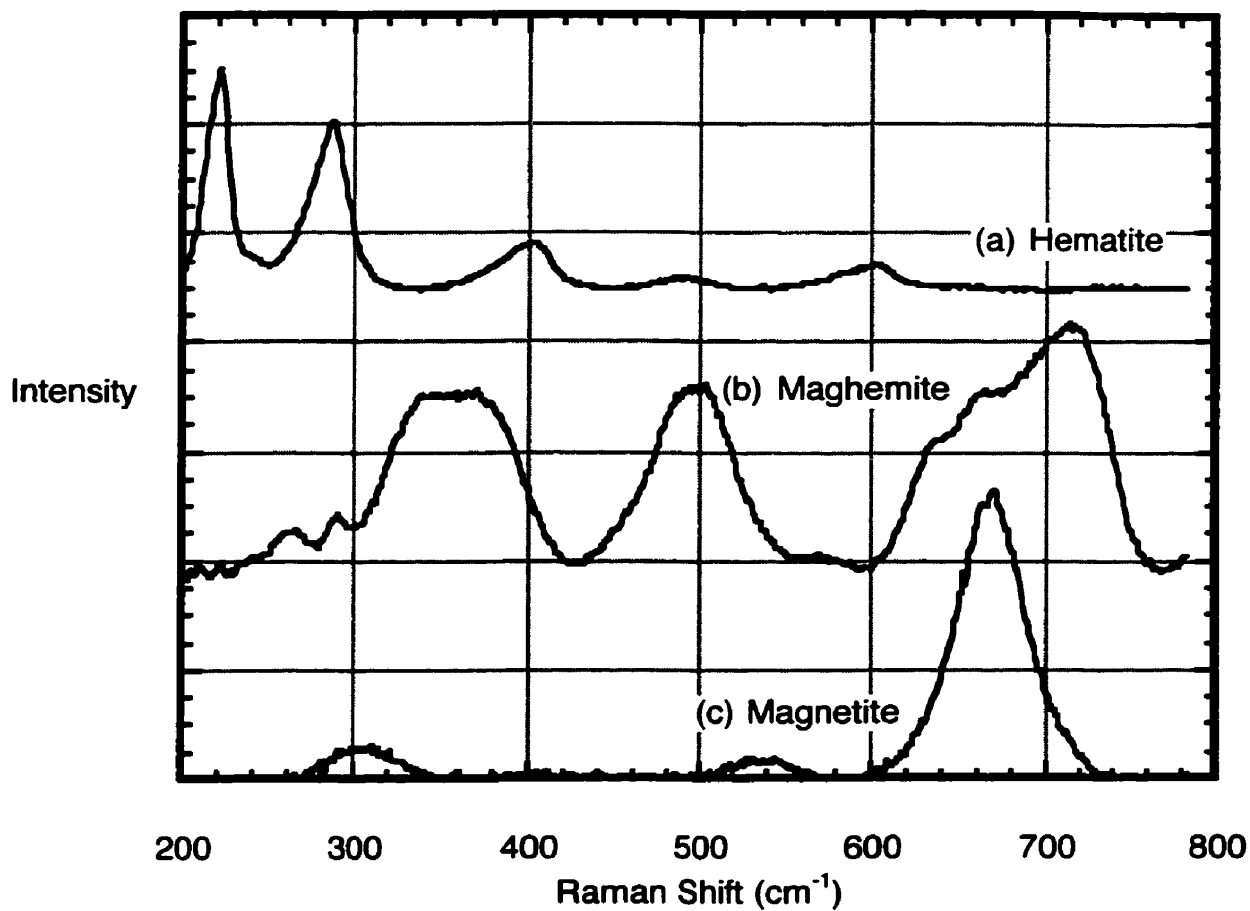
Figures 3.2(a), (b), and (c) Representative spectra of (a) hæmatite (a-Fe$_2$O$_3$), (b) maghemite(g-Fe$_2$O$_3$), and (c) magnetite (Fe$_3$O$_4$). Spectra courtesy of Prof. D.E. Irish and his research group in the Chemistry Department, University of Waterloo.
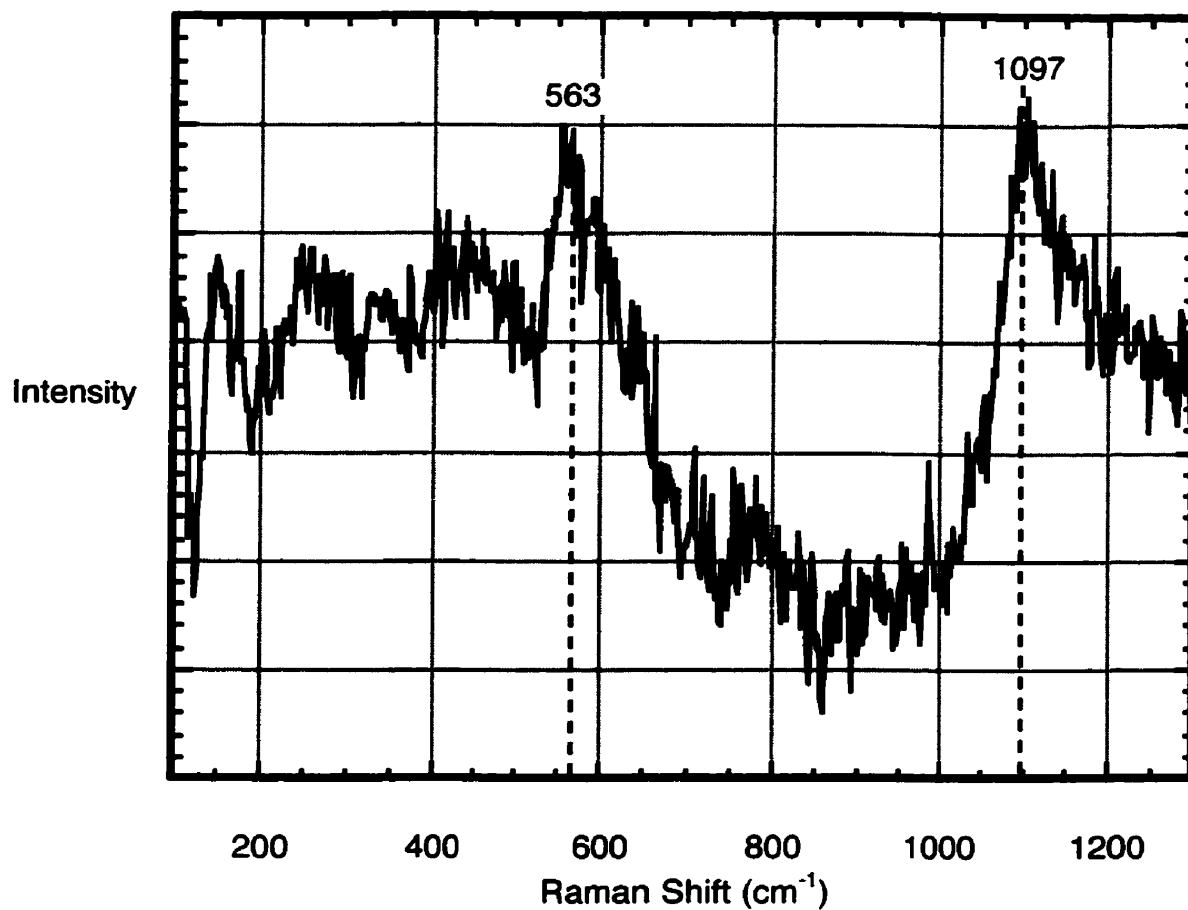
Figure 3.2(d) Spectrum obtained from lubrication fluid, ISOPAR M.

3.2.4 Microstructural Analyses

Optical and environmental scanning electron microscopy sections were prepared with a Struers Discoplan TS (consisting of a precision saw and a planing cup blade) using ISOPAR M (Exxon™) as a coolant. This coolant is an isoparaffinic hydrocarbon whose long

molecules were unlikely to interact with cementitious materials (i.e., leach ions such as chlorides or sulphates or leave chemical traces). Sections about 5-10 mm thick were produced with the precision saw. The sections were then mounted on glass slides and planed using a 35 μm cup blade. The flat specimens were then ground and polished to a 1 μm diamond finish using oil-based diamond suspensions and ISOPAR M to clean the samples between stages.

Polished sections were stored in a vacuum desiccator whose air had been evacuated and replaced with argon. Colour-indicating soda lime pellets and a reservoir of water were placed inside the desiccator to remove any carbon dioxide gas and humidify the chamber, respectively. The intention was to avoid the desiccation, oxidation, or reduction of any of the corrosion products present. To prevent the humidity from accelerating any naturally occurring corrosion and the formation of artifact corrosion products, each polished section was covered with a thin film of ISOPAR M. In addition, polished sections were repolished with a 1 μm oil-based diamond suspension prior to each viewing session to remove any artifact corrosion products. Figure 3.3 shows an area of corrosion product that formed within a crack within high performance concrete observed during the work of Chapter 6. This area was insufficiently polished after the section was stored for two months in a desiccator and shows the artifact corrosion products that form over long periods. Two distinct regions were observed: 1) a horse stirrup shaped region which was sufficiently polished and was predominantly composed of magnetite as shown by Figure 3.4(a); and 2) an insufficiently polished region which contained the original magnetite as well as a combination of goethite (α–FeOOH), haematite (α-Fe$_2$O$_3$), and maghemite (γ-Fe$_2$O$_3$), as shown in Figure 3.4(b). The additional compounds are a result of further oxidation of the corrosion products and were not fully removed during the final polish. The Raman spectrum shown as Figure 3.4(a) is similar to the original spectrum taken when the region was first polished immediately after sectioning.
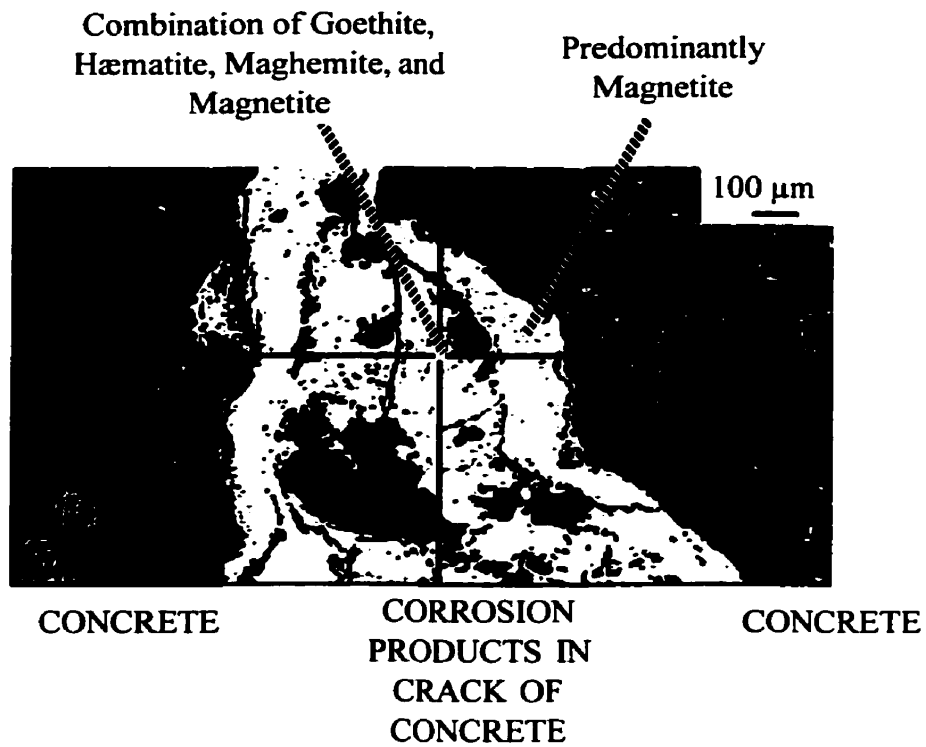
Figure 3.3 Optical micrograph of corrosion products that formed within a crack in high performance concrete.
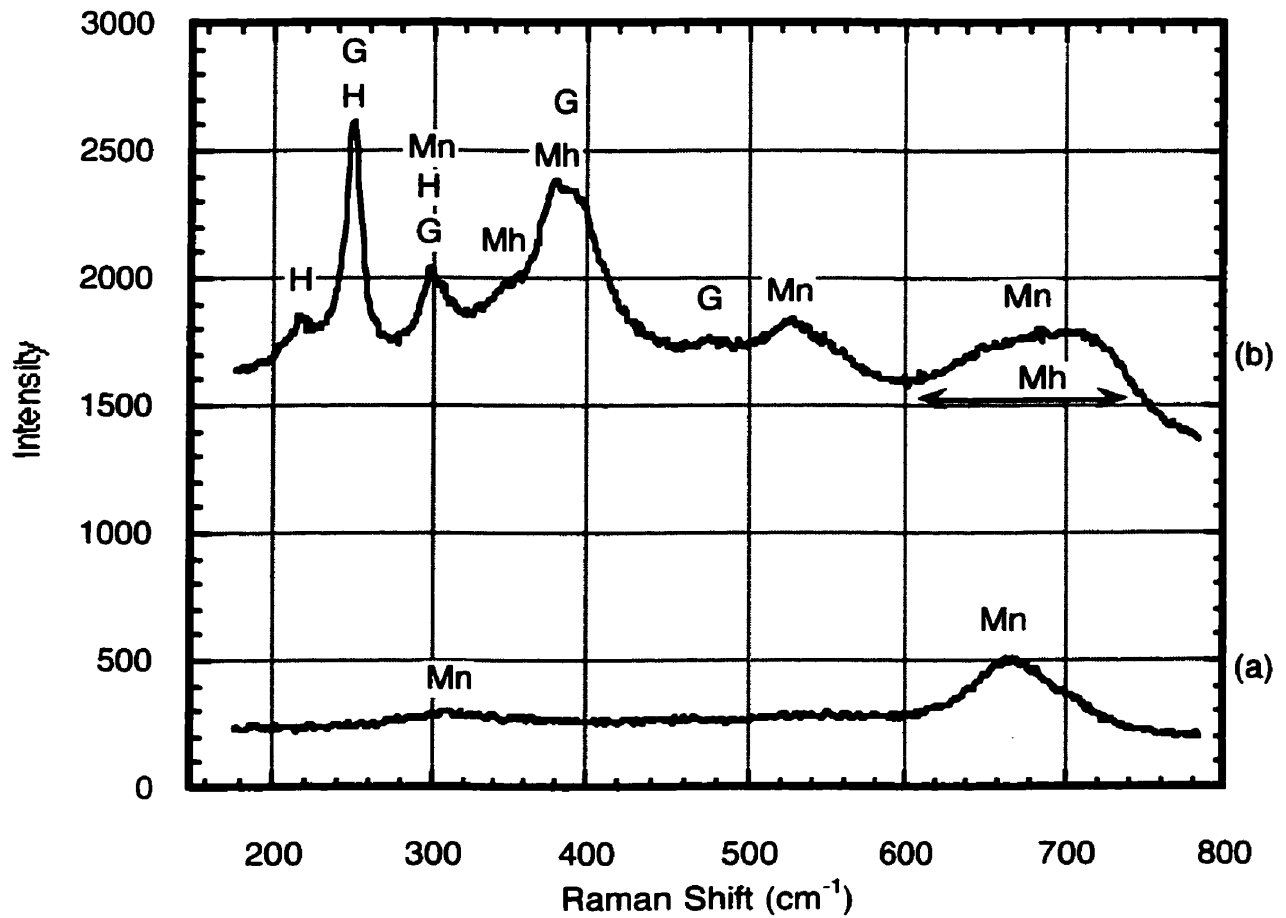
Figures 3.4(a) and (b) Raman spectra of regions indicated in Figure 3.2 showing (a) predominantly magnetite and (b) a combination of goethite, hæmatite, maghemite, and magnetite. G ≡ Goethite (α - FeOOH), H ≡ Hæmatite (α - Fe_2O_3), Mh ≡ Maghemite (γ - Fe_2O_3), Mn ≡ Magnetite (Fe_3O_4)

69

3.2.5 Porosity Measurements

For all measurements of the pore network presented in Chapters 4 through 6, each value represents the mean of at least three samples.

3.2.5.1 Total Porosity Measurements

All cementitious samples (approximately 10 x 10 x 10 mm each) were immersed in tap water for 24 hours prior to measuring their water-saturated surface-dry mass, and their mass in water. Each sample rested on a mesh stand in approximately 100 mL of water per sample. These conditions ensured that all sides of the sample were exposed to water and that sufficient water was present to enable complete saturation. The water-saturated surface-dry mass was determined by removing each specimen from the water, wiping the excess water off with a damp towel, and immediately weighing the section. Its mass in water was determined by placing the water-saturated surface dry sample in a wire basket which was immersed in water. The mass of the section was calculated by subtracting the mass of the basket in the water alone from the mass of the basket in the water with the section in it.

After the weighing was completed, the samples were dried at 105°C for 24 hours to remove all of the evaporable water. This time period was determined from monitoring the mass of water lost with time from ten similar samples. Reweighing these dried specimens provided the oven dry mass. From all these measurements, the total porosity was calculated for each specimen using Equation 2-2 (Section 2.2.3.1).

3.2.5.2 Pore Size Distribution Measurements

Cementitious samples (about 10 x 10 x 10 mm each) were placed on a mesh stand in 200 mL of anhydrous isopropan-2-ol (C_3H_8O) per sample to exchange the water in the samples

with the solvent. The isopropan-2-ol alcohol was replaced daily for two days. On the third day, the samples were placed in a vacuum desiccator for five days to evaporate the solvent. This procedure was developed from the behaviour of ten similar samples under similar conditions.

A Micromeritics Poresizer 9310, capable of a maximum pressure of 200 MPa, was used for the mercury intrusion porosimetry (MIP) measurements. Each sample was weighed, fitted into a penetrometer, reweighed, and placed into the porosimeter chamber. The intrusion process did not start until the pressure inside the chamber was reduced to 0.0004 MPa. At this pressure, the penetrometer was filled with mercury and the sample was incrementally pressurized at steps of about 0.0075 MPa. At each increment, the intruded volume of mercury was recorded. When the pressure reached 0.15 MPa, it was reduced to atmospheric pressure, approximately 0.101 MPa, and the entire assembly consisting of the specimen, penetrometer, and mercury, was reweighed. This measurement was used to calculate the volume of mercury necessary to completely fill the penetrometer. The penetrometer was then put back into the porosimeter chamber and the pressure was incrementally increased to the maximum pressure of 200 MPa, again recording the intruded volume of mercury for each pressure increase. The corrected pressure along with the volume of mercury intruded at each pressure change was used to calculate pore size distribution using the Washburn equation (Eq. 2-3) and the theory described in Section 2.2.3.2. The resulting data was corrected for compression and thermal expansion of mercury, sample compression and volume changes of glass penetrometer using the mathematical formulae and deductions presented in Appendix C. After each test, the samples were discarded because of mercury contamination.

3.2.6 Chloride Analyses

To measure the total chloride content (acid-soluble chlorides), which refers to both free chlorides and those chemically bound in the cement paste, ASTM Standard C114-89 (Section 19) was slightly modified according to the material studied (ASTM C114 1989). Samples of cementitious materials were cut (approximately 10 x 10 x 10 mm) with a precision diamond saw with ISOPAR M used as a lubricant. Each section was dried for 24 hours at 105°C to remove the evaporable water. Before grinding each sample, the mortar, pestle, and sieve were first rinsed with dilute nitric acid, followed by tap water, distilled water, and finally anhydrous isopropan-2-ol alcohol. The dried sample was ground using the mortar and pestle until the powder passed a 250 μm sieve. After grinding, the powder was weighed to the nearest tenth of a milligram and transferred to a 250 mL beaker to which 120 mL of dilute nitric acid (1:10 concentrated acid dilution with water by volume) were added. The samples were thoroughly dispersed with glass stirring rods. Controls were prepared which contained only 120 mL of dilute nitric acid and did not contain any powder, to measure any extraneous sources of chloride ions. The slurries and controls were covered with watchglasses and heated on hotplates until they had boiled for 5 minutes.

After the boiling process, all beakers were removed from the hotplates and the slurries were filtered through Whatman No. 4 filter paper (retains >20-25 μm) into 400 mL beakers. The beakers and the stirring rods were rinsed using hot distilled water at least three times into the filter until all of the residue was removed from them. The filter paper was washed at least 6 times with hot distilled water to remove all chlorides from the solids. The filter paper was removed and their exteriors were washed along with the funnels using hot distilled water into the beakers.

The filtrates were cooled to approximately 23°C and 2 drops of methyl orange indicator were added to the beakers. The solutions were made up with distilled water to 250 mL. This solution was acidified with a few drops of concentrated nitric acid. The

required number of drops was determined by methyl orange indicator which had been added. When the indicator turned deep pink or red, the solution was at or below the desired pH of 3.2. Approximately 45 mL of the total 250 mL available for each solution were titrated against a 0.06 M $AgNO_3$ solution using a Radiometer TIM800 semi-automatic titrator each test. This titrator slowly added 0.1 M $AgNO_3$ in increments as small as microlitres to determine the equivalence point of the chloride solution. The equivalence point corresponds to the maximum change in millivolt readings occurring when the chloride solution is neutralized to a pH of about 7. The volume of titrant used to reach this point was used to calculate the concentration of chlorides present in the solution. To provide an internal standard for those samples which were anticipated to have low chloride levels, 0.4 mL of a 1 M NaCl solution was added to each test which could then be subtracted from the final measurement. Furthermore, each solution was analyzed three times to get an average value. One of the controls was tested for every three tests performed to estimate the background level of chlorides such that they could be subtracted from any sample measurements.

3.2.7 Thermal Analyses

Two distinct thermal analysis techniques, thermogravimetric analysis (TGA) and differential thermal analysis (DTA), were performed simultaneously on cementitious samples using a TA Instruments Thermal Analyst 2100 System with a SDT 2960 Simultaneous DTA-TGA unit. The unit can be used to study mass loss and enthalpy changes over temperatures from ambient to 1500°C. This information corresponds to chemical and phase changes which occur (e.g., dehydration and decomposition of C-S-H, dehydroxylation and decomposition of calcium hydroxide) and can indicate the presence and proportion of compounds within a sample. These techniques are significantly less

sensitive to crystallinity than XRD.

Samples were ground to pass a 250 μm sieve with an agate mortar and pestle without lubrication just prior to performing the tests to prevent any chemical alterations of the samples (i.e., addition of lubricant peaks or carbonation). Desiccated alumina (Al_2O_3) was used as a reference material for DTA. Approximately 20 mg of both the sample and the reference alumina were used for each test. The test method involved equilibrating the sample and reference at 40°C and then increasing the temperature at 10°C/min. to 1100°C in a He atmosphere with a flowrate of 120 cm^3/min. Mass and temperature changes of the sample were recorded as the temperature was increased to 1100°C. These data were then plotted either as mass lost or temperature changes with temperature and were interpreted according to the theory and previous research presented in Section 2.2.4. In addition, samples of calcite and ettringite were also analyzed as reference standards for the analysis of the cementitious samples. Overall, the curves presented in Chapter 5 were considered representative of at least three measurements.

CHAPTER FOUR

CORROSION PRODUCTS FORMED ON STEEL

IN SIMULATED PORE SOLUTIONS

4.1 INTRODUCTION

Considerable work has focussed upon identifying the corrosion products that form on steel exposed to various alkaline electrolytes (Thierry, Persson et al. 1991; Simpson and Melendres 1996), including solutions containing chlorides (Raharinaivo and Génin 1986; Boucherit, Hugot-Le Goff et al. 1991; Melendres, Pankuch et al. 1992; Raharinaivo, Guilbaud et al. 1992; Refait and Génin 1993; Guilbaud, Chahbazian et al. 1994). These have either examined the corrosion rates that are measured at different chloride levels or identified corrosion products, usually *ex situ*, but not simultaneously. This chapter presents work which coordinated the measured corrosion rates with *in situ* observations of steel in simulated solutions that were very similar to the pore solution of concrete. This was accomplished by casting cement paste cylinders, expressing the pore solution from the cylinders, analyzing the solution, and preparing a simulated solution based upon the primary constituents of the expressed solution. It was the objective of this work to simulate the environmental conditions of steel-reinforced concrete as closely as was possible to provide a foundation for the work presented in later chapters. Given the environmental dependence of the corrosion products, *in situ* investigations are considerably more reliable than others, for the reasons described in Section 2.3.2.2. Thus, electrochemical polarization was performed concurrently with *in situ* Raman spectroscopy measurements of the surface of the steel and any products that formed. Both ground steel and as-received steel surfaces were studied in solutions designed to simulate the expressed pore solution of both Type 10 and white cement with varying chloride levels.

4.2 EXPERIMENTAL PROGRAMME

4.2.1 Preparation of Cement Paste Cylinders

To investigate the significance of cement type, the same cement paste mix was prepared for all specimens using either white or ordinary Portland cement. The mixture proportions are given in Table 4.1.

Table 4.1 Mixture proportions for cylindrical cement paste specimens.

Component	Mass (kg)
Cement	4.0
Water	1.8
w/c	0.45

Distilled water was slowly added to the cement powder over one minute in a paddle mixer (maximum capacity of about 3 L). The resulting cement paste was mixed for five minutes, allowed to rest for five minutes, and then mixed for a final five minutes. The cement paste was cast into cylindrical moulds (Ø51 x 102 mm) and compaction was aided by rodding. The amount of rodding necessary to achieve satisfactory compaction was determined by the length of time it took for large bubbles to stop surfacing, typically 10 seconds. Each cylinder was covered first with parafilm and then its corresponding lid. One batch of each cement type was mixed and 15 specimens were cast from both batches. The cylinders remained in the ambient conditions of the laboratory (about 22°C and about 50% relative humidity) for one day and then were stored in a wet atmosphere (about 25°C and 100%

relative humidity) until the pore solution was expressed. Even though the cylinders were considered to be sealed, they were stored in the wet atmosphere to ensure that the ambient conditions of the laboratory could not desiccate the cement paste.

After 120 days of curing, the pore solution of a representative cylinder for each cement type was expressed and analyzed in the manner described in Section 3.2.1. Since these results were consistent with the results of other cement pastes prepared in parallel laboratory experiments by other University of Waterloo researchers using the same cement and mixture proportions, the analysis of one cylinder was considered sufficient. The results of the analysis are presented in Table 4.2. The following species were not detected in the analysis: aluminum, arsenic, cadmium, cobalt, chromium, manganese, molybdenum, selenium, titanium, and vanadium.

Table 4.2 Composition of the expressed pore solutions as determined by inductively coupled plasma and ion chromatography. "<DL" represents levels that were below the detection limit. The pH of the solutions was not determined during this analysis.

Species	White Portland (mmol/L)	Ordinary Portland (mmol/L)
Barium	0.003	0.023
Boron	0.275	2.690
Calcium	3.740	2.550
Chloride (Cl^-)	0.082	0.223
Copper	0.008	0.208
Iron	<DL	0.039
Lead	<DL	0.066
Magnesium	<DL	0.021
Nickel	0.150	< DL
Nitrate (NO_3^-)	0.124	0.045
Potassium	49.107	319.707
Silicon	0.239	0.456
Sodium	207.919	130.928
Strontium	0.316	0.083
Sulphate (SO_4^{2-})	1.874	3.237
Zinc	0.071	0.517

4.2.2 Steel Sample Preparation

Approximately 100 samples (10 x 10 x 3 mm) were cut from the 10 mm thick bar (Section 3.1.5) such that there were approximately 50 samples each of the bare steel and the as-received surface. 1.6 mm (1/16") holes were then drilled into one of the sides of the

samples to accommodate a connecting rod. One surface of the bare steel samples was ground until plane and subsequently ground on 220 grit SiC paper using water as a lubricant. The surfaces were subsequently cleaned with mild soap and water, and rinsed with isopropan-2-ol. Stainless steel welding rod was press-fit into the holes. Round stickers (Ø8 mm) were centred on the prepared surfaces of the steel samples and the entire assembly, including all exposed surfaces of the steel rods, was painted with epoxy to prevent undesired corrosion in these areas. Once the epoxy had cured, the stickers were lifted to expose the prepared surfaces. A schematic illustration of the entire assembly is shown as Figure 4.1.

Epoxy covered
Ø1.6 mm stainless
steel welding rod

Epoxy covered
10 x 10 x 5 mm
steel sample

Exposed Ø8 mm of
steel surface, either
ground or as-received
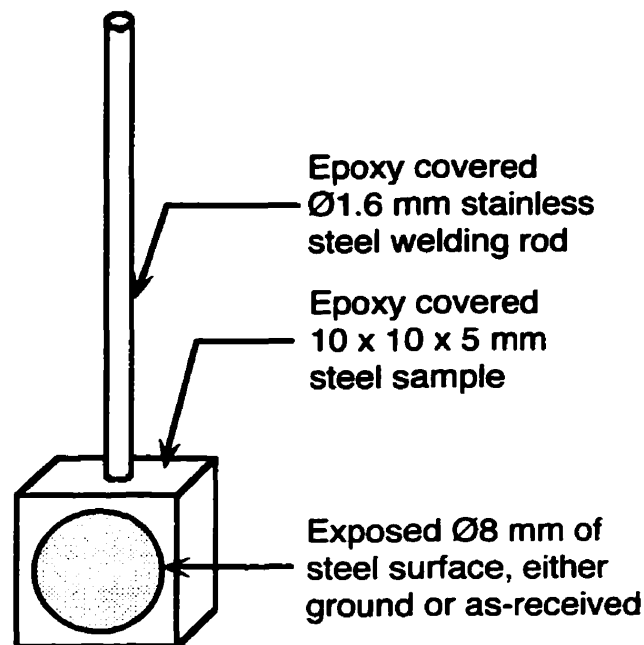
Figure 4.1 Schematic illustration of steel samples (NOT TO SCALE).

Surface roughness measurements were conducted on the steel plates presented in the next chapter and were considered representative of these smaller steel samples. The mean roughness[1] of the ground surfaces was measured to be 0.222 ± 0.023 μm while the mean roughness of the as-received steel surface (mill scale) was 1.926 ± 0.723 μm. Figures 4.2(a) and (b) are stereomicrographs of representative regions of the prepared surfaces.
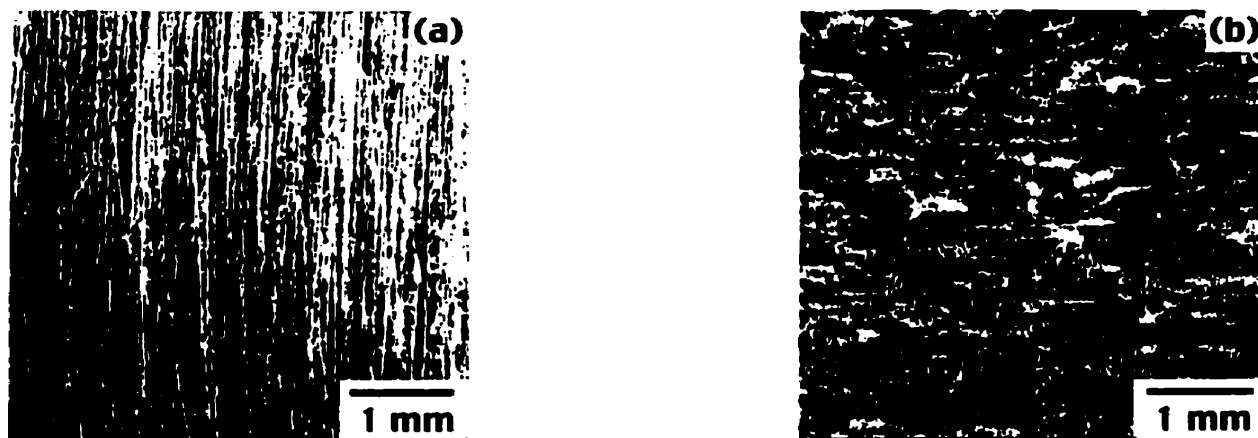
Figures 4.2(a) and (b) Stereomicrographs of (a) the ground steel surface, and (b) the unaltered as-received surface with mill scale.

4.2.3 *In Situ* Cell Preparation

A Ø1.6 mm hole was drilled into a polystyrene Petri dish to allow the stainless steel welding rod to exit the Petri dish such that an electrical connection could be made, as shown in Figure 4.3. The samples were inserted into the Petri dish such that either the as-received or the bare steel surfaces were oriented upright in the dish. The clearance between the

---

[1] The arithmetic mean, Ra, of the departures of the profile from the mean line is an internationally recognized parameter of roughness.

stainless steel rod and the Petri dish was sealed with 5 min. epoxy.
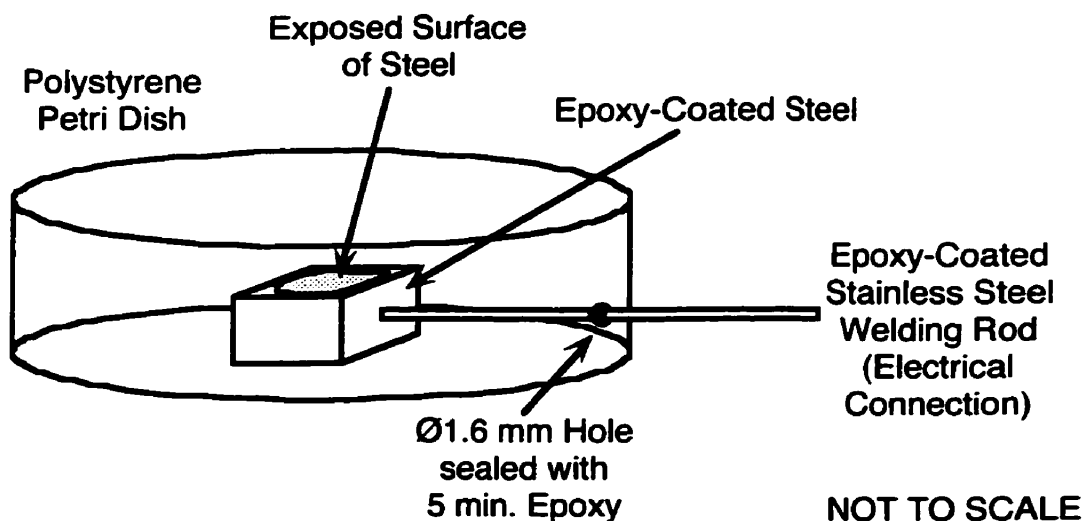
Figure 4.3 Schematic illustration of the *in situ* cell.

4.2.4 Preparation of Simulated Pore Solutions

Simulated pore solutions were prepared based upon the proportions of the most abundant constituents present in the expressed solutions (i.e., calcium, sodium, potassium, and sulphate). The resulting solutions prepared from NaOH, KOH, $CaSO_4$, and an excess of $Ca(OH)_2$ were analyzed by Solutions (formerly Water Quality Laboratory) of the University of Waterloo and confirmed that the constituents of the simulated solutions were within ± 5% of the molar quantities present in the pore solutions expressed from the cement paste cylinders. Once the pH values of both the simulated Type 10 and white

cement pore solutions were measured, oven-dried sodium chloride (140°C for 1 hour) was added to samples of both solutions to make chloride/hydroxide ratios of 0.70, 1.42, 2.00, and either 4.00 or 11.00 for the simulated Type 10 or white cement solutions, respectively. The 4.00 and 11.00 ratios are the chloride levels sufficient to make a 1 M NaCl solution in both of the solutions, respectively, and were intended for comparison purposes with the work of the next chapter. Table 4.3 details the corresponding chloride molarities for each chloride/hydroxide level. Steel samples were immersed in a larger polyethylene tub which contained these solutions for at least one hour prior to any polarization tests, and the solution was continuously stirred during this period. All *in situ* cells were immersed in about 500 mL of simulated pore solution prior to testing to reduce the possibility of carbonation which would influence the corrosion processes of the samples. These solutions were not stirred during the tests to better simulate the internal environment of concrete.

Table 4.3 Comparison of the chloride ion concentrations in white and Type 10 simulated pore solutions with pH values of 12.9 and 13.3, respectively.

Chloride/Hydroxide Ratio	White Chloride Ion Concentration (mol/L)	Type 10 Chloride Ion Concentration (mol/L)
0.7	0.07	0.18
1.42	0.13	0.36
2	0.18	0.50
4	n/a	1.00
11	1.00	n/a

4.2.5 Electrochemical Testing

The electrochemical testing was performed in two phases. The objective of the first phase was to determine the applied potential ranges where the corrosion behaviour of the steel changed (i.e., from passivation to active corrosion) in simulated pore solutions. The objective of the second phase was to identify any corrosion products by combining the electrochemical methods with *in situ* Raman spectroscopy.

Initially, samples were studied under two potential sweeps: a) from the open circuit potential up to +500 mV (SCE), down to -800 mV (SCE), and finally returning to the open circuit potential; and b) from the open circuit potential down to -800 mV (SCE), up to +500 mV (SCE), and returning to the open circuit potential similar to that shown in Figure 2.10. These different scanning regimes were intended to replicate the effect of portions of the steel becoming more anodic and causing others to become more cathodic. All sweeps were performed in duplicate at 1 mV/s with a new sample used each test. The resulting applied potential/log current density curves are presented in Appendix A and representative curves are presented in Section 4.3.1. These experiments are summarized in Table 4.4.

The applied potential ranges where corrosion changes occurred were studied in greater detail using *in situ* Raman spectroscopy under potentiodynamic control to study any corrosion products that might have formed during the electrochemical experiments. To aid comparisons between chloride levels, the behaviour at the same applied potentials was studied for all samples. The polarization experiment performed on all samples is presented as Figure 4.4. The samples were stored for an hour in about 500 mL of the desired simulated pore solution, with or without added chlorides, before they were studied with Raman spectroscopy. After an hour of exposure, each *in situ* cell was removed from the large tub which contained the simulated pore solution, and placed under the optical microscope of the Raman spectroscopy system for study. Saturated calomel reference and

stainless steel counter electrodes were added to the cell at this time, and approximately 4 mm of solution covered the exposed steel surface. When the applied potentials of interest were reached during the experiment, some of the simulated pore solution was removed such that approximately 1 mm of solution covered the surface of the steel, the reason for which is described in Section 4.3.3. Raman spectra were collected at this time, as shown in Figure 4.5. If corrosion products were observed, these were studied in detail. Otherwise, random areas of the surface of the steel were studied. The simulated pore solution was replaced to its former level over the surface of the steel when the electrochemical potential increases of the steel resumed, as shown in Figure 4.4. The Raman spectra obtained for this series of experiments is presented in Section 4.2.2 while the corresponding electrochemical measurements are presented in Section 4.2.3. This work is summarized in Table 4.4.

Table 4.4 Summary of Experiments and Samples Studied

Experiment	Full Cyclic Polarization	Raman Spectroscopy & Potentiostatic Control	Visual Assessment during Experiment	Visual Assessment at Conclusion of Experiment
Preliminary Full Cyclic Polarization Experiments (Section 4.3.1)	80 steel samples (40 tests by 2 duplicates)	n/a	n/a	Yes
In Situ cell Experiments (Sections 4.3.2 and 4.3.3)	n/a	18 steel samples (6 tests by 3 duplicates)	Yes	Yes
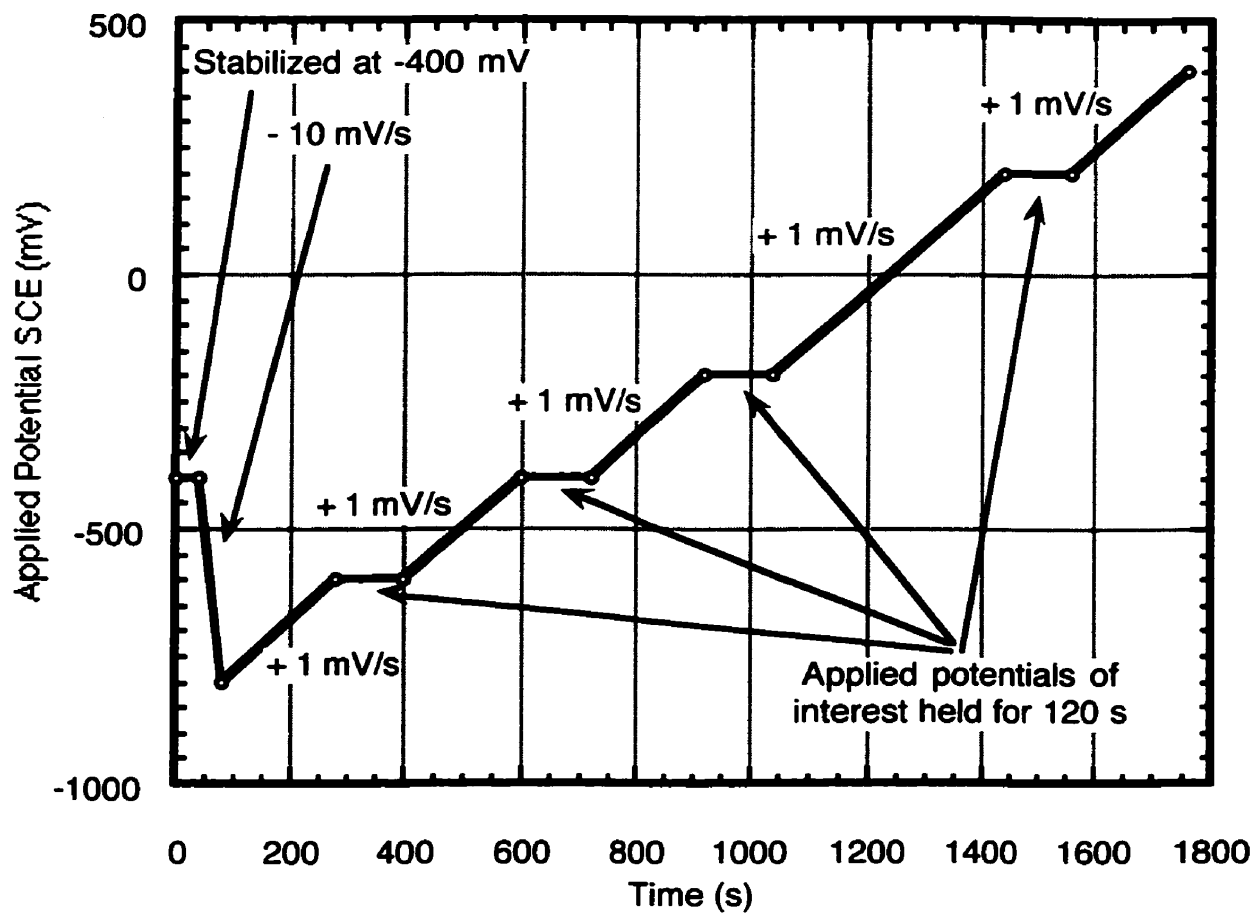
Figure 4.4 Polarization experiment performed simultaneously with *in situ* Raman spectroscopy during the second series of the electrochemical experiments.
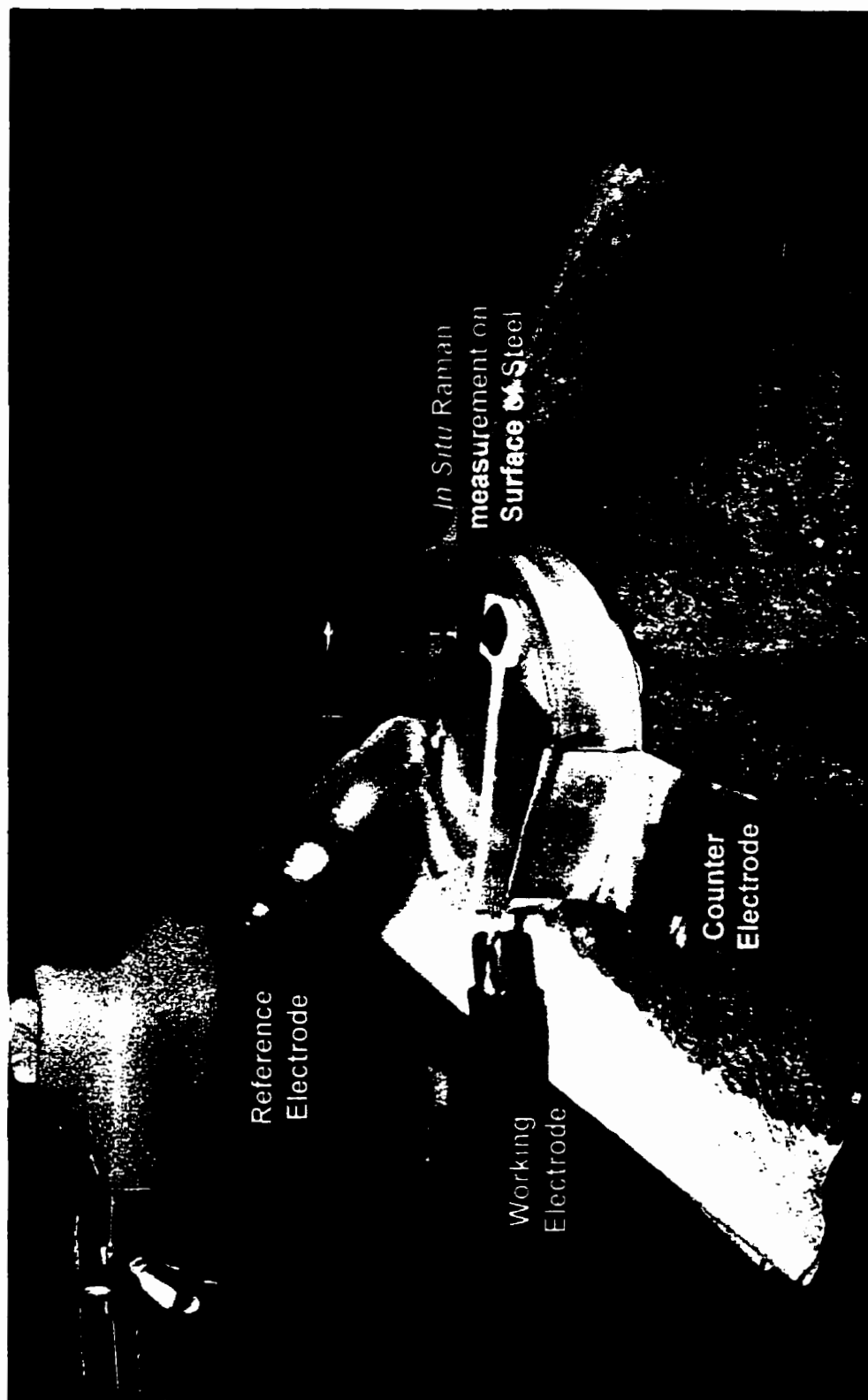
Figure 4.5 Photograph of the *in situ* Raman experiment which permitted simultaneous Raman measurements while the steel was maintained under potentiodynamic control.

4.3 RESULTS

4.3.1 Full Cyclic Polarization Curves

Full polarization curves (i.e., potential versus log current density) were obtained in the manner described in Section 4.2.5 and all curves are presented in Appendix A. From these curves, the effect of various experimental conditions on the electrochemical behaviour of the steel was assessed. As described in Section 2.4.2 (Chapter 2), changes in the curves correspond to changes in the products that cover the surface of the steel as it interacts with the simulated pore solution (e.g., passivation, corrosion initiation).

4.3.1.1 Effect of Ramp Direction

A review of all curves presented in Appendix A indicates that the ramp direction affects the magnitude of the measured corrosion current density of steel samples immersed in chloride-free simulated pore solutions. Higher current densities result from the cathodic ramp of the applied potentials over the anodic ramp within 100 mV of the open circuit potential. Figure 4.3.1.1 illustrates this difference between ground steel samples immersed in a Type 10 simulated pore solution where one steel sample was tested with an anodic ramping procedure and the other, a cathodic ramping procedure. Overall, higher current densities were expected from the cathodic ramping procedure because the passive film on the steel would be removed as the applied potential decreased to -800 mV SCE. As the applied potential was subsequently increased, the passive film was not restored to its former level and higher current densities resulted. In addition, the removal of the passive film during the cathodic sweep made the corrosion potential more cathodic. With the anodic ramp procedure, the passive film naturally present at the beginning of the experiment would have been enhanced as the applied potential increased to +500 mV SCE.

It is reasonable to assume that the subsequent decrease of the potential would reduce the enhanced passive film to its former level. Thus, the surface of this steel would have retained its protection during the experiment. Overall, this behaviour was observed for all steel samples and was independent of the type of simulated pore solution and surface finish.
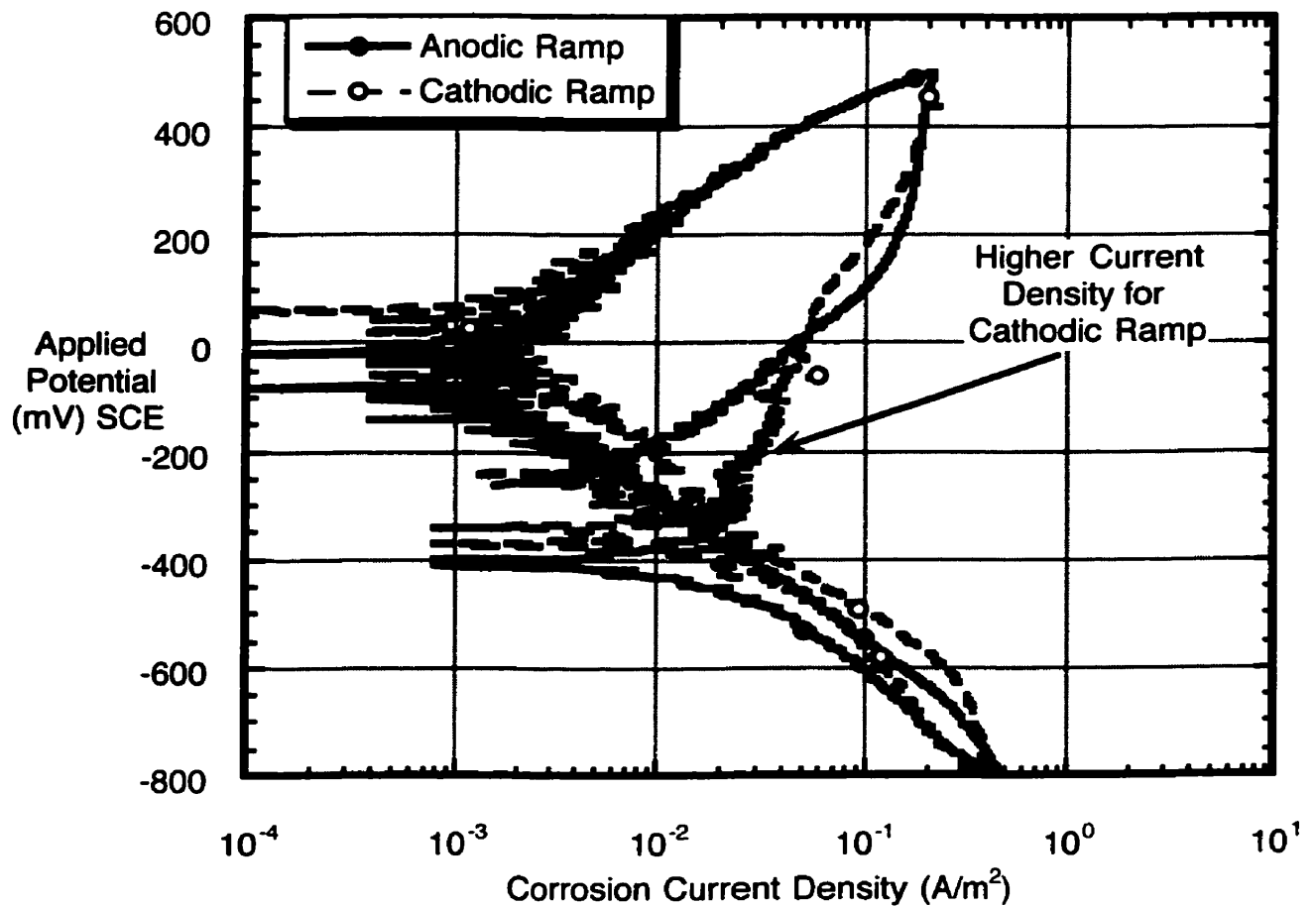
Figure 4.3.1.1 Comparison of applied potential-corrosion current density curves for ground steel samples exposed to a chloride-free Type 10 simulated pore solution.

This is to be expected with the inherent variability of the steel surfaces and the localized attack of the passive film by chlorides. Work by other researchers has also considered the effect of this procedural difference and concluded that greater experimental consistency is achieved by biasing the potential cathodically first followed by the anodic portion of the experiment (Raharinaivo, Guilbaud et al. 1992). Theoretically, any passive film present on the steel samples would then be reduced to bare steel thus reducing one source of variability. Since the experiments of this thesis did not indicate any other measurable difference between the two procedures, the cathodic biasing procedure was adopted for the *in situ* experiments (Sections 4.3.2 and 4.3.3).

However, no such clear trends were observed for any of the steel samples exposed to chloride-containing simulated pore solutions.

4.3.1.2 Effect of Chloride Exposure

A comparison of all applied potential-corrosion current density curves in Appendix A indicates that chloride/hydroxide ratios as low as 0.7 produced a significant effect on the corrosion behaviour of all samples. At this level, large increases in the corrosion current density consistent with chloride-induced pitting were not observed but the open circuit potential was generally observed to drop from approx. -200 mV SCE to -400 mV SCE. In addition, subtle changes in the anodic portion of the curves were observed when compared with the curves from steel immersed in the chloride-free simulated pore solution. These changes became larger as the chloride/hydroxide levels increased. Figures 4.3.1.2 (a), (b), (c), and (d) present representative applied potential-current density curves for both steel finishes and simulated pore solutions with chloride/hydroxide levels of 0, 2, and 4 or 11. These curves are considered representative of all curves presented in Appendix A and will be used to illustrate the corrosion behaviour of the steel.

89
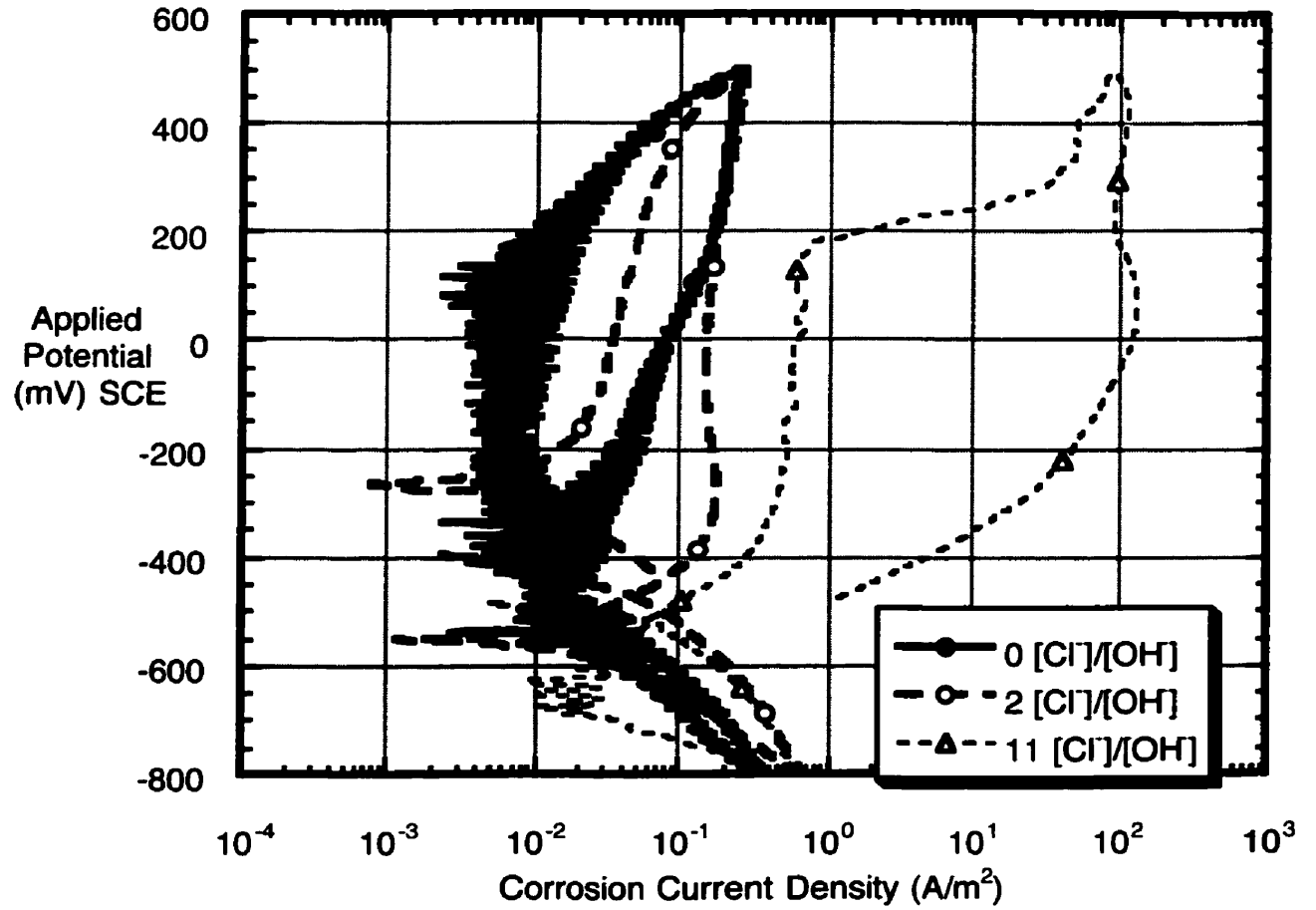
Figure 4.3.1.2(a) Comparison of applied potential-current density curves for ground steel in a white simulated pore solution with chloride/hydroxide ratios of 0, 2, and 11.
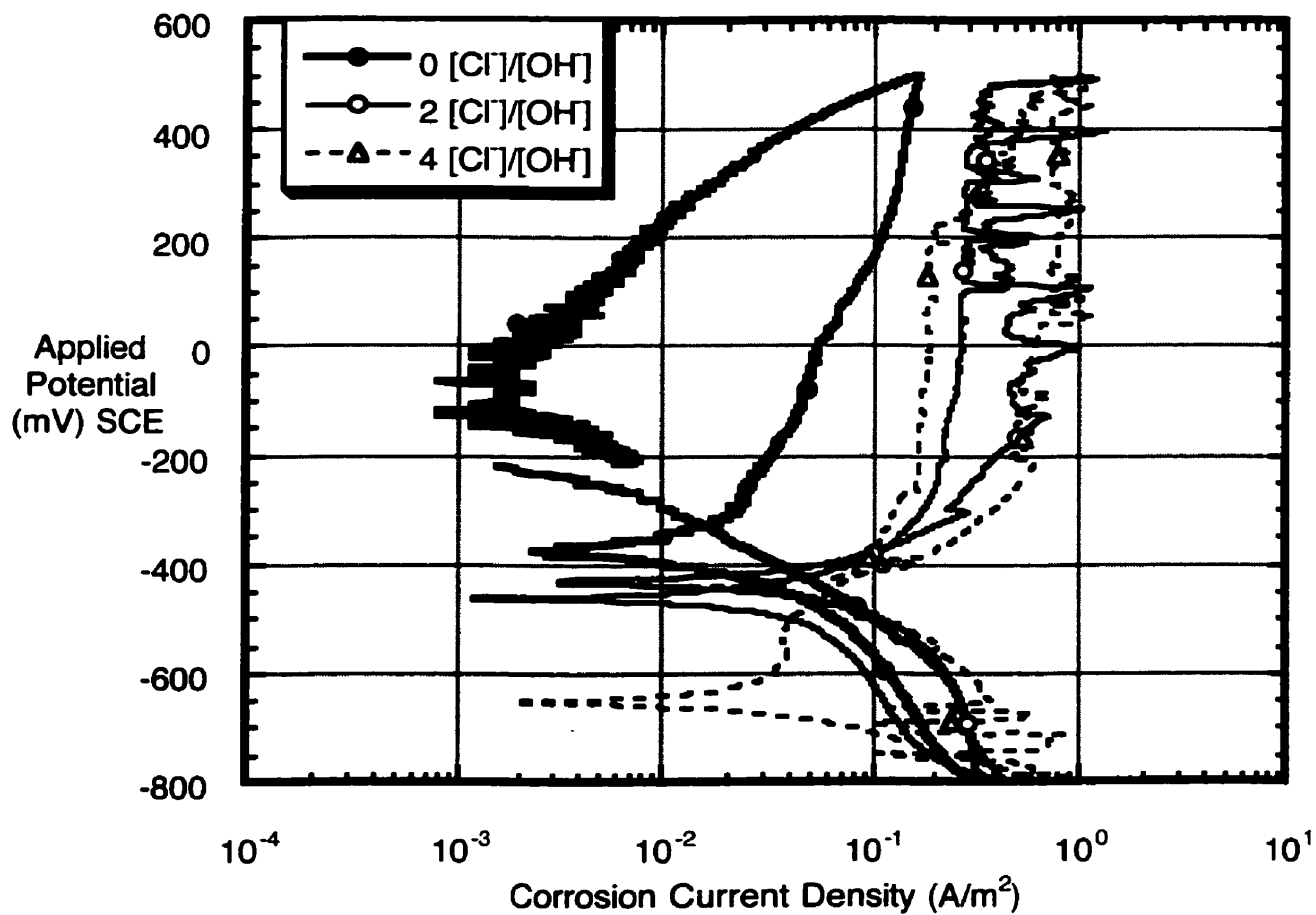
Figure 4.3.1.2(b) Comparison of applied potential-current density curves for ground steel in a Type 10 simulated pore solution with chloride/hydroxide ratios of 0, 2, and 4.
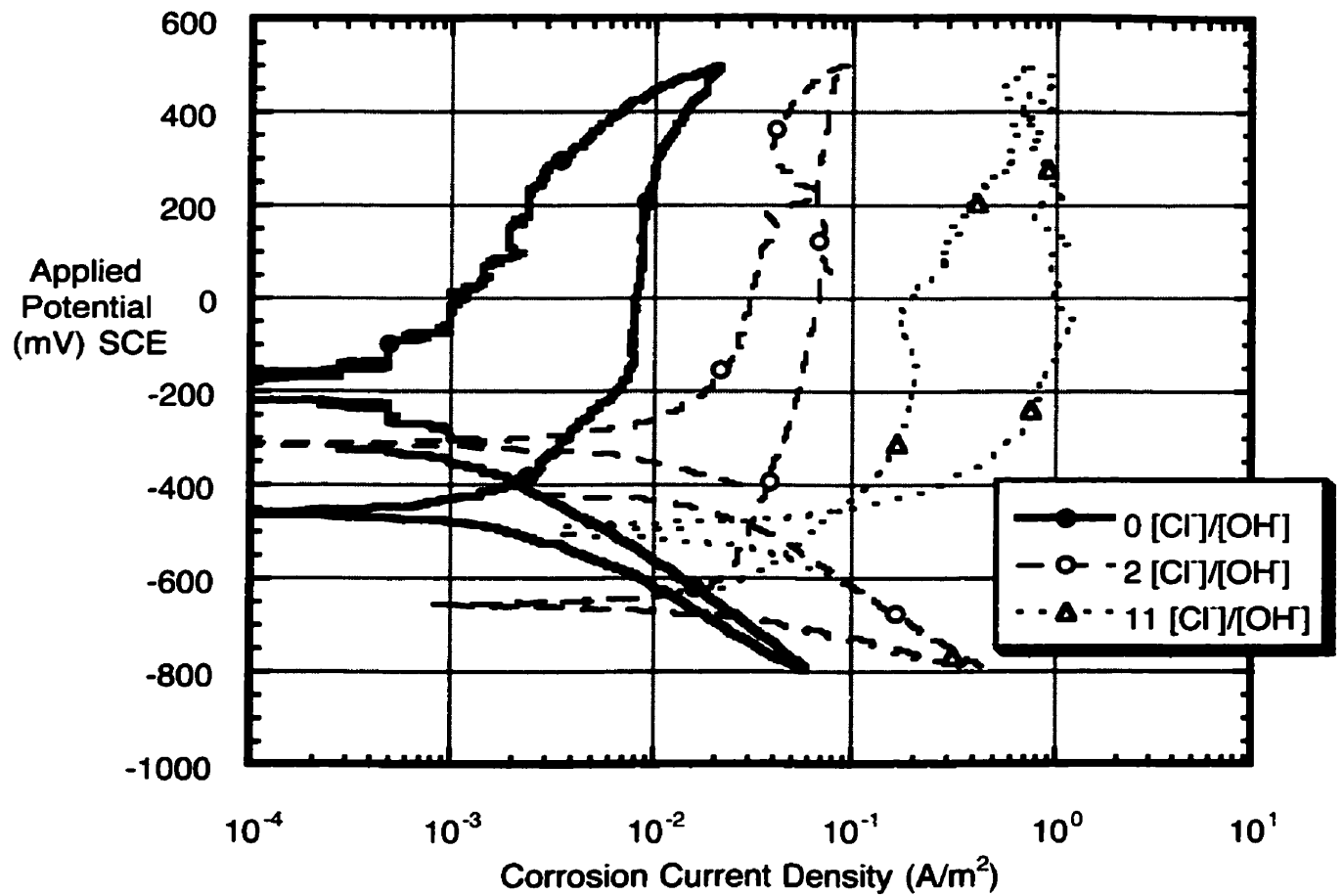
Figure 4.3.1.2(c) Comparison of applied potential-current density curves for as-received steel in a white simulated pore solution with chloride/hydroxide ratios of 0, 2, and 11.
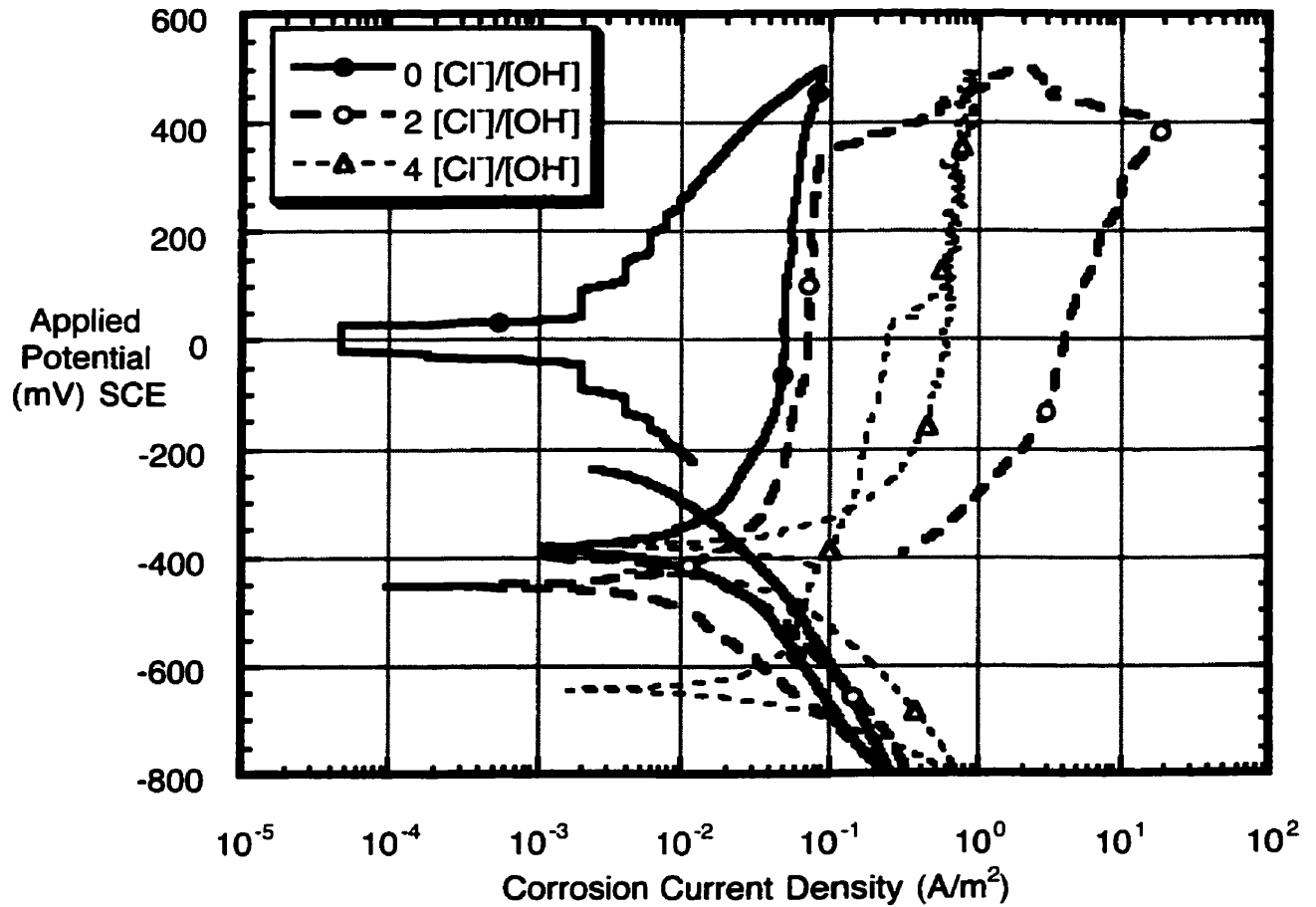
Figure 4.3.1.2(d) Comparison of applied potential-current density curves for as-received steel in a Type 10 simulated pore solution with chloride/hydroxide ratios of 0, 2, and 4.

Observed changes in the anodic portions of the curves included a gradual increase in the maximum average corrosion current density from 0.01 A/m^2 for steel in the chloride-free solutions to above 0.1 A/m^2 for steel in the chloride-containing solutions provided that pitting was not observed. Pitting was first observed at a chloride/hydroxide level of 1.4 for ground steel in a Type 10 solution. The highest corrosion current density observed was 1

A/m^2 but 0.1 A/m^2 was more commonly observed such as that shown in Figure 4.3.1.2(a).

Overall, pitting was not a consistently observed phenomenon as illustrated by Figure 4.3.1.2(d) where characteristic pitting behaviour was observed at a chloride/hydroxide level of 2 but did not occur at the higher chloride/hydroxide level of 4. This was typical for both steel finishes and simulated pore solutions and is discussed in greater detail in the next Sections. The potential at which pitting was observed to initiate was also variable but typically occurred within 0 to +200 mV SCE except for the as-received steel in the Type 10 solution with a chloride/hydroxide ratio of 2 where it initiated at approx. +350 mV SCE, as shown in Figure 4.2.1.2(d).

This variability in the corrosion behaviour is likely related to the inherent irregularity of the steel surfaces within a pool of "identical" samples in spite of any attempts to homogenize the steel with strict surface preparation techniques. This is supported by the observations of Wranglén who described extensive surface preparation techniques similar to the ones used in this work, but also explained that variations are inevitable (Wranglén 1985). It is because of this that only the chloride/hydroxide levels of 0, 2, and 4 or 11 (depending upon the simulated pore solution) were studied in the *in situ* Raman experiments presented in Sections 4.3.2 and 4.3.3. The study of all levels examined in this Section was not anticipated to produce any additional information that could not be achieved with the aforementioned chloride/hydroxide levels. Overall, the chloride/hydroxide level of 2 was considered to provide an intermediate level where corrosion was likely to be initiated while the chloride/hydroxide levels of 4 and 11 coincided with the 1 M chloride-containing simulated pore solutions used for the experiments presented in Chapter 5.

4.3.1.3 Effect of Pore Solution Composition

A review of the representative curves in Figures 4.3.1.2 (a) through (d) shows that

there is no significant effect of pore solution composition. Similar, albeit variable, corrosion behaviour was observed for all samples for each chloride/hydroxide level studied, including the different levels corresponding to a 1 M chloride solution (i.e., the chloride/hydroxide levels of 4 and 11). Differences in the corrosion behaviour of steel in the two solutions might have been discernable if the variability described in the previous Section had not been present. In addition, full potentiodynamic polarization experiments cannot indicate other important differences resulting from the type of simulated pore solution such as, the types of corrosion products which formed. The *in situ* experiments of Sections 4.2.2 and 4.2.3 are more appropriate under these circumstances.

4.3.1.4 Effect of Surface Finish

A review of the representative curves in Figures 4.3.1.2 (a) through (d) shows that there is no significant effect of surface finish. According to the conclusions of Addleson and Rice (Addleson and Rice 1995), higher corrosion current densities were expected for the as-received steel surfaces once corrosion initiated. However, the highest corrosion current densities in the work presented here were observed on the ground steel surfaces (approximately 1 A/m^2) and this value was attained for only two samples of the eighty samples studied.

Independent of the surface finish, most current densities for pitting were 0.1 A/m^2 which is approximately two orders of magnitude higher than the passive conditions in the chloride-free simulated pore solutions which is consistent with the general understanding of pitting behaviour. It is possible that the formation of corrosion products on the surface of the relatively rougher as-received surface was more effective in reducing the activity of any corrosion pits than that on the relatively smooth ground steel surfaces. Clearly, an understanding of the corrosion products formed during similar experimental conditions would help in the analysis of the pitting behaviour.

4.3.2 Analyses of Steel Surfaces using Raman Spectroscopy

4.3.2.1 Effect of Exposure to Simulated Pore Solution

A comparison of the spectra obtained with and without exposure to the simulated pore solutions for both the ground and as-received steel surfaces are presented in Figures 4.3.2.1(a) and (b), respectively. As anticipated, no distinct peaks were observed for the ground steel surfaces with or without exposure to the simulated pore solution. Any passive film that would have formed on the surface of the steel in the simulated pore solutions with one hour of exposure would have been too thin (on the order of 10 nm) to detect with normal Raman spectroscopy. On the other hand, the mill scale on the as-received sample was readily identified by Raman spectroscopy but, similar to the ground surfaces, no changes in this scale were observed after exposure to both pore solutions, as shown in Figure 4.3.2.1(b). Magnetite (Fe_3O_4), haematite ($\alpha\text{-}Fe_2O_3$), and goethite ($\alpha\text{-}FeOOH$) were detected on the original surface and after exposure to either of the simulated pore solutions.
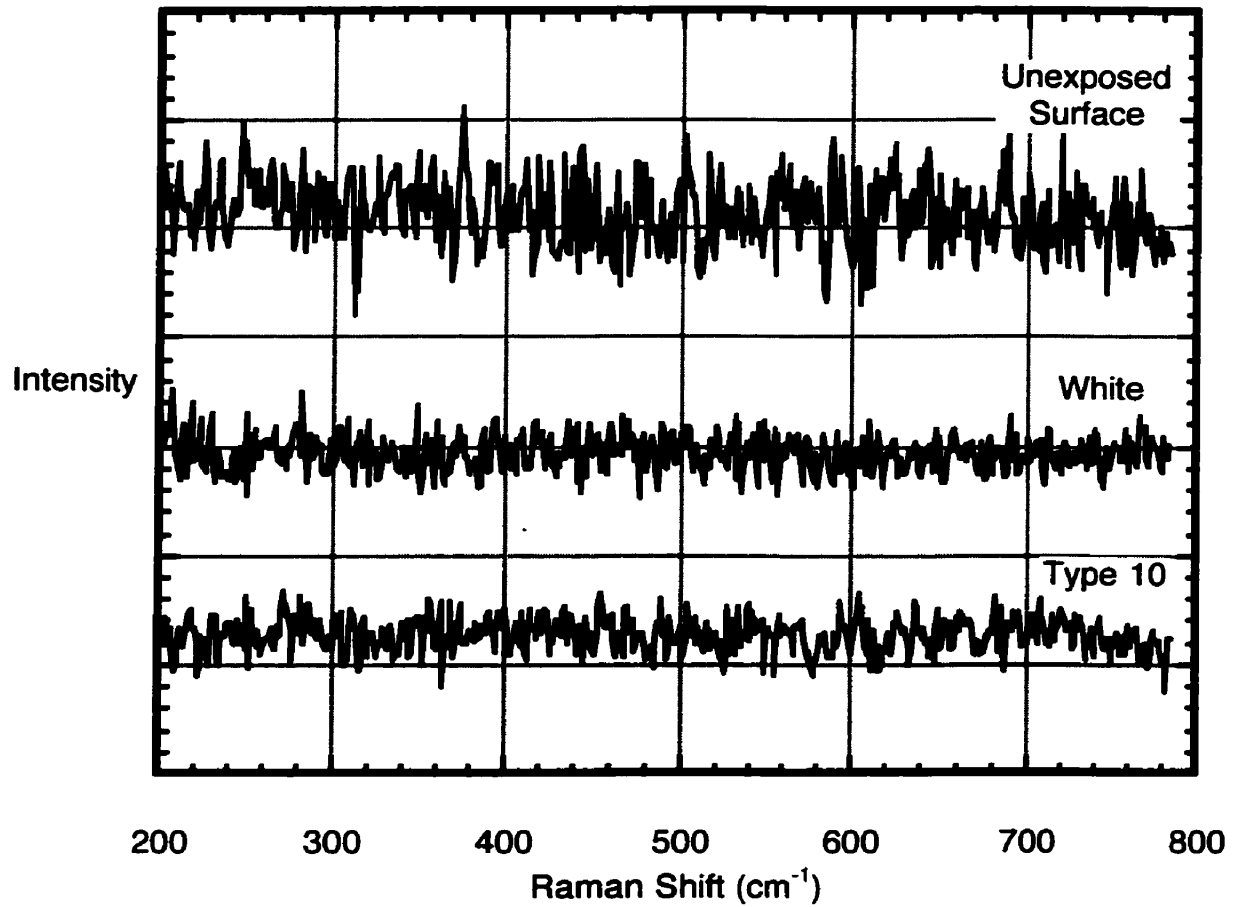
Figure 4.3.2.1(a) Comparison of ground steel surfaces before exposure, and after exposure to both white and Type 10 simulated pore solutions.
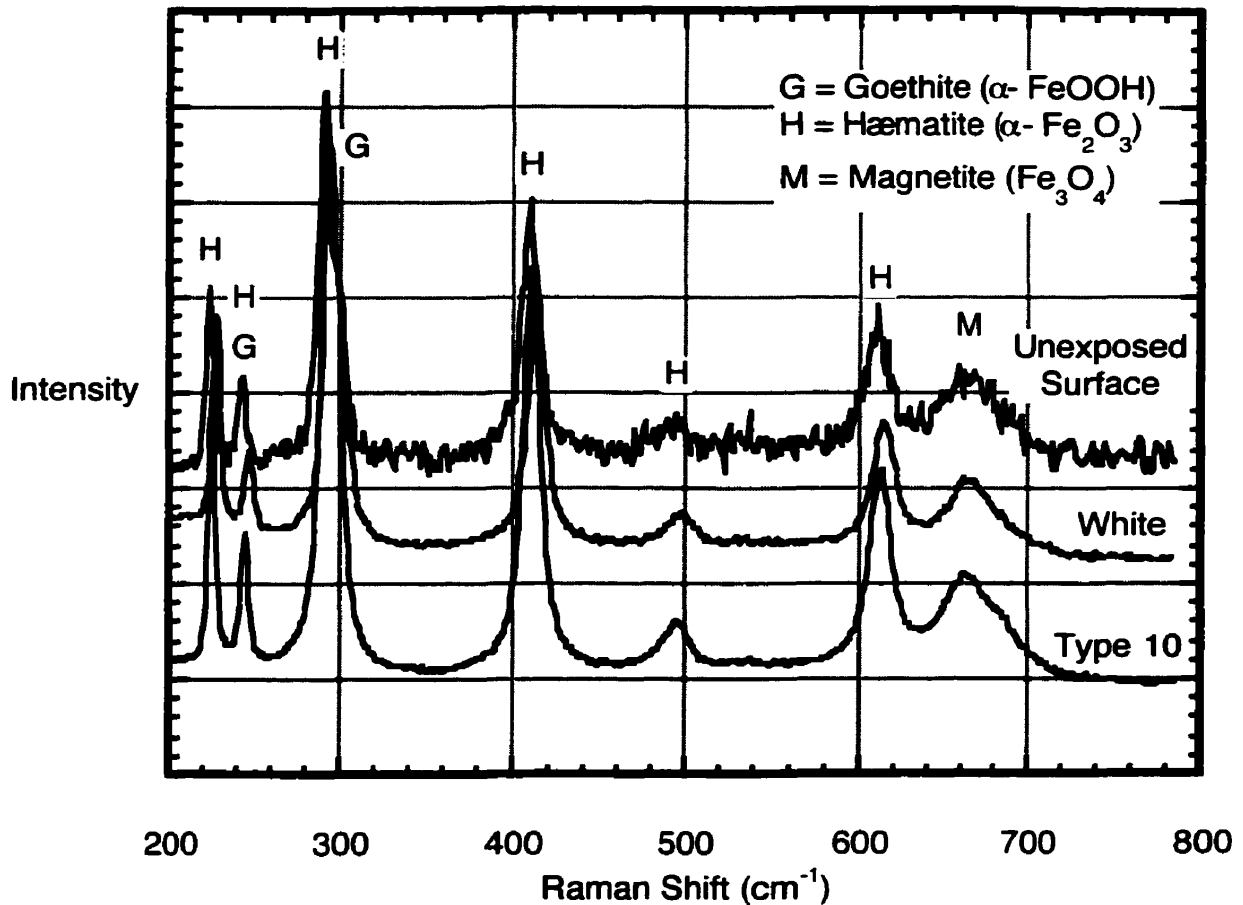
Figure 4.3.2.1(b) Comparison of as-received steel surfaces before exposure, and after exposure to both white and Type 10 simulated pore solutions.

4.3.2.2 Effect of Chloride Exposure

As anticipated, exposure to chlorides affected the surfaces of the steel by inducing corrosion products to form. For the as-received steel surfaces, no evidence (i.e., visual or Raman analysis) of corrosion was observed until a chloride/hydroxide ratio of 4 was reached

in the Type 10 simulated pore solution and the chloride/hydroxide ratio of 11 in the white cement simulated pore solution (corresponding to the same chloride molarity of 1). All collected spectra of the mill scale (i.e., the as-received surface) were similar to the unexposed mill scale surface shown in Figure 4.3.2.1(b) until these critical levels were reached.

At a chloride/hydroxide ratio of 4 and after an hour's exposure to the choride-containing pore solution, the steel immersed in the Type 10 solution initially had two oblong areas of corrosion near the centre of the exposed surface, each approximately 1 mm by 3 mm. These were coloured golden red but there was no detectable difference between the Raman spectra collected during the cathodic polarization of the steel (from the initial -400 mV to its return to -400 mV SCE) and the original spectrum (Figure 4.3.2.1(b)). Once the applied potential reached -400 mV SCE, however, maghemite (γ-Fe_2O_3) and magnetite (Fe_3O_4) were detected, as shown in Figures 4.2.2.2(a) and (b). The colour of the areas of corrosion also became darker and almost black during this time which corresponds to the change in the Raman spectra. Clearly, these relatively large areas of goethite and hematite were reduced to their more oxygen-deficient counterparts. The cathodic sweep of the experiment would have electrochemically reduced the oxygen in the corrosion product and there would have been insufficient oxygen to rebuild the product as the applied potential increased in the anodic direction. Magnetite (Fe_3O_4) and maghemite (γ-Fe_2O_3) persisted until the end of the entire experiment and no new changes in the mill scale were visually observed or detected by Raman spectroscopy.
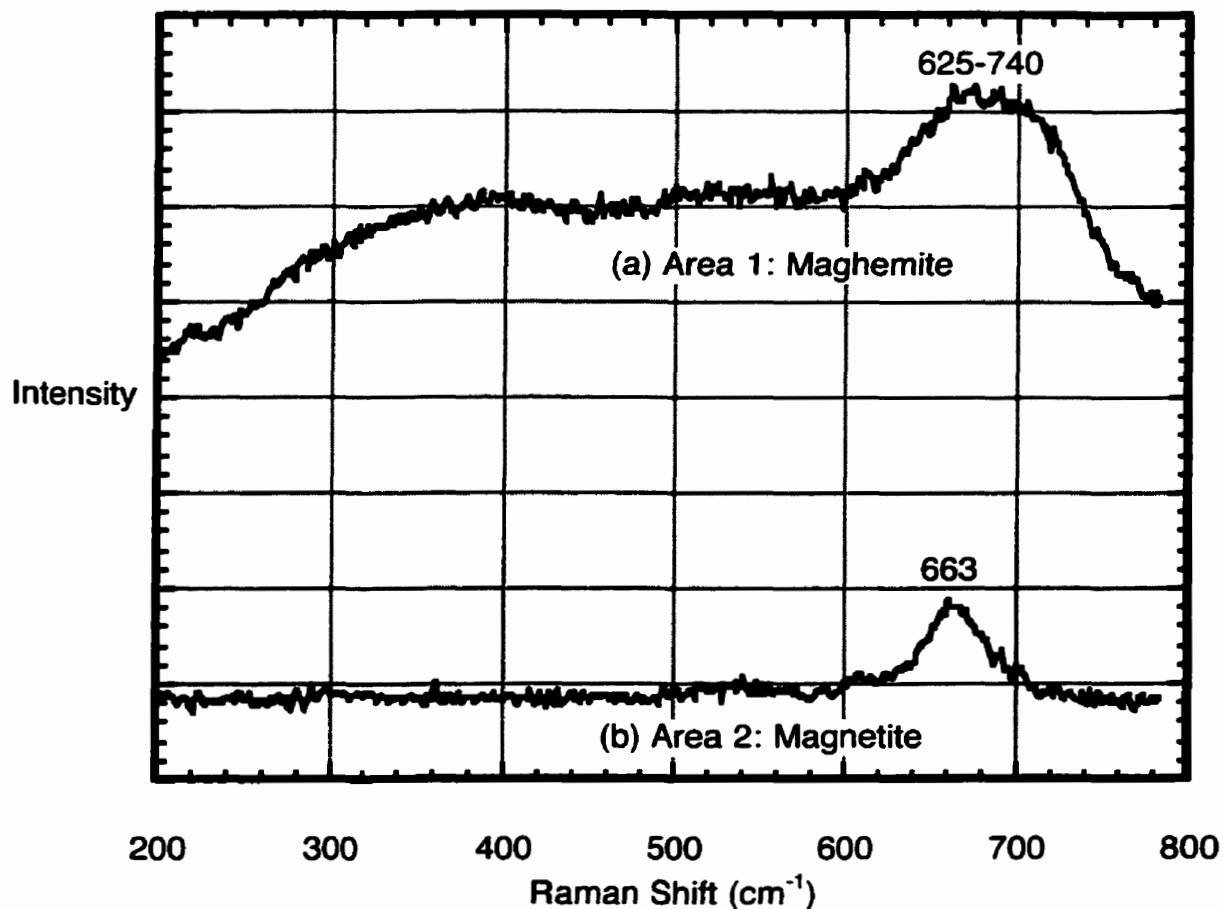
Figures 4.3.2.2(a) and (b) Raman spectra of the corrosion products observed on the surface of the as-received steel immersed in a Type 10 cement simulated pore solution while under potentiodynamic control at -400 mV SCE, (a) area 1, and (b) area 2.

Unlike the steel immersed in the Type 10 solution, no corrosion products were observed on the as-received steel in the white cement simulated pore solution until the applied potential reached +200 mV SCE. At this potential, three pit areas, each approximately 1 mm^2, initiated along the edge of the epoxy, likely at small flaws in the mill scale. These green-black coloured products grew away from the surface of the steel and towards the surface of the solution. They were approximately 1 mm thick at approximately +335 mV SCE. When the potential reached +400 mV SCE, the products were approximately 1.5 mm thick, as shown in Figures 4.3.2.2(c) and (d). The red arrows in the figures point to the location of the product. Unfortunately it is extremely difficult to resolve the black product on the black-coloured mill scale. Although no changes in the composition of the surrounding mill scale were noted, the accumulated corrosion product was composed of magnetite (Fe_3O_4), as shown in Figure 4.3.2.2(e).
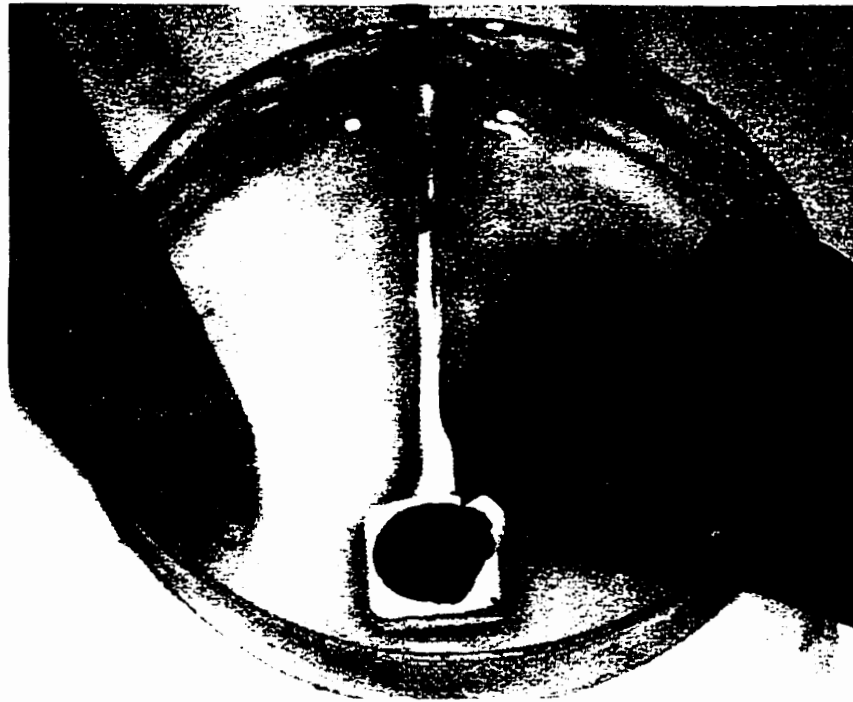
(c)

(d)

Figures 4.3.2.2 (c) and (d) Macrophotographs of green-black corrosion products that formed on the as-received surface of steel immersed in a simulated white cement simulated pore solution with a chloride/hydroxide ratio of 11. (Corrosion product is at the upper right-hand area of the steel surface at the interface with the epoxy.)
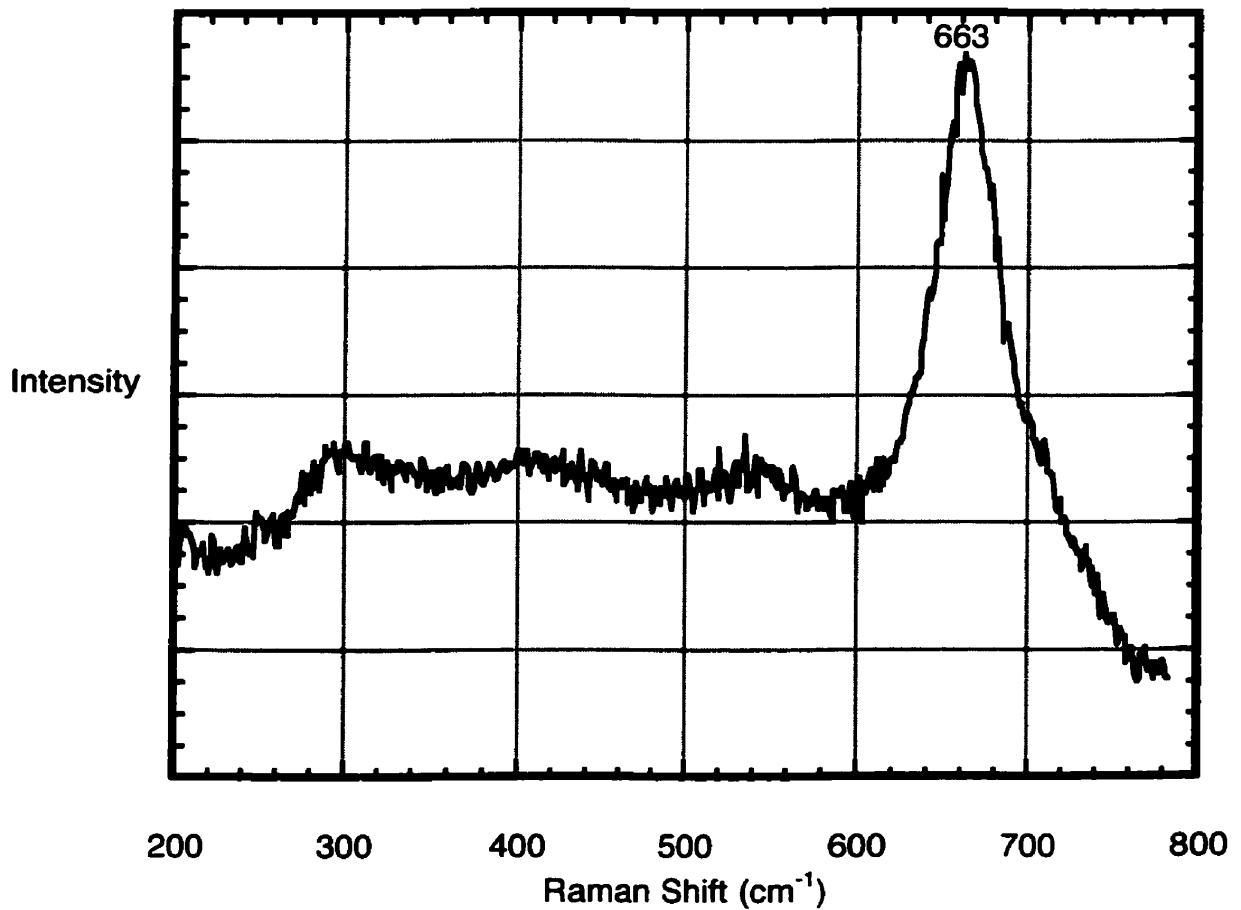
Figure 4.3.2.2(e) Raman spectrum obtained from the green-black corrosion product, identified as magnetite (Fe_3O_4), shown in Figures 4.2.2.2(c) and (d).

Unlike their as-received steel counterparts, changes in the surfaces of the ground steel specimens were identified at chloride/hydroxide ratios of 2 for both types of simulated pore

solution. The surfaces of the steel samples in the Type 10 simulated pore solution were observed to turn a dull grey colour over their entire surface and this effect lasted for the range of applied potentials. The composition of this product was never identified as the thinness of the film placed it beneath the detection limit of Raman spectroscopy despite attempts to obtain spectra for the entire monitoring period. A similar film formed on the steel samples in the white simulated pore solution but the colour of the film turned a golden red at the edge of the exposed steel (approx. 1 mm wide) at approx. 0 mV SCE, as shown in Figure 4.3.2.2(f). At this time, the product could not be identified using the Raman technique likely because the product was too thin. However, once the applied potential reached +400 mV SCE, this product became a brilliant crimson red/blood red in colour which then faded to a medium brown-red after the experiment was finished, as shown in Figure 4.3.2.2(g). This product was identified as magnetite (Fe_3O_4), and maghemite (γ-Fe_2O_3) at approximately +400 mV SCE using Raman spectroscopy, as shown in Figure 4.3.2.2(h). Some calcium hydroxide ($Ca(OH)_2$) was also noted which likely resulted from the simulated pore solution. The presence of these clearly defined corrosion products cannot be attributed to either the chloride/hydroxide ratio or overall chloride content because the ratio was similar to that in the Type 10 solution, and proportionately fewer chlorides were required in the relatively lower pH of the white simulated pore solution. This discrepancy is discussed in further detail in the next Section.

104

Figure 4.3.2.2(f) Macrophotograph of golden red film at edges of ground steel surface in white simulated pore solution with a chloride/hydroxide ratio of 2 while the applied potential was approximately 0 mV SCE. Corrosion product was extremely thin are barely perceptible with the unaided eye.

Figure 4.3.2.2(g) Macrophotograph of the formerly brilliant red film at edges of ground steel surface (circa +400 mV SCE) in white simulated pore solution with a chloride/hydroxide ratio of 2 after the experiment was completed.
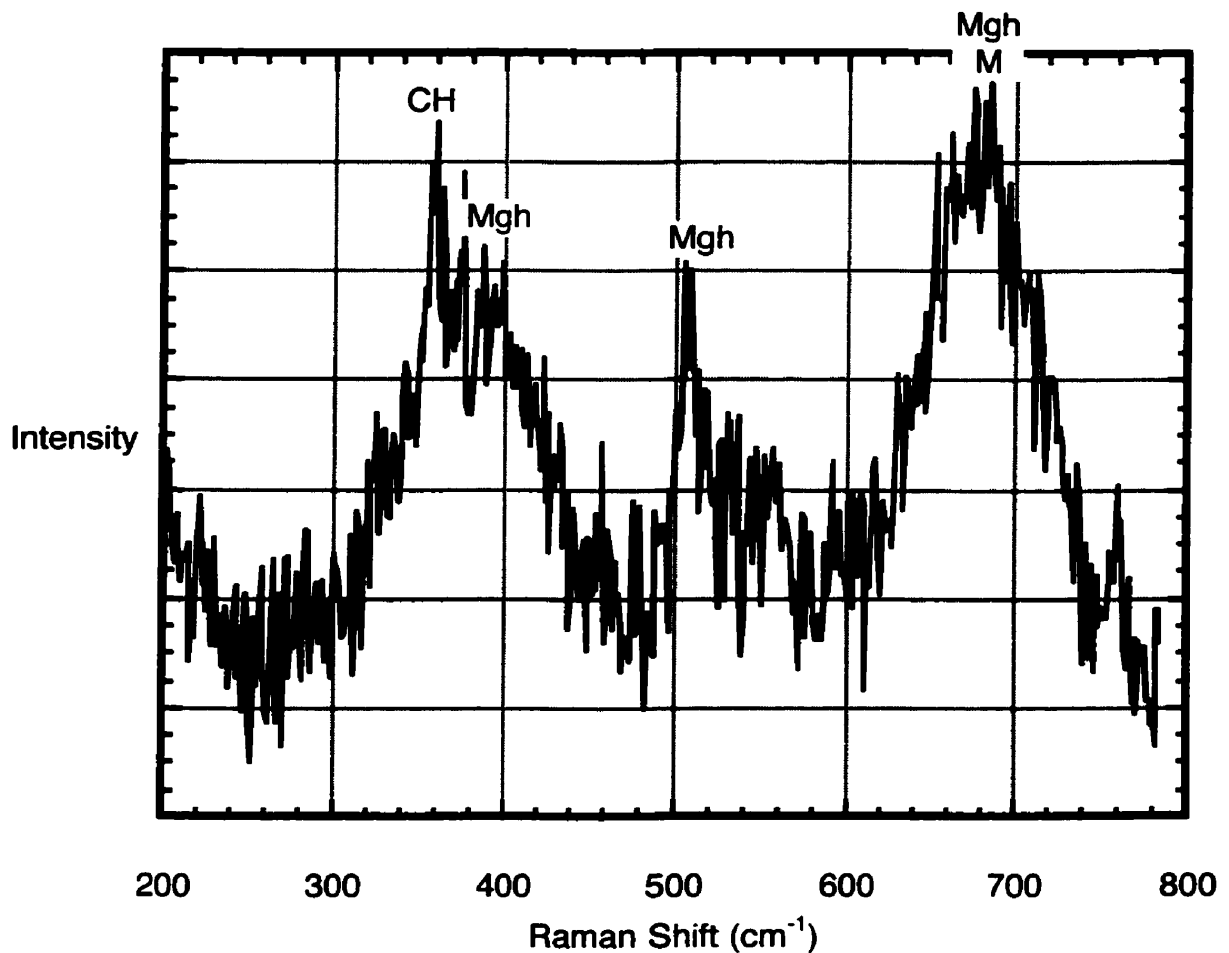
Figure 4.3.2.2(h) Raman spectrum of brilliant red film shown in Figure 4.3.2.2(g), identified as magnetite (Fe_3O_4) and maghemite (γ-Fe_2O_3). Some calcium hydroxide ($Ca(OH)_2$) was also observed in the spectrum.

With increasing chloride/hydroxide levels, the corrosion products which formed became considerably more localized. For the steel exposed to the Type 10 simulated pore solution with a chloride/hydroxide ratio of 4, a small, black area of corrosion, approximately

1 mm^2, was visually identified at +200 mV SCE. This product could not be identified using the Raman technique because it was extremely difficult to focus the optical system on this black particle. Above +400 mV SCE, a second black area was observed, also 1 mm^2, which was identified as Green Rust I from the two peaks centred on 423 and 500 cm^{-1}, presented as Figure 4.3.2.2(i). Upon exposure to the laboratory air at the conclusion of the experiment (i.e., an *ex situ* observation), this product became magnetite and hematite, as shown in Figure 4.3.2.2(j). The final appearance of the steel sample is presented in Figure 4.3.2.2(k) and the characteristic colours of magnetite and hematite, black and rust red, respectively, were observed. However, when this product was scraped off the surface, Green Rust I was again detected when analyzed using the Raman technique.
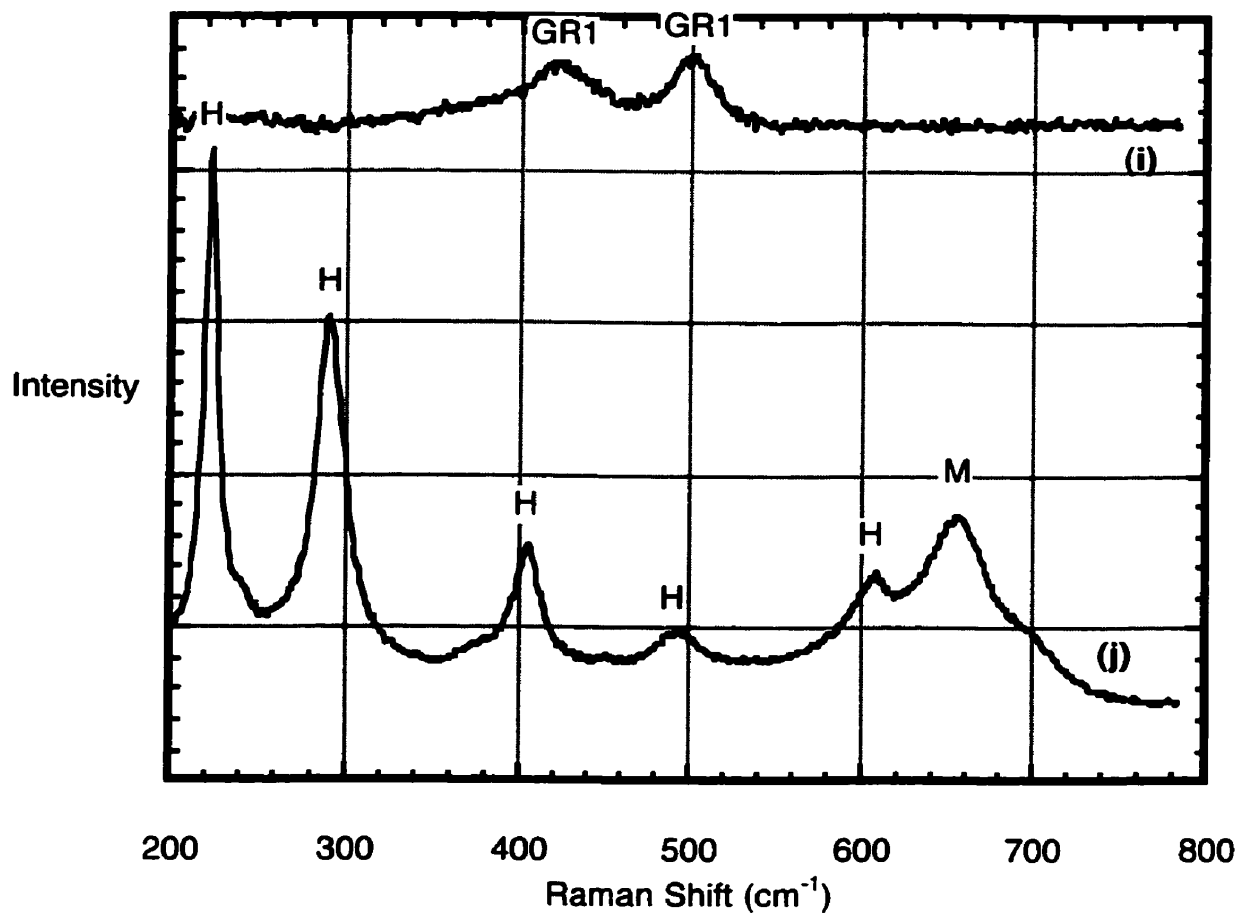
Figures 4.3.2.2(i) and (j) Raman spectra of **(i)** Green Rust I (GR1), and **(j)** magnetite (M) and hematite (H) which formed on the surface of ground steel in a Type 10 simulated pore solution containing sufficient chlorides to make a chloride/hydroxide ratio of 4.
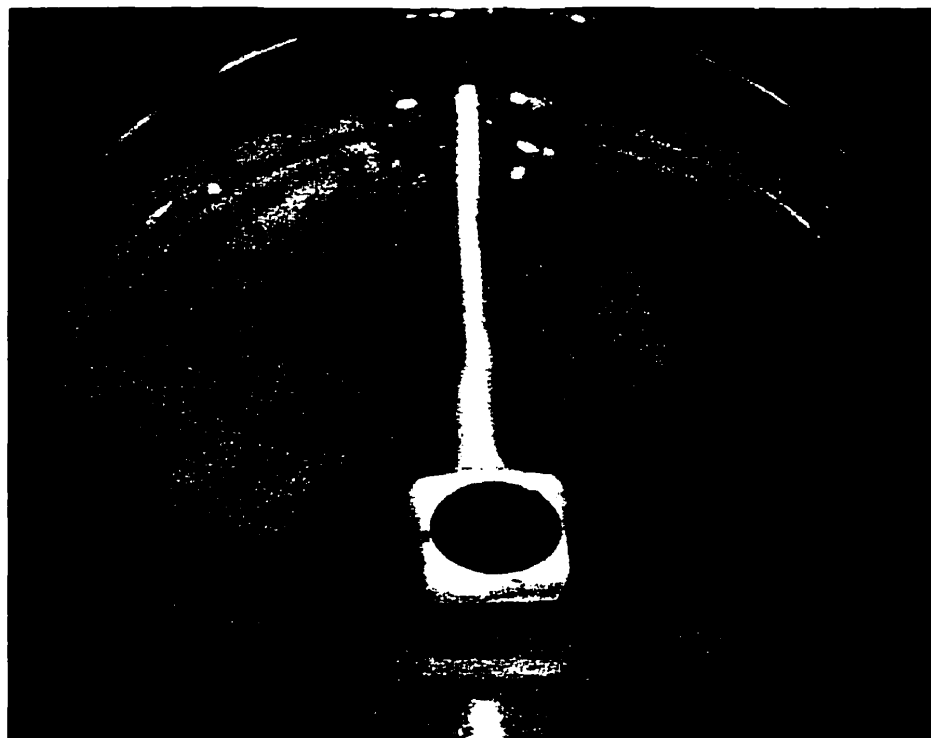
Figure 4.3.2.2(k) Photograph of the ground steel surface at the end of the *in situ* Raman experiment.

Similar localized corrosion products were noted on the surface of the steel samples in white simulated pore solutions with a chloride/hydroxide ratio of 11. However, the products were first observed at approximately -100 mV SCE possibly because of the relatively higher chloride/hydroxide ratio of the white solution (i.e., 11 versus 4 for the Type 10 solution). Raman analysis was again inconclusive on these products because of the difficulty in focussing the optical system on black products. One successful scan of the corrosion product at an applied potential of +200 mV SCE indicated the presence of Green Rust I and magnetite, shown in Figure 4.3.2.2(l). Other localized corrosion areas formed during the remainder of the experiment and the final appearance of the steel surface is shown in Figure 4.3.2.2(m). One area of corrosion product was observed to grow towards the surface of the immersion solution and its final height approached 3 mm, as shown in Figure 4.3.2.2(n). This remarkable height suggests that the high mobility of hydroxide ions in the simulated pore solution migrated to the corrosion pit to react with the iron ions resulting from the anodic dissolution of the steel. Also of interest is that this formation would likely not have occurred if the solution had been continuously stirred.
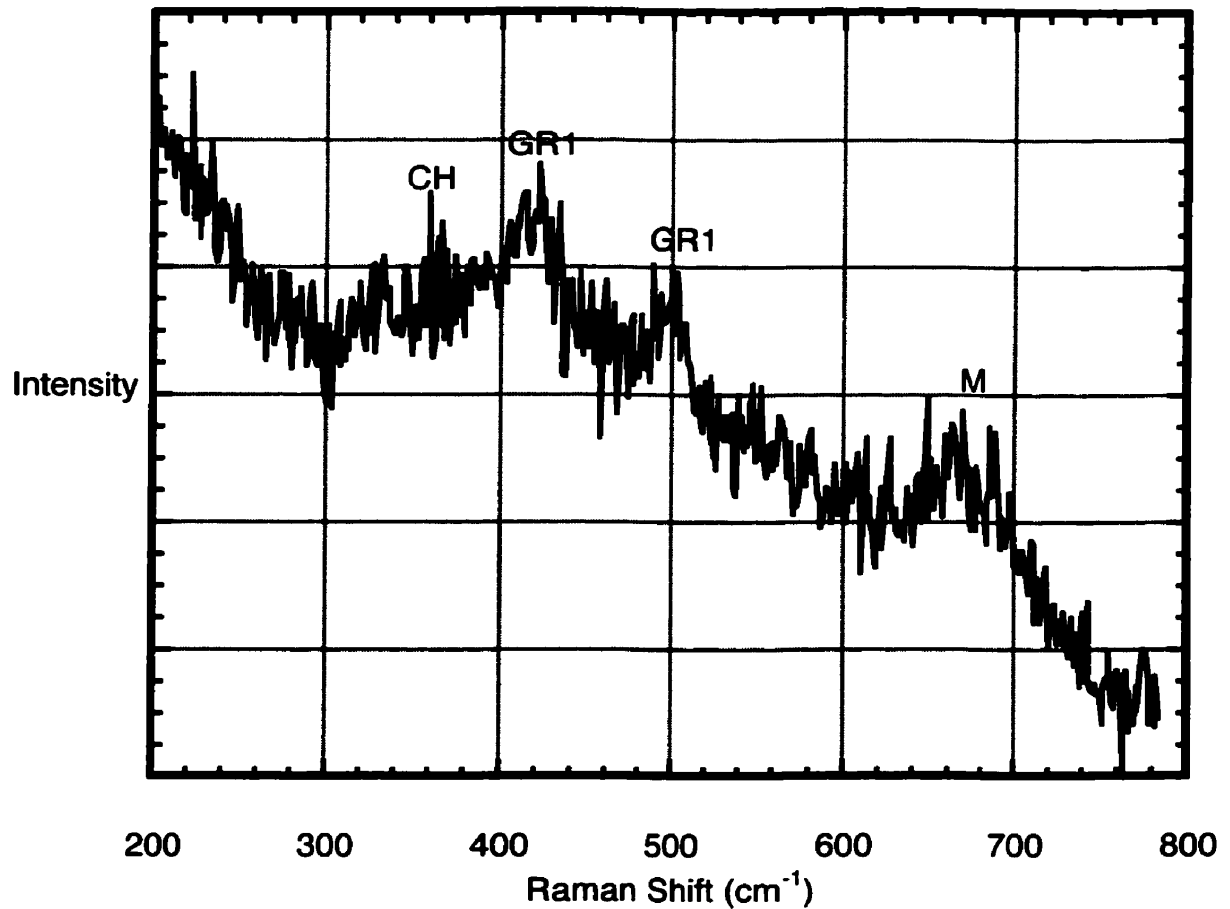
Figure 4.3.2.2(l) Raman spectrum indicating Green Rust I and magnetite which formed on the surface of ground steel in a white simulated pore solution containing sufficient chlorides to make a chloride/hydroxide ratio of 1 1. The calcium hydroxide peak resulted from the excess present in the simulated pore solution.
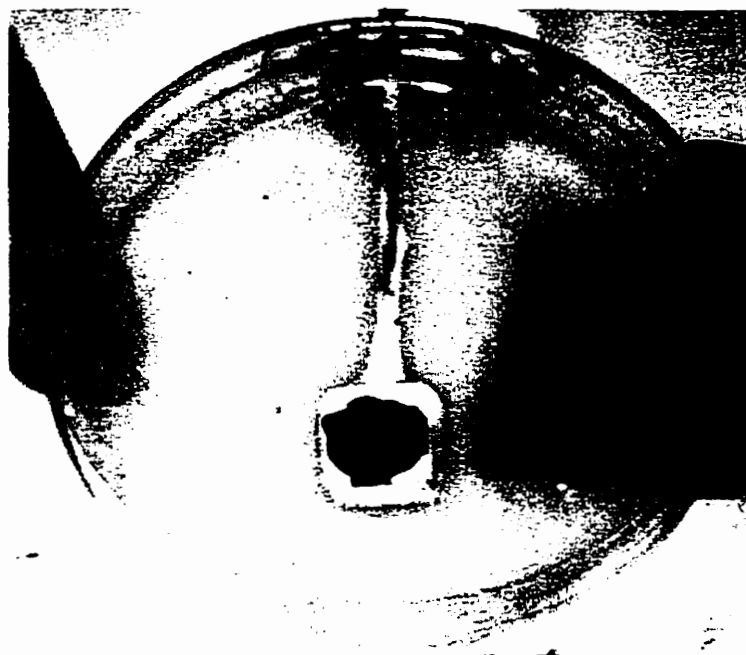
Figure 4.3.2.2 (m) Macrophotograph of the ground steel surface at the end of the *in situ* Raman experiment. The steel had been exposed to a white simulated pore solution with a chloride/hydroxide ratio of 11.

Figure 4.3.2.2(n) A side view of the ground steel surface shown in Figure 4.2.2.2(m) at the end of the *in situ* Raman experiment.

A review of all corrosion products observed on the ground steel surfaces indicates that higher chloride/hydroxide levels (greater than 2) permitted corrosion to initiate at locations other than the epoxy/steel perimeter as was the case with the intermediate chloride/hydroxide ratio of 2. This was not observed with the as-received steel surfaces where corrosion initiation was more likely governed by the imperfections in the mill scale as discussed in greater detail in Section 4.3.2.4. In addition to the location of the corrosion product, the higher chloride/hydroxide ratios also altered the type of product and permitted the formation of Green Rust I on ground steel surfaces in both simulated pore solutions. The work of Génin et al. and Refait et al. indicates that chloride/hydroxide levels of at least 1.025 are necessary for Green Rust I to form (Génin, Rezel et al. 1986; Refait and Génin 1993). It is possible that this product did form at the chloride/hydroxide ratio of 2 but in quantities too small to be detected. Overall, observable corrosion products formed at lower applied potentials in the white simulated pore solution than that in the Type 10, -100 mV versus +200 mV SCE. Although the chloride/hydroxide levels are dissimilar, the chloride content was the same (i.e., 1 M Cl⁻ solution) and this suggests that the passive films that formed were different. This is discussed in greater detail in the next Section.

4.3.2.3 Effect of the Pore Solution Composition

As was shown in the previous Section, the presence of chlorides had a significant effect on the type and distribution of corrosion products that formed. However, the correlation between the corrosion products and the chloride/hydroxide ratio was less clear. As described in Section 2.3.2.2 (Chapter 2), several researchers (Raharinaivo and Génin 1986; Refait and Génin 1993; Génin, Refait et al. 1997) have concluded that certain corrosion products form within precise chloride/hydroxide ratio ranges. This is clearly contradictory to the results of the present study in which corrosion products formed (i.e.,

magnetite, maghemite, etc.) at chloride/hydroxide ratios outside the ranges reported in the aforementioned published work. This discrepancy is explained by considering that the published work studied equilibrium mineral/solution interactions rather than the steel/mineral/solution steady-state (or metastable) relationships examined in this Chapter.

Within the system studied in this Chapter, the solution pH has a strong effect on the corrosion behaviour of immersed steel. Table 4.3 details the concentration of chlorides in both types of simulated pore solution and their corresponding chloride/hydroxide ratios. As mentioned in the previous Section, this table illustrates that identifiable corrosion products (i.e., of sufficient thickness to be detected by the Raman technique) formed on the ground steel in the white simulated pore solution which contained a lower chloride ion concentration than the Type 10 solution. This suggests that the passive film formed on the ground steel in the relatively higher pH Type 10 simulated pore solution was more protective than the passive film formed in the lower pH white simulated pore solution. This conclusion could not be confirmed for the as-received steel surfaces because no corrosion was detected when the chloride/hydroxide level was 2 and the evidence would have been clear. It was apparent, however, that significantly larger volumes of corrosion products were observed on those specimens which were exposed to the white simulated pore solution rather than the Type 10. This likely occurred because corrosion initiated on the steel in the white simulated pore solution at lower potentials than in the Type 10 solution and was, therefore, corroding for a longer period of time by the end of the experiment.

Overall, it is unlikely that the interaction of other ionic species in the simulated pore solution produced any of these effects because the solutions are essentially the same with the exception of the mass of sodium and potassium hydroxides added. Since the formation of a chloride-induced corrosion pit is accompanied by a localized drop in pH, it is reasonable to conclude that lower pH pore solutions would facilitate this process.

114

Furthermore, other published work which studied multiple formulations of simulated pore solutions observed that the pH of the solution had the most significant impact on whether corrosion products formed and their composition upon formation (Guilbaud, Chahbazian et al. 1994; Mammoliti 1995). This is reinforced by a review of the iron Pourbaix diagram (i.e., Figure 2.3, Chapter 2) which shows a theoretical range of iron products for the pH range typically expected in uncontaminated cementitious materials (i.e., pH values from 12.5 to 14). Presumably, these different products would vary in their ability to protect the steel.

The conclusion that the chloride/hydroxide ratio is a poor predictive tool in cementitious systems is not entirely correct, however. A review of Table 2.3 (Chapter 2) indicates that with increasing chloride/hydroxide ratios, a certain progression of corrosion products is expected which satisfy the thermodynamic and kinetic interrelationships between the corrosion products. This pattern outlined in Table 2.3 was consistent with the observations of the *in situ* Raman experiments where the lower chloride/hydroxide levels produced magnetite, maghemite, and hematite while the higher levels produced Green Rust I. Thus, it appears most appropriate to conclude that chloride/hydroxide ratios should not be applied indiscriminately to predict corrosion products in any pore solution but rather must be individually determined for each particular solution. This conclusion can partly explain the wide variability of corrosion initiation periods and the observed products in field structures as within a inhomogeneous cover, the chloride and hydroxide contents are likely to vary widely over the embedded rebar. This supports the use of probabilistic and stochastic service life models which can accommodate a range of conditions.

4.3.2.4 Effect of the Surface Finish of the Steel

First and foremost, the presence of mill scale added additional complexity to the analysis of results because it was very difficult to visually detect corrosion products on the dark-coloured mill scale. Figure 4.3.2.2(c) demonstrates this difficulty as the green-black corrosion product is not readily detected on the black mill scale. Nonetheless, the type and distribution of corrosion products which formed on the mill scale seemed different from their ground steel counterparts.

At similar chloride concentrations in the simulated pore solutions, a smaller volume of corrosion products was observed to form on the as-received surfaces than on the ground surfaces, if products formed at all. It appears that the mill scale did provide a physical barrier that resisted corrosion initiation. In addition, the areas where corrosion initiated appeared to be determined by existing flaws in the mill scale while corrosion on the ground steel often initiated at the edge of the epoxy. Whether the corresponding corrosion rates were higher once corrosion initiated in the existing flaws, as suggested by Addelson and Rice (Addleson and Rice 1995), cannot be ascertained from observations of the corrosion products and must be determined from the analysis of the simultaneous electrochemical measurements. This work is presented in the next Section.

4.3.3   *In Situ* Electrochemical Analyses during Raman Spectroscopy

During the *in situ* Raman experiments described in the previous Section, the immersed steel samples were under potentiodynamic control, and as such, the current required to achieve each applied potential was recorded. Figures 4.3.3(a) through (d) present the applied potential-current density curves for ground and as-received steel samples in either a white or Type 10 simulated pore solution, some of which contained chlorides. Each figure compares the curves for increasing chloride/hydroxide ratios: 0, 2, and 11 for the white

simulated pore solution, and 0, 2, and 4 for the Type 10.
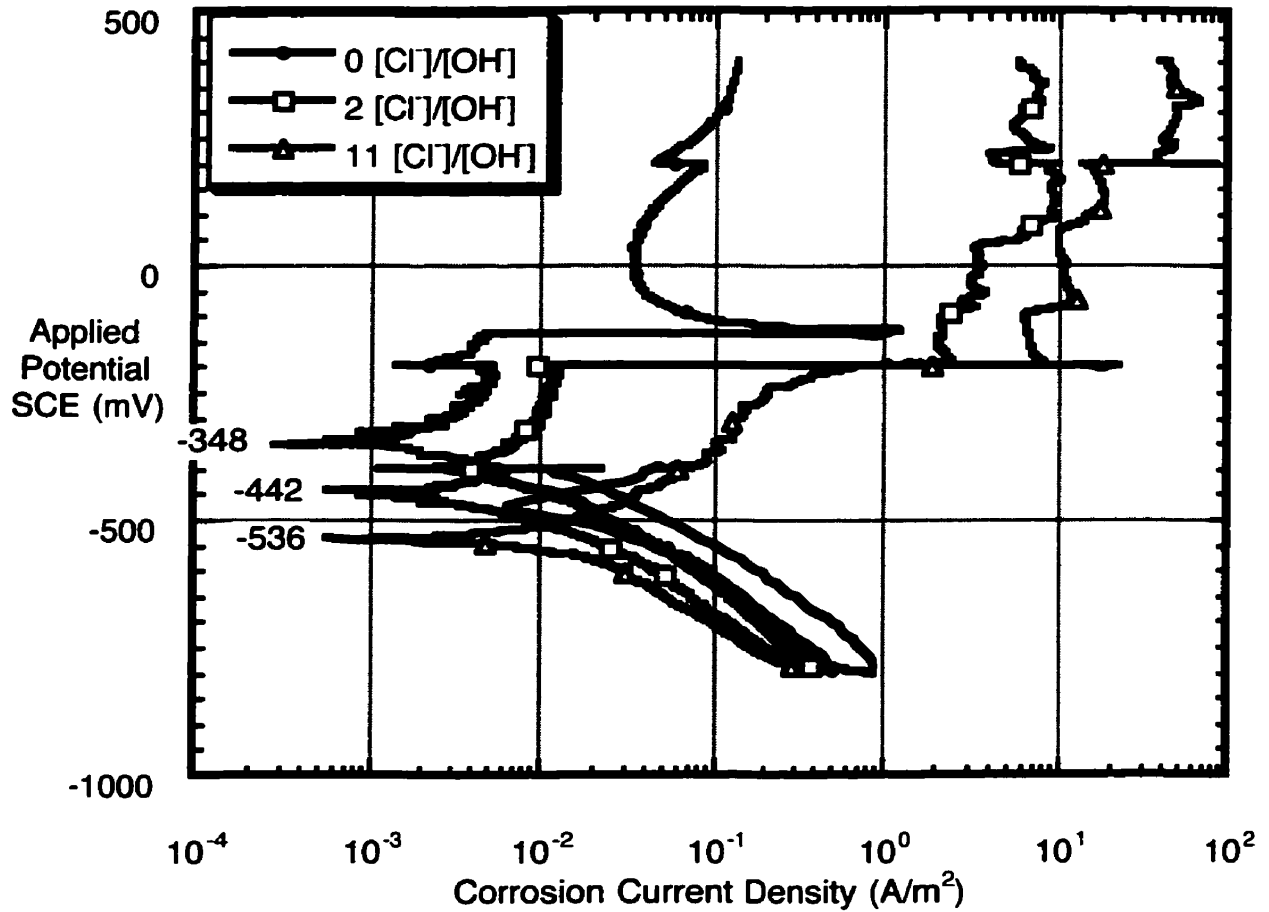
Figure 4.3.3(a) A comparison of the applied potential/corrosion current density curves obtained from ground steel samples in white simulated pore solution during *in situ* Raman experiments.
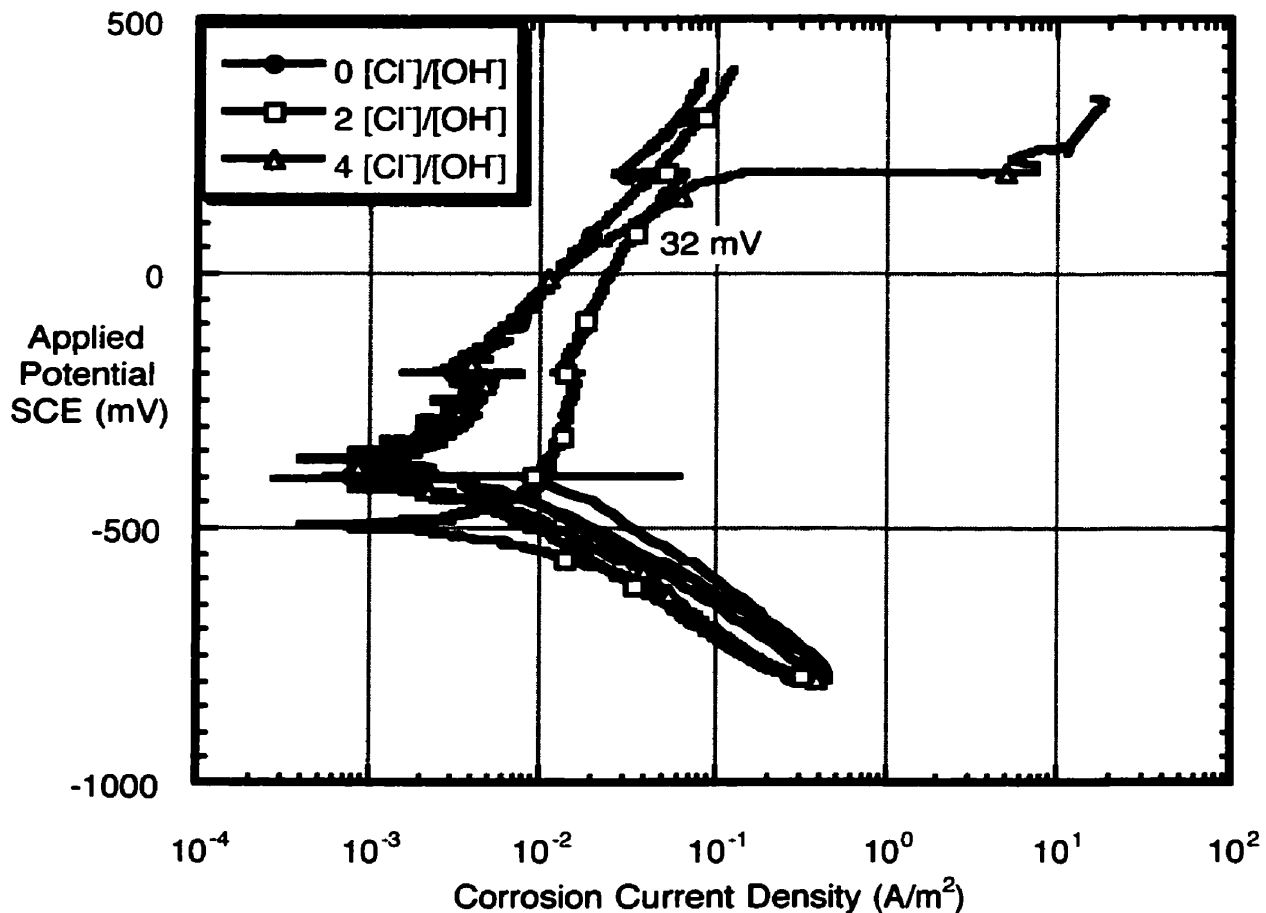
Figure 4.3.3(b) A comparison of the applied potential/corrosion current density curves obtained from ground steel samples in Type 10 simulated pore solution during *in situ* Raman experiments.
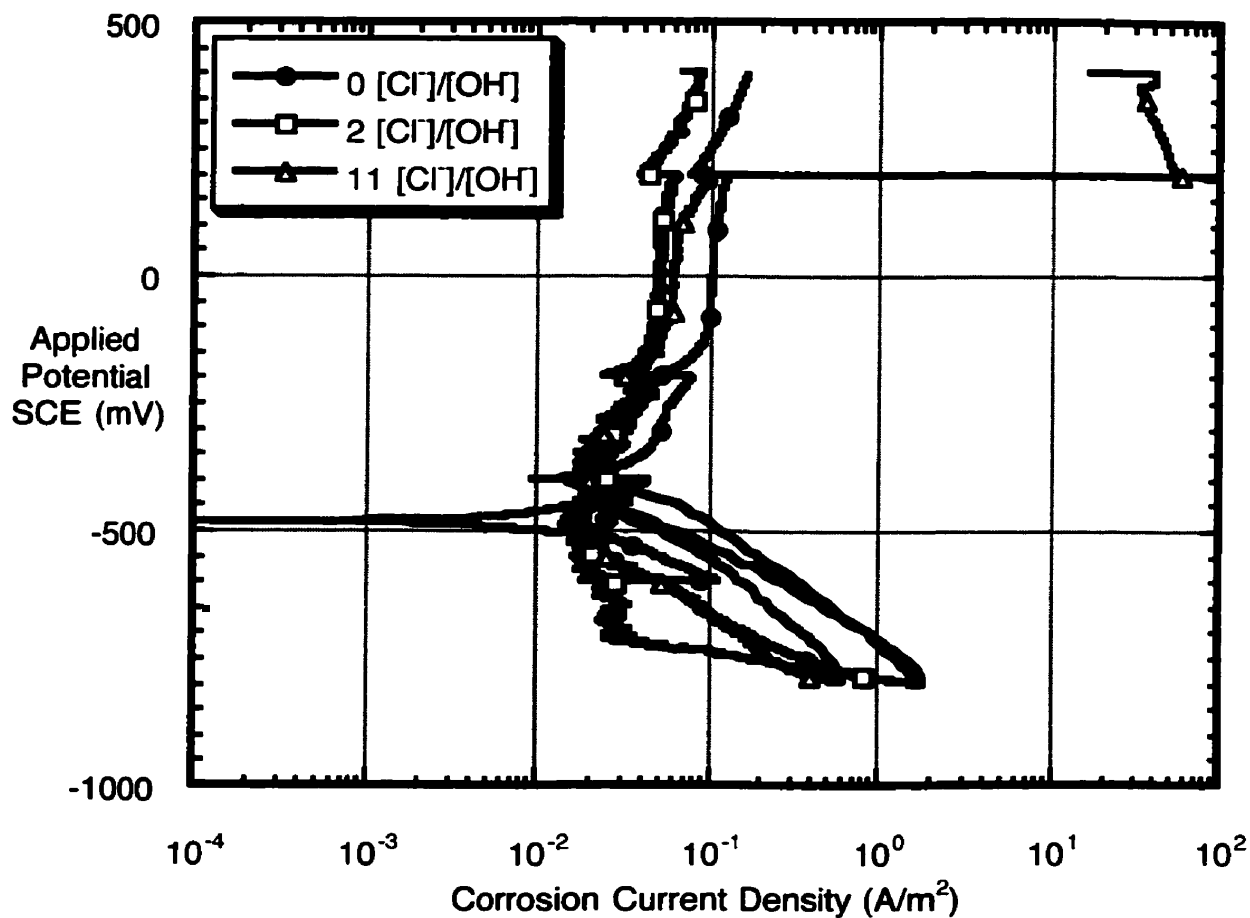
Figure 4.3.3(c) A comparison of the applied potential/corrosion current density curves obtained from as-received steel samples in white simulated pore solution during *in situ* Raman experiments.
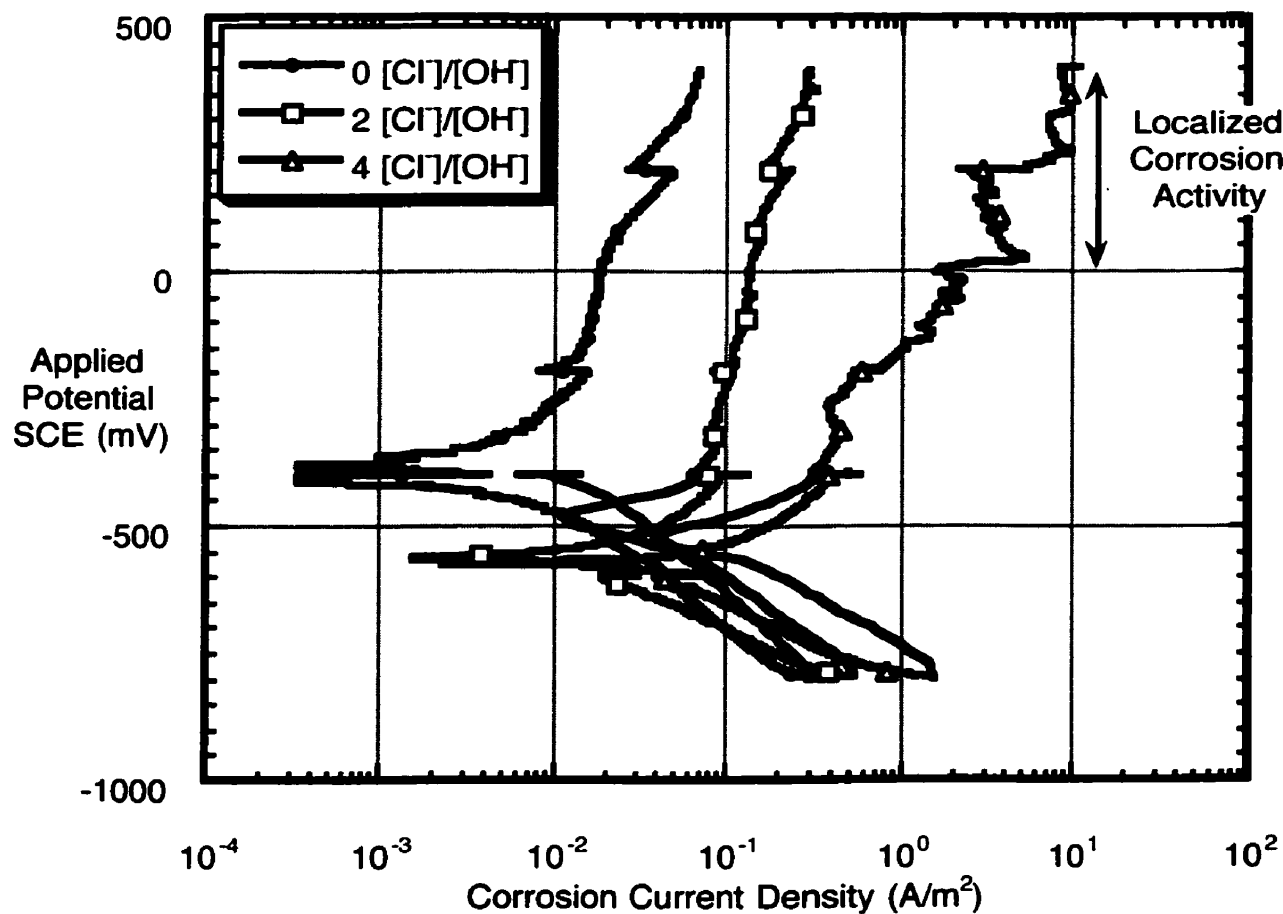
Figure 4.3.3(d) A comparison of the applied potential/corrosion current density curves obtained from as-received steel samples in Type 10 simulated pore solution during *in situ* Raman experiments.

4.3.3.1 Comparison of Ground Steel Surfaces

The comparison shown in Figure 4.3.3(a) indicates that the presence of chlorides in the pore solution increased the anodic corrosion current density by approximately two orders of magnitude. This is observed as a general shift of the anodic portion of the curves from approximately 0.1 A/m^2 to 10 A/m^2 at approximately -200 mV which corresponds to

average current densities that range from 0.001 A/m^2 to almost 0.1 A/m^2 when measured near the open circuit potential. In addition, the current densities of the steel immersed in chloride solutions vary over a significantly larger range above -200 mV than that observed with the steel immersed in the chloride-free simulated pore solution. These variations suggest the formation of corrosion products which would affect the corrosion current density by covering active corrosion sites. Changes in the types of products formed and the number of active sites would also contribute to the variability. Alternatively, no clearly defined changes were noted in the cathodic portion of the curves with the exception that the potentials which corresponded to the bare steel decreased with increasing chloride levels, from -348 to -536 mV (SCE). This is consistent with the change in the surface film of the steel due to the presence of chlorides.

Other dramatic shifts were observed in the anodic portions of the curves which can be attributed to periods of the *in situ* experiment where the level of the simulated pore solution over the steel was dropped from approximately 4-5 mm to 1 mm (i.e., periods when Raman spectra were gathered). A severe example of this was measured for the steel immersed in the chloride-free simulated pore solution. Figure 4.3.3(e) compares this curve with a similarly prepared steel sample within an identical *in situ* cell which did not have the level of its pore solution changed over the course of the experiment. Clearly, the changing level of the pore solution over the surface of the steel introduced some experimental artifacts in the corrosion current density measurements. However, these shifts did not appear to affect the overall interpretation of the results because once the level of the pore solution was raised at the end of the Raman collection period, the corrosion current density returned to a lower, presumably steady-state level. However, similar large shifts were maintained for the steel samples immersed in the chloride-containing simulated pore solutions. With the presence of chlorides, it is likely that the increased exposure to oxygen in the simulated pore solution stimulated any corrosion reactions. Overall, this result indicates relative

comparisons of the curves are appropriate but their results cannot be directly compared with other curves obtained with different experimental conditions.
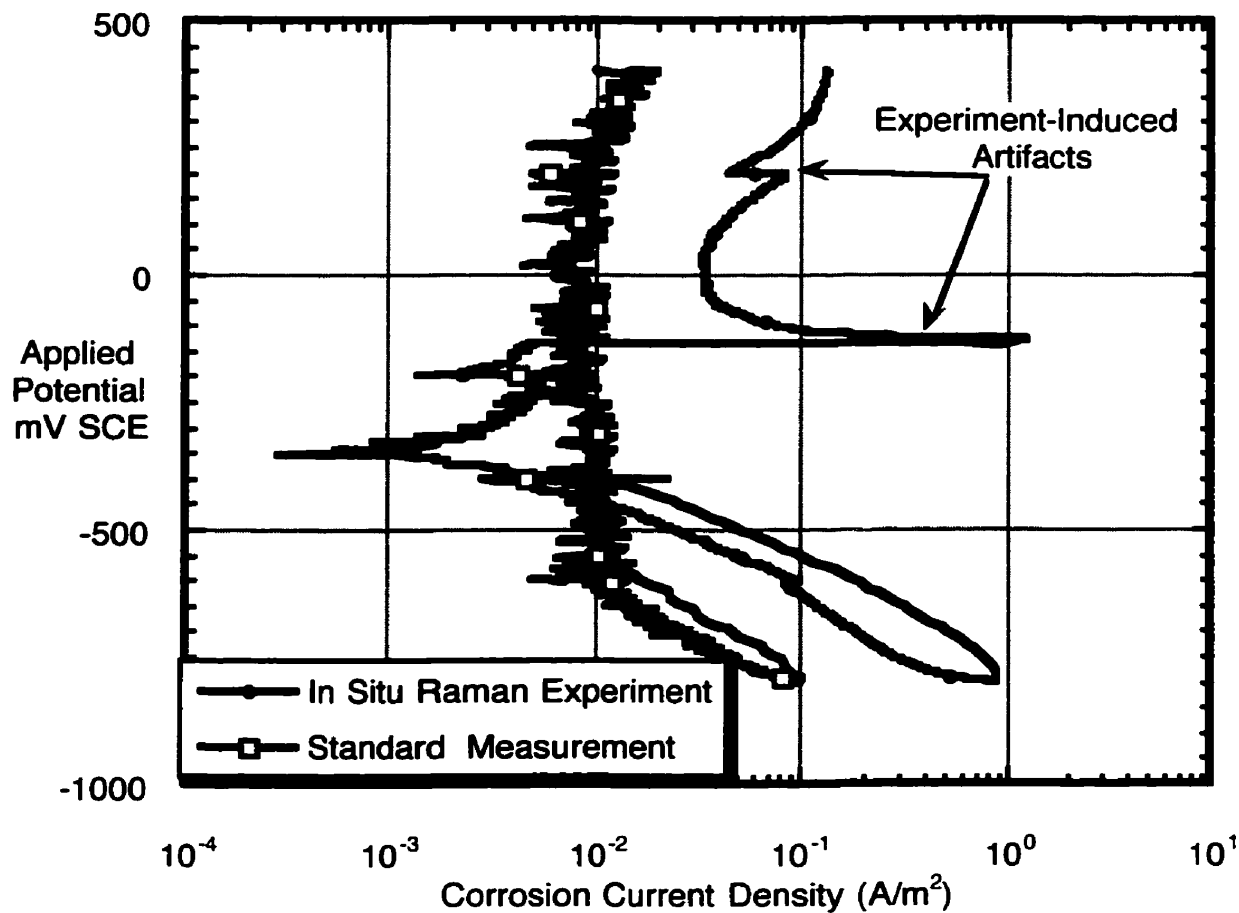
Figure 4.3.3(e) A comparison between applied potential/current density curves demonstrating the effect of pore solution height over the steel during *in situ* Raman experiments.

These conclusions are reinforced by the trends observed with steel samples immersed

in the Type 10 simulated pore solutions, as shown in Figure 4.3.3(b). Small, momentary shifts were observed for steel samples immersed in the chloride-free simulated pore solutions and the solution with sufficient chlorides to make a chloride/hydroxide ratio of 2 when the applied potential reached +200 mV (SCE). This, and the overall corrosion current density of slightly above 0.001 A/m^2 suggests that no corrosion activity was occurring on these samples. Alternatively, a large, permanent shift was observed for the steel within the 4 [Cl$^-$]/[OH$^-$] solution at the same potential, and the two orders of magnitude increase to 10 A/m^2 at +200 mV SCE suggests that corrosion was occurring. This corresponded to an average current density of approximately 0.01-0.1 A/m^2. Although stimulated by the increased exposure to oxygen during the Raman accumulation, the gradual increase in current density around +32 mV SCE indicates that corrosion initiated independently.

This potential is considerably higher than the potential at which the steel was observed to corrode in the white chloride-containing simulated pore solutions (i.e., -200 mV (SCE)). Moreover, corrosion was not observed for the steel immersed in the Type 10 solution with a chloride/hydroxide ratio of 2 as it was in the equivalent white solution despite the much higher chloride activites/concentrations. This difference in corrosion behaviour of the steel samples suggests that the higher pH of the Type 10 simulated pore solution formed a more protective passive layer on the surface of the steel than that in the white, in spite of the similar chloride/hydroxide ratios.

4.3.3.2 Comparison of As-Received Steel Surfaces

The results from the as-received steel surfaces have similar trends to that observed for the ground steel surfaces, as shown in Figures 4.3.3(c) and (d). Figure 4.3.3(c) presents the curves obtained for as-received steel surfaces exposed to white simulated pore solutions, without chlorides and chlorides sufficient to make chloride/hydroxide ratios of 2 and 11. These curves show an overall corrosion current density of 0.01-0.1 A/m^2 until +200 mV

(SCE) is reached in the 11 $[Cl^-]/[OH^-]$ solution, and current density increased almost three orders of magnitude to 100 A/m^2. This coordinated with an estimated average corrosion current density of approximately 0.1 -1 A/m^2. Thus, no corrosion was observed for these steel samples until the applied potential reached +200 mV (SCE) in the 11 $[Cl^-]/[OH^-]$ level solution.

Similar steel samples in the Type 10 simulated pore solutions exhibited different behaviour, as shown in Figure 4.3.3(d). Each increase in the chloride level in the simulated pore solution caused the corrosion current density to increase approximately one order of magnitude with a maximum current density of 10 A/m^2 for the highest chloride/hydroxide ratio of 4. At the highest level of chlorides for the Type 10 solution, localized corrosion behaviour was possibly indicated by the minor variations in the anodic portion of the curve beginning at approximately 0 mV (SCE). These variations suggest the formation of corrosion products which would limit the accessibility of chlorides to any active corrosion sites.

Overall, the differences in behaviour of steel in similar pore solutions suggests that the inherently inhomogeneous as-received steel surface produced the significant variability observed among the steel samples. The localized pitting behaviour noted for the steel in the white simulated pore solution likely resulted from a small break in the mill scale as well as the relatively higher chloride/hydroxide level (i.e., 11 versus 4). With a theoretically more uniform mill scale (i.e, an absence of large flaws) over the surface of the steel immersed in the Type 10 solution, the expected corrosion behaviour would be more general, as shown in Figure 4.3.3(d). It is likely that if a chloride/hydroxide ratio of 11 were studied with the Type 10 solution, localized pitting at the level noted with the white solution would be observed.

4.3.3.3 Comparison of Ground versus As-Received Steel Surfaces

A comparison of Figures 4.3.3(a) through (d) shows that the interpretation of corrosion measurements derived from steel with varying surface finishes is difficult. In spite of the duplicate samples and similar surface treatments, no consistent trends can be deduced except for those already noted in the previous Sections. For the steel in the white simulated pore solutions, the mill scale appeared to provide better protection from corrosion until a critical level of corrosion and applied potential was reached. However, once these levels were met, localized corrosion was observed which exceeded the corrosion current density measured for any other sample by approximately an order of magnitude. This is consistent with the work of Addleson and Rice (Addleson and Rice 1995) who showed that the physical barrier provided by mill scale can protect the steel to a certain level but that corrosion is more severe once it initiates, presumably at flaws in the mill scale.

4.4 DISCUSSION

4.4.1 Effect of Chloride Exposure

Of all the factors studied in this Chapter, it is not surprising that the chloride concentration of the exposure solution had the greatest significant impact on the corrosion rates, and the type and distribution of corrosion products which formed. However, a precise quantification of this effect is difficult because of the inherent variability of the surface of the steel and its effects on corrosion initiation. In spite of this difficulty, consistent results were obtained from the first series of full potentiodynamic polarization experiments and the *in situ* Raman experiments which facilitate a better understanding of the interrelationship between measured corrosion rates and the formation of corrosion products to be developed.

125

Specifically, minor fluctuations in the anodic portion of the curves (i.e., in situations where pitting was not indicated) shown in Figures 4.3.1.2(a) through (d) indicated that chlorides were attacking the surface of the steel but a significant pit activity had not been established. This activity corresponded to average corrosion current densities of 0.1-1 A/m^2 and was approximately only one order of magnitude larger than the current densities measured for steel in chloride-free simulated pore solutions (i.e., passive conditions). Similar rates were measured for the steel during the *in situ* Raman experiments and no corrosion products, with the exception of thin films at the perimeter of the steel samples, were observed (Figures 4.3.2.2(f), (g) and (h)). These current densities can then be considered to indicate a pseudo-uniform attack on the steel where multiple corrosion pits are initiated but do not grow and may repassivate. This most likely occurred because the immersion solutions were not stirred and the lower chloride levels in the solution might have become exhausted locally and the any pits would not have been sustained.

As the chloride levels increased in the simulated pore solutions, the probability of a sustained pit became greater. Indeed, large corrosion current density increases in the anodic portion of the curves consistent with the initiation and growth of one or more large pit(s) were observed in both experiments once chloride/hydroxide ratios of at least 1.4 were reached. In these instances, the current density increases were approximately two to three orders of magnitude larger than those measured for steel in chloride-free solutions. Typically, these rates ranged from 100-1000 A/m^2 at a potential of +400 mV SCE (average corrosion current densities of approx. 0.01-0.1 A/m^2) and during the *in situ* Raman experiments, localized accumulations of corrosion products were observed to grow towards the surface of the solution. In reality, the corrosion rates were considerably higher as the area of these localized accumulations was not used to revise the corrosion current densities. A corrected calculation suggests that average corrosion current densities of 0.5-5 A/m^2 occurred at these localized sites (conservatively assuming that 2% of the area was

corroding). This magnitude of corrosion rate would prove catastrophic in a steel-reinforced concrete structure within a short period of time.

It is possible, however, that a sufficient volume of corrosion products could form to provide a physical barrier to reduce or prevent the diffusion of chlorides, water, and oxygen to the surface of the steel in the manner postulated by Ashworth, Boden et al. and Leek (Ashworth, Boden et al. 1970; Leek 1997), as described in Section 2.3.2.2. However, this was not observed to occur during any of the simulated pore solution experiments, and was unlikely to occur as the formation of corrosion products without any constraints such as a cementitious cover would not likely produce dense, protective products. Indeed, magnetite was one of the earliest corrosion products to form at lower chloride levels and is the predominant corrosion product comprising most mill scales. Mill scales are thought to provide a measure of corrosion protection but it is clear that the formation of magnetite did not reduce the corrosion activity of the immersed steel samples. At higher chloride levels, it was merely a precursor to other products such as maghemite and hæmatite. Overall, these products have estimated specific volumes of approximately 2 when compared to iron, as shown in Figure 2.6 (Chapter 2). Whether higher specific volume products would have formed with higher chloride exposures is uncertain.

4.4.2 Effect of Pore Solution Composition

When comparing the results of the full potentiodynamic polarization experiments with those from the *in situ* Raman experiments, there appears to be a discrepancy concerning the effect of the simulated pore solution composition. During the former experiments, differences in the pore solution composition did not appear to have an effect of the corrosion behaviour of the steel. This seems to contradict the results of the latter experiments where ground steel immersed in the white simulated pore solution was observed to pit at lower potentials and chloride concentrations than those observed for the

Type 10 solutions.

This difference was likely produced by variations in the experimental procedures between the two experiments, and the most probable cause was likely the changes in the solution depth over the immersed steel during the *in situ* Raman experiments. Such changes would have replenished the dissolved oxygen at the surface of the steel which would have enhanced the corrosion reactions occurring on the steel.

During the analysis of the Raman experiments, it was speculated that a less protective passive film might have formed on the steel immersed in the relatively lower pH, white simulated pore solution. This is consistent with the observations of Li and Sagüés (2001) who noted that chloride corrosion thresholds increased with increasing pH. The reasons for this were not elucidated in the published work but it is possible that this result can be attributed to increased ionic competition at the surface of the steel and the dissolved oxygen content of the varying solutions. Thus, the corrosion of ground steel immersed in the white chloride-contaminated simulated pore solution could be accelerated by increased exposure to dissolved oxygen relative to steel in a Type 10 solution.

4.4.3 Effect of Surface Finish

A comparison of the applied potential-current density curves for as-received steel versus ground steel suggests that the as-received steel surface does provide some enhanced protection from corrosion attack. Although the measured electrochemical activity on the as-received surface indicated that corrosion was occurring and at rates similar to its ground steel counterparts for most experimental conditions, the highest average corrosion current densities were observed for the ground steel. The explanation for this rests upon the imperfections within the mill scale that would permit chloride ions to easily accumulate and initiate corrosion. However, this does not necessarily result in a growing pit because the corrosion products would also accumulate within the pit and reduce the diffusion to it, thus

reducing the overall rate of corrosion, as shown in Figure 2.8, Chapter 2. The roughness of the mill scale would constrain the corrosion products to become denser and more protective.

On the relatively smoother surface of the ground steel, the formation of corrosion products was not observed to prevent diffusion to the active site, as described in greater detail in Section 4.4.1. This conclusion is supported by the observations of the as-received steel surfaces during the Raman spectroscopy experiments. Considerably smaller volumes of corrosion products were observed on the surface of the as-received steel when compared to those on the surface of the ground steel. In effect, corrosion products more easily blocked access to the small corrosion pits within the relatively rougher mill scale surface, and the active site was shifted to another site on the surface of the steel, as indicated by Figure 4.3.3(d). Occasionally, the surface imperfections were likely too large to be adequately blocked and an active pit would result such as that resulting in the rapid current increase at +200 mV SCE for the Cl/OH ratio of 11 in Figure 4.3.3(c). However, in contrast with the conclusions of Addleson and Rice (Addleson and Rice 1995), the corrosion behaviour under such circumstances approached that of the actively pitting ground steel because the resulting corrosion products could not effectively occlude the pit and reduce diffusion to the area.

4.5 CONCLUSIONS

1. The published assertion that certain corrosion products form within precise chloride/hydroxide ratio ranges is not corroborated in these experiments. However, the previously published work was performed under different experimental conditions. Thus, chloride/hydroxide ratios indicating the formation of various

corrosion products depend upon the system under consideration. It was noted, however, that the transition from one corrosion product to the next does correspond with increasing chloride/hydroxide ratios and does not depend upon the experimental conditions.

2. Pseudo-uniform corrosion activity was observed to occur for chloride/hydroxide levels under 1.4. Corrosion current densities of 0.001-0.01 A/m^2 were noted which corresponded to the formation of thin films of products such as magnetite and maghemite

3. Above chloride/hydroxide levels 1.4, the initiation and sustained growth of a pit was observed. As the ratios increased, the probability of the formation of an active pit increased. The current densities associated with these pits ranged from 0.5-5 A/m^2. Localized accumulations of corrosion products such as magnetite, maghemite, Green Rust 1, and hæmatite were observed to form with estimated specific volumes of approximately 2.

4. The formation of corrosion products over localized corrosion pits was not observed to reduce the measured corrosion current densities indicating that the pits were not being "stifled" by the corrosion products.

5. The lower pH of the white simulated pore solution produced a less protective passive film than that on steel in the Type 10 simulated pore solution, allowing chloride attack at lower concentrations and this was stimulated by increased exposure to dissolved oxygen.

6. The presence of mill scale can provide some enhanced corrosion protection through the formation of corrosion products within its relatively more irregular surface which reduces diffusion to and from the active site than that experienced by ground steel surfaces. Once corrosion initiates, however, the corrosion rates of the as-received steel are similar to the ground steel surfaces.

CHAPTER FIVE
COMPARISON OF CORROSION PRODUCTS
FORMED WITHIN MODIFIED CEMENT
PASTE

5.1 INTRODUCTION

This Chapter investigates the influence of a cementitious cover on the formation and composition of corrosion products and is intended to serve as a bridge between the work of Chapters 4 and 6. The previous Chapter investigated the corrosion products that form in simulated pore solutions to which chlorides in increasing quantities were added. Although useful, the conclusions drawn from this type of work are sometimes difficult to reconcile with field reinforced concrete studies because the experiments cannot replicate environmental variation on the surface of the steel induced by the presence of a cementitious cover (Mammoliti, Brown et al. 1996).

Concurrently, the work of the next Chapter studied the corrosion products that form in different commercially prepared concrete mixes. Within studies of concrete mixes, it can be difficult to clearly assess the impact of different parameters on chloride-induced corrosion because of the large variability in the materials, curing practices, and exposures that are inevitable in commercially prepared field concrete. Moreover, the component of the concrete that has the greatest impact on its durability, the cement paste, represents only a fraction of the material and is, therefore, more challenging to isolate and study. This is often compounded by the advanced level of corrosion present in these types of samples. Overall, it was the intent of these experiments to simulate natural concrete conditions as closely as possible and remove some of the inherent variability.

Thus, the work of this Chapter expands upon the work of Chapter 4 by introducing

the modified cement paste[1] cover which is anticipated to: (i) reduce the number of active corrosion sites on the steel relative to the steel in the simulated pore solution; and (ii) affect where any corrosion products will initiate and accumulate. This work also investigates the effect of cracks in the cementitious cover but overcomes the complicating effects of coarse aggregate, supplementary cementitious materials, and admixtures in the work of Chapter 6. Overall, this simplified design concept was not entirely successful as will be shown, because new complexities were introduced.

5.2 EXPERIMENTAL PROGRAMME

5.2.1 Steel Plate Preparation

Twenty steel plates (76 x 76 x 10 mm) were cut from the same bar as that used in the work of Chapter 4 and its nominal composition is detailed in Table 3.2 (Chapter 3). Holes were then drilled and tapped into three edges of the plates to accommodate 6 mm diameter (0.25") threaded plain carbon steel rods. Prior to inserting the rods into the tapped holes, one surface of each plate was milled to remove the existing mill scale (i.e., the as-received surface) and was subsequently ground on 220 grit SiC paper using water as a lubricant. The prepared surfaces were cleaned with mild soap and water, and rinsed with isopropan-2-ol. Masking tape was then applied to both 76 x 76 mm steel surfaces. The entire assembly, including all exposed surfaces of the steel rods, was painted with epoxy to prevent corrosion in these areas. Once the epoxy had fully cured, the masking tape was lifted to expose the surfaces. Surface roughness measurements were conducted on the steel plates using a Taylor Hobson Surtronic 3+ surface roughness tester. Six measurements were

---

[1] Cement paste to which 10% by mass of sand is added to provide dimensional stability against drying shrinkage.

performed on each of the ground and as-received surfaces (total of twelve for each plate). The mean roughness of the ground surfaces was 0.222 $\pm$ 0.023 μm while the mean roughness of the mill scale was 1.926 $\pm$ 0.723 μm. Figures 4.2(a) and (b) (Chapter 4) are stereomicrographs of representative regions of the prepared surfaces.

5.2.2 Mould Preparation

Polymethylmethacrylate (PMMA - Plexiglas™) moulds were assembled that produced modified cement paste specimens with the configuration detailed in Figure 5.2.2. Three epoxy coated threaded rods were used to position the steel plate correctly in the mould such that the cover depth of the modified cement paste was consistently 5 mm $\pm$ 0.25 mm when measured with a vernier caliper. These rods were also used as electrical connections during the corrosion measurements described in Section 5.2.5.
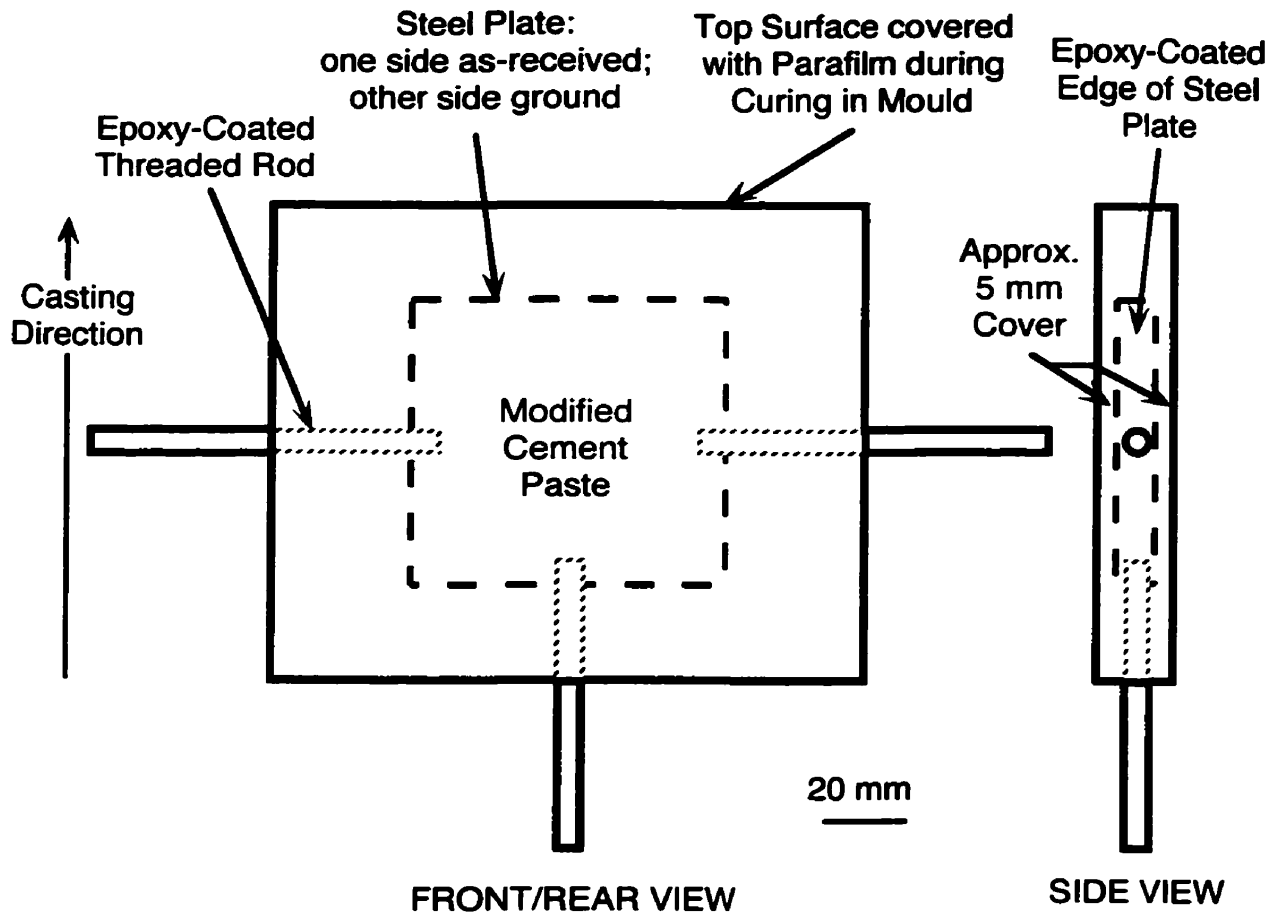
Figure 5.2.2 Detailed diagram of the modified cement paste specimens (approx. 150 by 125 by 20 mm).

5.2.3 Modified Cement Paste/Steel Plate Specimen Preparation

To investigate the significance of cement type, the same modified cement paste mix was prepared using either the white or Type 10 cement which were described in Section 3.1.1 (Chapter 3). The mixture proportions are given in Table 5.1.

Table 5.1 Mixture proportions for modified cement paste specimens.

Component	Proportion by Mass
Cement	1
Sand	0.1
Water	0.45
w/c	0.45

The cement and sand were mixed together for one minute to ensure assimilation of the dry materials prior to the addition of water. Distilled water was slowly added over the next minute to generate a water/cement ratio of 0.45. The resulting modified cement paste was mixed for five minutes, allowed to rest for five minutes, and then mixed for a final five minutes. The modified cement paste was cast into the prepared moulds (Section 5.2.2) and compaction was aided by rodding. The amount of rodding necessary to achieve satisfactory compaction was determined by the length of time it took for large bubbles to stop surfacing, typically 10 seconds. One batch of each mix with 10 specimens per batch was cast. The prisms remained in their moulds for 120 days covered in parafilm in the ambient conditions of the laboratory (approximately 20°C and 40-55% relative humidity). Every day a small portion of the parafilm was lifted off the surface of the prisms to allow ponding with water, and then the specimen was resealed in the mould with the parafilm.

5.2.4 Exposure of Specimens

After 120 days of curing, the prisms were removed from their moulds, the pattern of any cracks, typically 0.3 mm wide, were photographed, and half of the specimens were

135

randomly selected to have their cracks filled with epoxy resin. Small samples (approximately 10 g) of both types of modified cement paste were sectioned from one corner of representative specimens for use in the analyses described in Section 5.1.6. The prisms were then partially immersed into the simulated pore solution that was devised from the pore solution expression experiment described in Section 4.1.1 (Chapter 4), as shown in Figure 5.1.4. The proportions of the primary constituents (i.e., Na^+, K^+, SO_4^{2-}, Ca^{2+}) were matched as closely as possible using NaOH, KOH, $Ca(SO_4) \cdot 2H_2O$, and excess $Ca(OH)_2$. In addition, sufficient chlorides were added in the form of NaCl to make a 1 M NaCl solution. The level of the solution was checked daily and adjusted as necessary to maintain the desired immersion level.
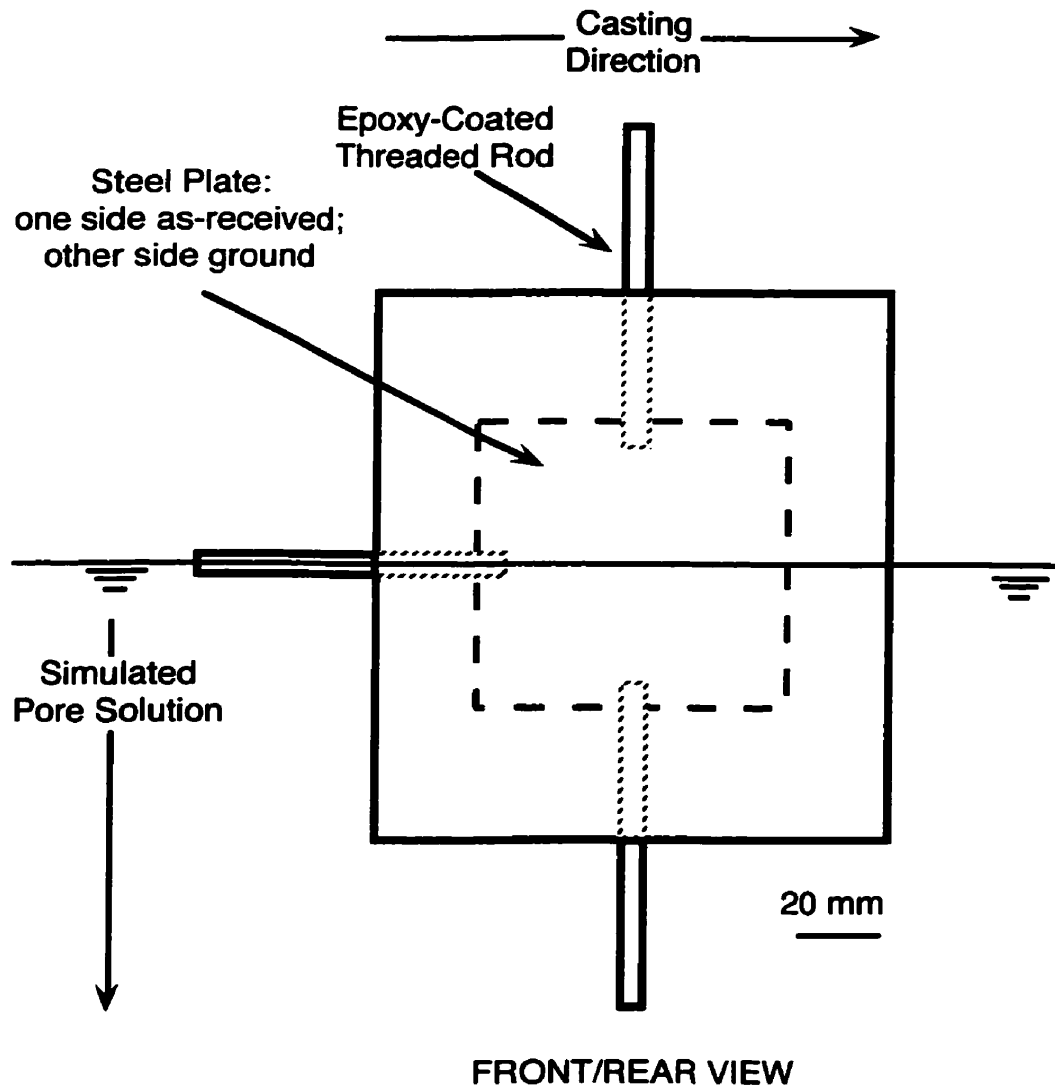
Figure 5.2.4 Orientation of steel plate/modified cement paste specimens during exposure to 1 M NaCl simulated pore solution.

5.2.5 Corrosion Monitoring

The corrosion monitoring of all specimens consisted of open circuit potential maps that

137

were coordinated with linear polarization resistance (LPR) measurements. The open circuit potential maps were conducted in a manner consistent with ASTM C 876 using a saturated calomel reference electrode (SCE). To ensure that the measurements were performed consistently on the same locations of each specimen over time, holes were cut in a transparent plastic sheet which allowed the electrode to contact the surface of the specimens at pre-determined locations approximately 6 mm apart, as illustrated in Figure 5.2.5. These measurements were performed at regular intervals along with LPR to estimate the average corrosion rate of the specimens. The linear polarization resistance technique is described in Section 2.4.3 (Chapter 2) and was performed with an EG & G Model 273A Potentiostat/Galvanostat that was interfaced to a computer for data acquisition and storage. The results from the open circuit potential maps are presented in Section 5.3.1 while the LPR results are presented in Section 5.3.2. In addition, the surfaces of the prisms were examined weekly to check for the formation of corrosion products.

Epoxy-Coated
Threaded Rod
used as electrical
connection

Open Circuit Potential
Measurements taken at
each intersection
on template,
including edges

20 mm

FRONT/REAR VIEW
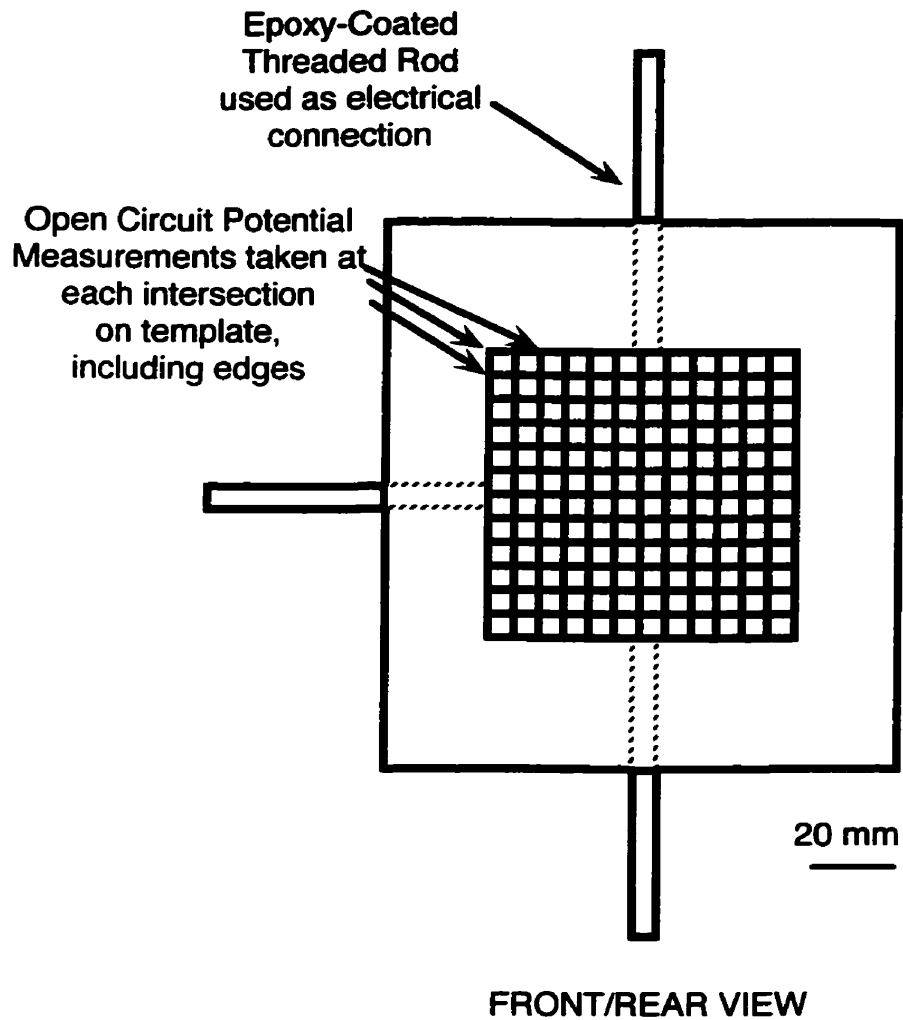
Figure 5.2.5 Detailed diagram illustrating open circuit potential measurement locations, similar to the method described in ASTM C 876.

5.2.6 Microstructural and Chemical Analysis of Specimens

As previously described in Section 5.2.4, small samples, approximately 10 g each, of both the white and Type 10 modified cement pastes were taken prior to the immersion of the

139

prisms such that any alterations to the modified cement paste from their subsequent exposure to the 1 M NaCl simulated pore solution could be assessed. Total porosity, pore size distribution measurements as well as thermal analyses (i.e., DTA/TGA) were used to characterize the modified cement paste at 120 days. These techniques were described in Chapter 3 and were subject to the limitations listed in the corresponding sections of Chapter 2.

After partial immersion in the 1 M NaCl simulated pore solutions for up to nine months[2], the three specimens from both the sealed and cracked specimens for both cement types that exhibited the highest corrosion rates were selected for further microstructural analysis (i.e., 12 specimens of the 20 were sectioned for further analysis). Each specimen was sectioned to provide modified cement paste samples (i.e., no steel) that were representative of the material above, at, or below the solution line for porosity, pore size distribution, chemical and thermal analyses as well as cross-sectional paste/steel slices for microscopy and Raman spectroscopy, as shown in Figure 5.2.6. The specimens selected for further microstructural analysis, along with other information, are presented in Table 5.2. The sections were ground and diamond polished to 1 μm using the cutting lubricant, ISOPAR M, to clean the surfaces between each polishing stage. Details of these preparation techniques as well as the characterization methods are given in Chapter 3.

---

[2] The Type 10 modified cement paste/steel plate specimens were sectioned after six months of immersion because orange stains were observed on the surfaces of the prisms.
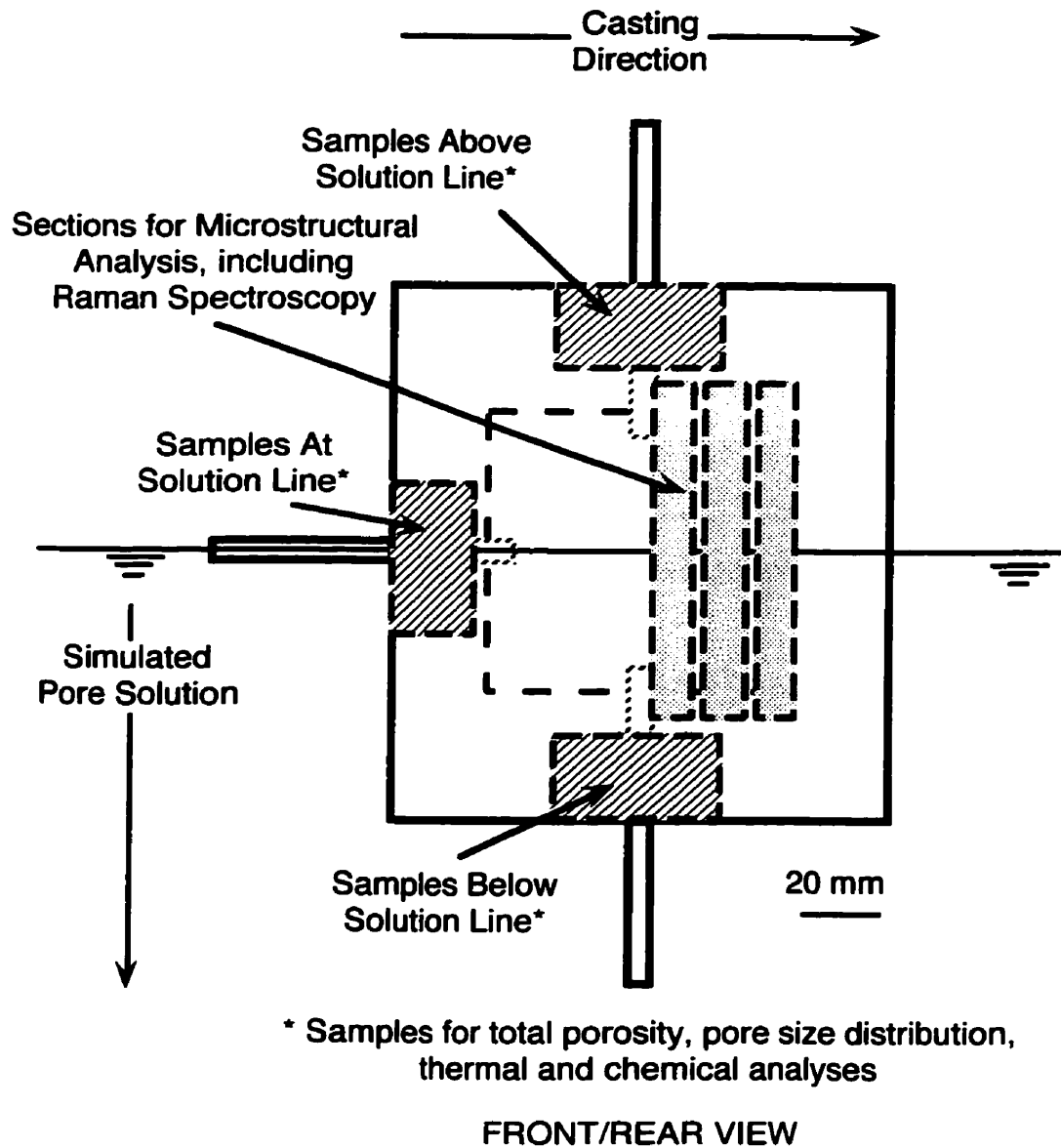
Figure 5.2.6 Detailed diagram of the specimen areas from which samples and sections were taken for microstructural, thermal, and chemical analyses.

Table 5.2 Summary of Modified Cement Paste Specimens

Specimen	Sealed cracks?	Length of Exposure (Days)	Corrosion Rate at Conclusion of Experiment $(10^{-3} A/m^2)$	Sectioned for Microanalysis?
White #1	Yes	260	8.3	Yes
White #2	No	260	10.4	Yes
White #3	No	260	11.8	Yes
White #4	No	260	8.2	Yes
White #5	Yes	260	11.4	Yes
White #6	No	260	7.2	No
White #7	Yes	260	12.1	Yes
White #8	Yes	260	4.5	No
White #9	No	260	9.3	No
White #10	Yes	260	4.7	No
Type 10 #1	No	160	3.7	No
Type 10 #2	Yes	160	4.1	No
Type 10 #3	Yes	160	4.1	Yes
Type 10 #4	Yes	160	4.4	Yes
Type 10 #5	No	160	7.8	Yes
Type 10 #6	Yes	160	4.7	Yes
Type 10 #7	No	160	4.5	Yes
Type 10 #8	No	160	5.2	Yes
Type 10 #9	Yes	160	4.0	No
Type 10 #10	No	160	4.5	No

5.3 RESULTS

5.3.1 Open Circuit Potential Maps

Over the course of the monitoring period, open circuit potentials measurements were taken regularly to the assess the overall corrosion state of the modified cement paste specimens. These measurements provided an average potential for each specimen and these individual values were pooled with others according to their respective cement type and whether any cracks had remained untreated or sealed. Figure 5.3.1(a) presents this comparison between potential measurements from the white and Type 10 modified cement paste specimens, both cracked and sealed.

Only one statistical difference (95% confidence interval) was observed over the monitoring period and occurred between the cracked versus sealed modified white cement paste specimens for the period between 15 and 30 days exposure. It is likely that upon initial exposure to the simulated pore solution, the presence of open cracks allowed the equilibrium between the embedded steel and the simulated pore solution to be established more quickly than the sealed specimens. The sealed specimens would have relied on diffusion to balance the concentration gradient of the ionic species and eventually similar potentials to the cracked specimens would develop. Once this equilibrium was established after approximately 30 days of immersion, all specimens maintained statistically similar potentials until the end of the monitoring period. It is also possible that the cracked specimens may have become partially sealed with deposits from the simulated pore solution and contributed to this convergence of the open circuit potential measurements. Although measurements were not recorded for the first 50 days of exposure for the Type 10 specimens, similar behaviour was noted for the Type 10 specimens during the remainder of the monitoring period.
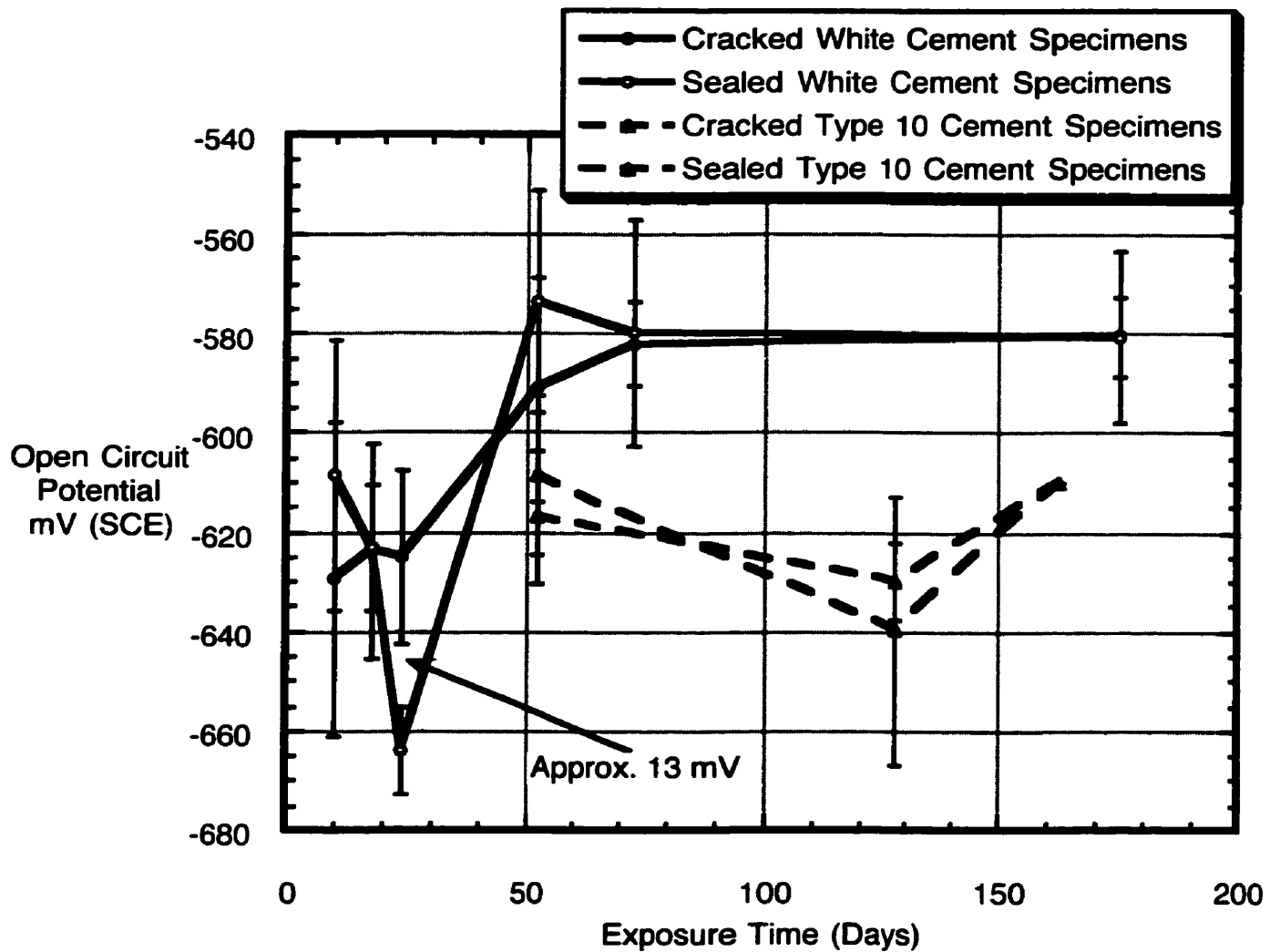
Figure 5.3.1(a) Comparison of the open circuit potential measurements from the cracked and sealed, white and Type 10 modified cement paste specimens.

The general behaviour described in the preceding paragraphs was also observed in the more detailed open circuit potential maps along with some additional features not observed in Figure 5.3.1(a). Figures 5.3.1(b) through (g) present representative potential maps

generated from measurements taken over the entire immersion period for both cracked and sealed, white modified cement paste specimens. The maps from all specimens are presented in Appendix B. The approximate crack pattern and any surface voids have been superimposed over each map using line weights and filled circles which are scaled to the size of the map area. Most cracks were typically 0.2-0.3 mm wide but those wider than 0.4 mm are individually indicated on each crack pattern. In addition to the thicker lines which denote the locations of cracks and voids, the thinner lines are isopotential lines.

Within 10 days of exposure to the chloride-contaminated simulated pore solution, the mean difference between the most positive and most negative potentials for each specimen ranged between 50-80 mV for all specimens and this range was maintained for the entire monitoring period. Of these potentials, the most negative potentials were recorded on the as-received steel surfaces on eight of the ten white and seven of the ten Type 10 cement paste specimens. This suggests that even though the mill scale provided a physical barrier over the surface of the steel, its rougher surface, 1.926 μm versus 0.222 μm for the ground steel, made it easier for chlorides to accumulate in localized areas and initiate an attack. This result is consistent with the observations of Mammoliti et al. (Mammoliti, Brown et al. 1996), Alonso et al. (Alonso, Andrade et al. 2000), and Li and Sagüés (Li and Sagüés 2001).

As-Received   Ground
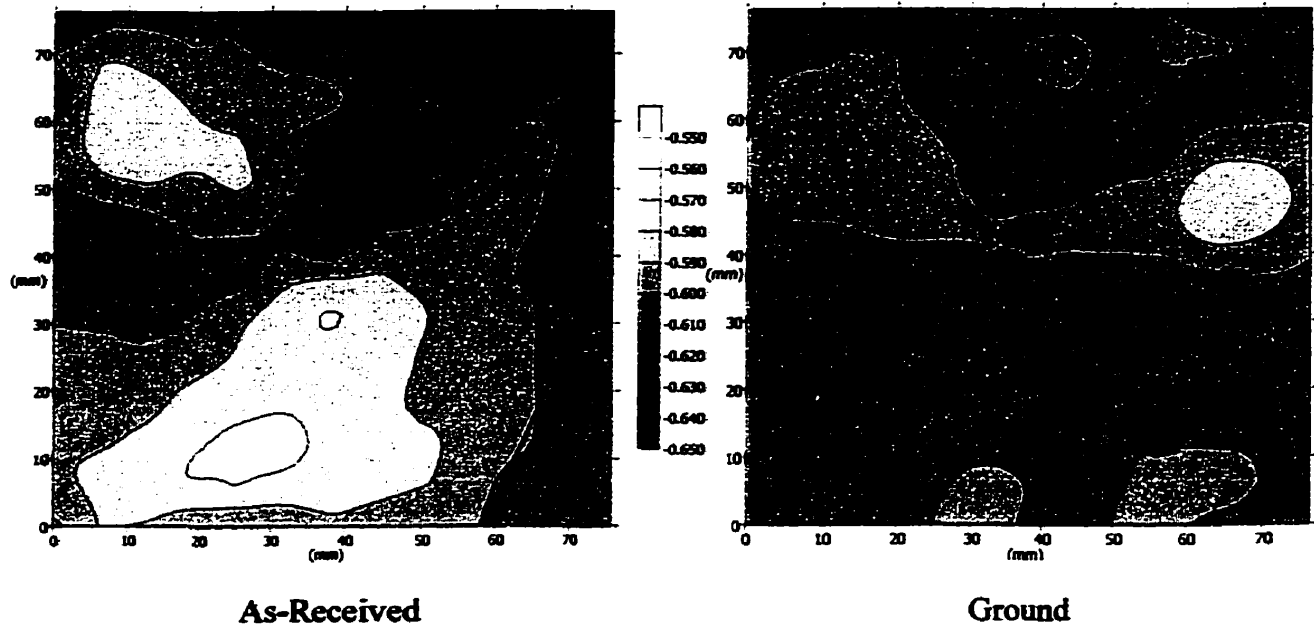
Figure 5.3.1(b) Open circuit potential maps of steel (mV SCE) embedded in cracked white modified cement paste (Specimen 3) after approximately 12 days exposure to chloride-contaminated simulated pore solution.

As-Received   Ground
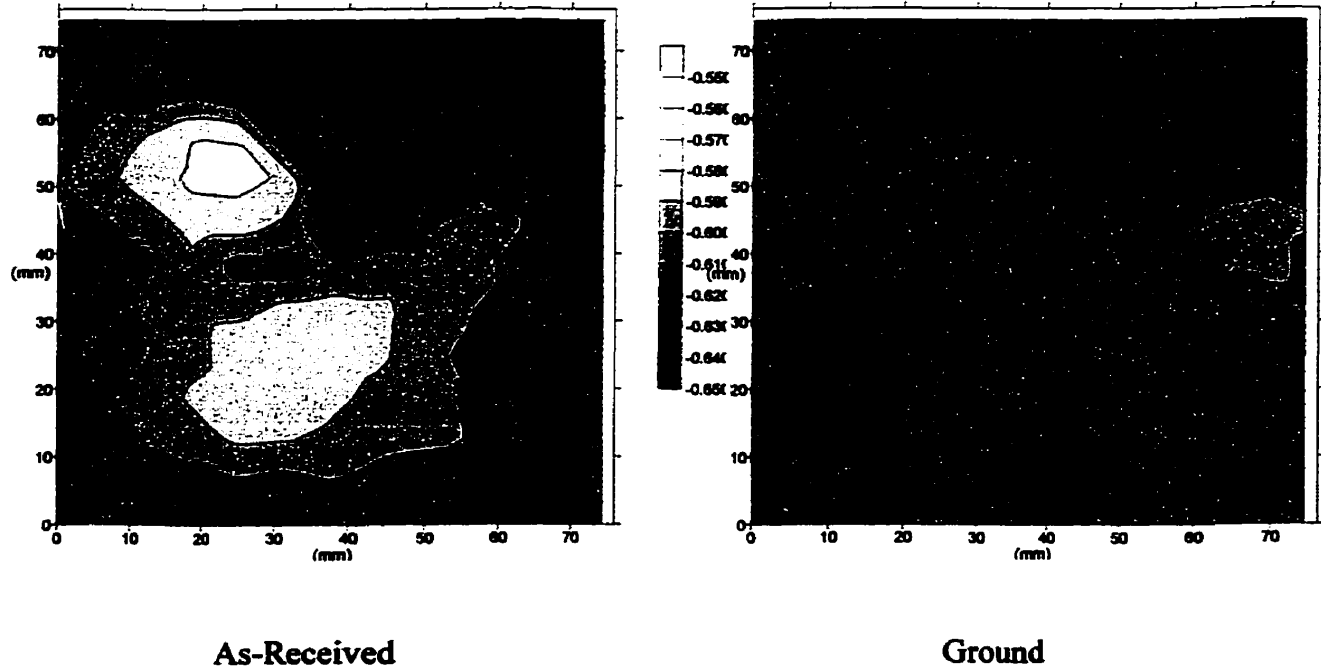
Figure 5.3.1(c) Open circuit potential maps of steel (mV SCE) embedded in cracked white modified cement paste (Specimen 3) after approximately 30 days exposure to chloride-contaminated simulated pore solution.

146

As-Received   Ground
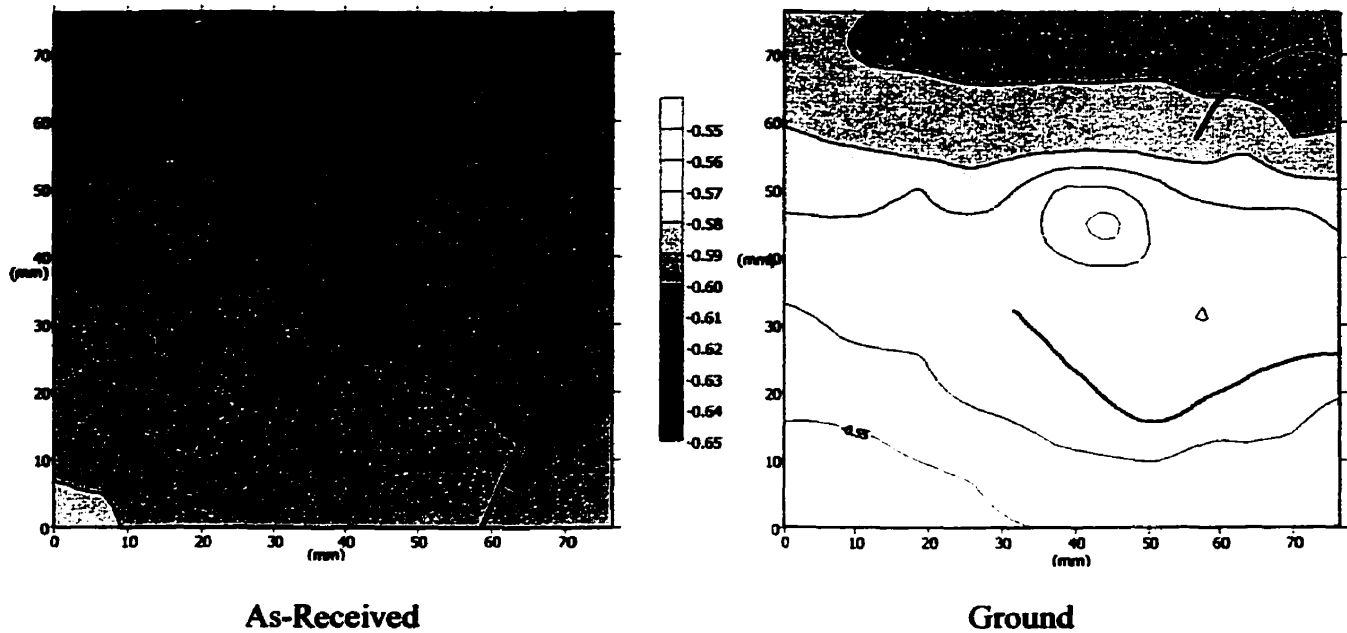
Figure 5.3.1(d) Open circuit potential maps of steel (mV SCE) embedded in cracked white modified cement paste (Specimen 3) after approximately 160 days exposure to chloride-contaminated simulated pore solution.

As-Received   Ground
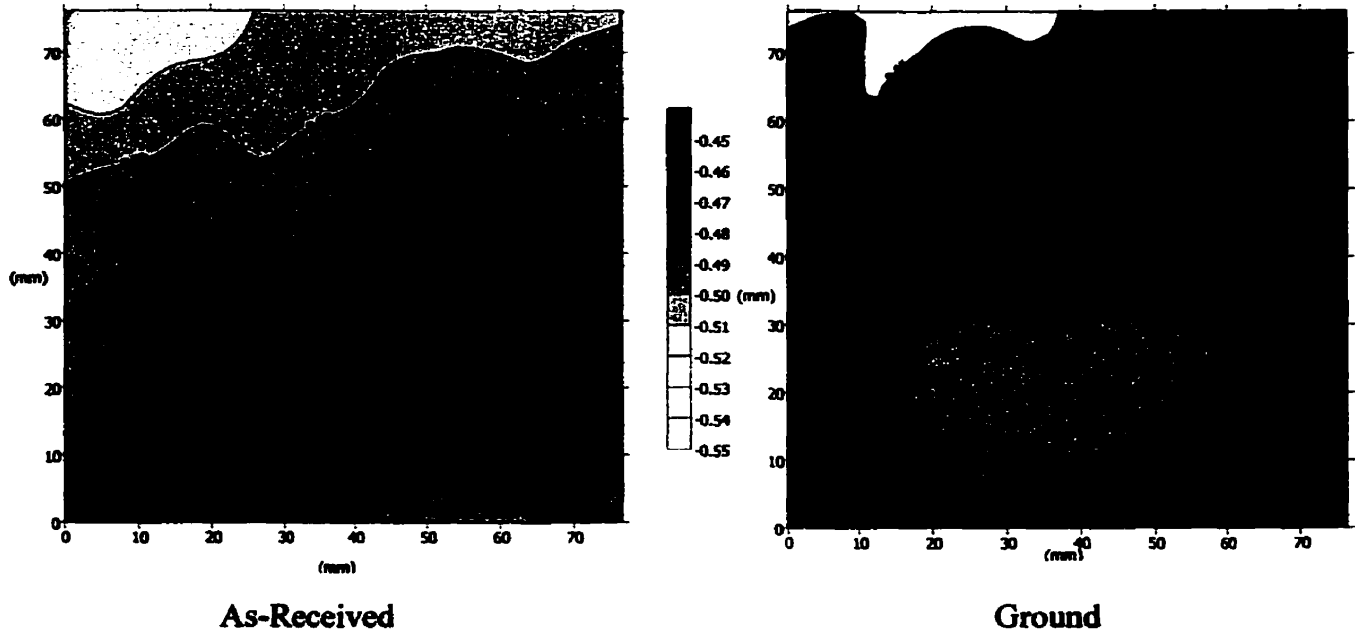
Figure 5.3.1(e) Open circuit potential maps of steel (mV SCE) embedded in sealed white modified cement paste (Specimen 1) after approximately 12 days exposure to chloride-contaminated simulated pore solution. Note: These maps are coloured green to highlight the more positive potential range, approx. 100 mV, measured for this specimen at this time.

147

As-Received   Ground
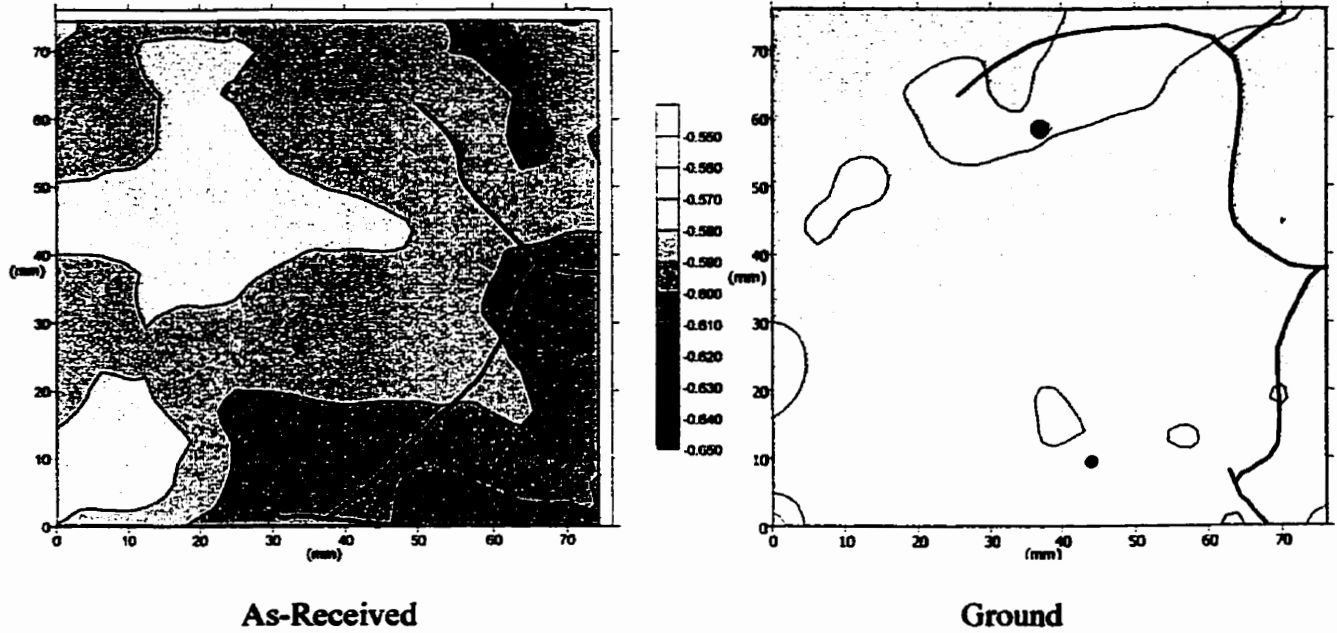
Figure 5.3.1(f)   Open circuit potential maps of steel (mV SCE) embedded in sealed white modified cement paste (Specimen 1) after approximately 30 days exposure to chloride-contaminated simulated pore solution.

As-Received   Ground
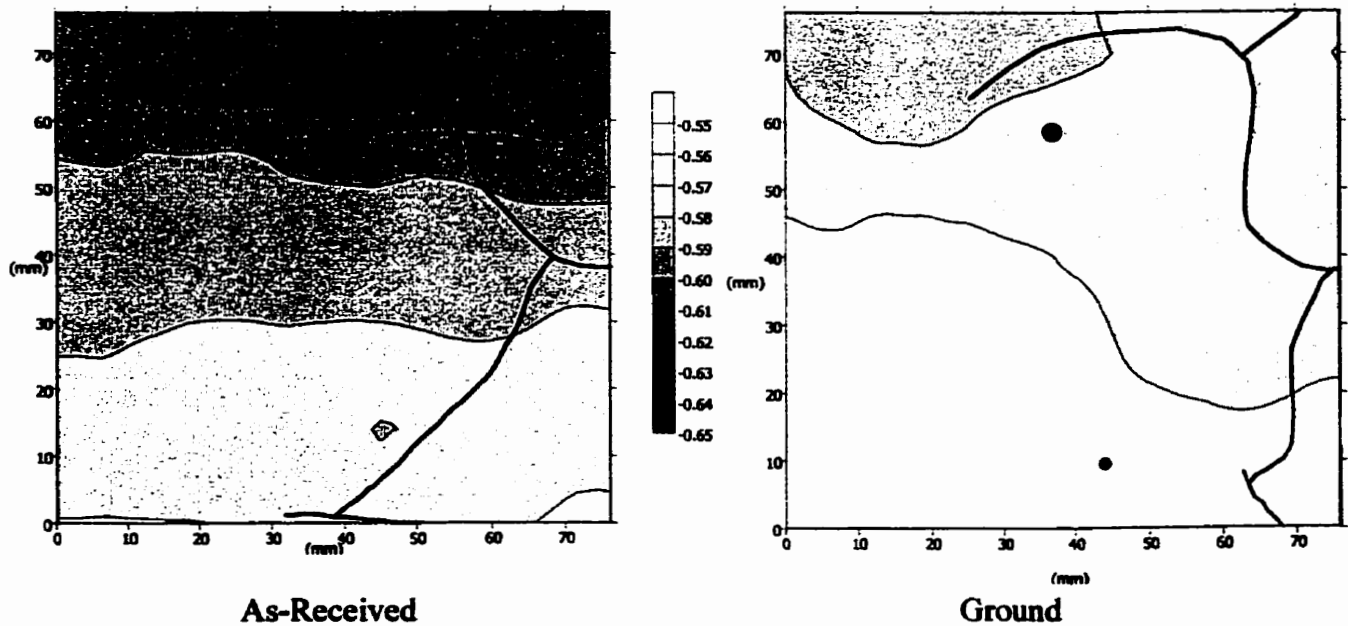
Figure 5.3.1(g)   Open circuit potential maps of steel (mV SCE) embedded in sealed white modified cement paste (Specimen 1) after approximately 160 days exposure to chloride-contaminated simulated pore solution.

148

When comparing the potential maps to determine the effect of cracks, minor differences were noted between those specimens with open cracks and those which were sealed with epoxy. Initially, any unsealed cracks had a clearly evident impact on the local potential measurements in the vicinity of the cracks—i.e., the potentials in these areas were distinctly more negative. This effect diminished within the first 30 days of exposure, however, and the potential maps from the cracked specimens became more uniform and similar to those from the sealed crack specimens. This trend is consistent with the overall open circuit potential measurements shown in Figure 5.3.1(a) where the differences between the sealed and cracked specimens became statistically insignificant with time.

At the end of the monitoring period, in all but two or three specimens for both cement types, the as-received side contained an area with the most negative potential and was, therefore, the most active corrosion site. In all cases, this area of the steel was located furthest above the solution line. This is consistent with the higher oxygen content, partially saturated water content, and higher chloride content due to capillary suction and water evaporation. These represent the ideal conditions to sustain corrosion, because below the solution line, considerably less dissolved oxygen would be available for corrosion reactions than above the solution line. In fact, the potentials were observed to become progressively more negative the further above the solution line the steel was positioned, as shown in Figures 5.3.1(c) and (g). This behaviour is similar to that observed for steel-reinforced structures which are partially immersed in sea water, and the splash zone experiences the most aggressive attack.

Similar trends were noted in the Type 10 modified cement paste specimens but with one unique difference: orange stains were noted on the surface of half of the specimens, on both surfaces, such as that shown in Figure 5.3.1(h). The stains were first noticed after only 30 days of exposure as faint orange areas which developed into more concentrated stains with time. Overall, the stains did not seem to coordinate with their respective

potential maps and some of the orange staining occurred in areas where there was no embedded steel. A comparison of representative potential maps from steel embedded in orange-stained versus unstained Type 10 modified cement paste specimens, Figures 5.3.1(i) and (j), respectively, did not show any distinct differences. However, the heaviest orange surface deposits were noted on cracked specimens and appeared to concentrate in those areas away from the cracks which were below or at the immersion line. Therefore, it is likely that the cracks acted as the anodic sites on the surface of the steel and the remaining areas of steel were the cathodic sites. The stains would have precipitated in the locations of the cement paste cover where the iron and hydroxide ions generated by the corrosion reactions met. Unsealed cracks would have allowed these anodic sites to be established more quickly than their sealed counterparts and would have resulted in more of the product forming over time. A detailed compositional analysis of the stains was performed using Raman spectroscopy and this work is presented in Section 5.3.6.

Embedded Steel

Immersion
Line

151
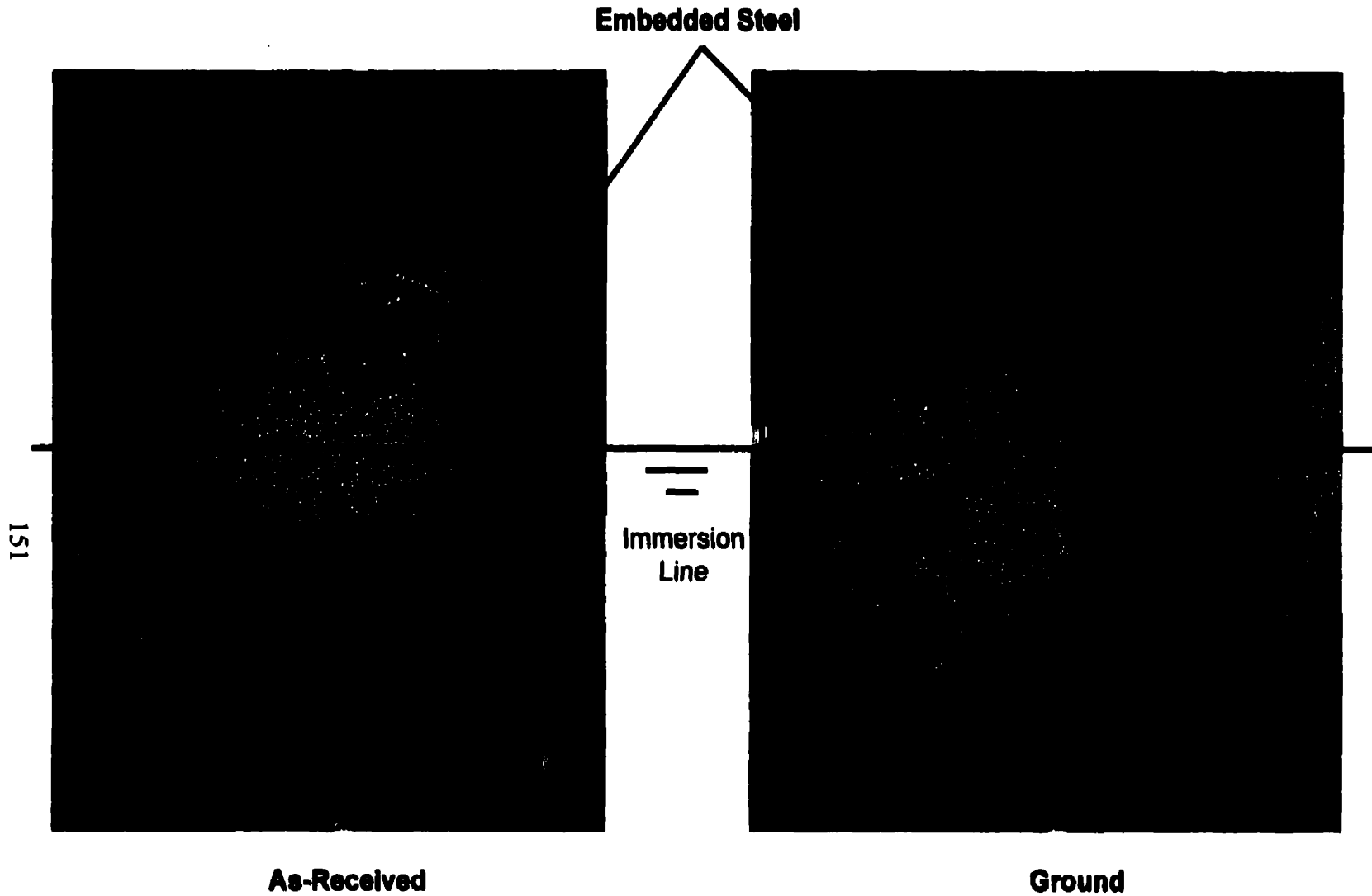
As-Received

Ground

Figure 5.3.1(h) Macrophotographs of the orange-stained, cracked Type 10 modified cement paste (Specimen 8) covering the as-received and ground steel surfaces after approximately 160 days exposure to the chloride-contaminated simulated pore solution. Note: The macrophotograph of the cement paste covering the ground surface has been mirrored about its vertical axis so that it can be directly compared with the corresponding open circuit potential maps in Figure 5.3.1(i).

As-Received　　　　　　　　　　　　　Ground
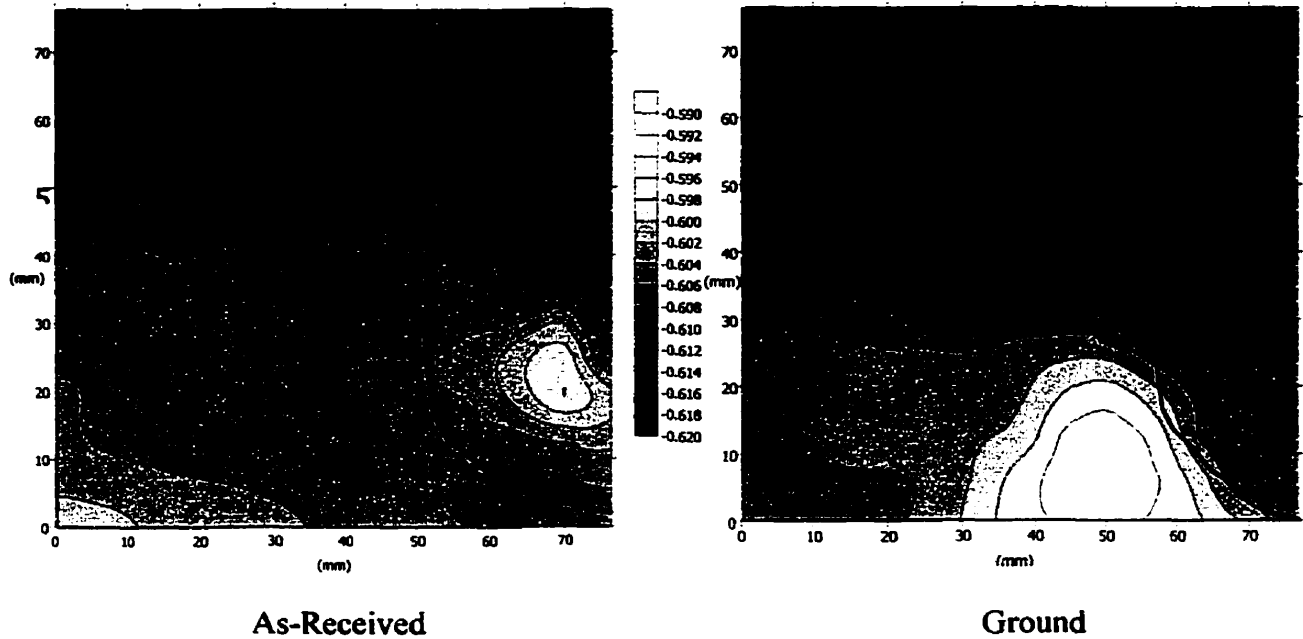
Figure 5.3.1(i) Open circuit potential maps of steel (mV SCE) embedded in orange-stained, cracked Type 10 modified cement paste (Specimen 8) after exposure to the chloride-contaminated simulated pore solution for approx. 160 days.

As-Received　　　　　　　　　　　　　Ground
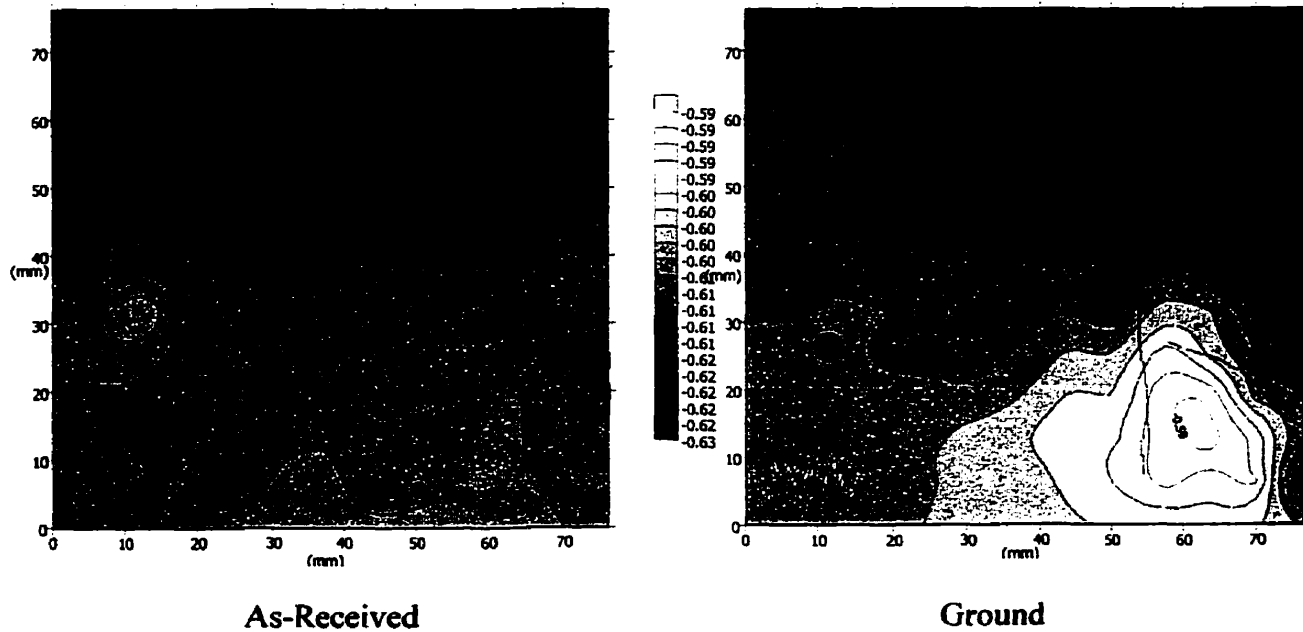
Figure 5.3.1(j) Open circuit potential maps of steel (mV SCE) embedded in unstained, sealed Type 10 modified cement paste (Specimen 3) after exposure to the chloride-contaminated simulated pore solution for approx. 160 days.

5.3.2 Linear Polarization Resistance Measurements

Figure 5.3.2 presents the mean corrosion rates for all specimens which were measured using linear polarization resistance. In general, the corrosion rate of all specimens increased with time and the white cement paste specimens approached 0.01 A/m^2 after 260 days of exposure to the chloride-contaminated simulated pore solution. Since this rate is really a mean value for the entire surface of the steel, the corrosion rates of localized regions on the surface of the steel are likely higher. In addition, the gradual increase in the corrosion rates suggests that a progressively larger area of the steel is becoming active.

Figure 5.3.2 also shows that similarly prepared steel in Type 10 cement paste specimens had corrosion rates that were lower than the white cement paste specimens at similar time intervals. The difference between the two types of cement paste can be possibly related to the chloride-binding characteristics of the cement as the Type 10 cement contained almost three times the amount of C_3A and C_4AF as the white cement (16.2 mass % versus 5.5 mass %, Table 3.1(b), Chapter 3). The Type 10 cement paste specimens would, therefore, require a greater number of chlorides to diffuse into the specimens to achieve the critical level for corrosion initiation.
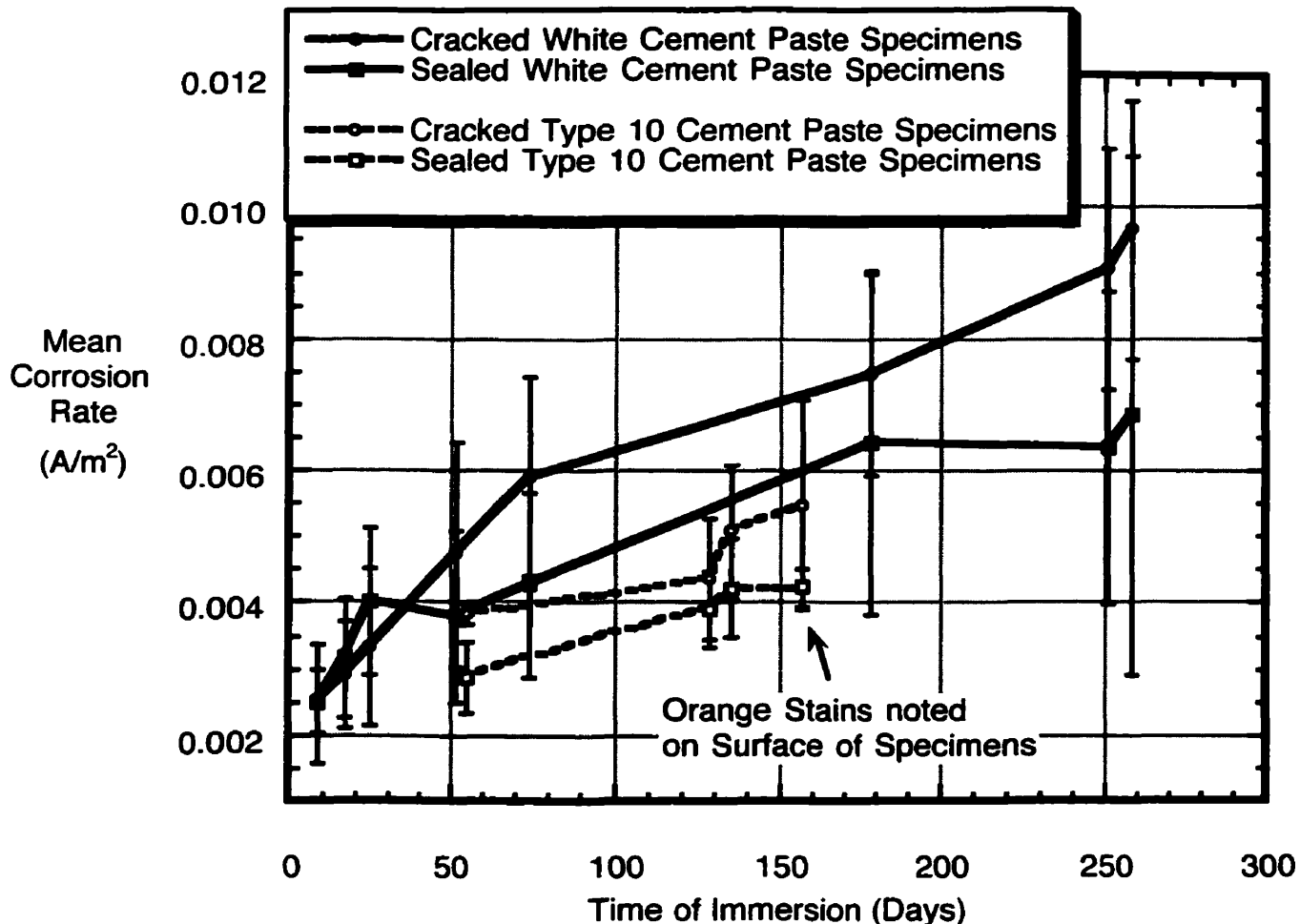
Figure 5.3.2 Comparison of the mean corrosion rates for both the cracked and sealed specimens. The error bars represent a 67% confidence interval.

In addition to the effect of cement type used to prepare the specimens, a small difference was noted between the mean corrosion rates for cracked versus sealed white modified cement paste specimens. While the mean corrosion rate of the cracked specimens continued to increase until the specimens were sectioned, the sealed specimens maintained a constant corrosion rate of approximately 0.0065 A/m^2 from 175 days to the final

154

measurements before sectioning. A similar trend was not noted in the Type 10 cement paste prisms probably because the presence of stains on the surface of the prisms caused the specimens to be sectioned earlier than anticipated.

However, a more detailed review of the data shows that there is little statistical difference between the cracked versus sealed, as well as the Type 10 versus white cement paste specimens because of the high variability in comparable specimens. This likely resulted from the random cracking that occurred during the curing process: the cracks did not occur in the same locations on each specimen and their proximity to the simulated pore solution level varied. As a result, the localized areas of probable corrosion attack (i.e., within the cracks) were different for every specimen. Although this variability complicated the interpretation of the corrosion rates, it is consistent with observations made for field structures with their inherent inhomogeneities.

5.3.3 Total Porosity and Pore Size Distributions

Figure 5.3.3(a) presents the total continuous porosity measurements for all specimens at the time when the specimens were sectioned: after 270 days of immersion for the white modified cement paste and 180 days for the Type 10. This figure shows that there is no statistical difference between any of the specimens, either Type 10 or white cement, cracked or sealed. The overall mean was 36% (± 0.44, 95% confidence interval) and is consistent with the work of other researchers for cement paste, a general presentation of which is given by Taylor (Taylor 1990). It is unlikely that the difference in age between the white and Type 10 modified cement paste is significant with this type of measurement because the majority of the hydration reactions would have completed after 112 days of moist curing in the moulds followed by up to 270 days of partial immersion in simulated pore solutions. In addition, no supplementary cementitious materials were used in the mix

155

designs which could have caused latent refinements of the continuous pore networks.
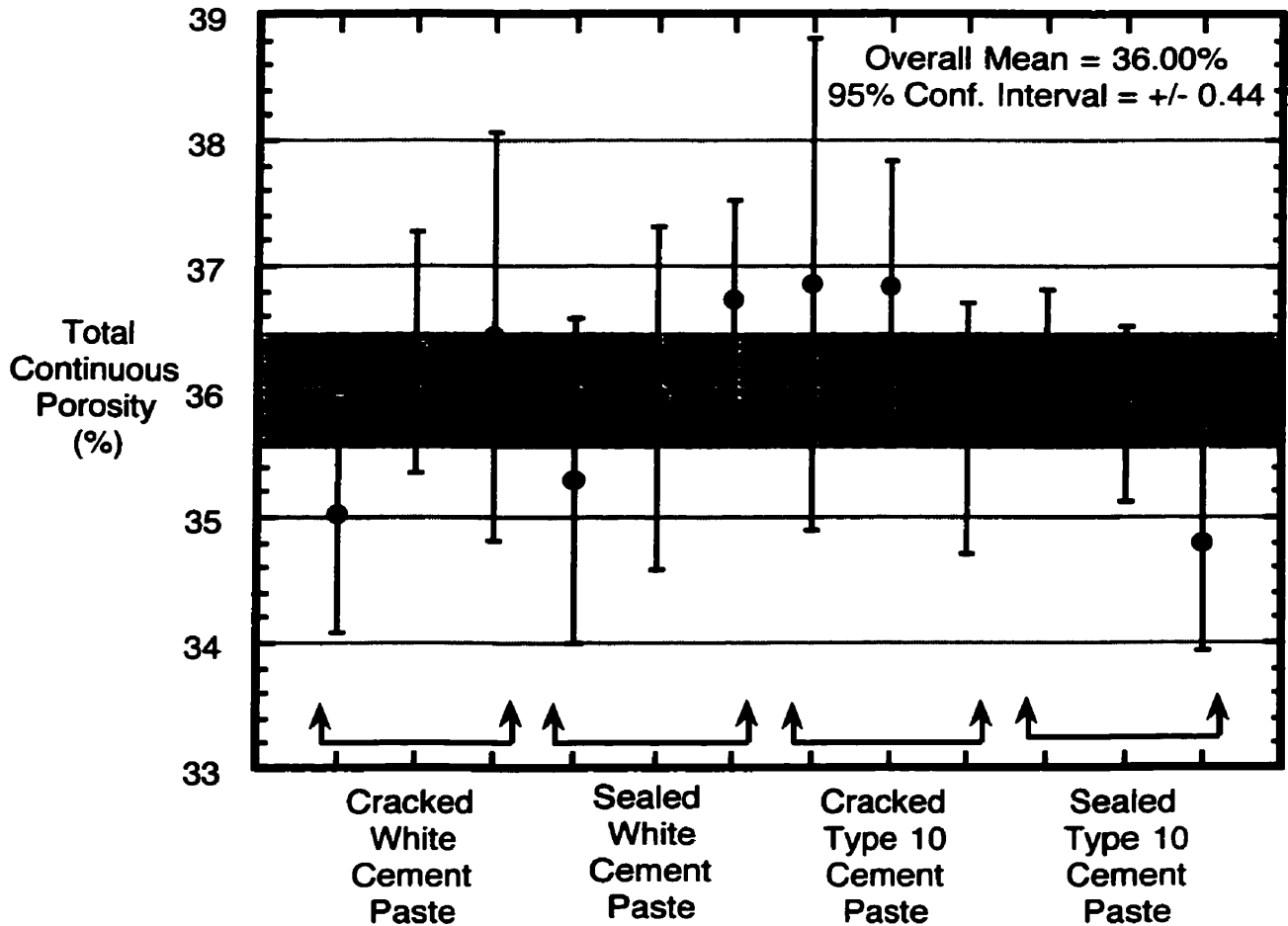
Figure 5.3.3(a) Comparison of the total continuous porosity 95% confidence intervals for all specimen types: cracked, sealed, white and Type 10 modified cement paste.

This conclusion is supported by mean cumulative intrusion volume curves measured

156

for both the white and Type 10 modified cement paste specimens after immersion in the simulated pore solutions as compared to the original curves, shown as Figure 5.3.3(b). Reductions in both threshold pore diameters and total pore volume reductions were noted as a result of the immersion period. Moreover, the Type 10 total pore volume was statistically larger than the white for both time intervals. This difference was small when the specimens had been only moist cured for 16 weeks, as shown in Figure 5.3.3(c), but increased with immersion in the simulated pore solution, as shown in Figure 5.3.3(b). Although the cement pastes were sectioned at different exposure ages, the difference in hydration between 180 and 270 days is likely minimal. Instead, the differences are likely due to the inherent differences between the cements. The white cement contained significantly more C_3S and was more finely ground (Table 3.1(b), Chapter 3) and would have produced a denser paste upon full hydration. Theoretically, this denser paste should provide better corrosion protection when any embedded steel is exposed to chlorides.

A comparison of the mean pore size distribution measurements for both the white and Type 10 modified cement pastes is presented in Figures 5.3.3(d) and (e), respectively. A review of both plots shows that only the samples taken from above the solution line in the cracked white modified cement paste specimens were significantly different from their Type 10 counterparts in both the cracked and sealed specimens. This suggests that the cracks in the white modified cement paste increased the evaporation of any water in the exposed portions of the specimens and reduced the rate of cement hydration in these areas. Similar sensitivity was not noted in the Type 10 modified cement paste prisms possibly because the more open pore structure reduced the effect of cracks in these areas.
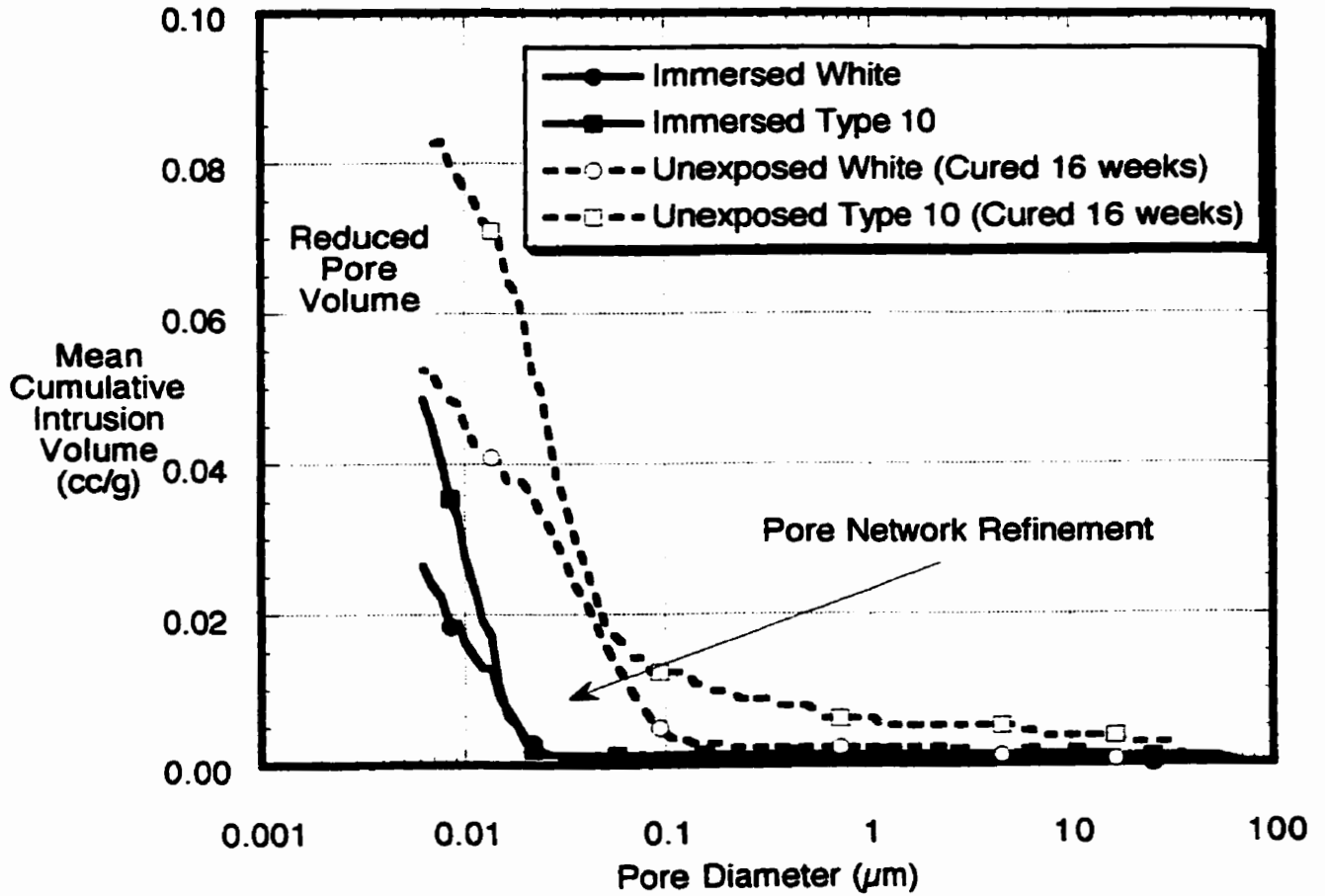
Figure 5.3.3(b) Comparison of the mean cumulative intrusion volumes for white and Type 10 modified cement paste samples after 16 weeks of curing versus up to nine months of immersion in a chloride-contaminated simulated pore solution. Each curve is the mean of either three samples (16 weeks curing) or twelve samples (up to nine months of immersion).
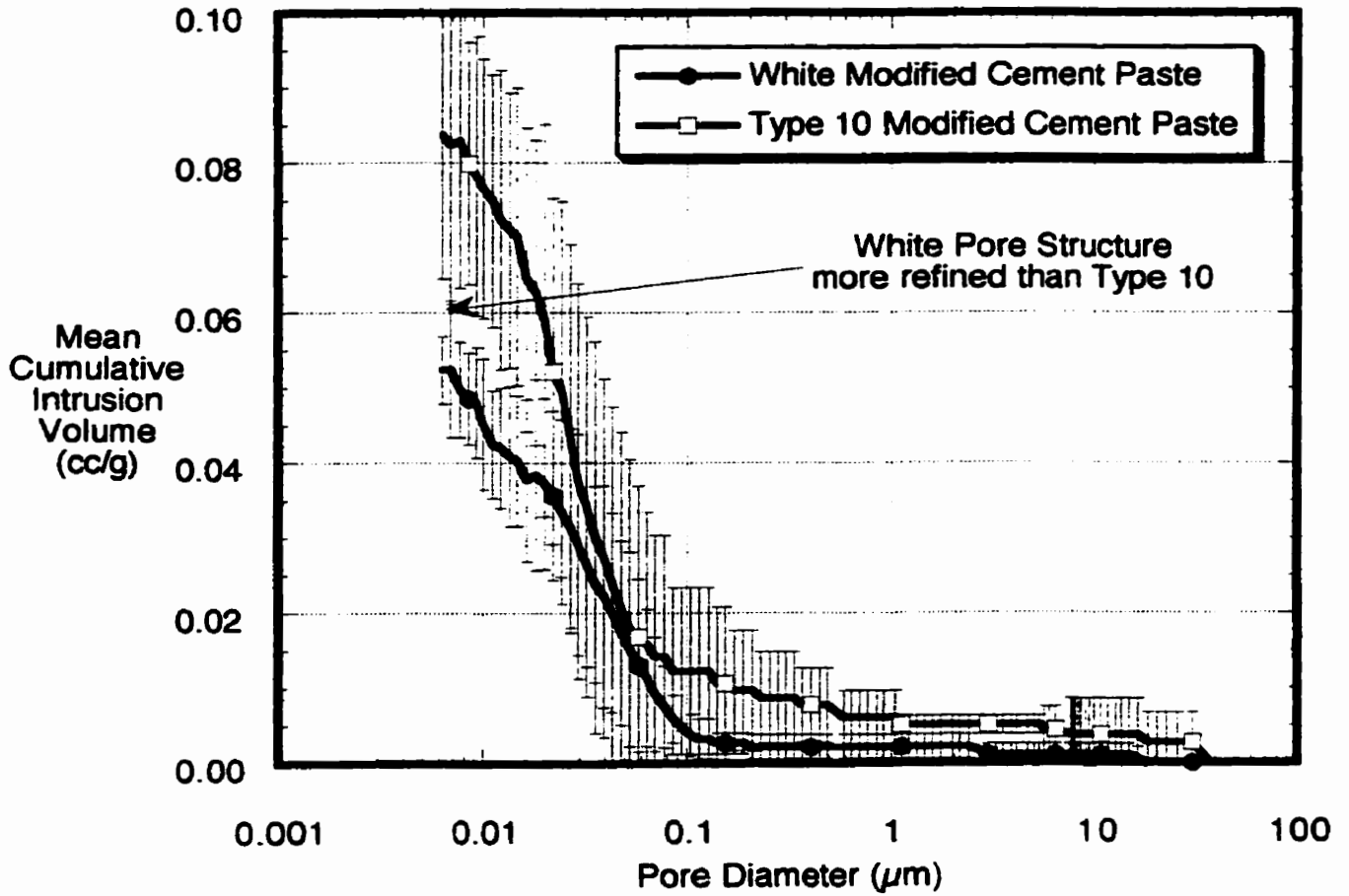
Figure 5.3.3(c) Comparison of the mean cumulative intrusion volumes after moist curing for 16 weeks in their moulds. Each curve is an average of three samples and a 80% confidence interval was applied.
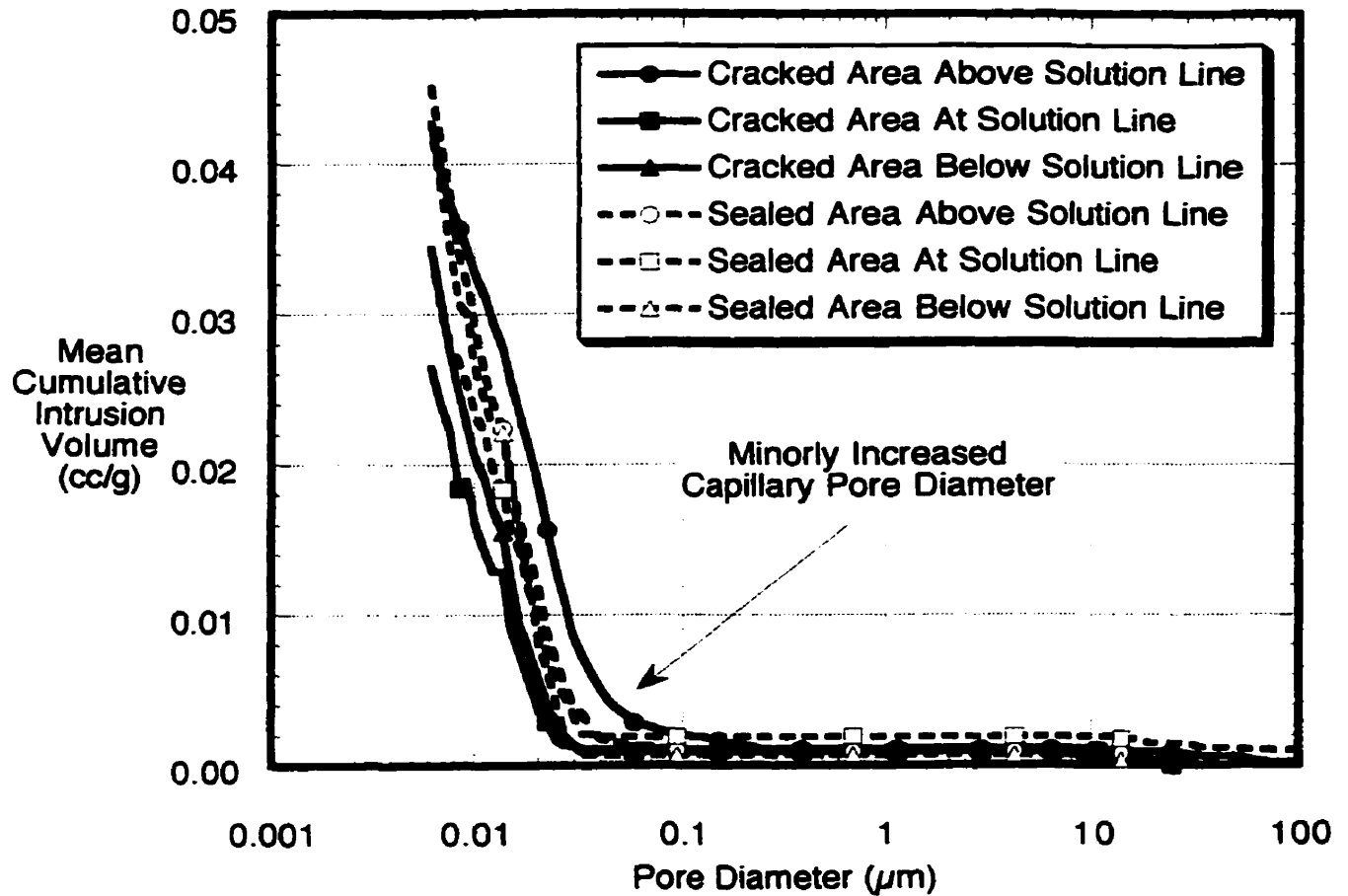
Figure 5.3.3(d) A comparison of the mean cumulative intrusion volume for white modified cement samples from above, at, and below the solution line. Each curve is the mean of three samples, one sample from three different specimens.
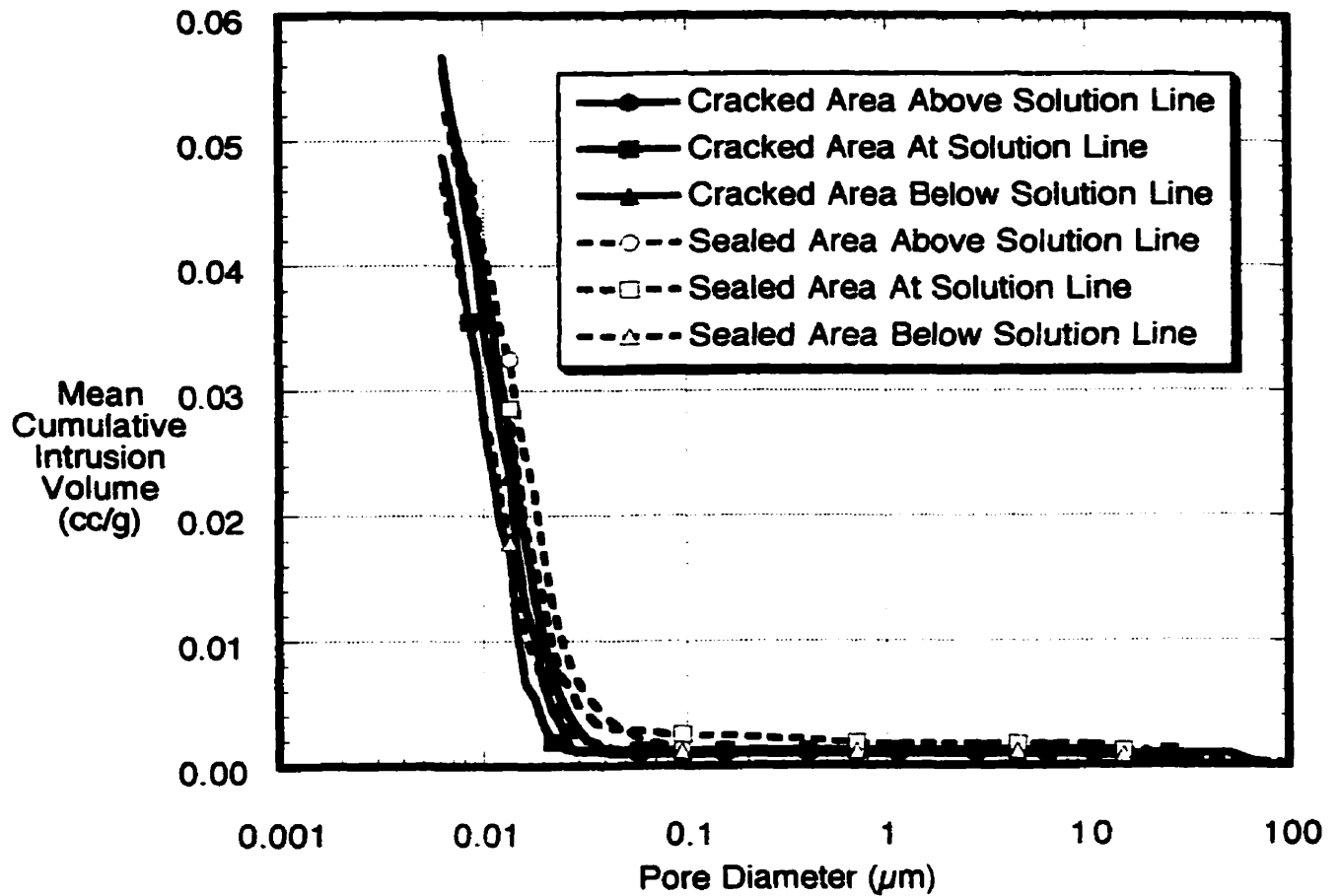
Figure 5.3.3(e) A comparison of the mean cumulative intrusion volume for Type 10 modified cement samples from above, at, and below the solution line. Each curve is the mean of three samples, one sample from three different specimens.

5.3.4 Chloride Content

Figure 5.3.4 presents the mean acid-soluble chloride contents (i.e., the total chloride content) for all specimen types according to the immersion level in the

chloride-contaminated simulated pore solution. A comparison of these values indicates a significant level of chlorides for all specimens, well above any possibility of chloride-binding. All specimens except for the Type 10 below the solution line were considered at risk for chloride-induced corrosion below, at, and above the immersion line in the simulated pore solutions.

Overall the Type 10 modified cement paste specimens contained more chlorides than the white specimens after exposure for approximately 100 fewer days in the chloride-contaminated simulated pore solution. This is likely a result of the larger chloride-binding potential of the Type 10 cement with its significantly higher C_3A and C_4AF content. Presumably, the equilibrium chloride content between the solids and pore solution comprising the Type 10 cement paste would be higher than the white cement paste and more chlorides would diffuse to satisfy the concentration gradient. In addition, the higher C_3S content and fineness of the white cement likely produced a denser cement paste than the Type 10 which would have reduced the rate of chloride diffusion.

In addition, the mean chloride levels generally were at their lowest below the immersion line, and reached their maximum at the immersion line for all specimens. Above the immersion line, the chloride levels remained unchanged for the white modified cement paste specimens but decreased for the Type 10. This difference was likely related to the different pore structures of the cement pastes that would affect the capillary absorption from below to above the solution line and the crack patterns, as well as the shorter immersion time for the Type 10 specimens. However, the high degree of variability of these measurements as shown by the 67% confidence interval calculated for both modified cement pastes does not allow any direct conclusions to be drawn. It is possible that if these specimens had been exposed for a longer period of time until a full equilibrium with the chloride-contaminated pore solution were reached, these values might have become less varied. However, it was the intent of this work to study the corrosion product distribution

162

as they were initiated before excessive volumes of corrosion products were developed.
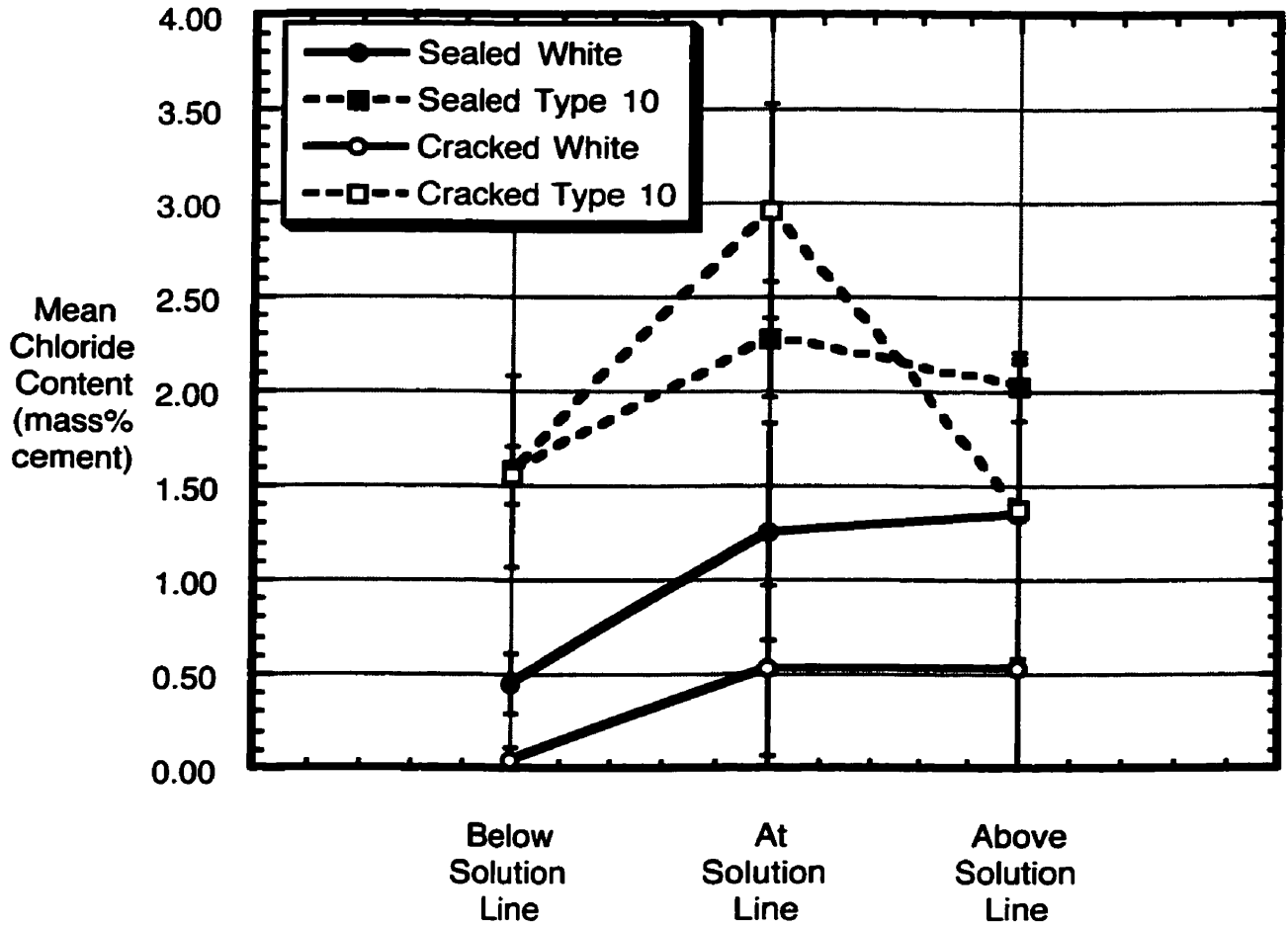
Figure 5.3.4 Comparison of the mean chloride contents for the white and Type 10 modified cement paste samples. The error bars represent a 67% confidence interval.

5.3.5 Thermogravimetric Analysis

To aid the analysis of the white and Type 10 modified cement paste specimens, hydrated

reference standards of C_3S, C_3A intermixed with an appropriate quantity of gypsum ($CaSO_4 \cdot 2H_2O$), and synthetic calcium monochloroaluminate (Friedel's salt - $C_3A \cdot CaCl_2 \cdot 10H_2O$) were analyzed using thermogravimetric analysis. The first derivative of the mass loss with time which accentuates any changes in the original mass loss curves, and is known as differential thermogravimetry (DTG) is presented in this Section. Using this procedure, changes in the hydration state (loss of moisture or structural water), phase changes, and the subsequent decomposition of these phases were noted for the hydration products of C_3A/gypsum and C_3S hydration: monosulphate ($C_4A\overline{S}H_{12}$), C-S-H, and calcium hydroxide (CH), as shown in Figure 5.3.5(a). The curve for Friedel's salt, shown as Figure 5.3.5(b), also shows dehydration and phase decomposition and is consistent with the experimental observations of Ramachandran (Ramachandran 1976).
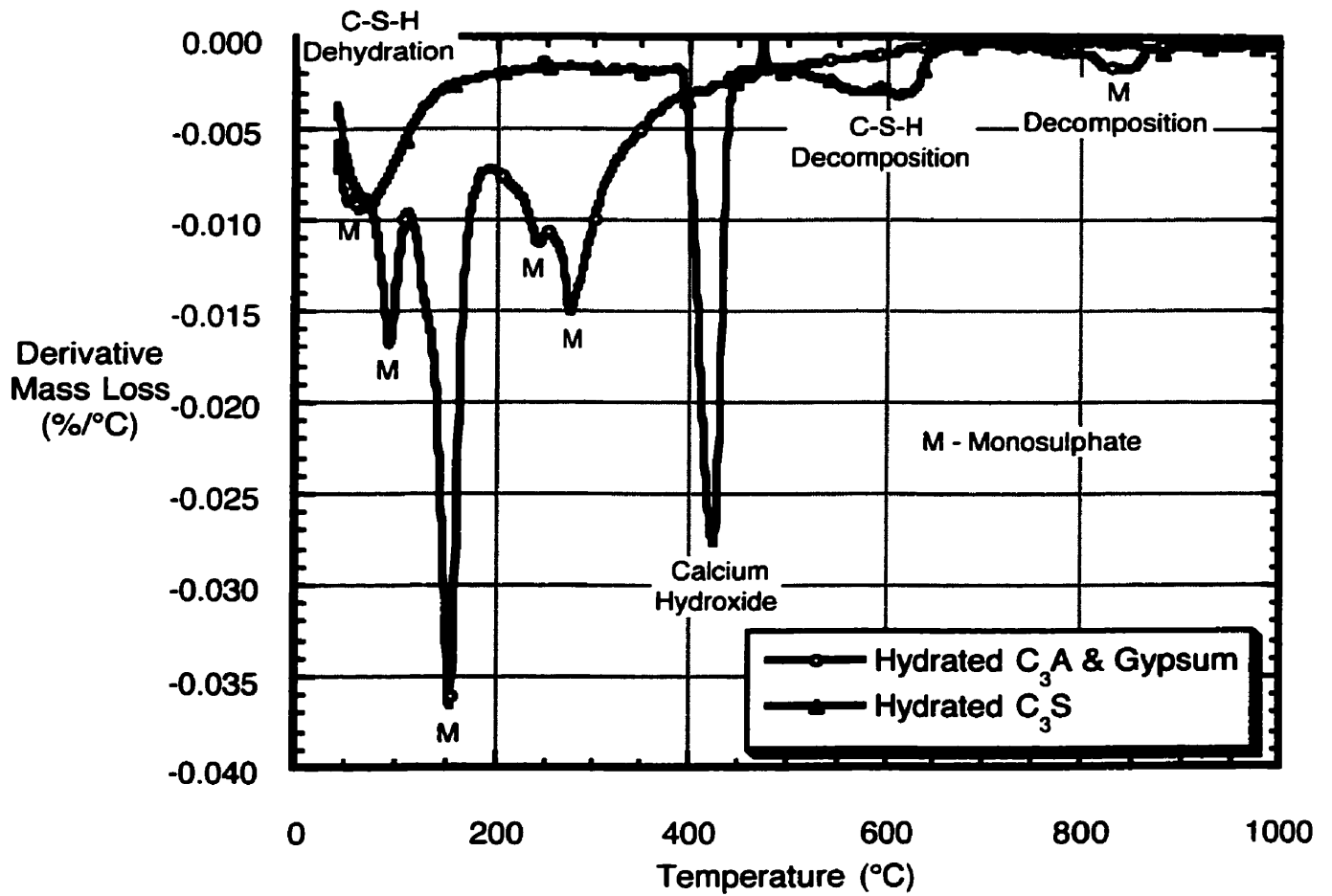
Figure 5.3.5(a) The differential thermogravimetric curve for mineral reference standards of C_3S and C_3A intermixed with an appropriate quantity of gypsum ($CaSO_4 \cdot 2H_2O$).
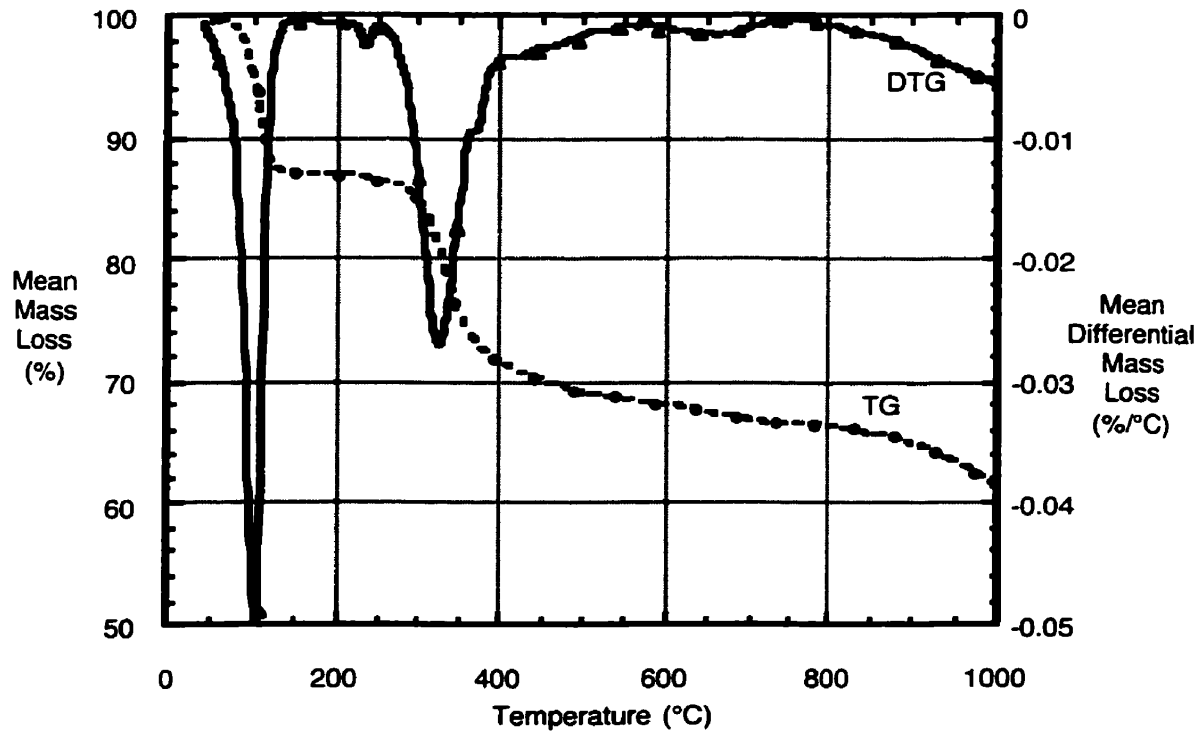
Figure 5.3.5(b) The mass loss and differential thermogravimetric curves for mineral reference standard of synthetic calcium monochloroaluminate (Friedel's salt - $C_3A \cdot CaCl_2 \cdot 10H_2O$).

In a similar manner, thermogravimetric analyses were conducted on three key areas (detailed in Figure 5.2.6) from both white and Type 10 modified cement paste specimens. These areas corresponded to portions of the specimens above, at, or below the solution line of the chloride-contaminated simulated pore solution. Since no statistically significant effect was noted for the presence of open cracks versus cracks that were sealed with epoxy for either cement type, the results for all specimens were pooled together according to the location from which the samples were taken. Figures 5.3.5(c) and 5.3.5(d) present these

166

results for the white or Type 10 modified cement paste specimens, respectively.

Figure 5.3.5(c) shows the anticipated features of a hydrated, sulphate-resisting white cement with its strongest peaks corresponding to the dehydration of the C-S-H, and the dehydroxylation of the calcium hydroxide. Since the white cement contains only 4.5% C_3A and 1.0% C_4AF, large peaks of hydrated aluminated phases were not anticipated or observed. Instead, peaks associated with the decomposition of calcium carbonate ($CaCO_3$) were observed and largest of which was noted for samples taken from above the solution line. The size of the peaks decreased with increased proximity to the simulated pore solution. Carbonation would have been slowed or reduced altogether by immersion in the simulated pore solution.
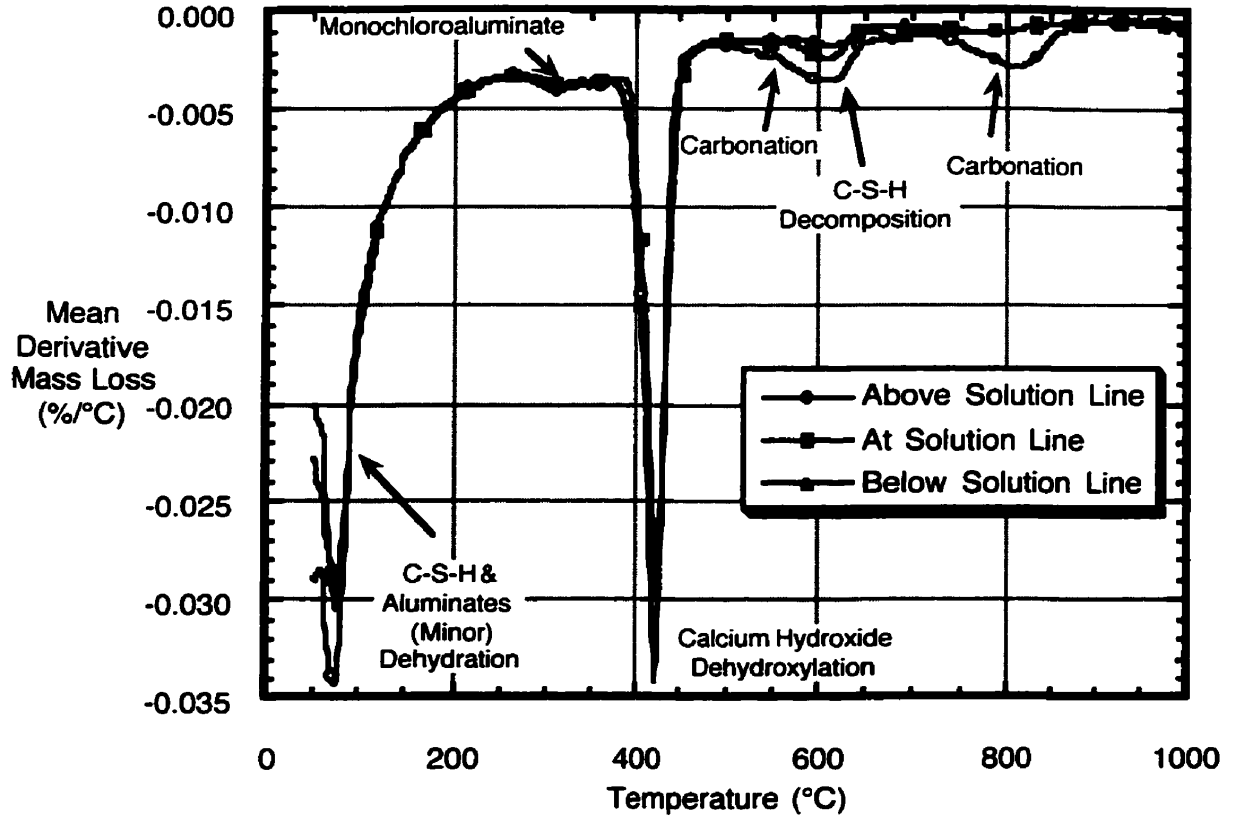
Figure 5.3.5(c) The differential thermogravimetric curve for white modified cement paste samples taken from above, at, and below the solution line.
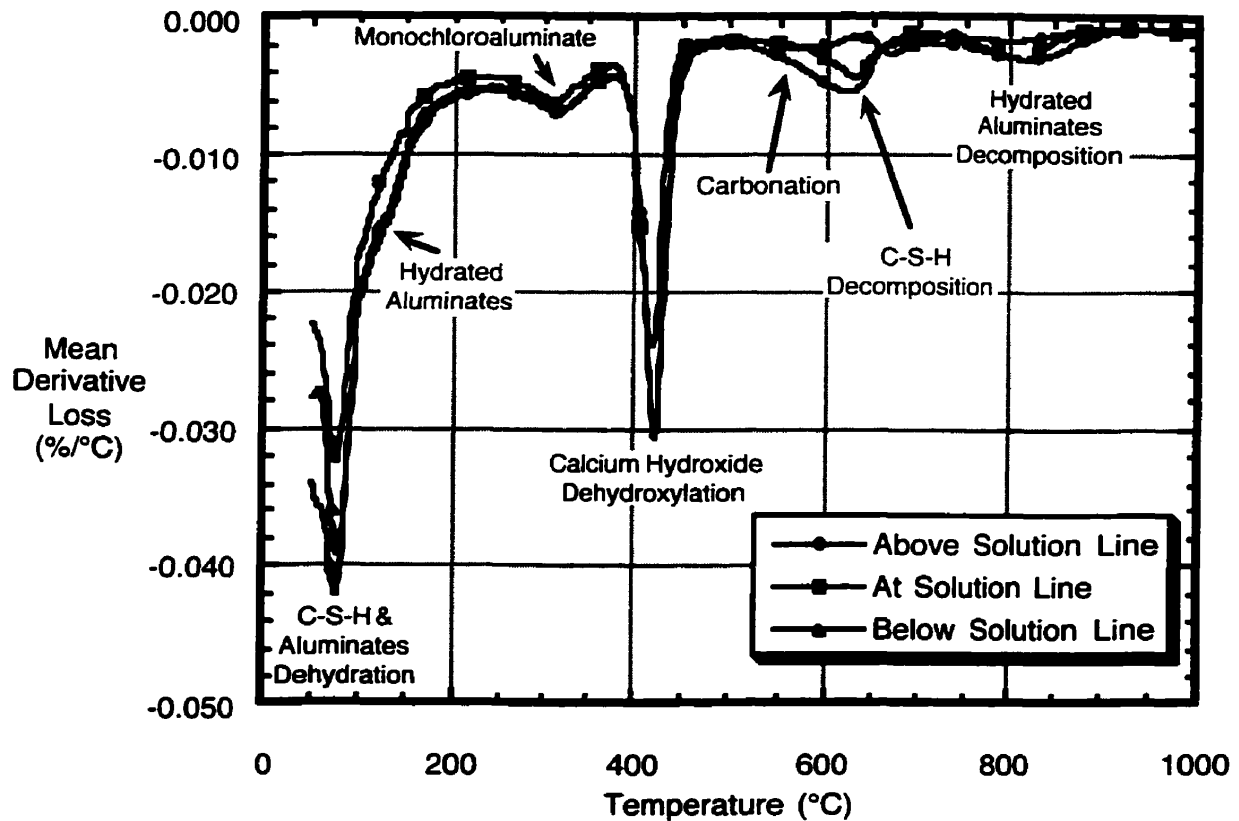
Figure 5.3.5(d) The differential thermogravimetric curve for Type 10 modified cement paste samples taken from above, at, and below the solution line.

In addition to the carbonation peaks, a small, broad peak with a maximum at approximately 313°C was noted which can be attributed to calcium monochloroaluminate (Friedel's salt - $C_3A \cdot CaCl_2 \cdot 10H_2O$). This profile was the same for all curves and suggests that the amount of monochloroaluminate formed was independent of the position of the sample location with respect to the solution line and the corresponding variable chloride content. The presence of the monochloroaluminate was confirmed by comparing the results of the samples exposed to the chloride-contaminated simulated pore solution with the

results obtained from unexposed samples, as shown in Figure 5.3.5(e). The amount of monochloroaluminate present in the samples could not be determined because no observable change in the original mass loss curve could be accurately measured. Thus, monochloroaluminate was detected but in quantities too small to be accurately measured with this analytical technique.
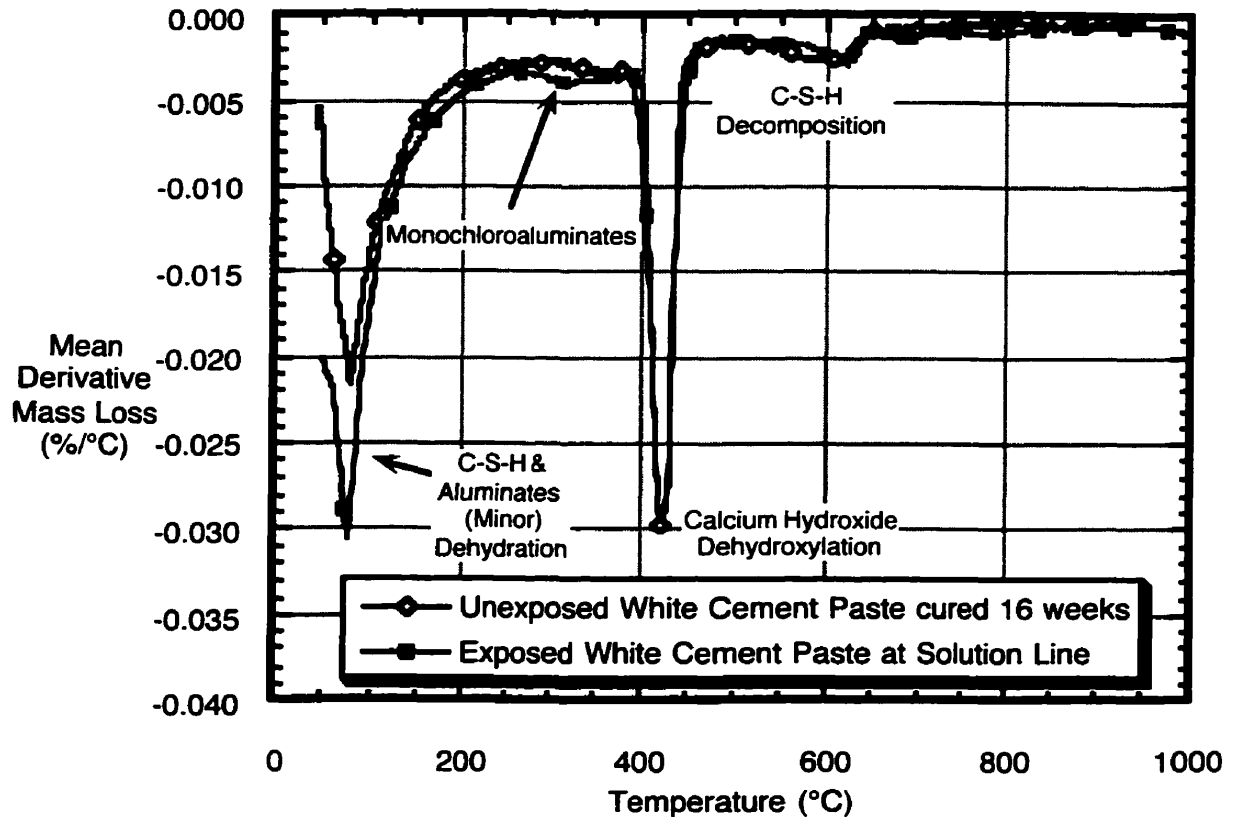
Figure 5.3.5(e) A comparison of the mean differential thermogravimetric curves for samples of white modified cement paste that were not exposed to the chloride-contaminated simulated pore solution (only moist-cured for 16 weeks) with those that had for almost one year. Each curve is the mean of six samples.

Similar trends were noted in the Type 10 modified cement paste with the exception that the higher C_3A and C_4AF contents in this cement, 8.7% and 7.5%, respectively, produced a correspondingly higher level of hydrated aluminates in the cured and exposed specimens. As shown in Figure 5.3.5(f), peaks consistent with hydrated aluminates were noted in the samples taken from unexposed Type 10 modified cement paste. Once this

cement paste had been exposed to the chloride-contaminated simulated pore solution, these peaks were no longer evident and new peaks corresponding to calcium monochloroaluminate were observed. The amount of the calcium monochloroaluminate present was approximately 1.8% $\pm$ 0.5% (95% confidence interval). This indicates a significantly higher chloride-binding capacity for the Type 10 cement paste than that for the white cement and suggests that more chlorides would be required to initiate and sustain corrosion of any embedded steel within Type 10 cement paste.
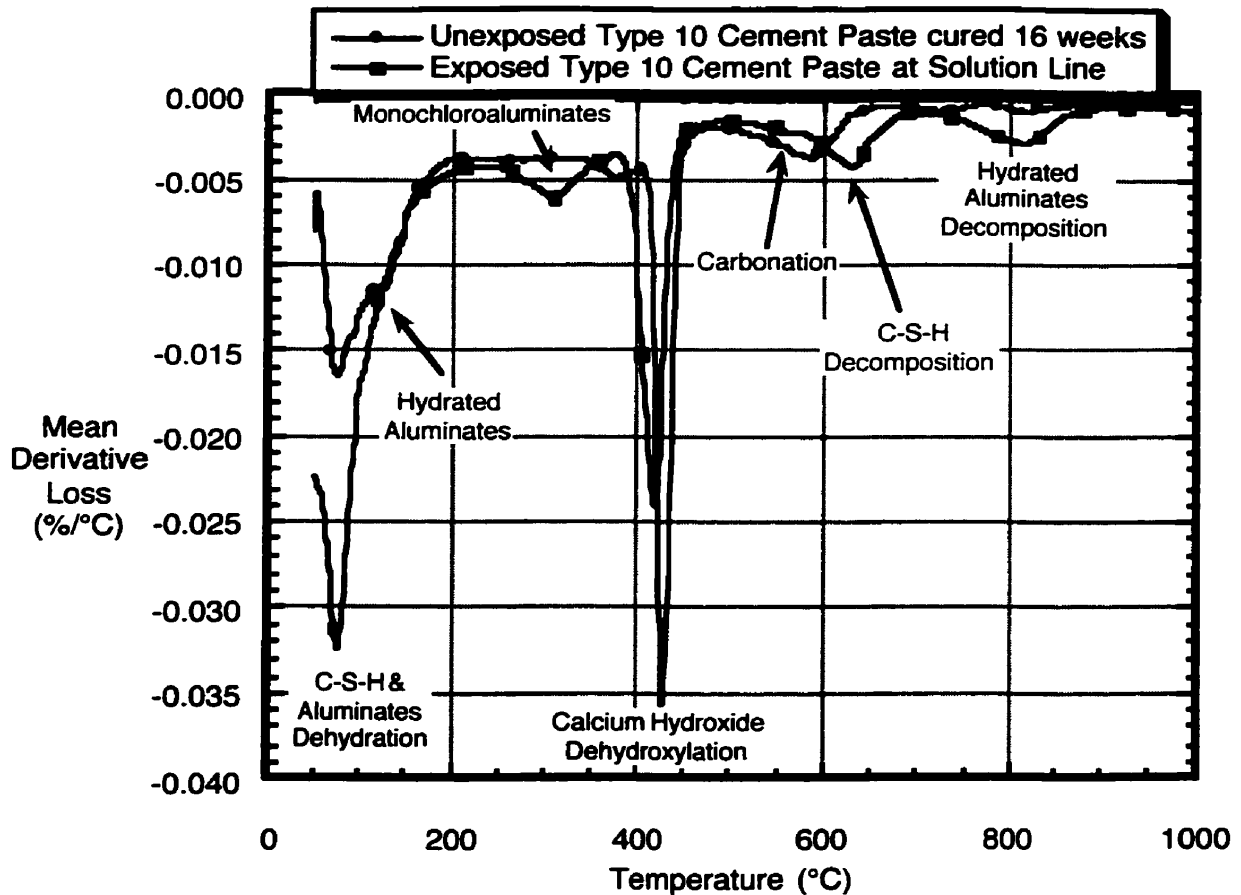
Figure 5.3.5(f) A comparison of the mean differential thermogravimetric curves for samples of Type 10 modified cement paste that were not exposed to the chloride-contaminated simulated pore solution (only moist-cured for 16 weeks) with those that had for almost one year. Each curve is the mean of six samples.

Another aspect of corrosion resistance is the buffering capacity of the pore solution provided by the available amount of calcium hydroxide. Figure 5.3.5(g) presents the mean ignited mass of calcium hydroxide which was calculated for all sample locations and both cement types. In general, these results are consistent with the previously noted carbonation trends as the highest calcium hydroxide contents were noted in the samples taken from below the solution line where the rate of carbonation would be slowest. In

addition, Table 5.3.5 shows that the actual yield of calcium hydroxide in the cement paste approached the theoretical values and confirms that the cement pastes were well-hydrated.

Overall, the calcium hydroxide contents measured in the white cement paste samples were larger in the unexposed sample and all other locations once the paste had been exposed to the chloride-containing simulated pore solution. This suggests that the white cement paste could provide better corrosion resistance for any embedded steel with respect to buffering capacity provided that the hydroxide ions can successfully diffuse through the pore network to where they are required.

Table 5.3.5 Comparison of the theoretical and the actual calcium hydroxide contents after 16 weeks of moist curing.

Cement Type	Theoretical CH Content (mass %)	Actual CH Content (mass %)	CH Yield (%)
White	26.2	21.8	83.2
Type 10	23.3	17.7	75.9
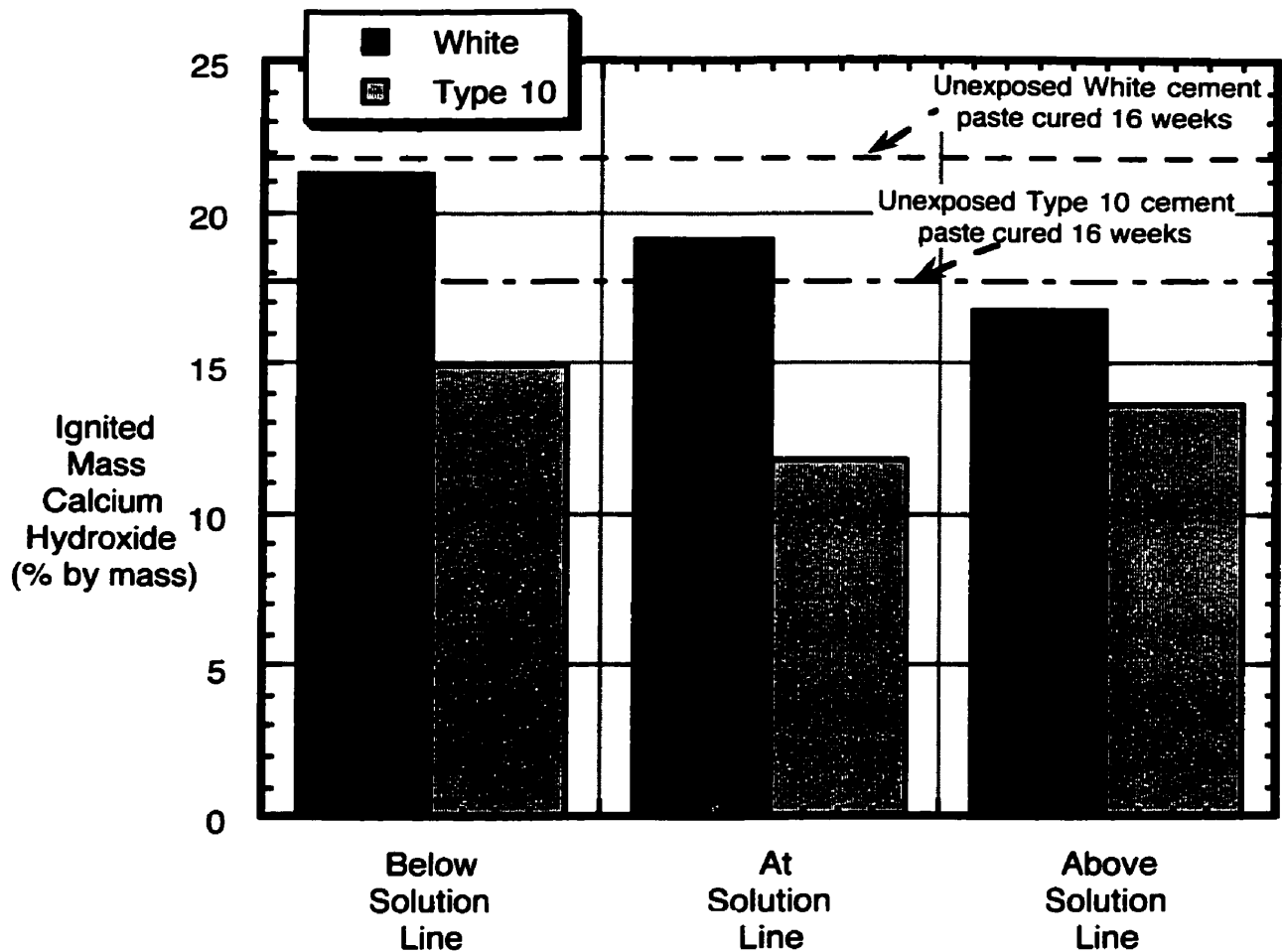
Figure 5.3.5(g) A comparison of the mean ignited mass of calcium hydroxide measured in samples taken from above, at, or below the solution line. Each measurement is the mean of six samples and contained an error of ± 0.5% for a 95% confidence interval.

5.3.6 Raman Spectroscopy

As detailed in Figure 5.2.6(a), cross-sections of all sectioned modified cement paste specimens were analyzed using Raman spectroscopy. Particular attention was paid to the

precise location of the corrosion products such that they could be coordinated with their respective potential maps. To aid the analysis of the spectra, some representative spectra of magnetite (Fe_3O_4), maghemite (γ-Fe_2O_3), and haematite (α-Fe_2O_3) were presented Chapter 3 as Figures 3.2.3(a), (b), and (c). A sample of the lubrication fluid, ISOPAR M, was also analyzed and its spectrum is shown as Figure 3.2.3(d) (Chapter 3). exhibiting only two peaks, centred at 560 cm^{-1} and 1099 cm^{-1}. Neither of these overlap experimentally observed corrosion peaks and, therefore, were not anticipated to interfere with the interpretation of the work of this section even if residual traces of the ISOPAR remained on the surface of the sections.

A comparison of the corrosion products formed within the modified cement paste specimens focussed first upon the corrosion products observed with the unaided eye and their location within the samples. Variations were expected with the cracks, the surface finish, and the position of the sample with respect to its immersion in the simulated pore solution. Figure 5.3.6(a) shows a representative section which contains typical crack locations and their proximity to the chloride-contaminated simulated pore solution.
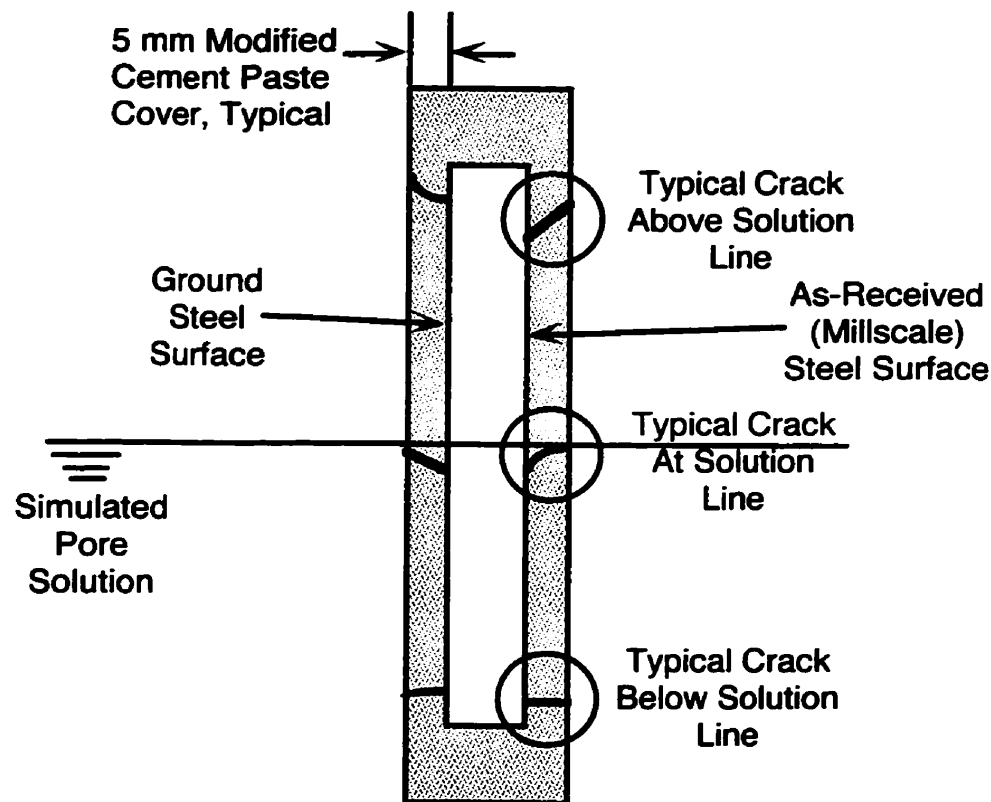
Figure 5.3.6(a) Schematic illustration of a section taken from the modified cement paste specimens indicating typical crack locations.

Immediately upon sectioning the specimens, the colour and location of any observed corrosion products was noted. A green coloured corrosion product which changed with time was observed at the steel/cement paste interface in three of the white and one of the Type 10 sections. Its location corresponded to the portion of the steel between the solution line and 20 mm above the solution line where the corrosion rates would be anticipated to be the highest. The product was up to 0.5 mm thick and was located on the as-received side of the sections for two white and one Type 10 cement paste sections. The presence of Green Rust could not be confirmed by Raman spectroscopy as the peaks for

177

chloride-containing Green Rust I are typically observed on steel in aqueous solutions with Raman shift values of approx. 427 and 518 cm^{-1} (Trolard, Génin et al. 1997). These Raman peaks result from ferrous and ferric hydroxide complexes (Fe-OH^{+} and Fe-OH^{2+}) which are likely to be highly unstable once exposed for even one minute to the ambient laboratory environment. In spite of this instability, this product is often observed at the steel/concrete interface (ACI Committee 222-Corrosion) within the oxygen-limited conditions that are assumed to exist within concrete and is a precursor to magnetite during chloride-induced corrosion. However, the Raman spectroscopy peaks centred on 216, 278, 386, and 580 cm^{-1} were obtained which suggest the presence of haematite and this would be the anticipated corrosion product observed once the Green Rust I was exposed to the laboratory environment for a period of time and if not under potentiostatic control.
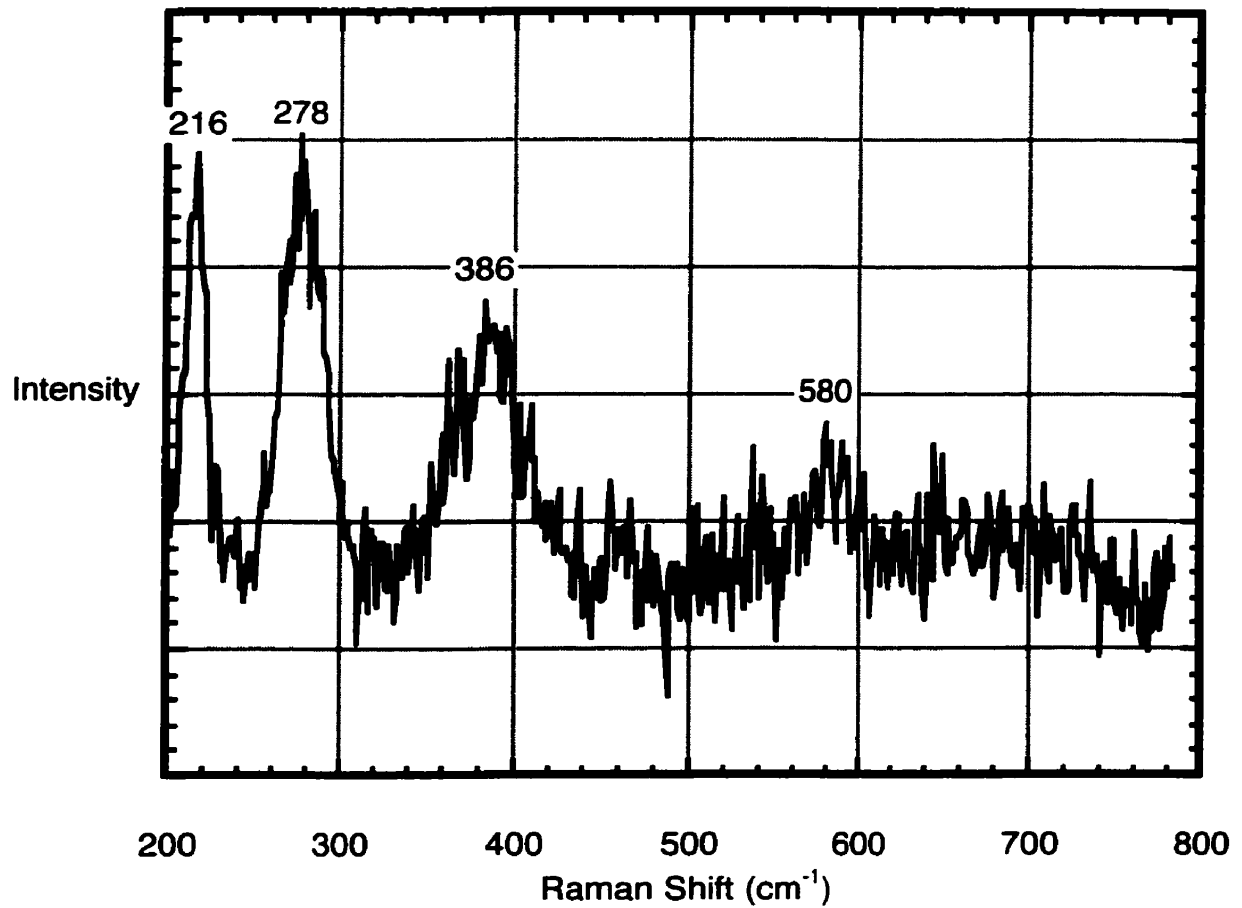
Figure 5.3.6(b) Representative spectrum from an area of a white cement paste section containing a green coloured corrosion product--spectra identified as hæmatite.

In spite of the unclear results concerning the green coloured corrosion product, other

179

corrosion products were easily identified at the steel/cement paste interfaces and within the cracks of all sections of both cement types. These products were observed on both surfaces of the steel simultaneously (i.e., corrosion products did not form preferentially on either the ground or as-received surfaces), and were observed within all cracks, below, at, and above the solution line. These products were most often coloured dark brown-black and usually only half-filled the crack (i.e., the area closer to the steel was completely filled while the area closer to the exposed surface of the cement paste remained empty). At higher magnifications, the corrosion product was typically coloured dark red in locations closest to the surface of the specimen. This was also true for samples in which the cracks had been sealed prior to immersion in the chloride-contaminated pore solution as the cross-section showed that the epoxy had not completely filled the cracks to the level of the steel. It is clear that once the chlorides had penetrated behind the surface barrier of the epoxy, corrosion could proceed as if the cracks had not been sealed.

Figures 5.3.6(c), (d), and (e) present representative spectra derived from a crack located below the solution line in white cement paste. Figure 5.3.6(c) was taken from an area close to the steel/cement paste interface while Figures 5.3.6(d) and (e) are taken progressively closer to the exposed surface of the cement paste. Figure 5.3.6(c) shows one broad peak characteristic of magnetite. Approximately 2 mm from the steel/cement paste interface, this product became intermingled with goethite (α-FeOOH), as shown in Figure 5.3.6(d). Although this analysis was from the paste below the water line, it was close to the paste surface and presumably was formed because of the higher level of dissolved oxygen in this region. This result is consistent with the dark red colour observed at higher magnifications. At the outer limit of the corrosion product, the part which would be directly exposed to the simulated pore solution, the calcium carbonate polymorphs of calcite and aragonite were observed, as indicated in Figure 5.3.6(e). The corrosion products observed within cracks above the solution line were similar with the exception that

hæmatite was also observed, as shown in Figure 5.3.6(f). This product likely formed because of the reduced water or increased oxygen availability above the solution line within the cement paste (i.e., it is a dehydrated form of goethite).
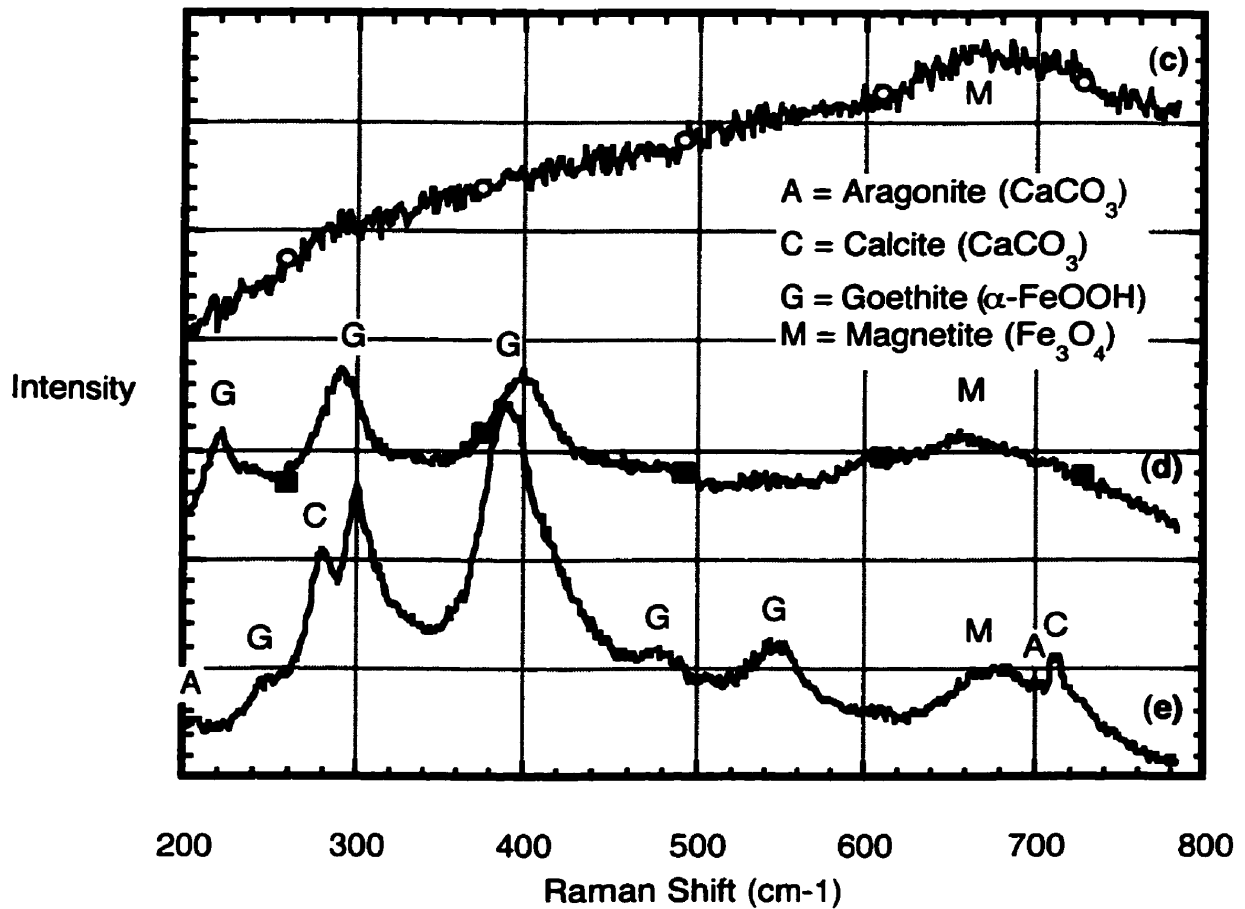
Figures 5.3.6(c), (d), and (e) Representative spectra of corrosion products within a crack located below the solution line.

181
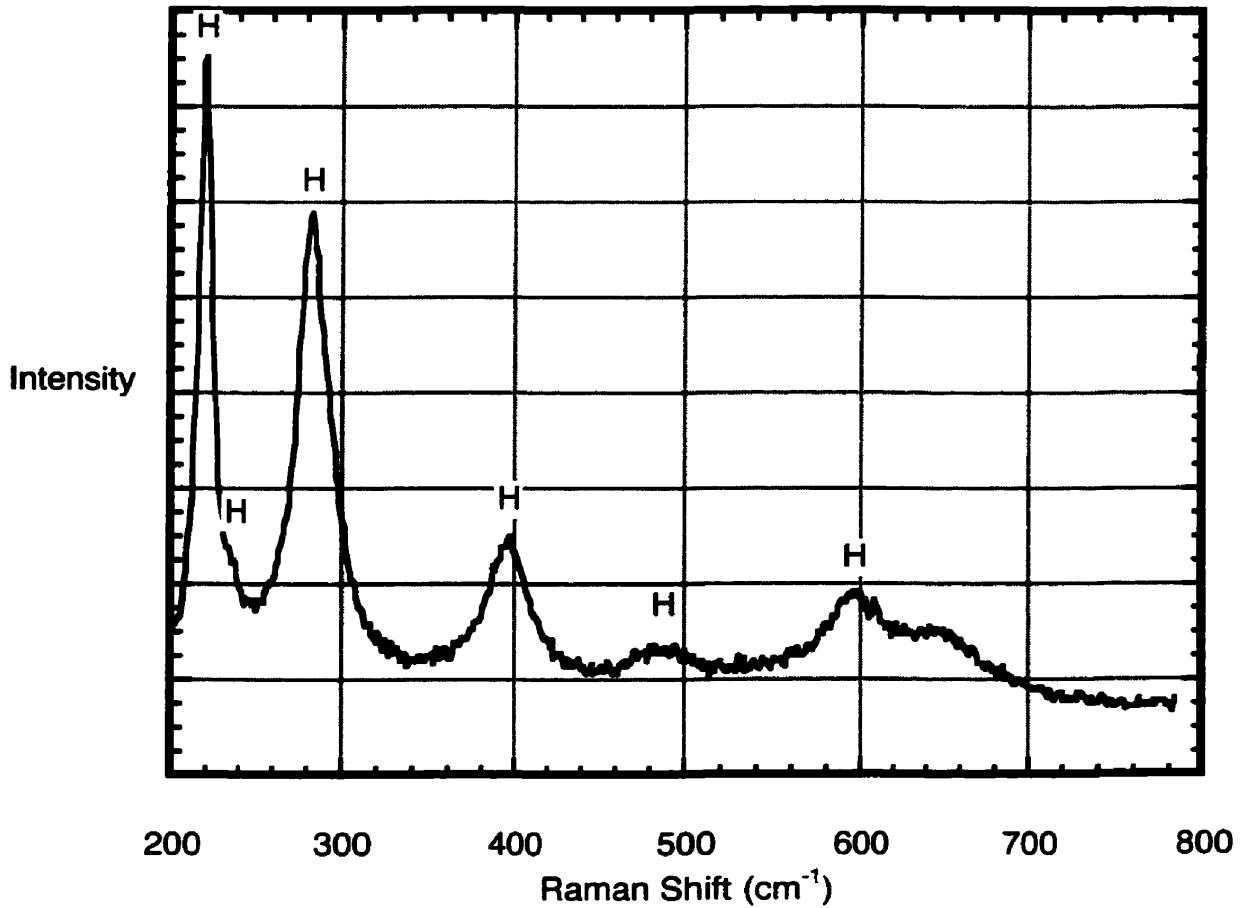
Figures 5.3.6(f) Representative spectrum of hæmatite (H) within a crack located above the solution line.

In addition to the previously described effects of surface finish, cracks, and the immersion level of the simulated pore solution, varying the cement type produced one notable effect: the Type 10 modified cement paste specimens formed orange stains over large areas which were not observed on the white cement paste specimens. These stains

were noted on the surface of most of the Type 10 specimens and penetrated approximately 1 mm of the surface, as shown in Figure 5.3.1(h). Figure 5.3.6(g) and (h) present representative spectra obtained from an area with concentrated stains, and an area of unstained cement paste, respectively. The major peaks shown in Figure 5.3.6(g) indicate the presence of hæmatite (α-Fe_2O_3), magnetite (Fe_3O_4), and calcite ($CaCO_3$). With the exception of the magnetite, the results of this spectrum are consistent with the orange colour of the stain. However, it would be difficult to distinguish the anticipated dark brown-black colour of the magnetite from the dark grey colour of the Type 10 modified cement paste. The presence of calcite is reasonable for the exposure of the specimens to the laboratory air in spite of any precautions to counteract it.
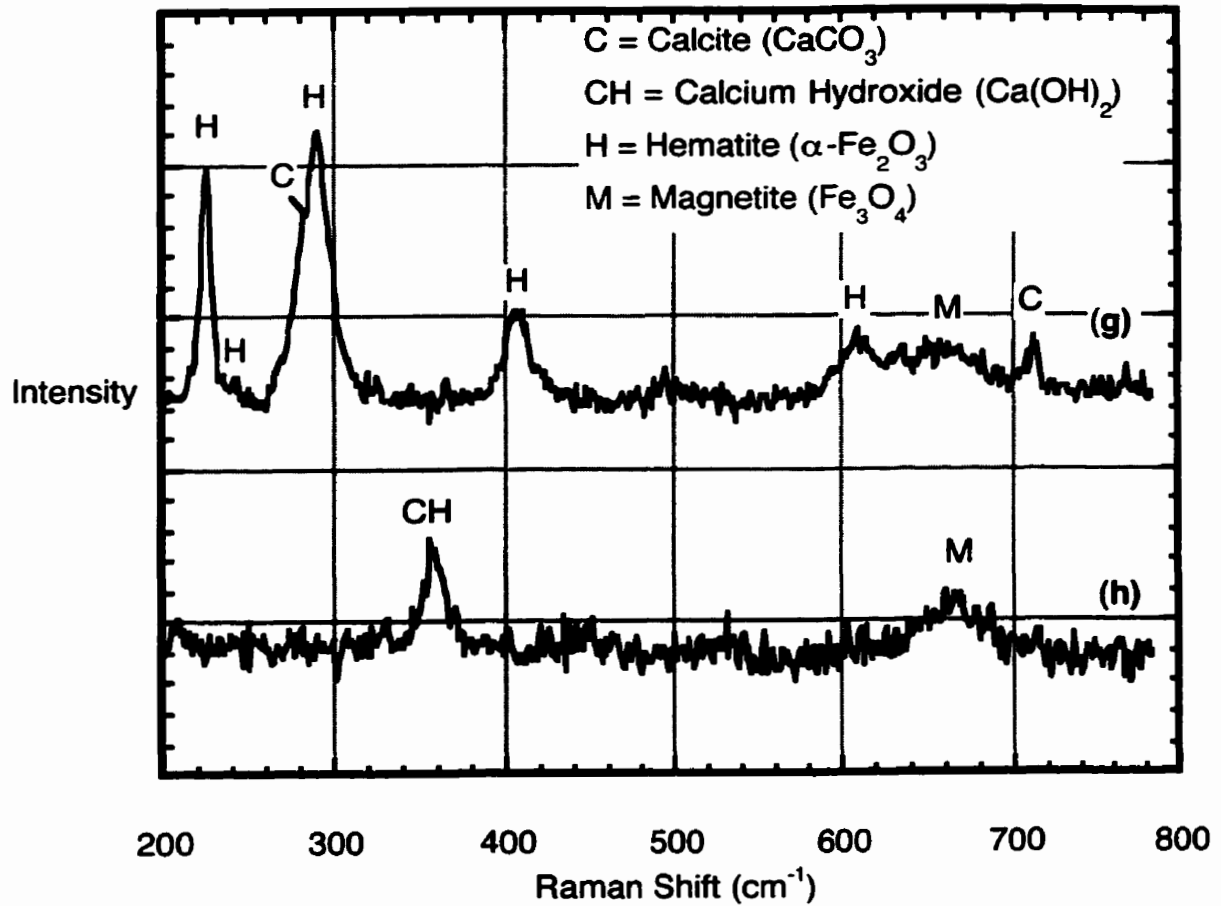
Figures 5.3.6(g) and (h) Comparison of Raman spectra from (g) an area of Type 10 modified cement paste with a concentrated orange stain and (h) an area of unstained cement paste.

The spectrum obtained from the unstained cement paste, shown in Figure 5.3.6(h), was taken approximately 2.5 mm from the steel/cement paste interface and contained two

184

clearly defined peaks: a broad peak centred at 664 cm^{-1} and a relatively sharper peak at 358 cm^{-1}. While the sharp peak centred at 358 cm^{-1} indicates the presence of calcium hydroxide (CH), the broad peak indicates the presence of magnetite and is consistent with the spectrum from the orange stain, Figure 5.3.6(g). It suggests that iron ions had diffused through the cement paste and depending upon the dissolved oxygen content, corrosion products ranging from magnetite to haematite formed (i.e., relatively low oxygen to high oxygen contents). Energy dispersive X-ray spectroscopy of this area and other areas showed considerable amounts of elemental iron (up to 5 at. %) within the cement paste which could not be directly attributed to a local accumulation of corrosion product (i.e., it was uniformly distributed) or the anticipated hydration products of C_4AF. A thorough literature search has not revealed any previous observations of magnetite at locations other than the steel/cementitious interface with the exception of the visual observations described in the work of Aligizaki et al. (Aligizaki, de Rooij et al. 2000). However, these authors observed the corrosion products as localized accumulations rather than the more uniform distribution observed here. The absence of the orange stains on the surface of the white modified cement paste specimens is likely related to the differences in chemistry and pore size distribution between the two cements. The finer pore structure of the white cement paste from its higher C_3S content and finer cement particle size range (Tables 3.1(a) and (b), Chapter 3) suggests that the diffusion of ionic species derived from corrosion processes would be more difficult in a denser paste and be more confined to the open space of a crack.

5.4 DISCUSSION

5.4.1 Effect of Surface Finish on the Corrosion Process

As shown by the open circuit potential maps of Section 5.3.1 and the Raman spectroscopy

observations of Section 5.3.6, the type of surface finish affected the location of corrosion initiation and the formation of a corrosion product assumed to be Green Rust I. In most specimens, corrosion initiated on the as-received side of the embedded steel plates which indicated that the presence of an adherent layer of mill scale composed of magnetite (Fe_3O_4), hæmatite $(\alpha-Fe_2O_3)$, and goethite $(\alpha-FeOOH)$ with a surface roughness of 1.926 $\pm$ 0.723 µm was not more protective than the ground steel surface with a surface roughness of 0.222 $\pm$ 0.023 µm. Macrophotographs of these surfaces (Figures 4.2 (a) and (b), Chapter 4) show that the surface of the ground steel is uniformly striated from the grinding process while the surface of the as-received steel is irregular with numerous small pits which might expose the underlying bare steel. It is clear that these pits would make it easier for chlorides to locally accumulate and initiate corrosion than the more uniform surface of the ground steel. Corrosion did, however, initiate on a few of the ground surfaces first but this variability is common in corrosion studies, especially chloride-induced corrosion work, and reinforces the need for studies of multiple samples to ensure that valid conclusions are drawn.

The location of corrosion initiation did not affect the composition or the locations of subsequent corrosion product formation over the remainder of the specimens, however. Corrosion products were observed at the steel/paste interface and within most, if not all, cracks, independent of the exposure condition to the simulated pore solution and surface finish of the steel. The areas of original corrosion initiation were, however, those areas where the green coloured corrosion product (assumed to be Green Rust I) formed over relatively large surface areas rather than adjacent to localized corrosion pits. The formation of this type of product is likely related to the optimal corrosion conditions present in those locations as described in greater detail in Section 5.4.3. It is anticipated that if the exposure of the specimens had continued for a few years, the greatest volume of corrosion products would have accumulated in these regions.

5.4.2 Effect of Cement Type on the Corrosion Process

It is clear that the cement type had a significant impact on the corrosion rates and the corresponding distribution of the corrosion products. Higher chloride contents were measured in the Type 10 modified cement paste even though this cement paste had been exposed to the chloride-contaminated simulated pore solution for 100 days fewer than the white specimens. A greater proportion of monochloroaluminates was formed in the Type 10 cement paste than the white cement paste as shown by the thermogravimetric results (Section 5.3.5). This accounts for the reduced average corrosion rates measured at similar time intervals for the Type 10 specimens (Figure 5.3.2) when compared to the white specimens. The formation of bound chlorides such as monochloroaluminates (Friedel's salt) would reduce the free chlorides in the pore solution able to participate in corrosion processes with the embedded steel. As such, the white modified cement paste would theoretically provide reduced corrosion protection for embedded steel because it cannot form a high proportion of monochloroaluminates because of its significantly lower C_3A and C_4AF content in the unhydrated cement powder.

In spite of this potential deficiency, the white modified cement paste did provide a degree of corrosion protection because orange stains composed of haematite and magnetite did not form from a uniform distribution of iron ions present within its pore solution as with Type 10 cement paste. This can be attributed to the finer pore size distribution and overall pore volume of the white cement paste when compared to the results for the Type 10 (Figure 5.3.3(b)). The finer pore size distribution of the white cement slowed the ingress of chlorides to the surface of the steel. In addition, the higher C_3S content in the unhydrated white cement powder produced significantly more calcium hydroxide upon hydration (Figure 5.3.5(g)) which would have improved the buffering capacity of the pore solution to prevent the localized drops in pH which accompany corrosion attack. This accounts for the differences in the corrosion product distribution noted for the two types of

cement.

The presence of any of the aforementioned corrosion products in either the Type 10 or white specimens was not predicted by their respective corrosion rates (Figure 5.3.2) if the criterion established by Alonso et al. is applied (Alonso, Andrade et al. 2000). A theoretical "threshold corrosion rate" of 0.01 A/m^2 suggests that corrosion had just initiated in the white cement paste but had not begun in the Type 10 specimens which is entirely contradicted by the presence of significant corrosion products in cracks and the cement paste cover. This criterion acknowledges that chloride-induced corrosion rates are difficult to estimate because it is not possible to non-destructively determine the anodic surface area of steel embedded in cementitious materials. With the relatively higher volume of corrosion products that formed in the Type 10 cement paste but with a relatively lower corrosion rate, it is clear that the concept of a "threshold corrosion rate" is not a reliable method to assess chloride-induced corrosion initiation of steel in cementitious materials without knowledge of the actual area which is corroding.

Other concepts used to model chloride-induced corrosion (Andrade and Alonso 1993; Molina, Alonso et al. 1993) which may be incorrect under certain conditions are the assumptions that all corrosion products form at the steel/cementitious materials interface and that their specific volumes can be as large as 6 to 7 times that of steel. From the work presented by Aligizaki et al. (Aligizaki, de Rooij et al. 2000) and the compositional results of this Chapter, these assumptions are clearly not always accurate as magnetite (Fe_3O_4) and haematite (α-Fe_2O_3) were observed within the modified cement paste cover. Moreover, they were not observed entirely as localized accumulations but as stains which is consistent with field observations of steel reinforced concrete structures. These stains which represent a fine distribution of corrosion products embedded in the cement paste are less likely to induce cracking of the cementitious cover. This possibly explains the longer than anticipated durability of field structures once the signs of deterioration have been observed.

Moreover, the compositional range of products that were observed suggests volume expansions of 2 to 3 times according to Table 2.6 (Chapter 2) rather than the more destructive 6 to 7 times which is commonly assumed. Thus, revising these two aspects of theoretical corrosion models should allow a more accurate estimation of the cracking potential of cementitious materials which contain iron corrosion products.

5.4.3 Effect of Exposure Conditions on the Corrosion Process

A review of the Raman spectroscopy results presented in Section 5.3.6 shows that corrosion products precipitated within the modified cement paste specimens under all exposure conditions. The types of corrosion products observed, however, depended upon the exposure conditions from which they were developed. These conditions can be loosely defined by steel sections of the specimens which were below, at, or above the solution line. Corrosion was observed to initiate in most specimens above the solution line where the cement paste would be only partially water saturated, contain a high level of chlorides from capillary suction (Figure 5.3.4), and have sufficient oxygen present for the cathodic reactions.

These exposure conditions also affected the corrosion products which formed within all shrinkage cracks in the specimens as the water saturated environment below and at the solution line permitted the formation of goethite (α-FeOOH). This product was not observed in cracks above the solution line because of the relatively drier environment where any water present resulted from capillary suction from the immersed part of the specimen.

Another corrosion product which appeared to depend upon the exposure conditions was the green corrosion product, assumed to be Green Rust I. As suggested by the research performed by Génin and others (Génin, Rezel et al. 1986; Refait and Génin 1993; Génin, Refait et al. 1997), Green Rust I requires relatively higher chloride/hydroxide ratios to form than other products such as magnetite and goethite. The presence of Green Rust I at or

189

above the solution line is, therefore, consistent with the high chloride contents measured in these areas (Figure 5.3.4). The higher chloride levels were also consistent with the observed decrease in the open circuit potential measurements the further an area of the steel was located above the solution line (Figures 5.3.1(d) and (g)). Clearly, higher chloride concentrations would increase the anodic corrosion processes in an area.

5.4.4 Effect of Shrinkage Cracks on the Corrosion Process

The effect of shrinkage cracks on the corrosion of the embedded steel in the modified cement paste specimens was first noted in the potential maps which were developed over the monitoring period, as shown in Figures 5.3.1(b) through (g). These figures showed that the presence of cracks permitted chlorides to reach the surface of the embedded steel faster than if the cracks had been sealed. It was also shown that this effect diminished with time as the chlorides penetrated the cement paste cover and bypassed the surface barrier of epoxy. This diffusion-dependent process remained slower than the direct access that open cracks provided, as shown by the minor difference noted in the corrosion rates for the white cement paste specimens (Figure 5.3.2). That a similar effect in the Type 10 modified cement paste specimens was not noted is probably because its pore network was considerably more open with its relatively larger volume of pores, as shown in Figure 5.3.3(b). Under these circumstances, the effect of cracks would become less significant.

Alternatively, the presence of cracks within a dense pore network such as that in the white cement paste specimens could have larger consequences: direct chloride access to only a small portion of embedded steel could concentrate corrosion damage only in cracked areas. Corrosion rate measurements under such conditions would be undervalued as mentioned previously in Section 5.4.2, and evaluations of these measurements with respect to "threshold corrosion rates" would be incorrect without taking into account for the area of the steel actually corroding.

5.5 CONCLUSIONS

1. A range of corrosion products was observed to form primarily within shrinkage cracks in the modified cement paste specimens: magnetite, goethite, hæmatite, and possibly Green Rust I. Magnetite and hæmatite were observed within the modified cement paste cover of the Type 10 specimens because of its relatively open pore structure. Goethite was observed only at or below the solution line in both types of paste while the unconfirmed Green Rust I was observed only at or above the solution line. Magnetite was observed closest to the steel/cement paste interface with higher oxygen content products (e.g., hæmatite, goethite) forming closer to the exposed surface of the cement paste, again in both types of paste.

2. The presence of shrinkage cracks had a greater impact on the corrosion rate of steel in white cement paste than the Type 10 specimens because of the relatively denser cement paste (i.e., lower pore volume) which would reduce the rate of chloride diffusion. With extended exposure to chlorides, it is anticipated that the steel within the white cement paste specimens would experience greater localized damage.

3. The concept of a "threshold corrosion rate" using linear polarization resistance is difficult to apply to steel embedded in cracked cementitious materials because the area of steel actually corroding cannot be assessed non-destructively.

4. The observed range of corrosion products have specific volumes 2 to 3 times that of iron rather than the commonly assumed values of 6 to 7.

5. The surface sealing of cracks did not prevent corrosion initiation from occurring on the steel under the epoxy. This suggests that cracks in field structures should be sealed to the level of the reinforcement to truly prevent corrosion.

CHAPTER SIX

COMPARISON OF CORROSION PRODUCTS
THAT FORM WITHIN STEEL-REINFORCED
CONCRETE

6.1 INTRODUCTION

The quality of concrete is known to have a significant effect on the service life of a structure. Factors that primarily influence concrete quality are mixture proportions, the addition of supplementary cementitious materials, proper placement and compaction, and adequate curing. Nonetheless, quantifying the effect of quality into the theoretical service life models described in Section 2.5.2 has been difficult because of the limited amount of information available about the chloride-induced corrosion process once corrosion has initiated. Indeed, almost all research to date has focussed on the time required for a sufficient number of chlorides to penetrate the concrete cover and initiate corrosion of the reinforcing steel (e.g., Delagrave, Marchand et al. 1996; Liang, Wang et al. 1999). Thus, the work of this chapter examines the effect of different concrete mixture proportions on chloride-induced corrosion, focussing upon coordinating corrosion rates of embedded steel with the type and distribution of corrosion products that form. Since it was also the intention of this work to be able to predict the performance of concretes in the field, laboratory specimens were commercially prepared and then studied in the cracked and loaded condition while exposed to simulated sea water.

In all, four different types of concretes were studied: a low quality concrete (0.54 w/cm), an industrial standard concrete (0.41 w/cm), a high performance concrete (0.27 w/cm), and a high performance concrete to which was added 10% by mass of cement of silica fume (0.25 w/cm). While the industrial standard concrete was based upon CSA/CAN

A23.1, a Canadian code for marine applications, both of the HPC mix designs were developed in accordance with the concrete design theory described in Section 2.1.5. Overall, these concretes were considered to represent the full range of microstructural characteristics that would affect which corrosion products form and where they form. It is exactly this sort of information that current theoretical service life models lack.

The "lifetime" of a structure (without any preventative maintenance) can be described as consisting of three periods: the first period is one soon after the structure goes into service in which cracks form as a result of loading or environmental stresses and then stabilize, as shown in Figure 6.1. During the second period, there is no active corrosion but aggressive species such as chlorides or carbon dioxide penetrate the concrete cover. The third period begins when corrosion initiates, t_0, and continues until a time, t_e, at which the damage to the concrete (and/or steel) are sufficient to warrant remedial action.
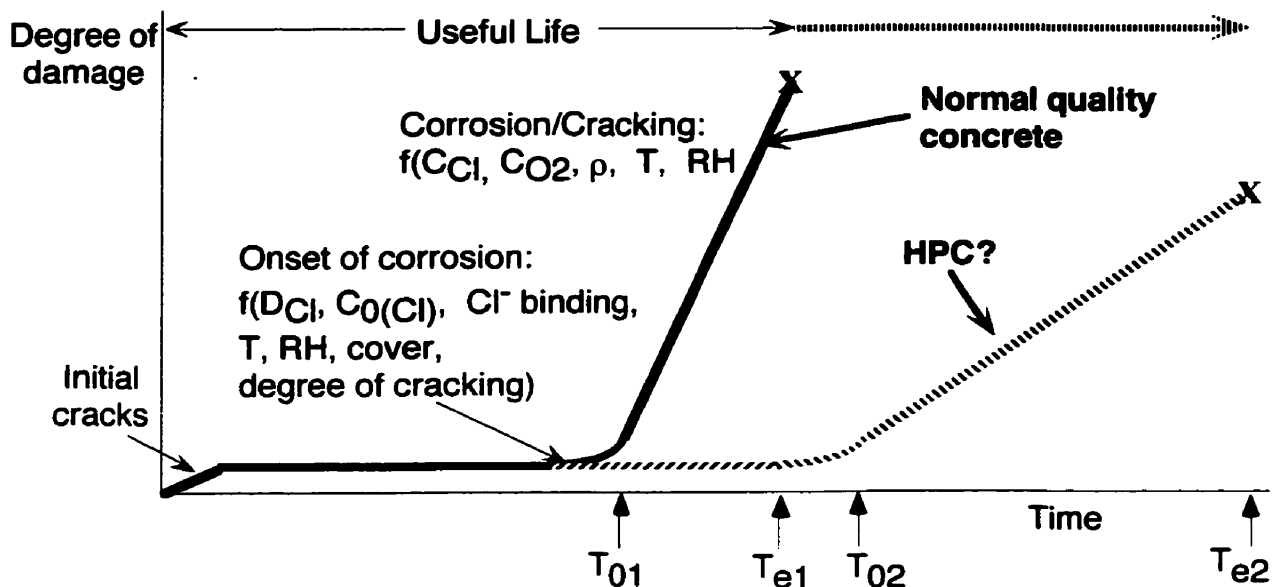
Figure 6.1 Schematic representation of the useful life of a concrete structure. $T_{0(x)}$ is the initiation time for the onset of corrosion and $T_{e(x)}$ is the end of practical service life (based on concept by Tuutti (1980)).

The anticipated beneficial effects of HPC are shown by the dashed extensions to the curve. As described in Section 2.1.5, the low porosity should reduce the diffusion of chlorides from the environment, thereby, increasing the time to corrosion initiation, and it should also limit oxygen diffusion such that the growth of corrosion products in the third period is stifled. In addition, the high electrical resistivity of the HPC should limit the corrosion rate in the third period. One expected negative effect is the brittleness of the HPC which would decrease its capacity to accommodate the corrosion products. Efforts at evaluating HPC with respect to rebar corrosion have almost exclusively concentrated on the second period: the penetration of the concrete cover by chlorides (e.g., Delagrave, Marchand et al. 1996). The research presented in this Chapter investigated the impact of the microstructural characteristics of different concretes on the rate of corrosion, and the type and distribution of corrosion products that form in the third period.

6.2 EXPERIMENTAL PROGRAMME

Four concrete mixtures were studied and their proportions are outlined in Table 6.1. Concrete prisms (500 x 100 x 100 mm) with an embedded five element corrosion probe (deformed steel Ø15 mm), as detailed in Figure 6.2, were cast commercially in 1995 for use in a previous project (Weiermair 1996). The prisms were covered with plastic sheets and field cured for two weeks. They were then stored outdoors for approximately three months. The physical properties of the concrete at 28 days are detailed in Table 6.2. Channels were sawn into the concrete prisms to position cracks subsequently induced under three-point bending in half of both types of prisms. The overlapping positioning of the five probe elements ensured that one of them was intersected by the crack. The induced cracks were held open with stainless steel wedges to give a crack opening displacement at the surface of ~0.3 mm. The prisms were exposed to simulated sea water (ASTM D1141)

in large plastic containers such that the crack was fully immersed. The composition of the sea water is given in Table 6.3 and was replaced every four months and air was continuously circulated through the sea water. Electrochemical measurements, including open circuit potentials, linear polarization resistance, and electrochemical noise, were performed at regular intervals for up to four years to assess the corrosion state of the prisms. The initial results of these measurements (i.e., those collected by other researchers for the first year) have been reported in other work (Weiermair, Hansson et al. 1995).

The two prisms from each type of concrete that exhibited the highest corrosion rates were selected for microstructural analysis, as detailed in Table 6.4. Two Ø50 mm cores were taken from each prism, one of which included an induced crack (with the exception of one core from a low quality concrete prism) and the rebar probe elements, as illustrated in Figure 6.3 (Region A), while the second was from an end of the prism, i.e., in an unstressed region (Region B). The cores were immediately photographed to document the corrosion state of the steel and the appearance of any corrosion products and then promptly stored in polyethylene bags. The cores taken from the ends of the prisms were sectioned lengthwise for chloride and pore size distribution analyses using chloride titration and mercury intrusion porosimetry, respectively. Sectioning was performed either dry or using ISOPAR M™ (Exxon), a non-leaching synthetic isoparaffinic hydrocarbon. The cores from the cracked regions were also sectioned lengthwise, perpendicular to the induced crack, as detailed in Figure 6.4. These regions were ground and diamond polished to 1 µm using more ISOPAR M to clean the surfaces between each polishing stage. These preparation techniques as well as the characterization methods described below are detailed in Chapter 3.

The concrete adjacent to the crack, the surfaces of the crack, and their corresponding corrosion products on the surface of the steel were analyzed using environmental scanning electron microscopy (ESEM) with energy dispersive X-ray spectroscopy (EDS) as well as

Raman spectroscopy. The steel samples were subsequently pickled using an inhibited acid[1] to remove the corrosion products without damaging the steel further. Samples of the corrosion products and the adjacent concrete were analyzed with X-ray diffraction over the 2θ range of 5-70° using Cu K_α radiation.

Table 6.1 Mixture proportions of the cast concrete prisms.

Material	Low Quality	Industrial Standard	HPC	HPC + Silica Fume
Cement, kg	233	280	430	431
Silica Fume, kg	n/a	n/a	n/a	45
Fly Ash (Type F), kg	60	69	74	87
Fine Aggregate, kg	865	559	653	602
Coarse Aggregate. kg	1034	963	1083	1071
Water, l	160	143	137	140
Air Entraining Agent Darex	As Required	As Required	As Required	As Required
Water Reducer, l	0.46 WRDA 82	0.45 WRDA 82	6.0 WRDA 19	6.0 WRDA 19
Superplasticiser Daratard 17, l	n/a	n/a	0.85	0.85
w/cm	0.54	0.41	0.27	0.25

[1] 20 g of Sb_2O_3 and 50 g of $SnCl_2$ were dissolved in 1000 mL of reagent grade HCl (designated as C.3.1) in accordance with ASTM G1. Corroded steel specimens were immersed in this vigorously stirred solution at 20-25°C for 1-25 minutes.
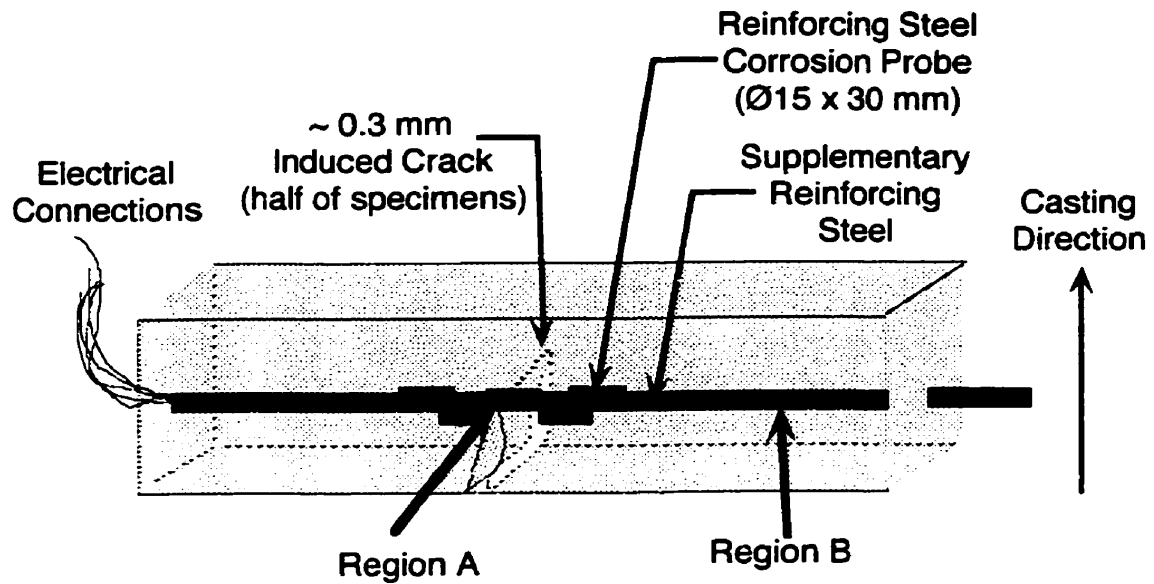
Figure 6.2 Schematic illustration of a concrete prism with its embedded steel corrosion probes.

Table 6.2 Physical properties of the cast concrete prisms at 28 days (Weiermair, Hansson et al. 1995).

Property	Low Quality	Industrial Standard	HPC	HPC + Silica Fume
Compressive Strength, MPa	32.7	41.5	77.4	82.6
Resistivity, Ω·cm	7000	10000	13000	52000

Table 6.3 Chemical composition of simulated sea water (ASTM D1141). The pH (after adjustment with 0.1 N NaOH solution) is 8.2 and the solution contains 0.56 M of chlorides.

Compound	Concentration, g/L
NaCl	24.53
$MgCl_2$	5.20
Na_2SO_4	4.09
$CaCl_2$	1.16
HCl	0.695
$NaHCO_3$	0.201
KBr	0.101
H_3BO_3	0.027
$SrCl_2$	0.025
NaF	0.003
$Ba(NO_3)_2$	0.0000994
$Mn(NO_2)_2$	0.0000340
$Cu(NO_3)_2$	0.0000308
$Zn(NO_3)_2$	0.0000096
$Pb(NO_3)_2$	0.0000066
$Ag(NO_3)_2$	0.00000049

Table 6.4 Corrosion rates of embedded steel as determined for each prism by linear polarization resistance.

Concrete Type	Age at Test (Years)	Prism	Induced Crack?	Corrosion Rate (A/m^2)	Cored and Analyzed?
Low Quality	4	1	Yes	5.0×10^{-2}	Yes
		2	Yes	2.0×10^{-2}	No
		3	No	3.8×10^{-2}	Yes
		4	No	2.8×10^{-3}	No
Industrial Standard	3	1	Yes	1.1×10^{-2}	Yes
		2	Yes	5.9×10^{-1}	Yes
		3	No	8.4×10^{-3}	No
		4	No	2.4×10^{-2}	No
High Performance	3	1	Yes	1.3×10^{-2}	Yes
		2	No	1.2×10^{-3}	No
		3	No	4.3×10^{-3}	No
		4	Yes	1.2×10^{-2}	Yes
High Performance + Silica Fume	4	1	Yes	5.9×10^{-3}	Yes
		2	Yes	2.5×10^{-2}	Yes
		3	No	3.5×10^{-4}	No
		4	No	5.6×10^{-4}	No

199
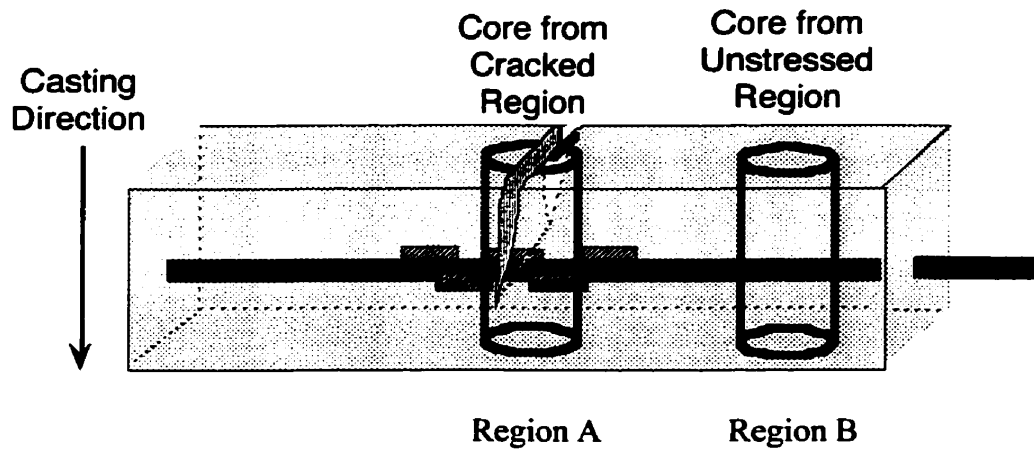
Figure 6.3 Location of cores taken for further microstructural analysis.
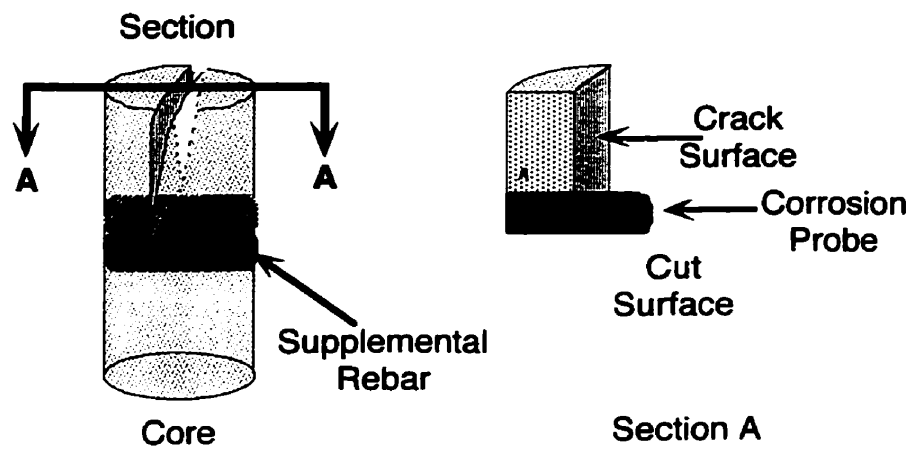
Figure 6.4 Sectioning the cores taken from the cracked region of the concrete prisms.

6.3 RESULTS

6.3.1 Corrosion Rate Measurements

Figures 6.5(a) and (b) show the mean corrosion rates measured for each type of concrete, cracked and uncracked, respectively, for up to four years of exposure to the simulated sea water. These data assumed that corrosion was taking place uniformly over the whole surface area of the probe element. For most of the first year of exposure, the steel probes in the high performance concrete without silica fume were corroding at higher than expected rates that even surpassed those in similar low quality and industrial standard concrete prisms during the first year of exposure (Weiermair, Hansson et al. 1995). However, these rates gradually decreased over the first year of exposure to the simulated sea water while the corrosion rates of steel in the low quality and industrial standard concretes continued to increase. The initially high rates for steel in HPC, both with and without silica fume, have been attributed to the higher density of microcracks with respect to normal quality concrete as well as differences in the pore structure that would have affected the nature and extent of capillary suction of moisture (Weiermair, Hansson et al. 1995). The subsequent decrease can be attributed to the ongoing hydration and pozzolanic reactions. These reactions would be slower in the high performance concretes because of the limited water available for the reactions to proceed unless the concrete was cracked (Marcotte and Hansson 1998).

Another atypical result was noted in Figure 6.5(a) where the range between the corrosion rates for both industrial standard specimens was so large that both curves had to be presented instead. The reason for this large range was identified when the prisms were sectioned and the size and orientation of the induced cracks was recorded. The specimen with the lower corrosion rate contained a crack perpendicular to the steel that was similar to all other sectioned concretes while the specimen with the higher corrosion rate was different: the three-point bending procedure had opened up a portion of the steel/concrete

interface (approx. 5 mm on either side of the crack) along with the desired ~0.3 mm crack perpendicular to the steel. Simulated sea water gained easier access to the steel surface and a higher corrosion rate resulted. This sort of variability is typical in concrete studies and reinforces the need for multiple specimens. Overall, the exclusion of the higher measurement because of the atypical crack configuration indicates that the corrosion rate of steel embedded in industrial standard concrete is in a similar range to that of the high performance concretes. This is consistent with the general expectation that this is a good quality concrete which provides reasonable protection against corrosion and explains why it is often specified for field structures.
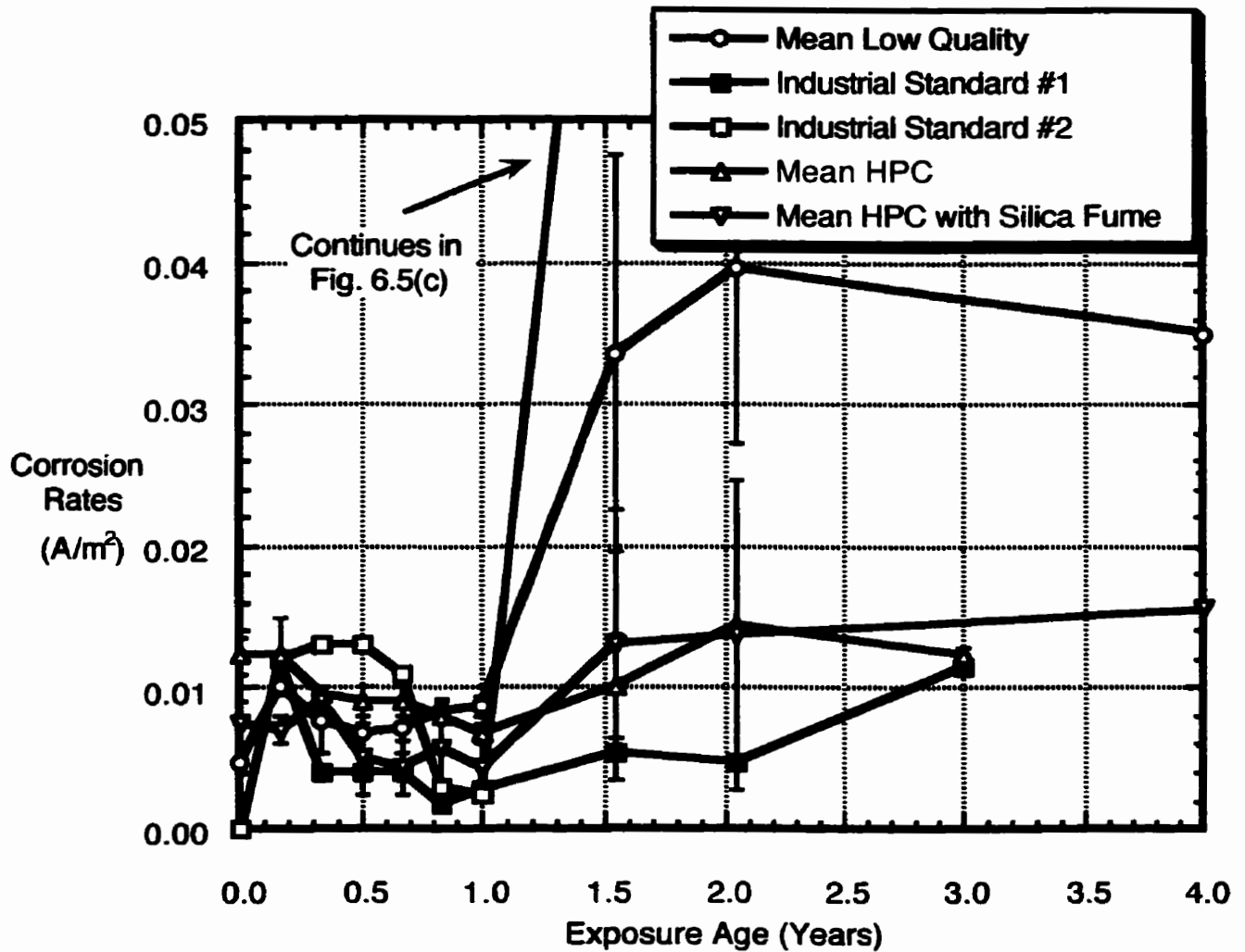
Figure 6.5(a) Comparison of the mean corrosion rates of the steel probes intersected by the crack. Note: Bars representing the range of measurements are shown for all concretes except for the industrial standard concrete. For this concrete, both curves are shown instead.
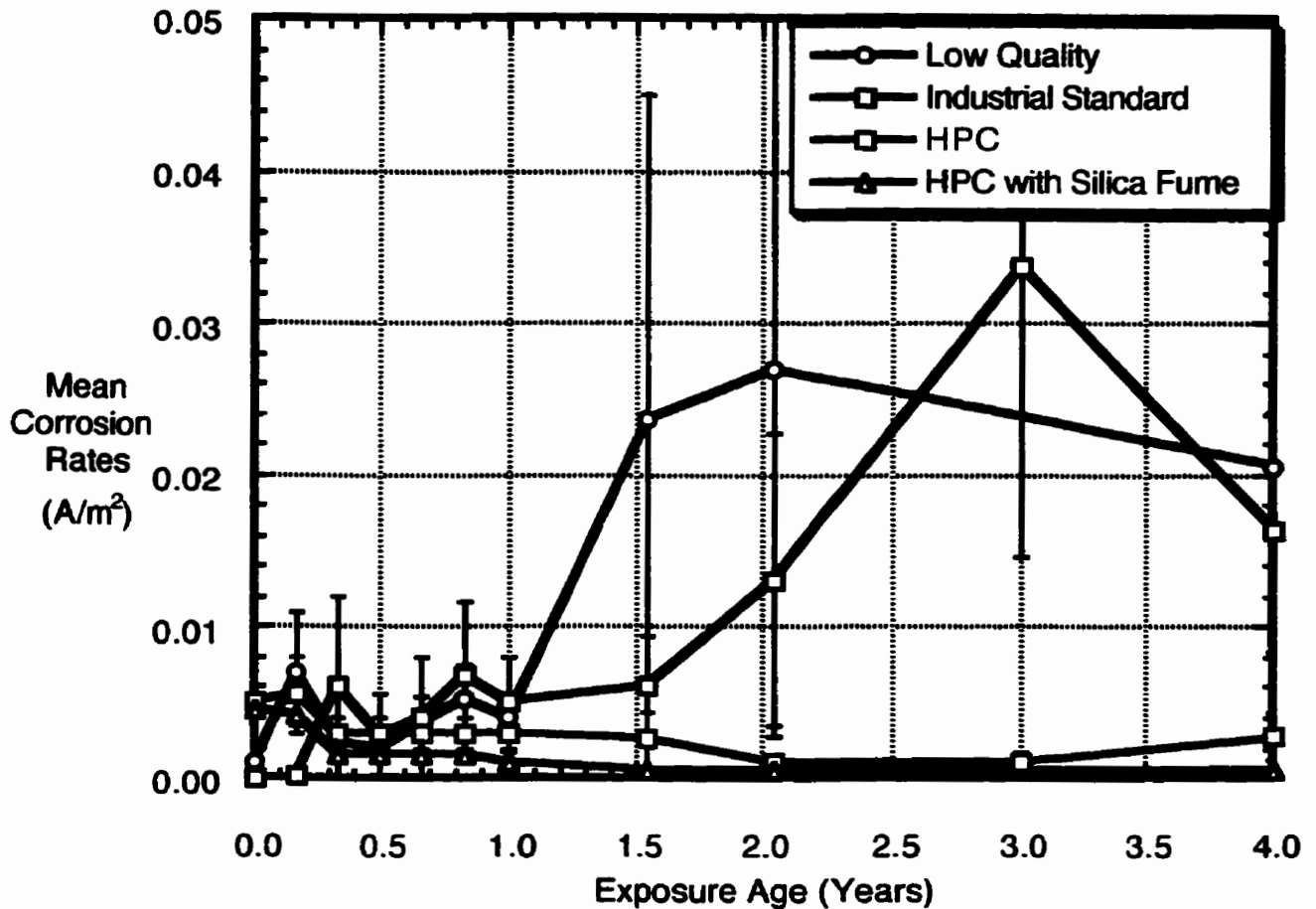
Figure 6.5(b) Comparison of the mean corrosion rates of the steel probes embedded within uncracked prisms. Note: Bars representing the range of measurements are shown for all concretes.

After the first year for all concrete specimens, the presence of the induced crack increased the overall corrosion rate of the embedded steel by an order of magnitude in all concretes over their uncracked counterparts except the low quality concrete in which the differences between cracked and uncracked regions was negligible (i.e., the presence of a crack did not affect the corrosion rate). This suggests that the pore network of the low

quality concrete was sufficiently voluminous and interconnected such that the additional chloride access to the reinforcing steel provided by the crack was superfluous. The other concretes were likely to have been sufficiently dense to limit the diffusion of chlorides such that the crack had a significant, deleterious effect. Furthermore, when the high performance concretes remained uncracked, the corrosion rate of embedded steel continued to decrease over the four year monitoring period, whereas it increased in the region of an induced crack. This result is entirely consistent with the anticipated behaviour of HPC and emphasizes the deleterious effect of cracks even if high quality concrete is used.

In addition to the effect of the induced crack, another trend was observed where corrosion rates reached a maximum level and subsequently decreased. This occurred after approximately two years' exposure to the simulated sea water for the uncracked low quality and cracked industrial standard concretes, and after three years' exposure for the uncracked industrial standard concrete. These maxima suggest that carbonation, the precipitation of minerals from the sea water, or the formation of corrosion products within the pore network or near the surface of the steel physically barred the ingress of chlorides, water, or oxygen that were necessary to maintain the corrosion rate at its previous level. It could also indicate that any dissolved oxygen has been locally consumed and the corrosion reactions cannot continue at the former rate until replenished from the environment. This behaviour is consistent with the observations of Leek (Leek 1997) and possibly accounts for the longer than expected service lives for deteriorating structures. Presumably, the more restricted pore networks of the high performance concretes would make it more difficult for corrosion to initiate and then would be easier to plug with corrosion products if corrosion were to initiate. Thus, this effect was either too small to be detected or did not occur within the monitoring period.

Figure 6.5(c) Comparison of the mean corrosion rates of the steel probes intersected by the crack (full scale version of Figure 6.5(a)). Note: Bars representing the range of measurements are shown for all concretes except for the industrial standard concrete. For this concrete, both curves are shown instead.
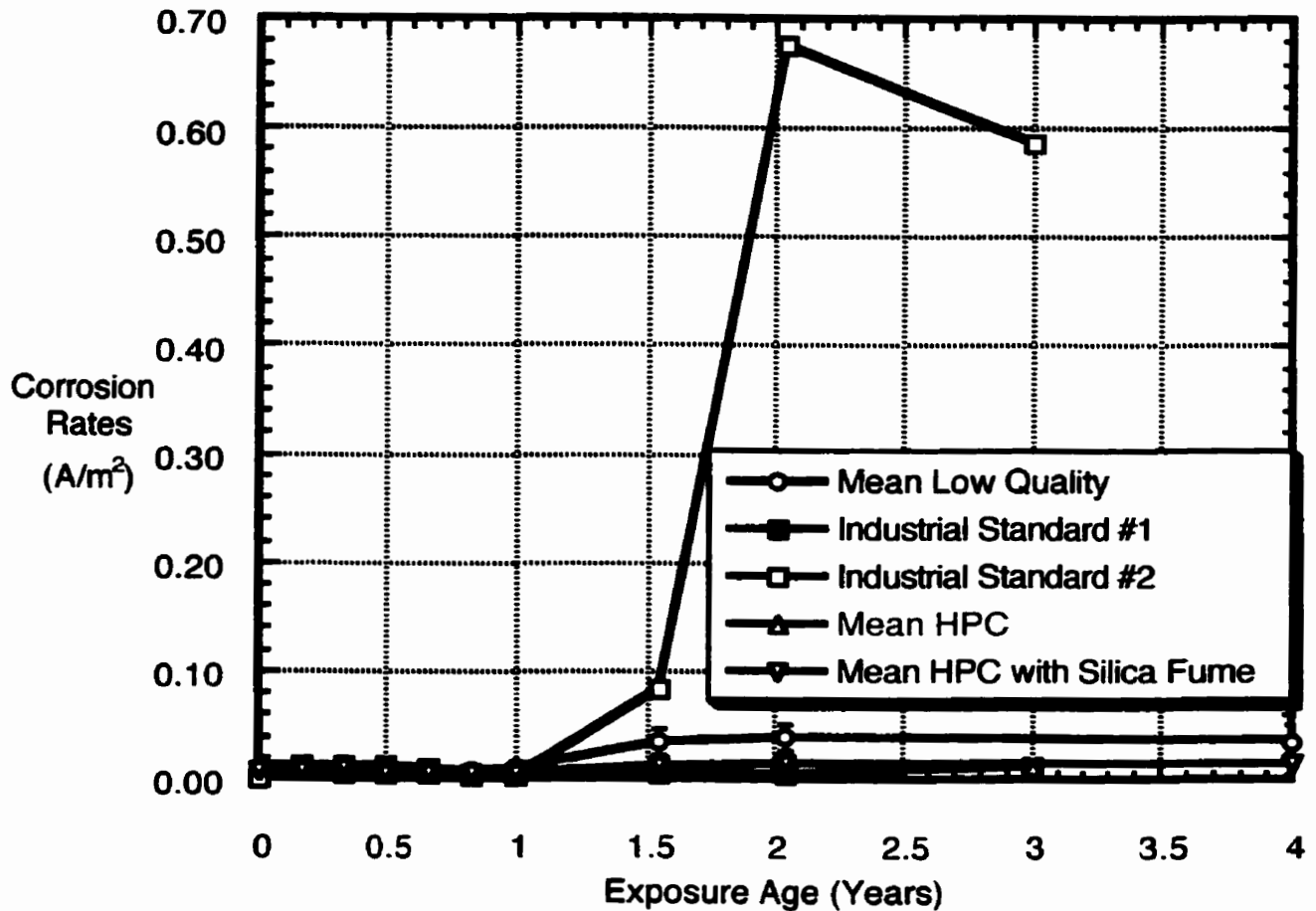
6.3.2 Chloride Analyses

Chloride content measurements are presented in Table 6.5 and shows that if the concretes remain uncracked, chloride diffusion is so slow that chlorides cannot be detected within the

206

first 10 mm of the surface of the steel after at least three years exposure to simulated sea water (detection limit of the technique of about 1 ppm by mass). The concrete cover depth in this region of the prism is approximately 40 mm which is approximately the minimum specified cover depth in reinforced concrete structures[2] and presents the least resistance to this type of environmental exposure.

Significant chloride levels were detected near the induced crack of the concrete prisms in the same period of time, however, which shows that cracks are a significant problem for the long-term service life of reinforced concrete structures. Current ACI standards (Committee 222-Corrosion) suggest a maximum acid soluble content of 0.2% by mass cement based upon field studies of bridge decks. The values presented in Table 6.5 are estimates of the total chloride content (i.e., acid-soluble chlorides) and are, therefore, intended to present the worst-case scenario for chloride exposure.

Under these circumstances, all prisms exceeded the chloride limit near the induced crack. Chloride levels were highest for the low quality concrete, followed by the HPC, the industrial standard concrete, and finally the HPC/SF. Overall, the HPC/SF had a chloride content that was almost an order of magnitude lower than the other concretes and barely exceeds the water-soluble and acid-soluble chloride limits even after four years exposure to the simulated sea water. To properly interpret these levels, however, it must be noted that the industrial standard and HPC prisms were sectioned after only three years exposure to the simulated sea water while the low quality and HPC/SF prisms were sectioned after four years. It is, therefore, possible that the HPC might have had the highest chloride level if it were exposed to the simulated sea water for an additional year which appears to be contrary to the anticipated characteristics of high performance concretes.

---

2 CAN/CSA A23.1-M90 (Section 15.1.7.1) specifies a minimum cover of 60 mm. It is acknowledged, however, that there is a 90% probability that the actual cover will be within 20 mm of that specified.

Table 6.5 Mean acid-soluble chloride contents (± 0.0001) within the first 10 mm of the steel/concrete interface from the regions indicated in Figure 6.2. Values are the mean of triplicate samples from two prisms with the exception of the measurements for the low quality prisms which are the means of triplicate samples from one prism each. All measurements in Region A were performed on cracked specimens except for one low quality prism marked with an asterisk (*).

Concrete Type	Exposure Age (years)	Region B (mass % concrete)	Region A (mass % concrete)	Region A (mass % cement)
Low Quality	4	Not Detected Not Detected	0.910 0.440*	7.30 3.09*
Industrial Standard	3	Not Detected	0.448	2.58
HPC	3	Not Detected	0.726	3.42
HPC + SF	4	Not Detected	0.050	0.21

These chloride levels can be explained, however, by the different pore structures for each concrete that resulted from the varying w/cm ratios and the presence of silica fume. Although a low w/cm ratio reduces the volume of pores within the concrete, the correspondingly smaller pore diameters increase capillary suction if the pore network is continuous. This would allow chlorides to reach the steel/concrete interface quickly in spite of the reduced number of pathways through the concrete cover to the surface of the steel. This effect can be counteracted by silica fume which has been shown to block capillary pores (Sellevold, Bager et al. 1982) and could ameliorate any microcracks which enhance the connectivity of the pore network. Thus, the low quality concrete likely had a high level of chlorides because it likely contained a large pore volume while the HPC had a relatively smaller volume of pores than the industrial standard concrete, but its smaller pore diameters

enhanced capillary suction. The HPC/SF had a similar, low w/cm ratio as its HPC counterpart but the presence of silica fume likely made its network of fine capillary pores more discontinuous and blocked any microcracks.

This hypothesis is corroborated by the comparison of chloride contents measured using an acid test (i.e., a bulk measurement) with those measured using EDS on cement paste areas that were within 10 μm of the crack (i.e., a localized measurement), presented as Figure 6.5. Clearly, the presence of the crack has the most impact on HPC and the least on the low quality concrete for the previously described reasons. It is also apparent that the continuity of the pore network is equally important for chloride diffusion as the chloride content of the HPC exceeds the HPC/SF value by an order of magnitude. Thus, the benefit of a low w/cm ratio to reduce the ingress of chlorides can only be realized with the addition of silica fume or any other admixture that would make the pore network more discontinuous.
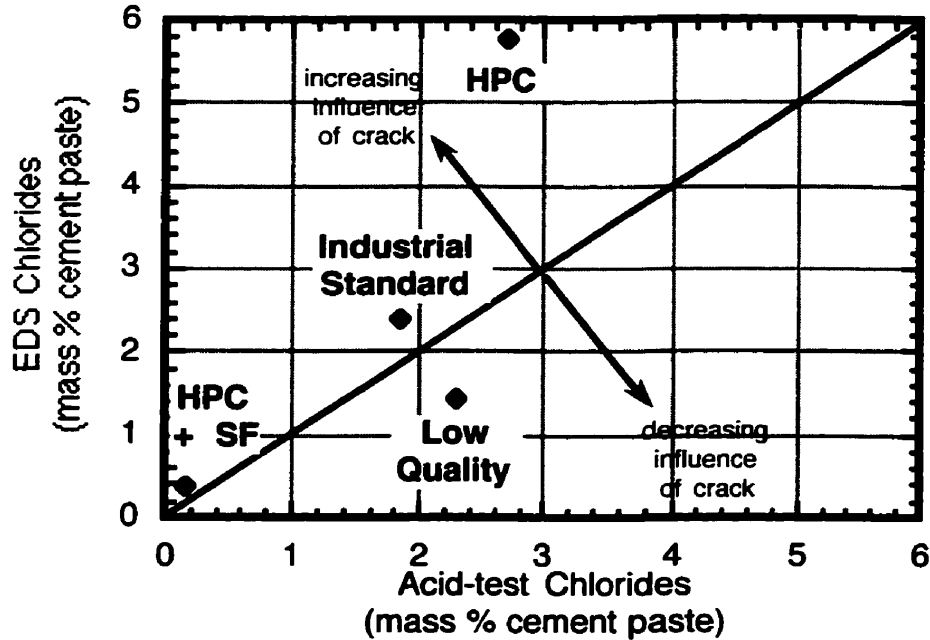
Figure 6.5 Comparison of the mean chloride measurements determined from an acid test (within the first 10 mm of steel/concrete interface) versus EDS ($\leq$ 10 μm) in the area indicated as Region A in Figure 6.2.

6.3.3 Pore Size Distribution Measurements

Figures 6.6(a) through (f) present the pore size distribution measurements for samples taken from each concrete at the steel/concrete interface near the induced crack (if present) and the unstressed region. Overall, a comparison of the samples within each concrete type shows that these regions are similar for the industrial standard and HPC prisms but there is a statistically significant difference between the two regions for the low quality and HPC/SF prisms. For the low quality prisms, Figure 6.6(b) shows that there was a large

statistical variability between the six samples that was independent of the whether an induced crack was present. Half of the samples in this region had pore size distributions that were similar to those measured in the unstressed region while the other half of the samples did not contain pores in the 0.04-10 μm range. This is not consistent with the relatively continuous pore structure that should result from a 0.54 w/cm ratio. Although the presence of fly ash in the mix could have caused the pore network to become more discontinuous, this effect was only observed in the low quality concrete even though all mixes contained fly ash. It is more probable that these pores were blocked from carbonation in a manner described by Edvardsen (Edvardsen 1999), the precipitation of mineral deposits from the simulated sea water, or the formation of corrosion products.

In contrast to the low quality prisms, the HPC/SF prisms showed a large variability in the six replicate samples from the unstressed region, shown in Figure 6.6(e). Microcracks about 8-10 μm in size were observed in three of the samples that resulted from autogenous shrinkage. All six samples had an overall pore threshold diameter of 0.02 μm. Near the induced crack, the 0.02 μm pore threshold diameter was maintained (Figure 6.6) but the microcracks were observed in only one of the six samples and pores in the 0.01-10 μm range were not detected. It is clear that the induced crack exposed the self-dessicated HPC/SF to sea water which rehydrated this internal region of the concrete and allowed further pozzolanic and hydration reactions to occur. This process was described in detail by Sellevold (Sellevold, Bager et al. 1982) for concretes that contain silica fume and is considered to be one of the potentially beneficial characteristics of high performance concretes that contain silica fume.

Comparisons of the mean pore size distributions amongst the concrete mixes show that there was no difference amongst the profiles from the unstressed region for the low quality, and both high performance concretes, except for those already noted amongst the individual samples. These concretes had pore threshold diameters of in the range of

0.01-0.04 μm while the industrial standard concrete had a significantly larger pore threshold diameter of 0.1 μm. While it was anticipated that the high performance concretes would have smaller pore threshold diameters than the industrial standard concrete because of their low w/cm ratios, the relatively low value for the low quality concrete can be attributed to the presence of carbonation or corrosion products that would have plugged the pore network. Overall, these differences amongst the concretes are not significant enough to suggest that any particular concrete type could resist chloride diffusion better than any other, as shown in Figure 6.6(g). However, this assessment changes if the concretes are cracked, as shown in Figure 6.6(h). The overall capillary volume and size range in the HPC/SF is reduced and, in general, it suggests that the inevitable cracking that occurs in reinforced concrete structures could be partly beneficial for this type of concrete with respect to a reduction in steel chloride exposure.
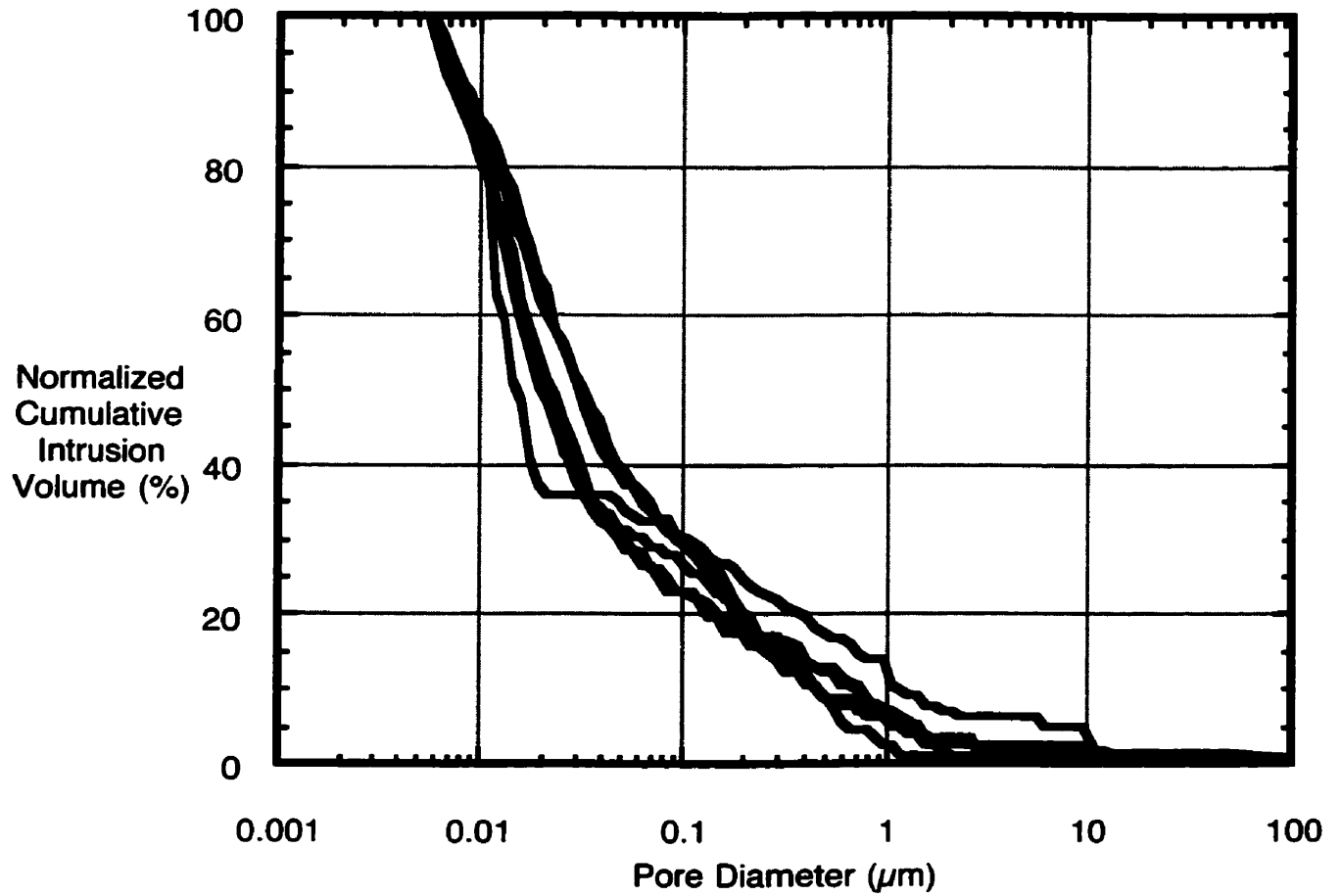
Figure 6.6(a) Comparison of the normalized cumulative intrusion volumes for concrete samples taken from the unstressed region of the low quality concrete.
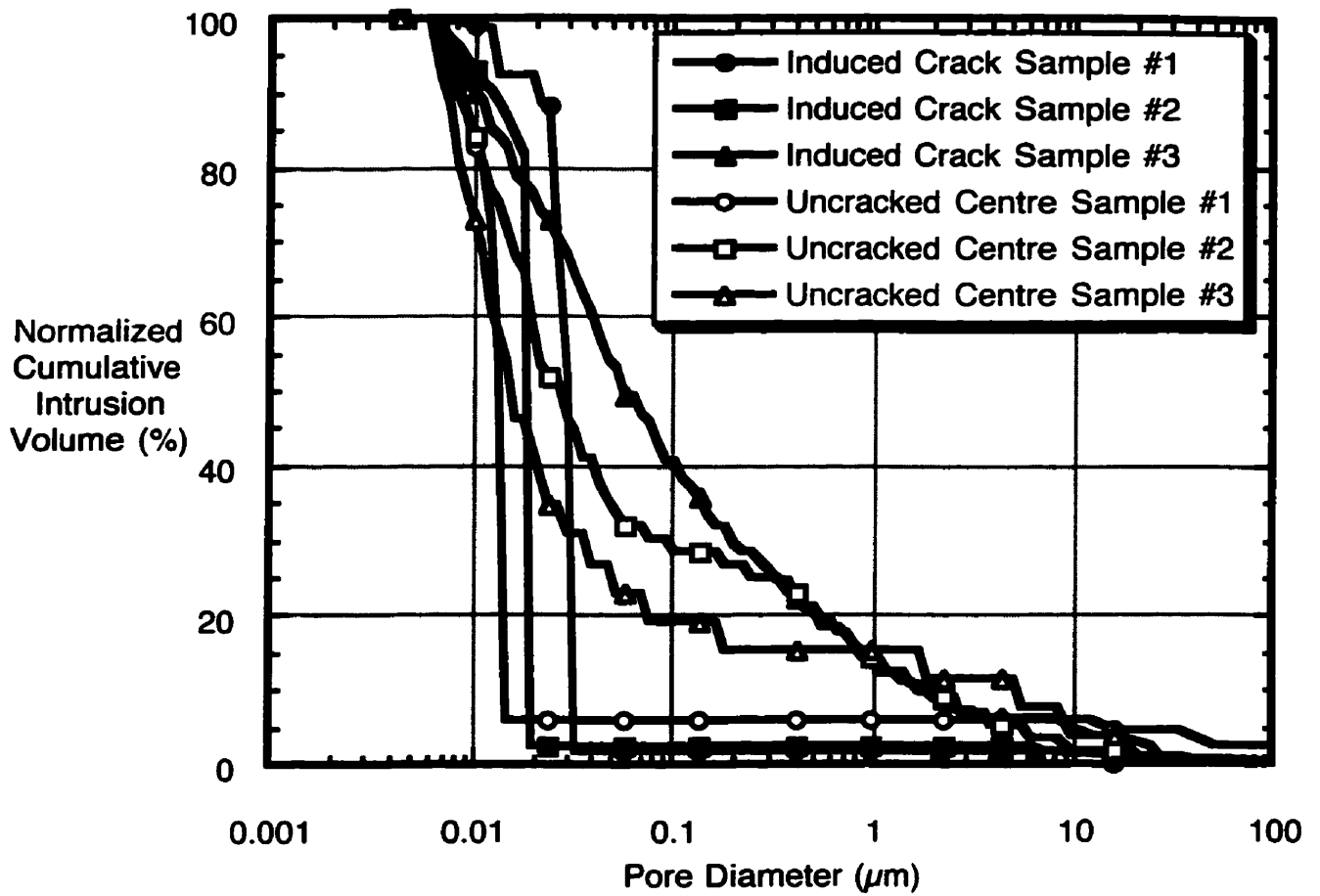
Figure 6.6(b) Comparison of the normalized cumulative intrusion volume for cracked and uncracked concrete samples taken from the low quality concrete.

214
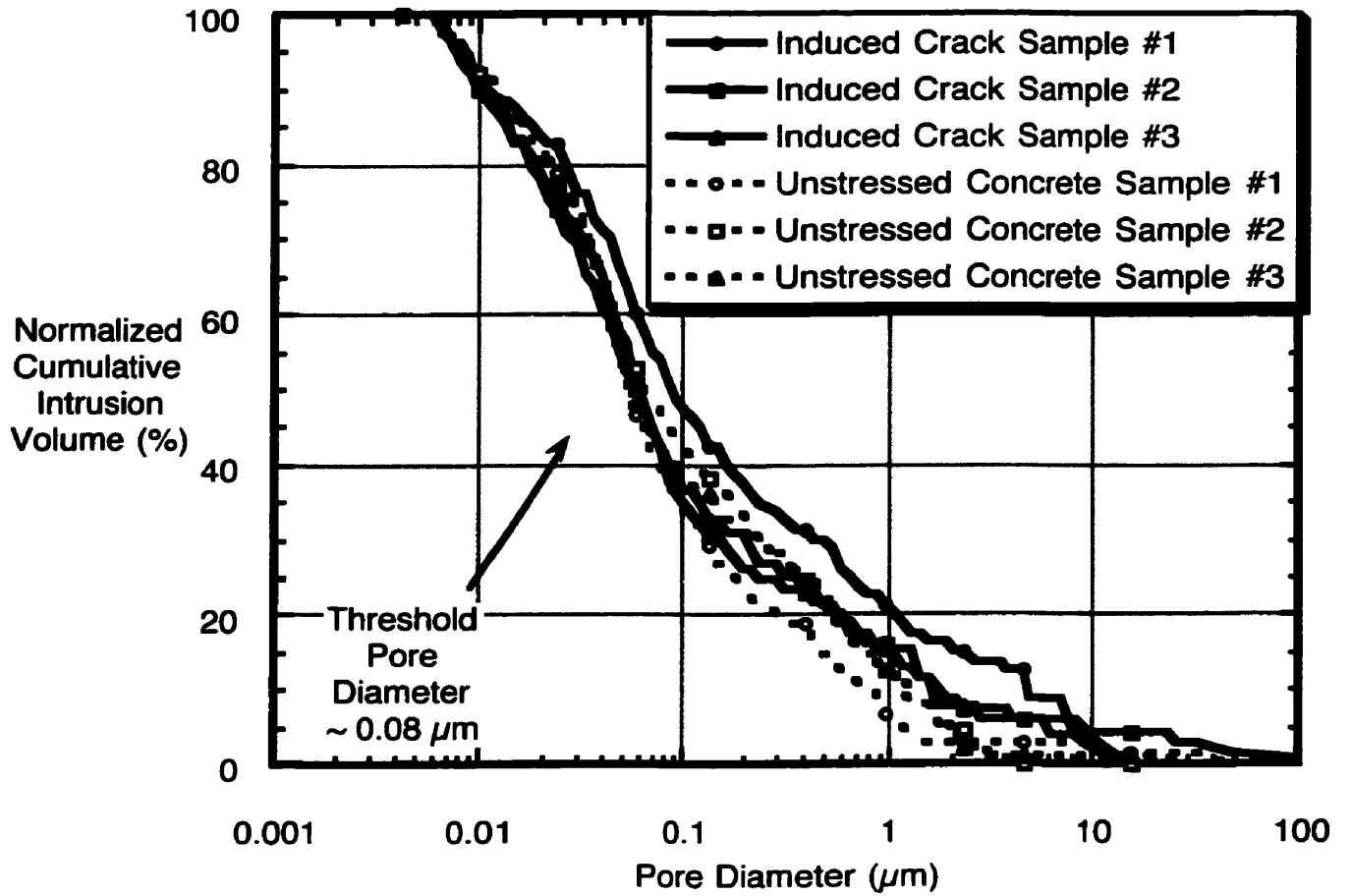
Figure 6.6(c) Comparison of the normalized cumulative intrusion volumes for concrete samples taken from the induced crack and unstressed regions of the industrial standard concrete.
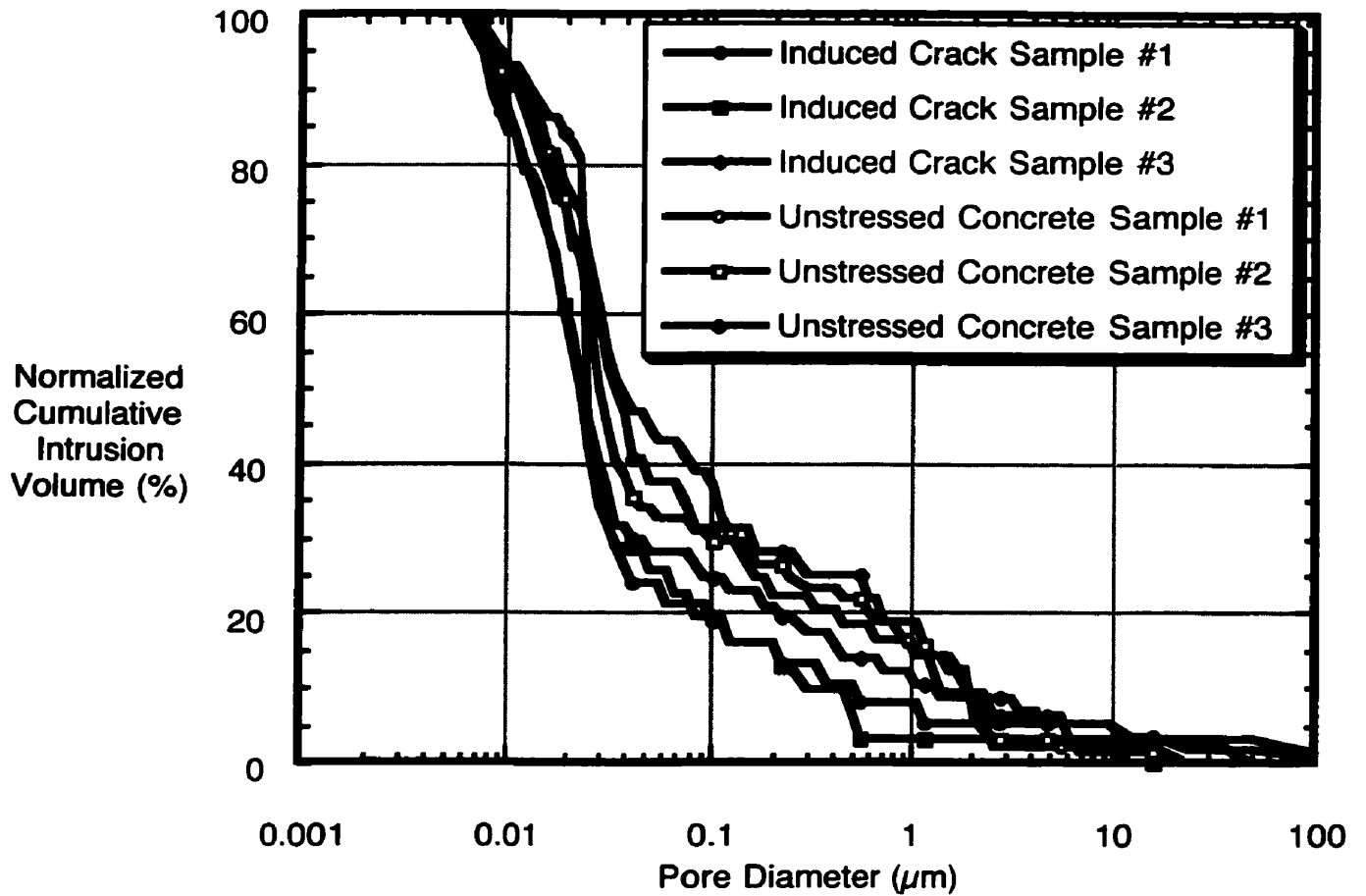
Figure 6.6(d) Comparison of the normalized cumulative intrusion volumes for concrete samples taken from the induced crack and unstressed regions of the high performance concrete (HPC).
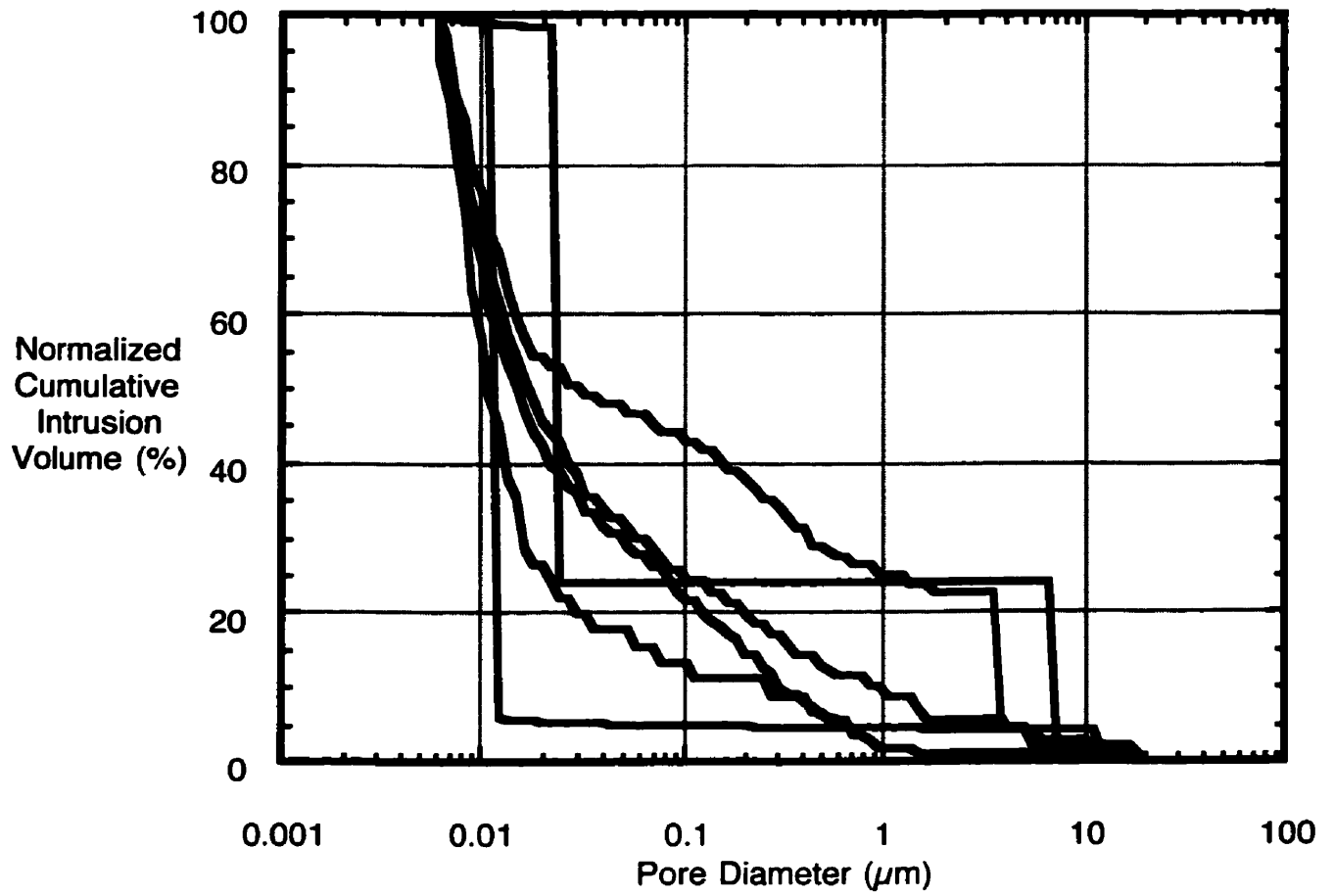
Figure 6.6(e) Comparison of the normalized cumulative intrusion volumes for concrete samples taken from the unstressed region of the high performance concrete with silica fume (HPC/SF).
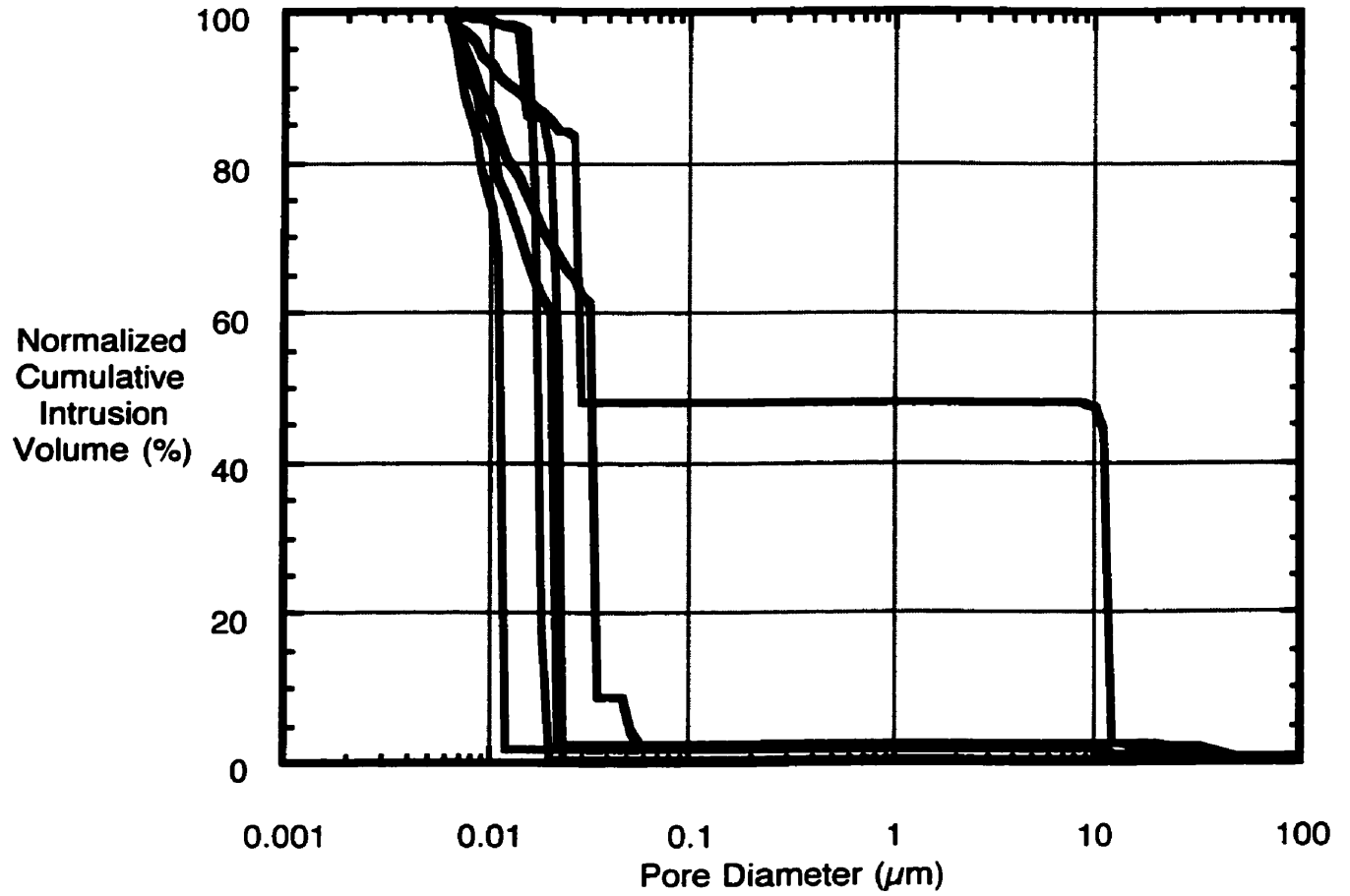
Figure 6.6(f) Comparison of the normalized cumulative intrusion volume for samples taken from the induced crack region of the high performance concrete with silica fume.

218
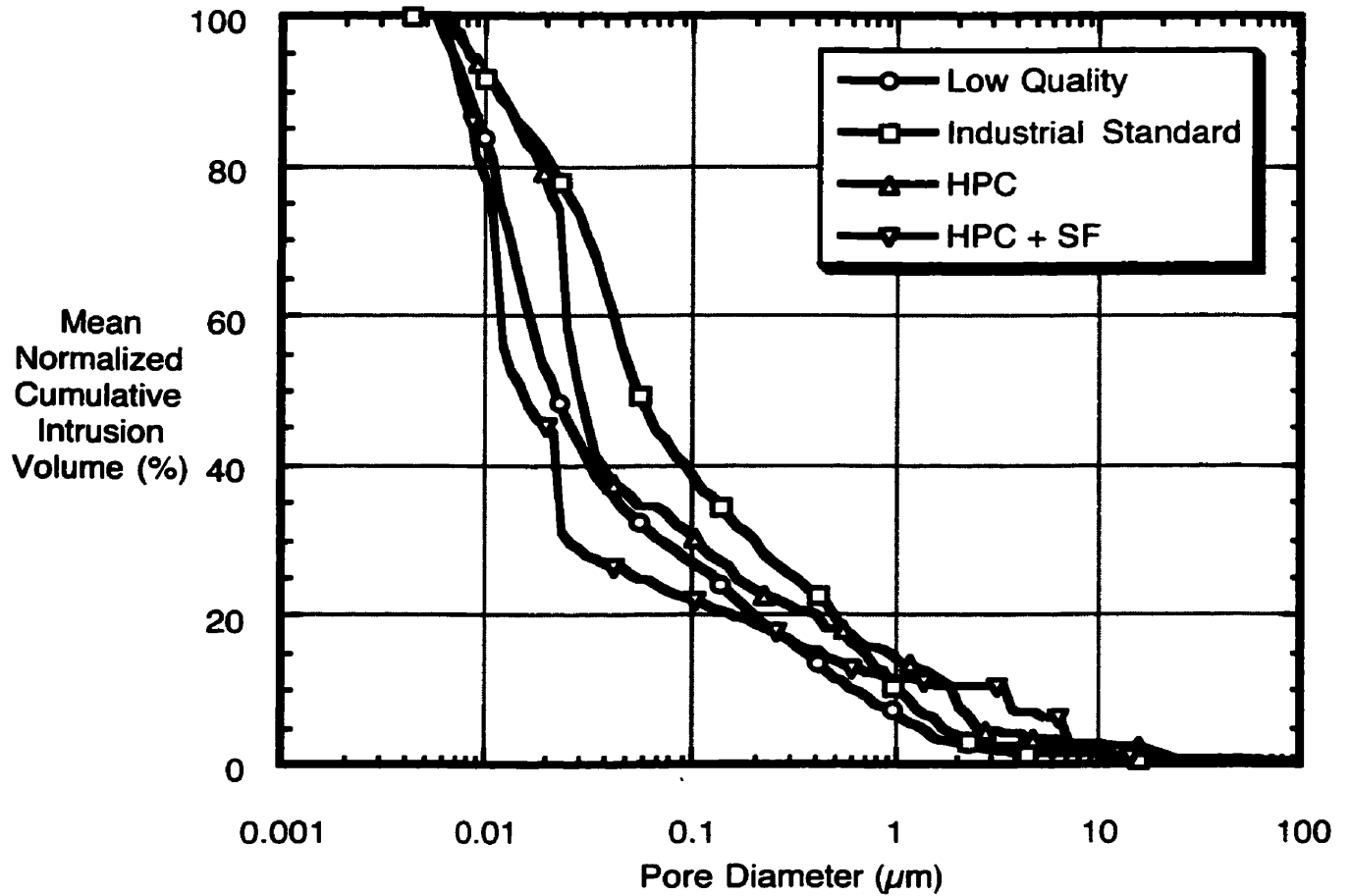
Figure 6.6(g) Comparison of the mean normalized intrusion volumes for concrete from the unstressed region of the concrete prisms.
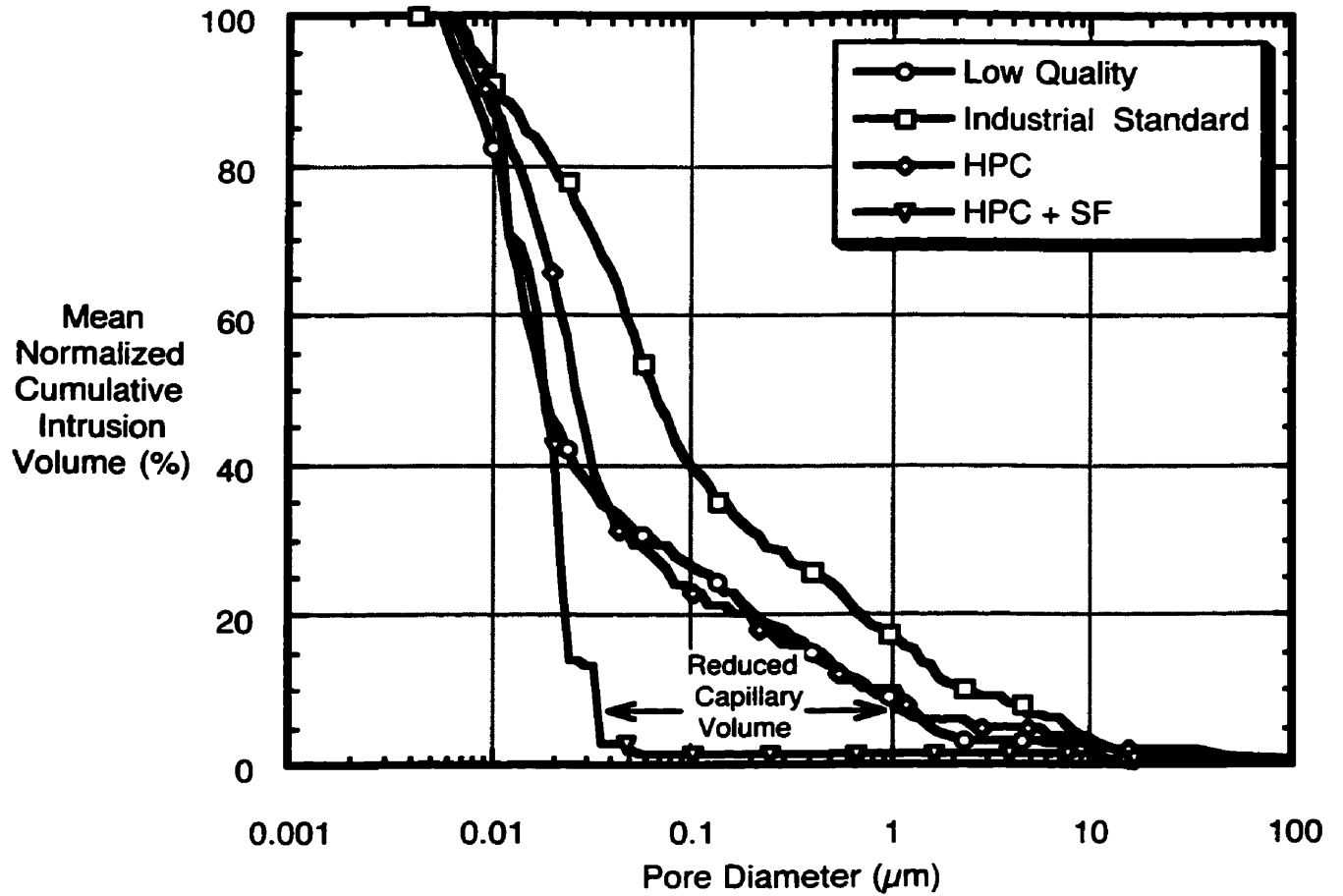
Figure 6.6(h) Comparison of the mean normalized intrusion volumes for the cracked region of the concrete prisms.

6.3.4 Macro- and Microstructural Observations of the Concrete

6.3.4.1 Mechanical Properties

In coring the prisms, it was clear that the mechanical properties of the concretes were very different: clean, intact cores were readily obtained from the industrial standard and HPC/SF prisms and these could be easily sectioned, as shown in Fig. 6.7 (a). The low quality and high performance concrete cores, however, fractured just below the rebar and, on attempts at further sectioning, broke into a large number of pieces. Since these cores were observed to contain red corrosion products within the concrete cover, it is likely that the formation of these corrosion products induced tensile stresses which reduced the tensile capacity of these cores by initiating cracks that readily propagated during coring. Moreover, the steel embedded within the industrial standard and HPC/SF required considerably more force to prise it from its surrounding concrete than the corresponding steel embedded in the either the low quality or HPC without silica fume. One such fractured piece that was adjacent to the rebar is shown in Figure 6.7(b).
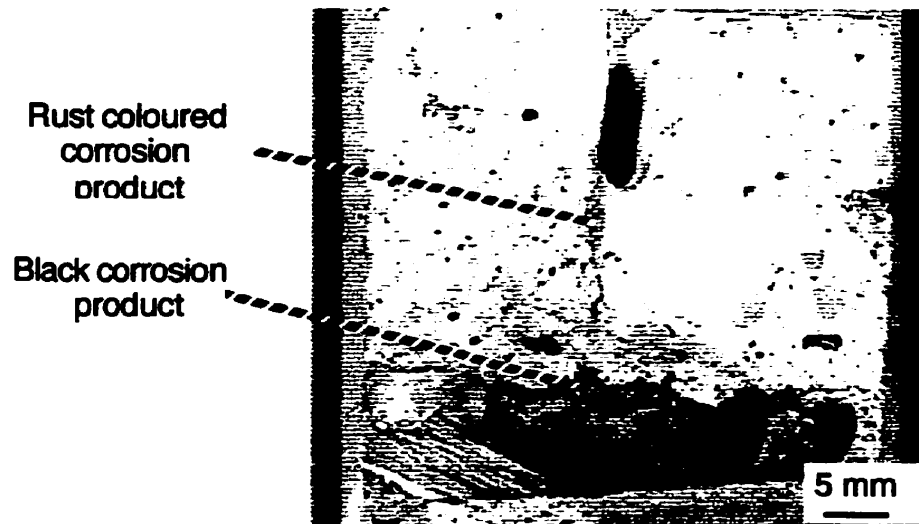
Figure 6.7(a) Cut section of core of industrial standard concrete showing the induced crack and two forms of corrosion: a dense black product adjacent to the steel and a rust coloured product in the crack.
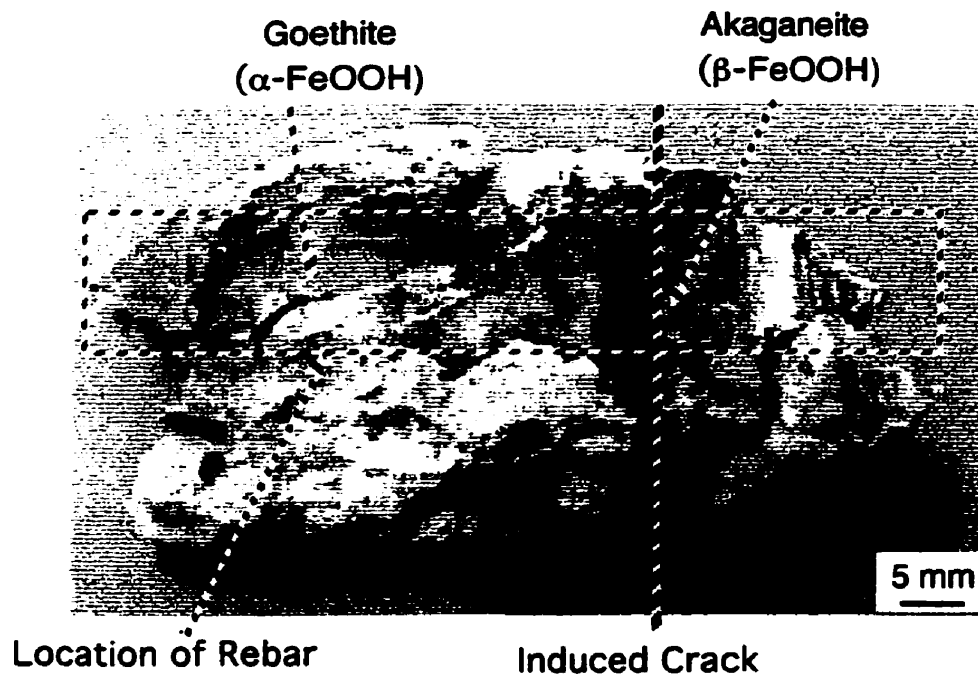
Figure 6.7(b) Fractured section of the HPC adjacent to the rebar showing two types of corrosion product, one dark brown (goethite, α-FeOOH) and the other a "dirty" yellow ochre colour (akaganeite, ß-FeOOH) (Marcotte and Hansson 1998).

6.3.4.2 Appearance and Distribution of Corrosion Products

Table 6.6 details the composition and location of the corrosion products observed in each type of concrete and the technique used to identify the products. All concretes had a dense dark brown to black corrosion product form at the steel/concrete interface but for two of the concretes, the industrial standard and HPC/SF, it was the only product that formed, as shown in Figures 6.7(a) and 6.7(c), respectively. In the industrial standard concrete, this dense, black band of corrosion product was approximately 2 mm thick but only about 300 μm thick in the other concretes. The morphology of this predominantly iron and chlorine-based product after it was prised from the surface of the steel was uniform but appeared porous at higher magnifications (Figure 6.7(d)). A trace amount of rust coloured corrosion product was observed to border the induced crack in the industrial standard concrete while the dark brown to black product plugged the crack in the HPC/SF, as indicated in Figures 6.7(a) and (c).

Figure 6.7(c) Cut section of core of high performance concrete that contains silica fume showing the magnetite (Fe_3O_4) that plugged the induced crack.

223
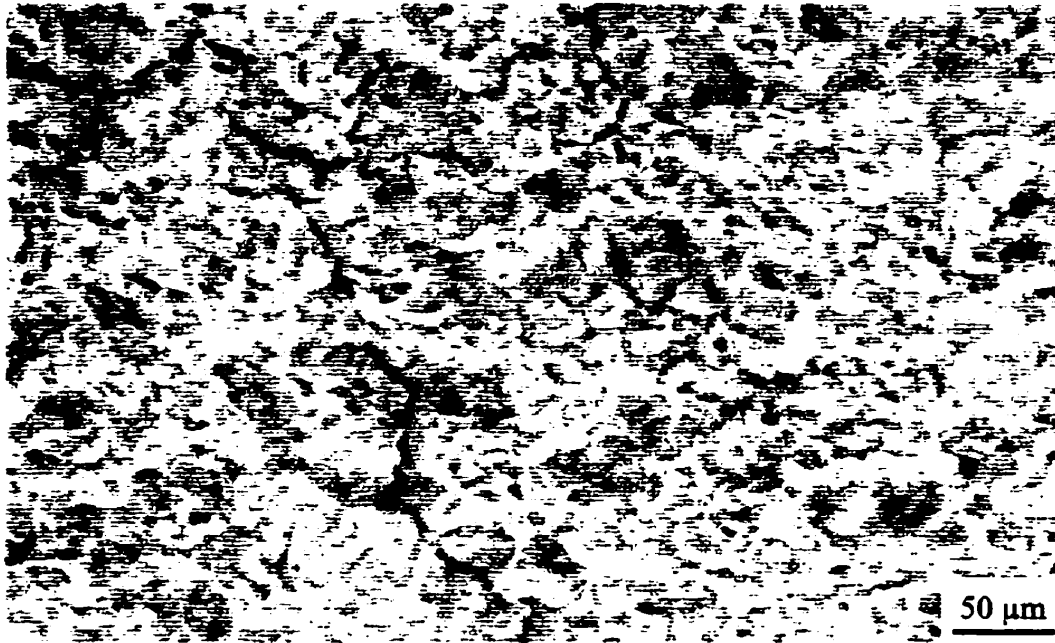
Figure 6.7(d) Black corrosion product observed adjacent to the rebar in the industrial standard concrete.

The elemental composition of the rust-coloured product in the industrial standard concrete could not be determined because it was indistinguishable from its cementitious matrix at high magnifications. However, goethite (α-FeOOH), akaganeite (β-FeOOH), and maghemite (γ-Fe$_2$O$_3$) along with the primary aggregate of the concrete (orthoclase, KAlSi$_3$O$_8$, and albite, NaAlSi$_3$O$_8$) were identified by X-ray diffraction, shown in Figure 6.7(e). Goethite, akaganeite, and other products have been previously observed in concrete (Suda, Misra et al. 1993; Wang and Monteiro 1996) but not maghemite. Since maghemite is an oxygenated form of magnetite (Fe$_3$O$_4$), this product was probably originally magnetite but transformed after limited exposure to the laboratory atmosphere.

224
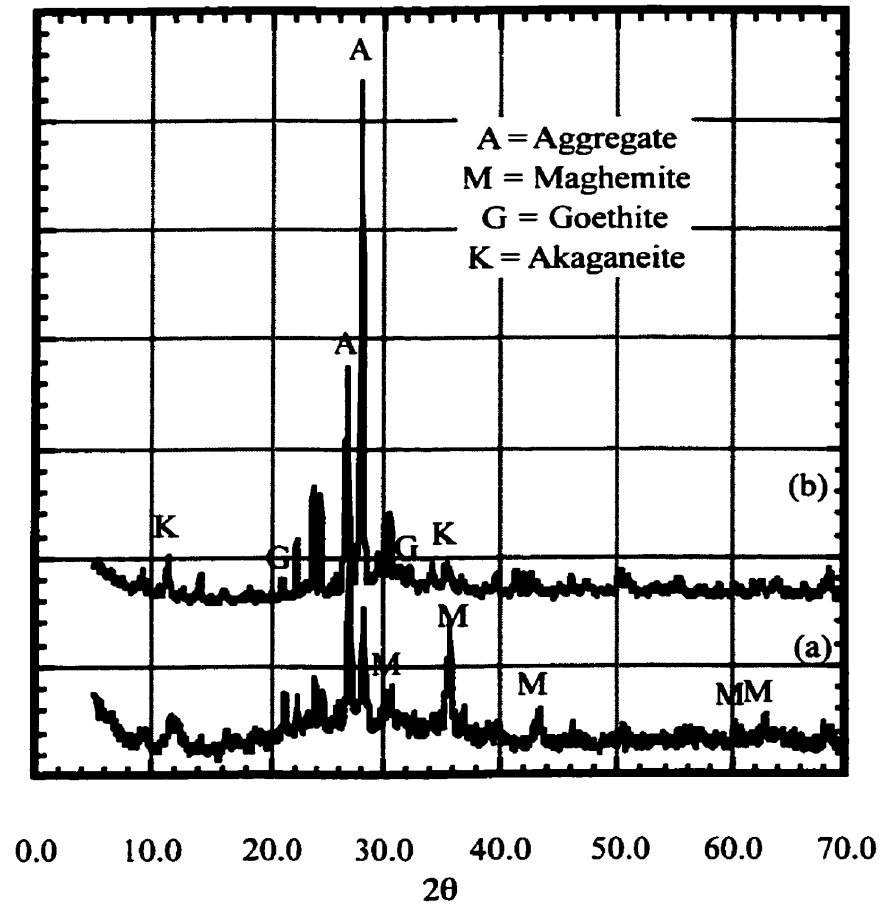
Figure 6.7(e) XRD spectra of the products observed at the steel/concrete interface for (a) industrial standard, and (b) high performance concrete. M = Maghemite, γ-Fe_2O_3; G = Goethite, α-FeOOH; K= Akaganeite, ß-FeOOH; and the main aggregate peaks (A) indicate orthoclase ($KAlSi_3O_8$) and albite ($NaAlSi_3O_8$) (Marcotte and Hansson 1998).

This hypothesis is supported by the analysis of a similar product, identified as magnetite (Fe_3O_4) by Raman spectroscopy, observed in the induced crack region and at the steel/concrete interface of the HPC/SF, shown in Fig. 6.7(f). Upon exposure of this product to the ambient conditions of the laboratory for an extended period (about 1 week), the magnetite at the steel/concrete interface oxidized to hæmatite $(\alpha-Fe_2O_3)$ and goethite $(\alpha-FeOOH)$, as shown in Figure 3.3 (Chapter 3). Maghemite would have been the transition product between the original magnetite and the end product of hæmatite which emphasizes the importance of *in situ* rather than *ex situ* observations of corrosion products, such as the *in situ* work presented in Chapter 4. The magnetite within the induced crack remained relatively unaffected by the week's exposure probably because of the limited surface area of the product within the crack.
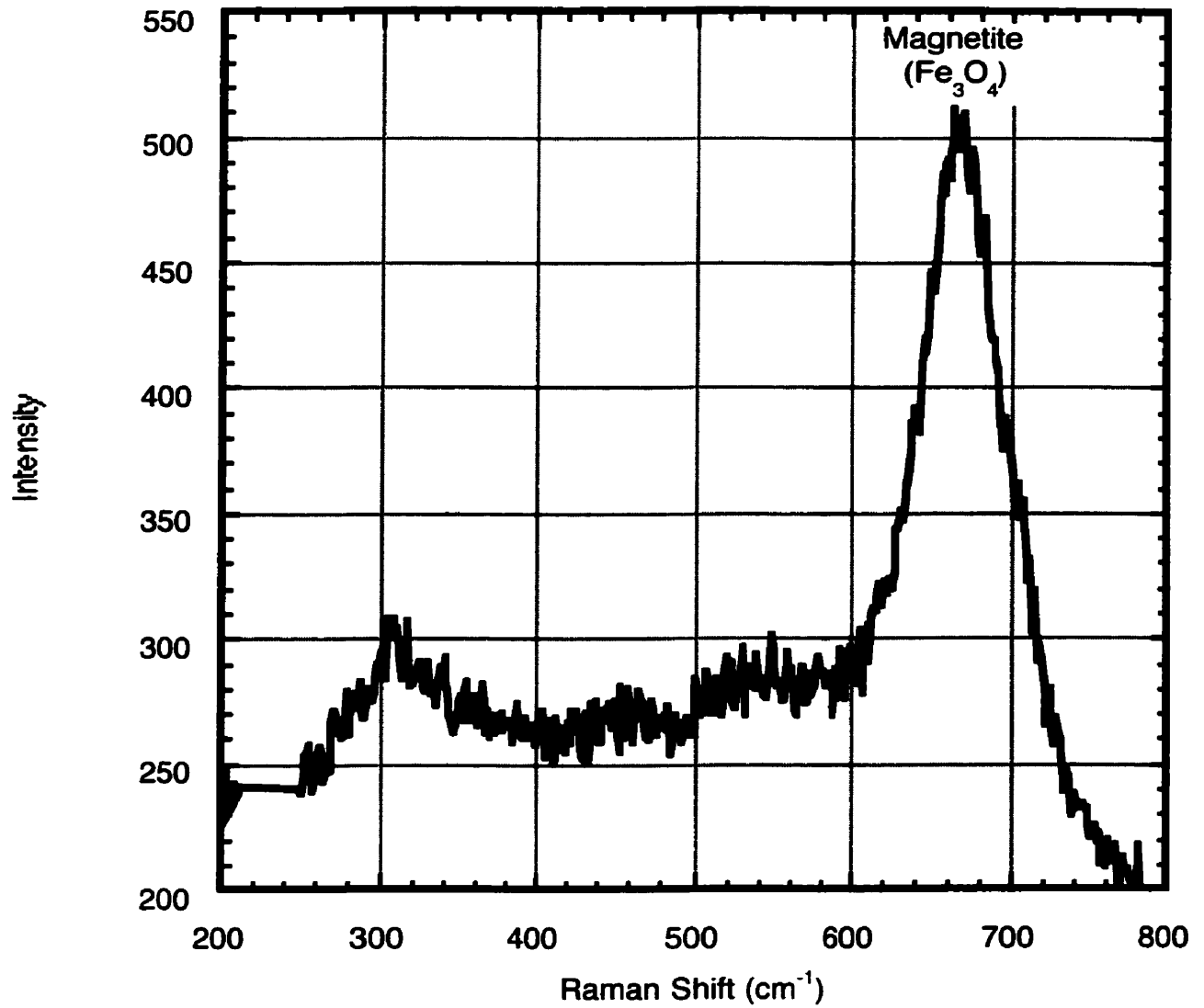
Figure 6.7(f) Raman spectra of the dense, dark brown/black corrosion product observed at the steel/concrete interface which also filled the induced crack of the HPC/SF. This product was predominantly composed of magnetite (Fe_3O_4).

227

High magnification elemental maps of a representative area of this induced crack show that the internal width of the crack was approximately 200 μm and was densely and completely filled with magnetite as evidenced by the iron elemental map, presented by Fig. 6.7(g). In addition, the surfaces of the crack were lined with a magnesium product, presumably from the formation of brucite $(Mg(OH)_2)$ upon exposure to the simulated sea water and prior to the deposition of the corrosion products. No other corrosion products were observed in this concrete.

100 μm
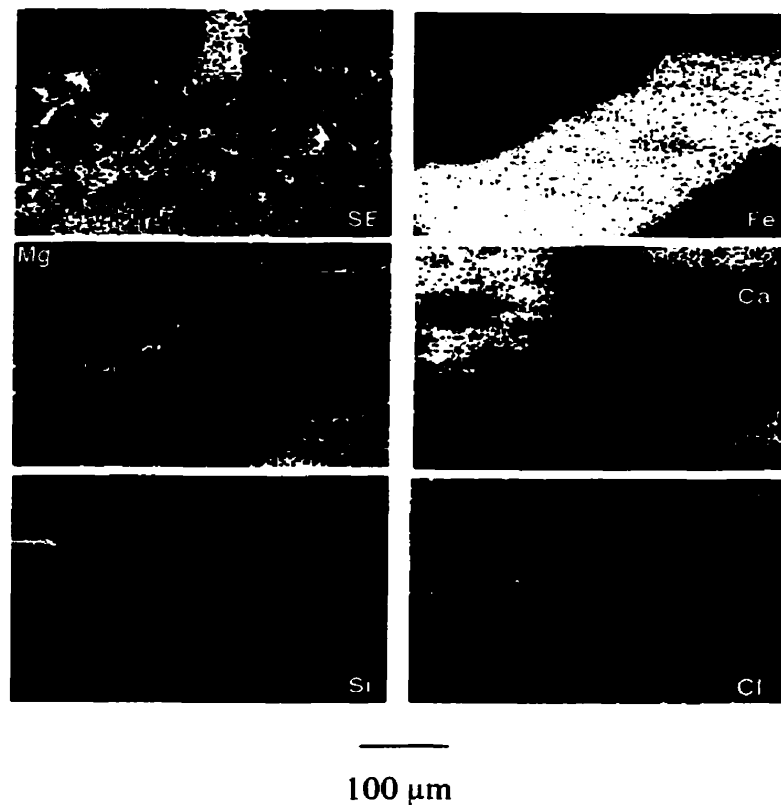
Figure 6.7(g) Secondary electron micrograph (SE) and elemental maps of the induced crack region of the HPC with silica fume indicated in Figure 6.7(c).

228

Unlike the corrosion products observed in the industrial standard concrete or HPC/SF, those observed in the low quality and the high performance concrete did not preferentially accumulate at the steel/concrete interface. Moreover, different corrosion products were identified both by appearance, and X-ray diffraction (Figure 6.7(e)). Within the high performance concrete cover these were: (a) akaganeite (β-FeOOH), which forms only in high chloride concentrations, was the yellow ochre product observed near the induced crack; and (b) goethite (α-FeOOH) was the dark brown corrosion product which formed farther away from the induced crack and was the more dense of the two products. These two products were also identified in the low quality concrete cover, as shown in Figures 6.7(h) and (i). In addition, lepidocrocite (γ-FeOOH), maghemite (γ-Fe_2O_3), and haematite (α-Fe_2O_3) were observed. An ESEM micrograph of the goethite is given in Figure 6.7(j) and shows that some of the product was extremely dense and cracked with very few discernable features. EDS indicated that this product was predominantly iron but also contained calcium, silicon, and chlorine. A second layer of corrosion product consisted of a network of randomly-oriented hexagonal plates, each about 5 μm wide. The crystalline plates contained relatively more calcium and chlorine. The presence of calcium and silicon in these products suggests that the corrosion products are forming within the voids of the cementitious products.
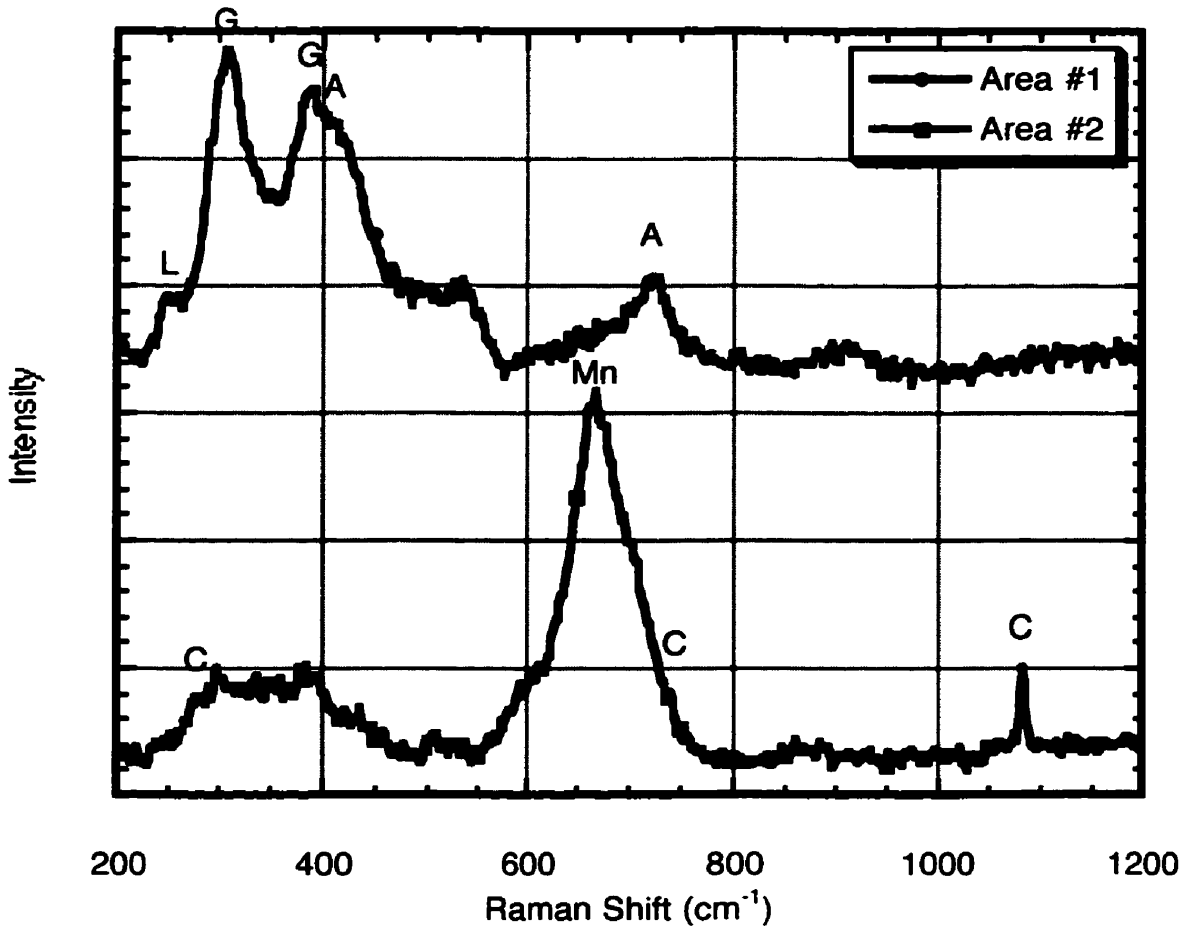
Figure 6.7(h) Raman spectra of the brown/red coloured corrosion products within the low quality concrete cover near the induced crack. Calcite was also detected near the induced crack of this concrete. Mn ≡ Magnetite (Fe_3O_4); A ≡ Akaganeite (β - FeOOH); Mn ≡ Goethite (α - FeOOH); L ≡ Lepidocrocite (γ - FeOOH); C ≡ Calcite ($CaCO_3$)
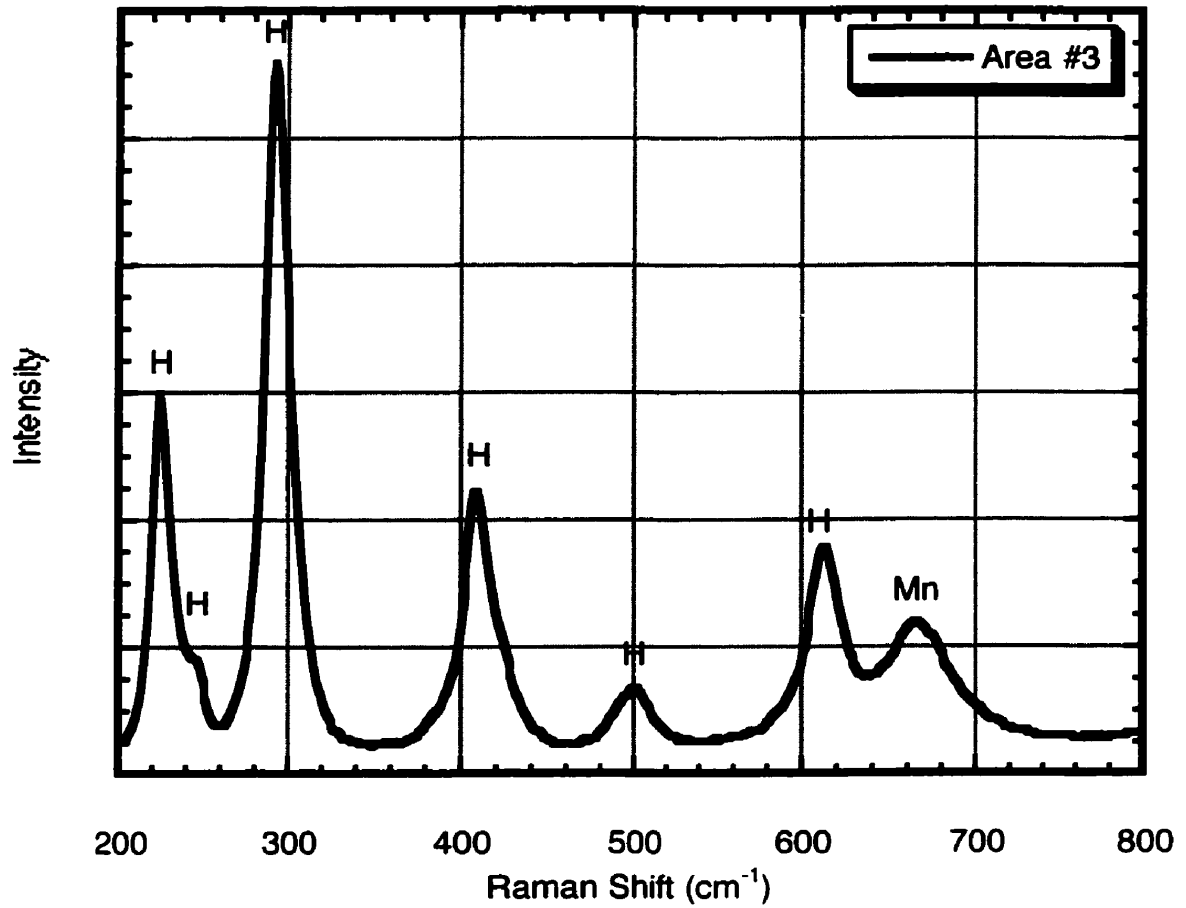
Figure 6.7(i) Raman spectra of the dark brown/red coloured corrosion products within the low quality concrete cover near the induced crack. Mn ≡ **Magnetite** (Fe_3O_4); H ≡ Hæmatite $(\alpha - Fe_2O_3)$

231
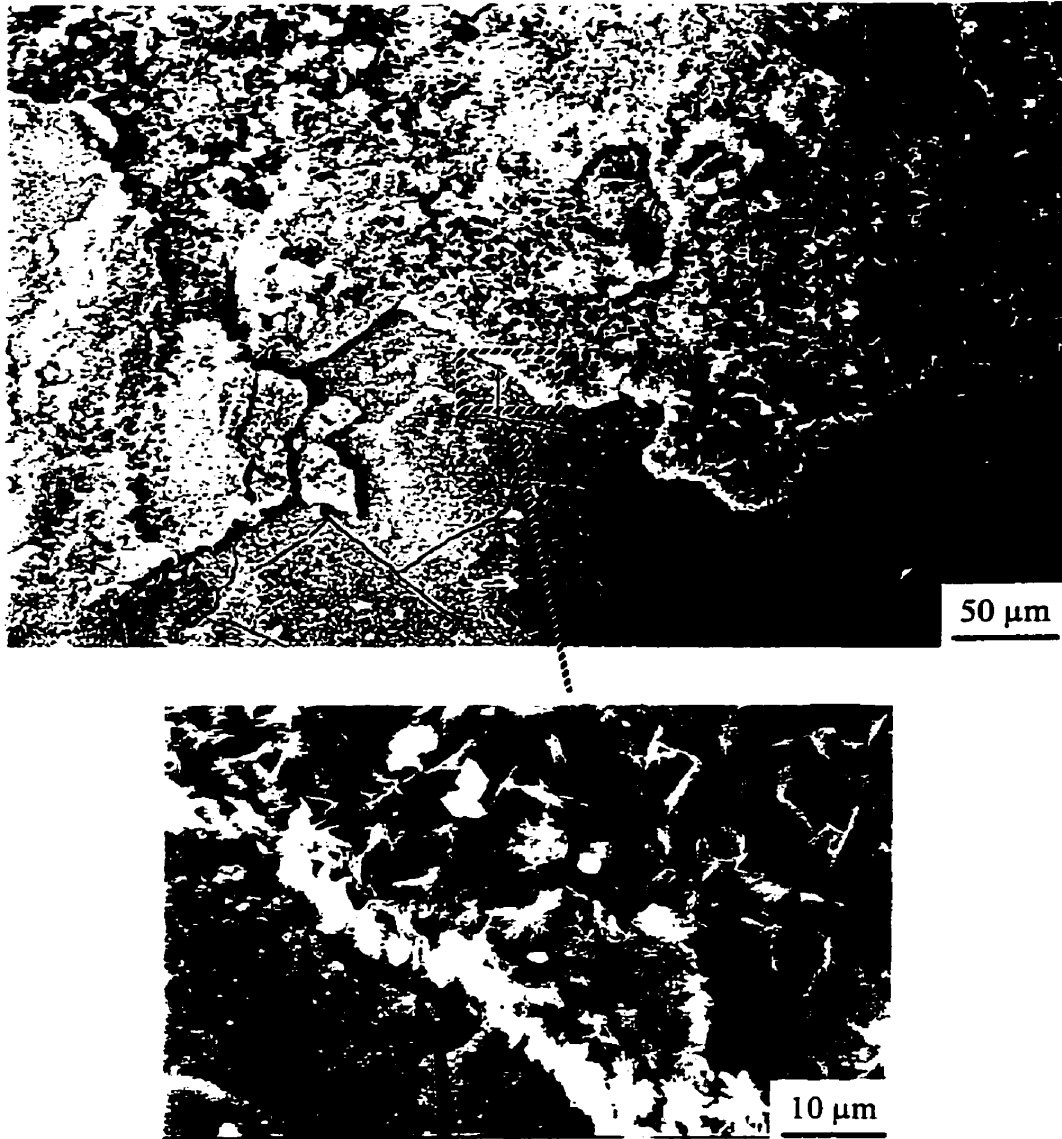
Figure 6.7(j) Micrographs of goethite (α-FeOOH) observed at steel/concrete interface in high performance concrete without silica fume (Marcotte and Hansson 1998).

232

Akaganeite, similar to goethite, was also intimately mixed with the cement paste to the extent that it was largely indistiguishable from the paste at higher magnifications, as shown in Figures 6.7(k) and (l). However, any other corrosion products detected in the low quality concrete with Raman spectroscopy could not be isolated at all because they were not as concentrated in the cover as the akaganeite. Akaganeite was more easily identified by its chemical composition than its morphology except for the iron-rich particles of relatively pure corrosion product such as that labelled "A" in Figures 6(k) and (l). The elemental maps presented in Figure 6.7(m) of this region shows the presence of iron in the surrounding cementitious products which suggests that iron species diffused to form preferentially within the void. The cracking of the matrix surrounding the iron-rich particle in Figure 6.7(l) supports the theory that the expansion of corrosion products due to further oxidation and hydration causes internal tensile stresses within the concrete. It is thought that this particle once filled the void but that the low pressure of the ESEM removed some water from the product and decreased its overall volume. This change again emphasizes the importance of *in situ* observations of corrosion products.
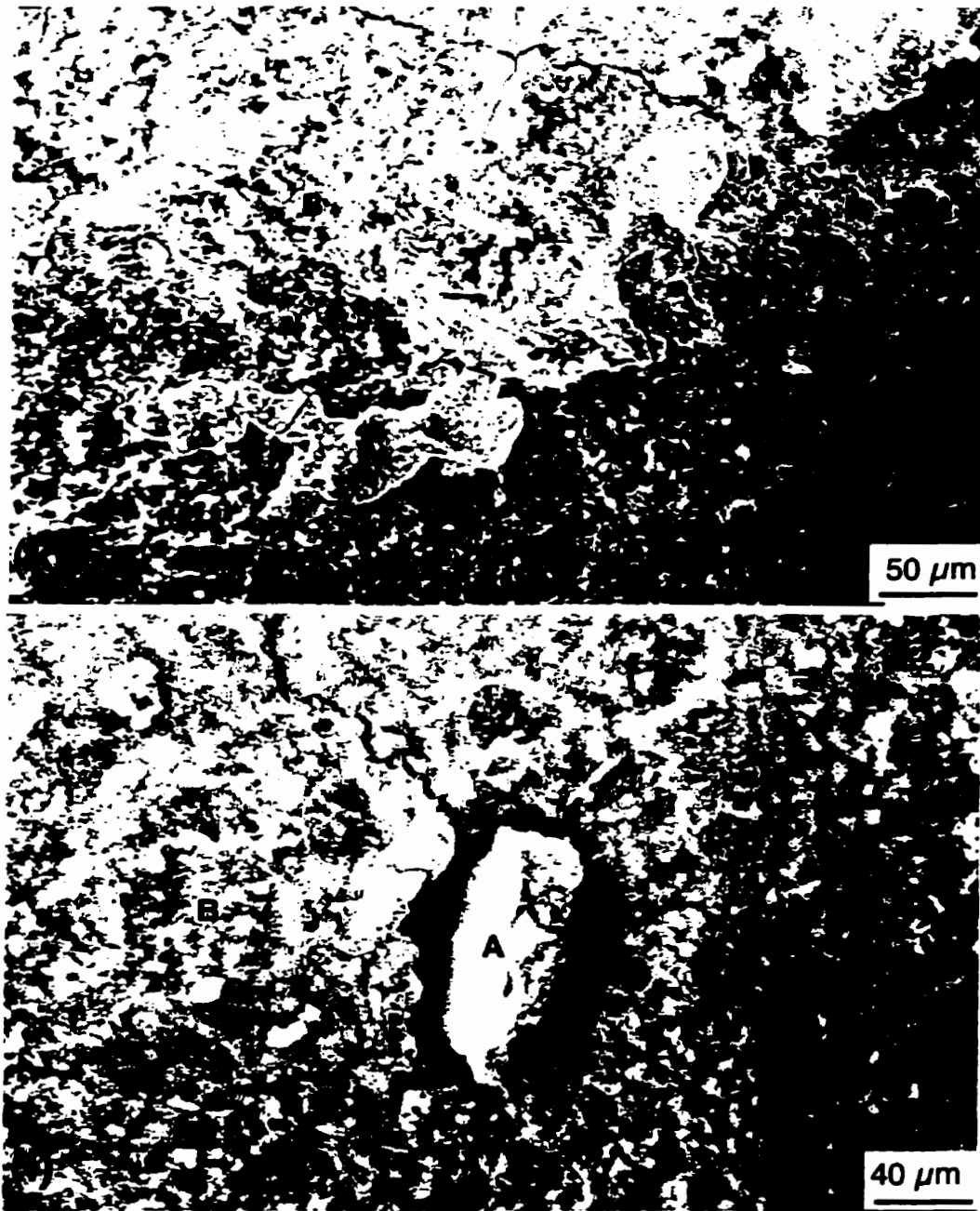
Figures 6.7(k) and (l) Akaganeite (β–FeOOH) in high performance concrete without silica fume. Regions of corrosion product containing approximately 40 at.% Fe are labelled "A" while the surrounding material containing approximately 18 at.% Fe are labelled "B" (Marcotte and Hansson 1998).

234
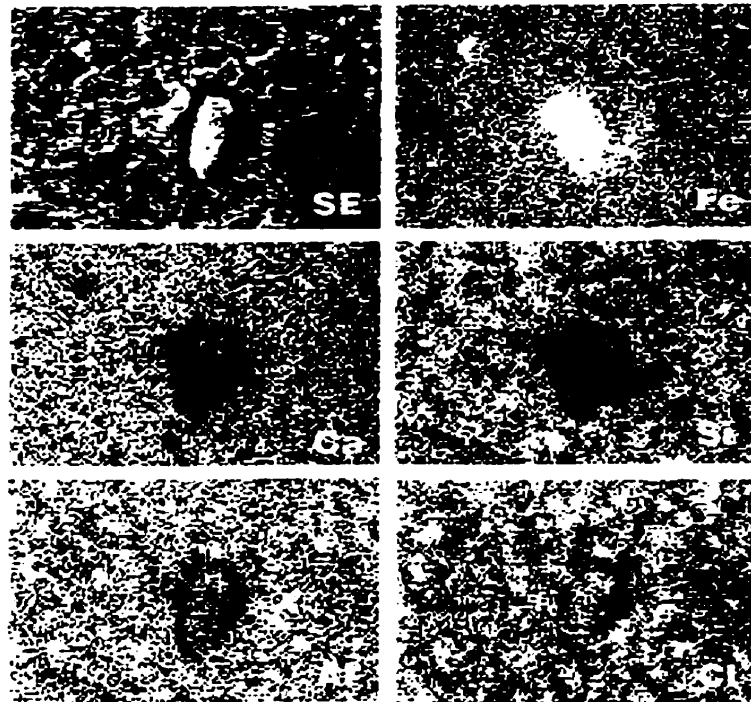
Figure 6.7(m) Elemental map of the embedded corrosion product shown in Figure 6.7(l) (Marcotte and Hansson 1998).

Table 6.6 Summary of the corrosion products observed in each of the concretes.
Akaganeite ≡ β-FeOOH; Goethite ≡ α-FeOOH; Haematite ≡ α-Fe$_2$O$_3$;
Lepidocrocite ≡ γ-FeOOH; Maghemite ≡ g-Fe$_2$O$_3$; Magnetite Fe$_3$O$_4$

Concrete Type	Exposure Age (years)	Analysis Technique	Corrosion Products near or within Induced Crack	Corrosion Products in Unstressed Region
Low Quality	4	Raman	Goethite, Haematite, Lepidocrocite, Maghemite, Magnetite,	none
Industrial Standard	3	XRD	Akageneite, Goethite, Maghemite	none
HPC	3	XRD	Akaganeite, Goethite	none
HPC + Silica Fume	4	Raman	Magnetite*	none

*Magnetite oxidized goethite and haematite upon exposure to air for 1 week

6.3.5 Corrosion Products on the Surface of the Steel

Figures 6.8(a) through (d) show representative pieces of steel that were intersected by the induced crack, or from the central region of the prism for the uncracked low quality concrete. The steel retrieved from the low quality concrete, industrial standard concrete, and HPC showed a relatively uniform distribution of corrosion products while the steel retrieved from the HPC/SF showed an accumulation of corrosion product only where the crack intersected the steel. When these corrosion products were removed, the steel

retrieved from the HPC showed fairly large superficial pits, more wide (e.g., 3 x 9 mm) than deep (approximately 0.7 mm), shown in Figure 6.8(e). The corrosion was located predominantly in the region between the ribs and about 20% of the total surface of the steel was active. It should be noted, however, that these pits are distinct from the fine striations oriented along the length of the bar that were noted at higher magnifications. These striations resulted from the extrusion manufacturing method used to produce the bars. Similar striations were noted on other steel samples as indicated in their respective figures.

In contrast, the ribs were no longer visible on the steel from either the low quality or industrial standard concretes and about 75% or 30% of the surface area was active, respectively, shown in Figures 6.8(f) and (h). At higher magnifications, the steel that was embedded in these concretes was observed to have developed smaller, deeper pits, shown in Fig. 6.8(g) and (i), than the steel in the HPC, Figure 6.8(e).

In further contrast, the steel retrieved from the HPC/SF had only one region of damage, the area where the induced crack intersected the steel, indicated as "C" in Figure 6.8(j). This region (approximately 3 x 12 mm) represented only about 5% of the total surface of the steel but was much deeper (approximately 2 mm) and appeared as if the corrosion process was cutting this steel like a knife.

These pit geometries are summarized in Table 6.7 along with an estimate of the cross-sectional area of the steel that has been destroyed by the corrosion process. According to reinforced concrete repair authorities (e.g., Emmons 1993), a loss of 25% to the cross-sectional area of a reinforcing steel bar requires that the bar be supplemented with new bars. This value does not include deep, localized corrosion pits that would not be resolvable with the unaided eye and, therefore may underestimate the actual loss of cross-section. With this criterion, the steel in the low quality concrete would require additional reinforcement likely because of the relatively open pore structure (w/cm of 0.5) and corresponding low electrical resistivity of the concrete, as shown in Table 6.2. All

other cross-sectional losses are within acceptable limits which is expected for these commonly used commercial reinforced concrete mixes.

However, the steel retrieved from the HPC/SF suffered the deepest damage of these mixes, and potentially the highest degree of damage overall because the rebar might be severed upon continue exposure and suggests that the presence of high concrete electrical resistivities can also have negative consequences. Using the approximate pit dimensions from Table 6.7, the previously presented mean corrosion rates of steel in cracked prisms (Figure 6.5(c)) can be corrected for the macroscopic area of the steel actually corroding, as shown in Figure 6.8(k). Once these corrections have been performed, the relationships between the corrosion rates change: where the corrosion rates of both high performance concretes were once the lowest, their rates now exceed the steel samples in the low quality and one of the industrial standard specimens by almost one order of magnitude. Presumably, higher electrical resistivities do not allow large distances to occur between the cathodes and anodes on the surface of the steel which localizes any macrocell corrosion attack and emphasises the role of microcell corrosion (where the anodic and cathodic half cell reactions take place at essentially the same location). Thus, cracked concrete with a high electrical resistivity could potentially suffer corrosion with consequences as severe as those for low quality concrete. Under these circumstances, the type and distribution of the corrosion products and whether they fill the cracks, in combination with the tensile strength of the concrete, would govern the long-term durability of these concretes. This type of result also underscores the difficulty in making valid corrosion rate measurements when the area of the corroding region cannot be known or even estimated non-destructively.
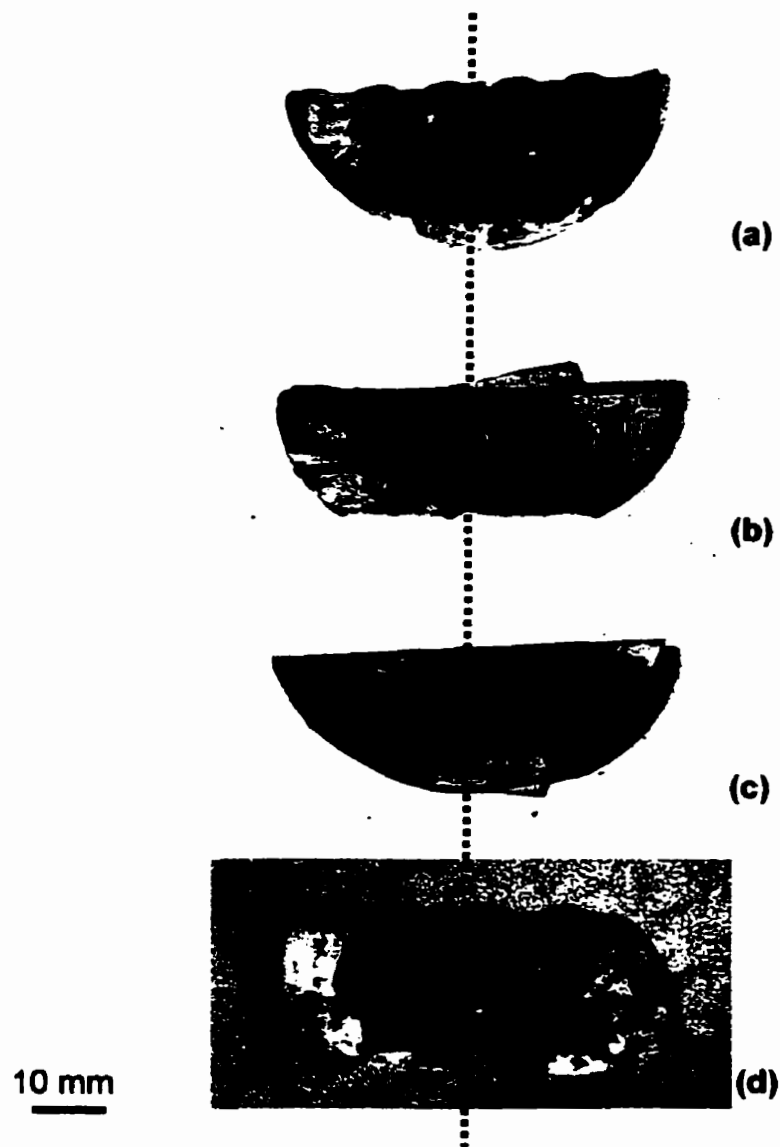
Figures 6.8(a), (b), (c), and (d) Photographs of the steel retrieved from (a) low quality concrete, (b) industrial standard concrete, (c) high performance concrete, and (d) high performance concrete with silica fume.
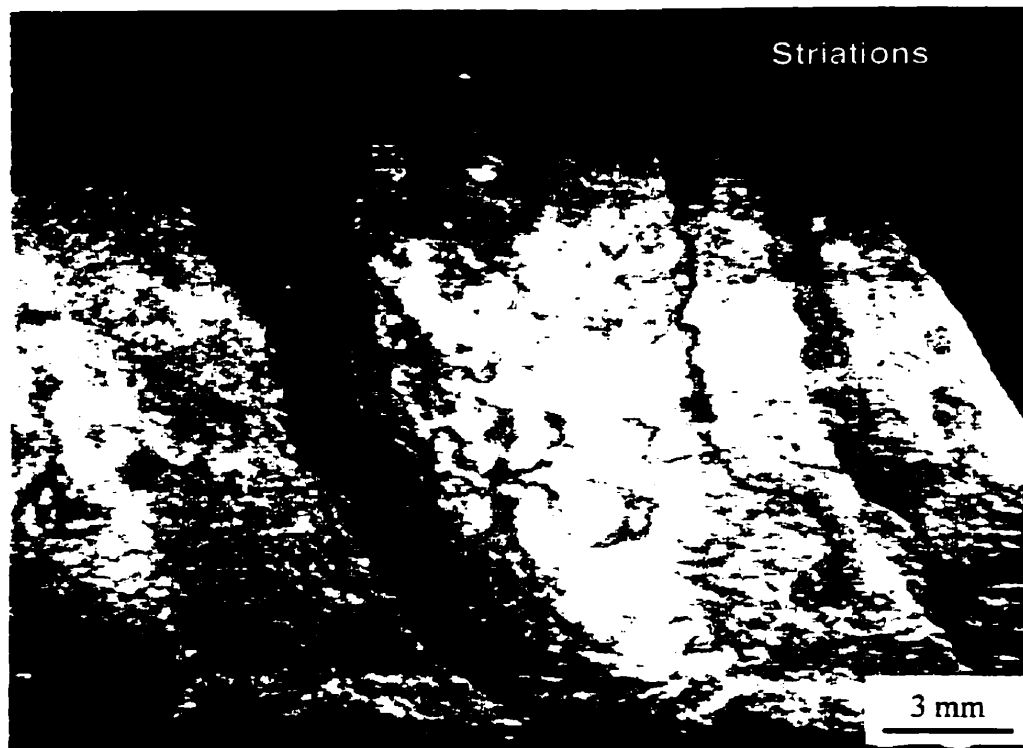
Figure 6.8(e) Macrophotograph of surface of steel from the induced crack region of the high performance concrete without silica fume after the removal of the corrosion products (Marcotte and Hansson 1998).

240
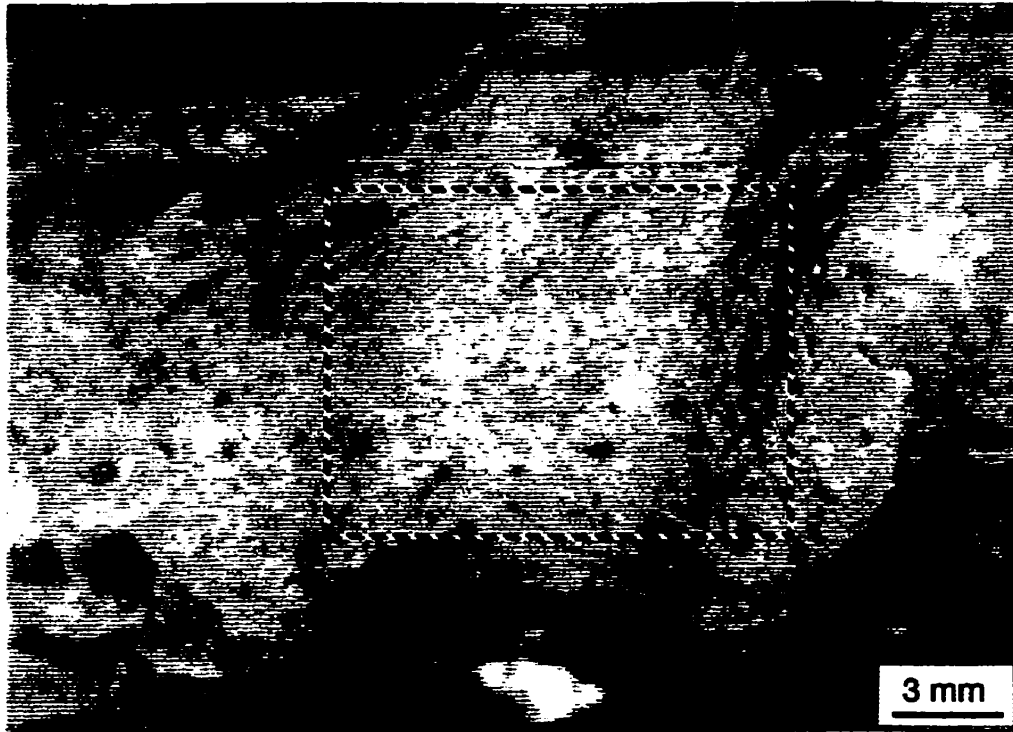
Figure 6.8(f) Macrophotograph of the surface of the steel from the induced crack region of the low quality concrete after the removal of the corrosion products.
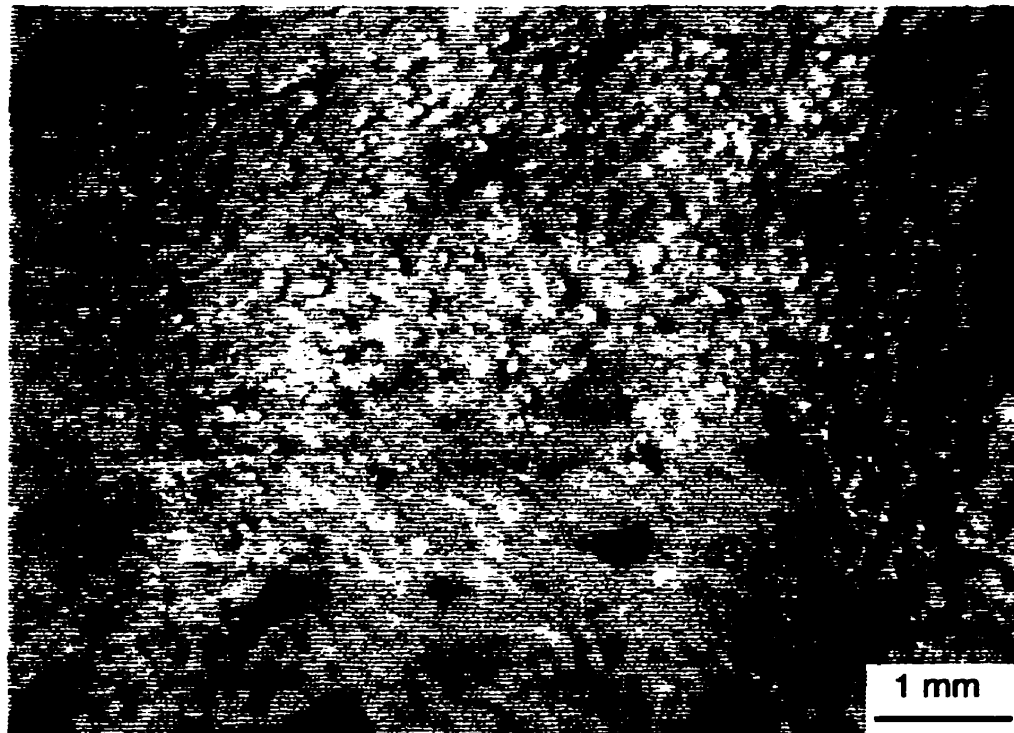
Figure 6.8(g) Higher magnification macrophotograph of the steel retrieved from the low quality concrete after the removal of the corrosion products.
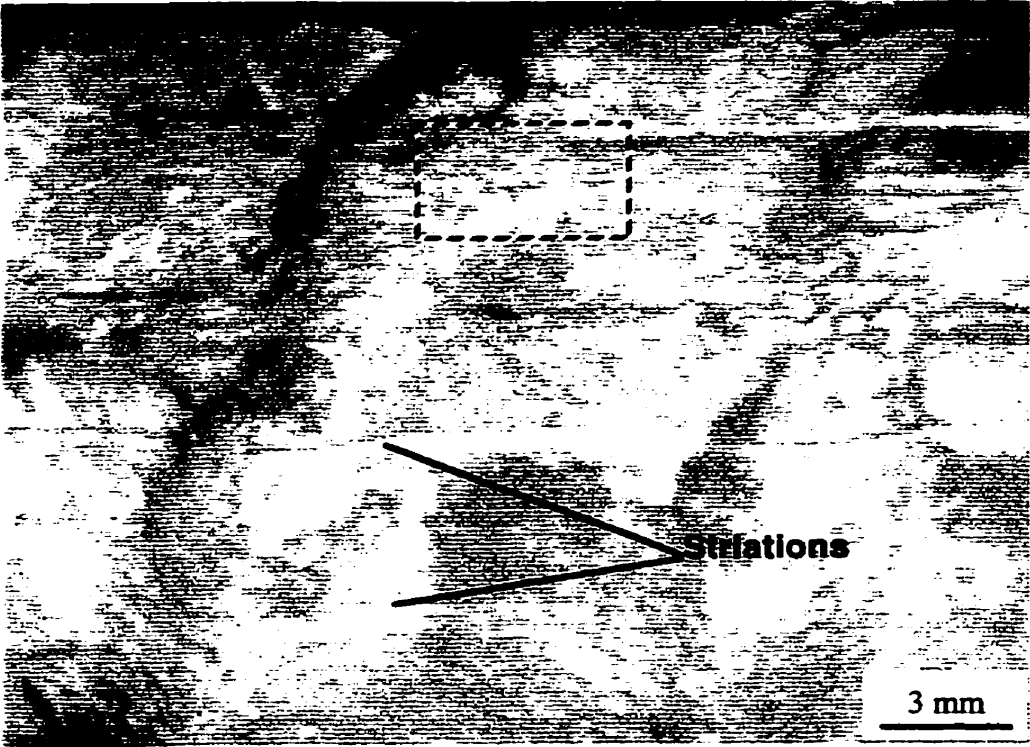
Figure 6.8(h) Macrophotograph of surface of steel from industrial quality concrete.
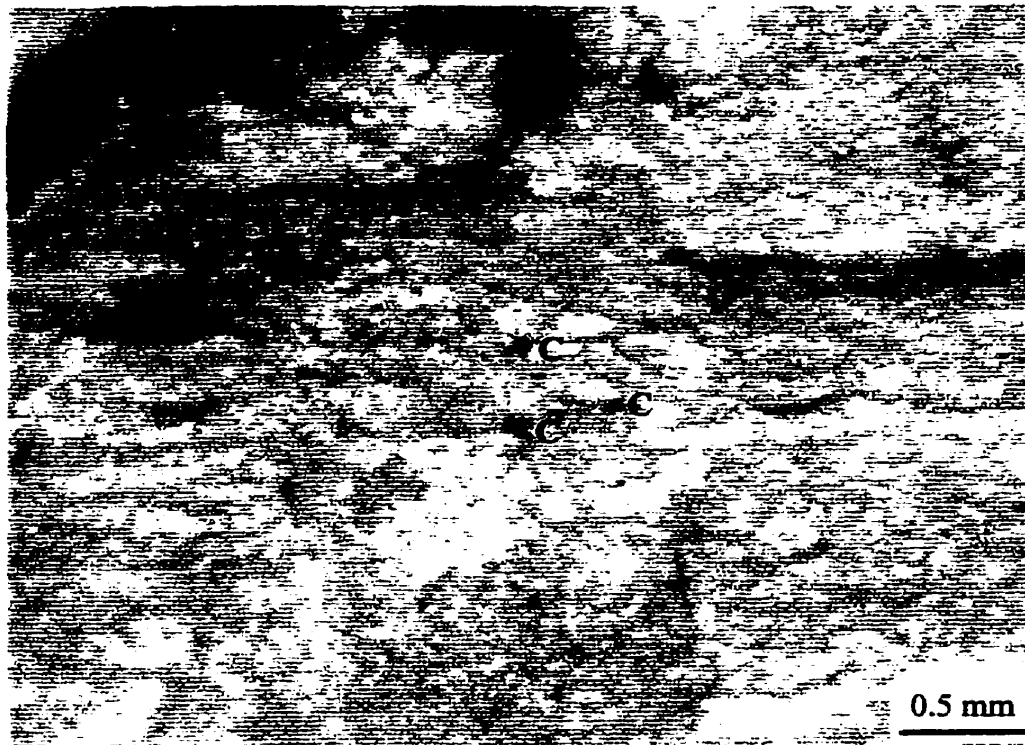
Figure 6.8(i) Enlargement of area shown in Figure 6.8(h). Small perforations are labelled "C"(Marcotte and Hansson 1998).
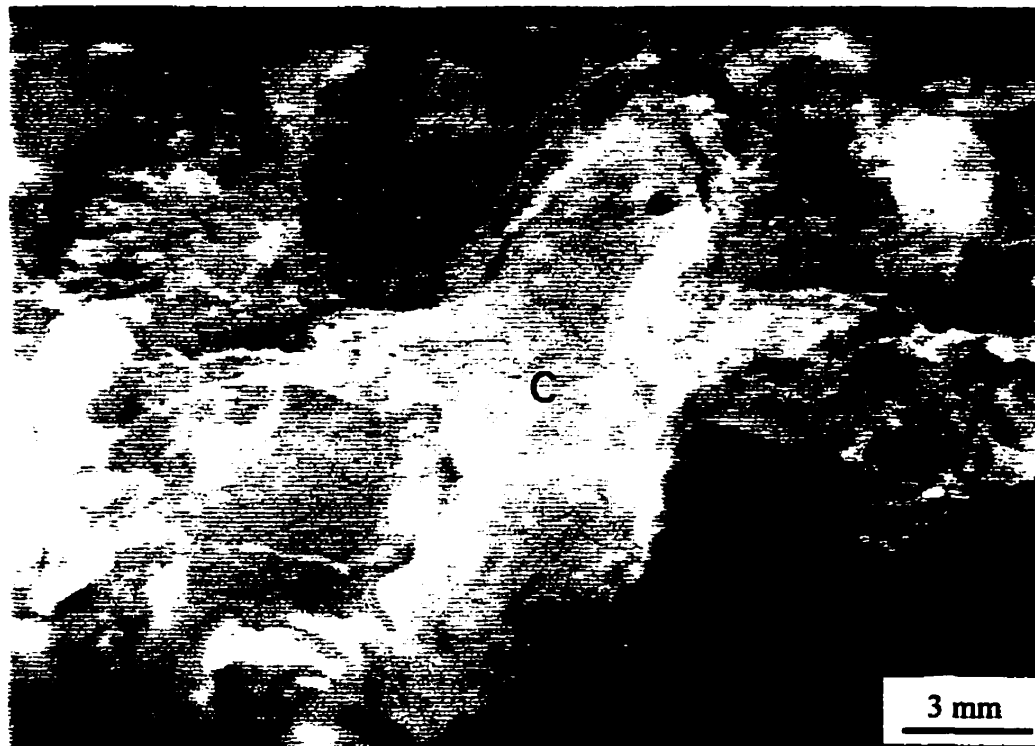
Figure 6.8(j) Macrophotograph of surface of steel from high performance concrete with silica fume. The area of deeper corrosion damage is indicated by "C".

Table 6.7 Comparison of the corrosion damage according to concrete type.

Concrete Type	Approximate Pit Dimensions*	Approximate Pit Depth (mm)	Estimate of Lost Steel Cross-sectional Area
Low Quality	75% of entire surface	1.5*	30%
Industrial Standard	30% of entire surface	1.0*	8%
HPC	3 x 9 mm	0.9	8%
HPC/SF	3 x 12 mm	2.0	14%

* Does not include those pits unresolvable with the unaided eye.

245
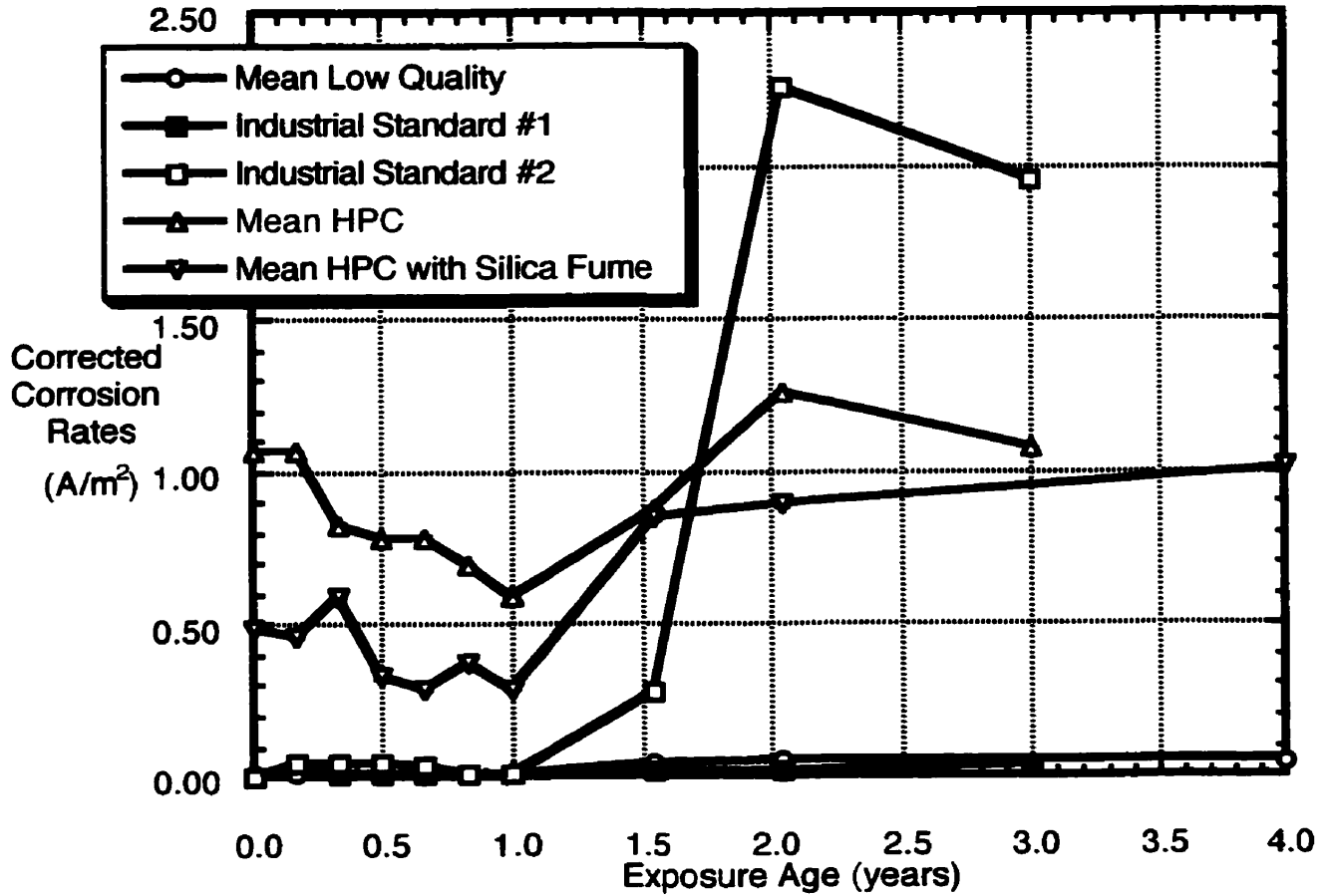
Figure 6.8(k) Comparison of the corrected mean corrosion rates of steel probes intersected by the crack which were calculated using the corroded area of the steel. Note: Bars indicating the range of values were applied to these data but are too small to be observed in this figure.

6.4 DISCUSSION

6.4.1 Effect of an Induced Crack on Chloride-Induced Corrosion

In general, the presence of a crack has a deleterious effect on reinforced concrete because if the concrete remained unstressed (i.e., without an induced crack--the only cracks present occurred naturally within the concrete microstructure), the corrosion rate remained relatively low, no corrosion products were observed at the steel/concrete interface or elsewhere within the cover, and chlorides were not detected. When cracked, however, corrosion products and critical levels of chlorides were detected along with moderate to severe damage to the reinforcing steel. This impact of the crack varied according to concrete type and is discussed in Section 6.4.3. The effect on corrosion rates was counteracted to some degree by the formation of corrosion products that effectively plugged the induced crack and any other convenient paths to the reinforcing steel as shown by the decrease in the corrosion rates of the reinforcing steel in both the low quality and the industrial standard concretes. This effect is anticipated to be only temporary as continued corrosion would likely generate excessive internal tensile stresses that would crack the concrete further. The presence of silica fume in the HPC/SF also reduced the effect of the induced crack and is discussed in greater detail in Section 6.4.2.

6.4.2 Effect of Silica Fume on Chloride-Induced Corrosion

The reaction of silica fume had the anticipated effect on the electrical and microstructural characteristics of high performance concrete which was shown by its high electrical resistivity presented in Table 6.2 corresponding to the decrease in the size and the number of continuous pores, shown by Figure 6.6(h). This had a strong impact on its ability to resist ingressing chlorides: the concrete with silica fume near the induced crack had a chloride concentration only about 7% of that in the cracked region of the sample without

247

silica fume even after an extra year of exposure to the simulated sea water. Overall, the presence of silica fume mitigated the effect of the crack by reducing the size and number of continuous capillary pores in the HPC/SF once the cracked region was exposed to the simulated sea water.

In spite of these enhanced properties, corrosion did initiate in the cracked region of concrete with silica fume. Although the chloride content was very low in the 10 mm layer of concrete adjacent to the induced crack, those that were present were concentrated very close to the induced crack surface, as indicated in Table 6.5 and Figure 6.5. There may also been a reduction in the chloride threshold value by a lower pH of the pore solution due to reaction of the silica fume and, at the early stages, by the limited degree of cement hydration.

The resulting corrosion products that formed in the HPC/SF were entirely different from the products that formed in the HPC. In addition, the corrosion product in the HPC/SF was confined to the space provided by the induced crack and the steel/concrete interface, while corrosion products in the HPC were more uniformly spread throughout the concrete cover and not confined to either the steel/concrete interface or the main crack. Moreover, while the corrosion products that formed in the HPC cover (approximately 5 mm from the steel/concrete interface) appeared to have cracked the concrete, as shown in Figure 6.7(l), there was no such cracking in the HPC/SF. This indicates that the pozzolanic reaction of the silica fume in the HPC/SF had two main effects: (a) it sufficiently densified and strengthened the concrete such that damage was reduced; and (b) the reaction occurred before any corrosion products could diffuse into the concrete cover and any that were present were confined to the induced crack (i.e., the observed magnetite (Fe_3O_4)). The latter effect suggests that any corrosion products forming in the silica fume concrete would plug the crack, effectively barring further direct chloride and oxygen exposure to the surface of the steel. The fact that magnetite formed (i.e., a corrosion product which forms in

oxygen deprived conditions) supports this conclusion. Thus, the pozzolanic reaction of silica fume densified the concrete and reduced the exposure of the steel to chlorides and oxygen by the formation of corrosion products which resulted in the low corrosion rates that were observed over a four year period.

This may have a potential drawback, however. The more uniform, superficial damage to the steel within the HPC without silica fume shown in Figure 6.8(e) may be preferable to the localized damage resulting from the presence of silica fume in the HPC/SF shown in Figure 6.8(j). It is possible, however, that the damage observed on the surface of the steel was the most that was to occur and that if the prisms had remained uncored, the corrosion rate may have decreased even further over time due to the plugged crack. The reduction of the corrosion rate in the first year of exposure as well as the further decrease in the corrosion rate at about three years in the unstressed industrial standard concrete presented in Figure 6.5(b) supports this hypothesis.

6.4.3 Effect of Concrete Type on Chloride-Induced Corrosion

A comparison of the corrosion rates measured for each concrete type for up to four years (Figure 6.5(c)) suggests that the embedded steel that is corroding the fastest should theoretically have the greatest volume of corrosion products at the steel/concrete interface or within the concrete cover. This theory was confirmed by the steel embedded in the industrial standard concrete which had the highest corrosion rate after three year's exposure and generated the largest magnetite corrosion layer of all observed, approximately 2 mm thick. This product has an estimated specific volume of 2.1 (from Figure 2.6, Chapter 2). In addition, the embedded steel with the second highest corrosion rate from the low quality concrete contained the broadest range of corrosion products within the concrete cover with specific volumes ranging from 2.2 to 3.5. These values are considerably lower than those generally assumed in theoretical service life models. It is possible, however, that with

continued exposure to chlorides or different exposure conditions where the concrete undergoes wet and dry cycling that higher volume expansions might have been noted. Thus, the evaluation of corrosion products in a theoretical model must also include a prediction of the service conditions.

While corrosion products in the industrial standard and HPC/SF concrete were confined mainly to the steel/concrete interface and induced crack, those in the low quality concrete and HPC were more uniformly spread throughout the concrete cover and not confined to either the steel/concrete interface or the main crack. Two possible explanations for this difference include: (a) the low quality concrete and HPC contains a higher proportion of "mini-cracks" and voids (less than approximately 0.3 mm) and, therefore, the corrosion products can more easily diffuse away from the steel/concrete interface; and (b) the formation of corrosion products causes any microcracks in the HPC or voids in the low quality concrete to open further. Although these microcracks and voids filled with corrosion products could not be directly confirmed with the MIP measurements of Section 6.3.3, their presence was supported by the poor cohesion of the cores that were taken from the induced crack region of these two concretes while the corresponding cores taken from the ends of the prisms were intact.

The presence of a network of cracks and voids in the HPC or low quality concrete would allow more oxygen to be available at the steel/concrete interface in these concretes rather than in the industrial standard concrete and HPC/SF. Since maghemite (γ-Fe_2O_3) and magnetite (Fe_3O_4) were detected only at the steel/concrete interface of the industrial standard concrete (Figure 6.7(e)) and the HPC/SF (Figure 6.7(f)), it is likely that corrosion processes occurring on the steel in these concretes were oxygen deprived.

A comparison of the measured corrosion current densities shows that oxygen deprivation is not limiting the corrosion activity of the steel in the industrial standard concrete, however, as its corrosion rate is at least 10-20 times higher than that of the steel in

both types of high performance concrete (Figure 6.5(c)). Instead, it supports the hypothesis that the higher proportion of fine cracks within the HPC allowed corrosion products to diffuse away from the steel/concrete interface and effectively block these paths of ingress from further chlorides and oxygen. The microcracks within the HPC/SF were blocked by the continued hydration and pozzolanic reastions that are described in Section 6.4.2. This is consistent with previously published findings which showed that the steel within both high performance concretes initially was corroding at higher rates than the steel within the low quality and industrial standard concretes but eventually this relationship reversed (Weiermair, Hansson et al. 1995). The initially higher rates for steel in HPC and HPC/SF were attributed the differences in microcracking, ongoing hydration reactions, and differences in the pore structure and pore solution pH that would have affected the nature and extent of capillary suction and the development of passivity. These processes may also have subsequently reduced the corrosion rate in a manner similar to autogenous healing. It remains unclear whether the formation of more corrosion products could cause any microcracks to open further given sufficient time. The cracks emanating from the corrosion particle in Figure 6.7(l) indicate this to be the case.

6.4.4 Relationship between Concrete Quality and Service Life

It is clear from the aforementioned descriptions and analyses of corrosion rates, corrosion products, and materials properties, that quantifying the effect of concrete quality in theoretical service life models is complex. Once active corrosion has initiated, an extended service life results from the capability of the concrete to minimize the corrosion rate, and withstand the damage that occurs from the formation of corrosion products. To minimize the corrosion rate, concretes that have high electrical resistivities and reduced chloride and oxygen diffusivities will theoretically perform best with time. These characteristics were demonstrated by the HPC/SF and it did have the lowest corrosion rate by almost two

orders of magnitude over the four year monitoring period. Provided the tensile strength of the concrete is sufficient, this concrete is the most durable of all. The only possible detrimental consequence was the increased localization of the corrosion activity. In practice, it, therefore, suggests that this type of concrete requires a regular maintenance schedule to seal any structural cracks such that the optimal properties of this concrete can be realized.

A low corrosion rate is not all that is necessary, however, to ensure an extended service life as the type and distribution of the corrosion products influences the long term durability of the concrete. Theoretically, the formation of dense corrosion products such as magnetite (Fe_3O_4) that cover the reinforcing steel under attack could reduce the corrosion rate by barring the ingress of water and chlorides to the corroding area. This type of corrosion product has the least volume expansion of all observed corrosion products, as shown in Figure 2.6 (Chapter 2), and would, therefore, minimize the internal tensile stresses that crack the concrete. Although it was observed in all concretes, only the industrial standard and HPC/SF had a sufficiently restricted pore network and minimal voids to resists the diffusion of iron species and the subsequent formation of corrosion products within the concrete cover. The products formed within the concrete cover where there was greater access to oxygen and water and as a result, larger volumes of corrosion products formed that will eventually crack the concrete cover. Although these products can plug the pore network and reduce the corrosion rate, the industrial standard concrete demonstrated that the formation of a dense corrosion product does not guarantee a low corrosion rate. Overall it is clear that the most durable structural concrete will confine the corrosion products thereby restricting access to water and oxygen and limiting any destructive volume expansion, and have a low corrosion rate.

These characteristics are summarized in Figure 6.9, a modification of Figure 6.1, which shows a comparison between the corrosion process that occurs in cracked industrial

standard concrete (normal quality) versus the relatively ideal behaviour of the HPC/SF (high quality). This figure details the relationship between the damage accomodated in the concrete up to an unacceptable level with the corresponding corrosion rate for both types of concrete.

Initially, there is a measurable corrosion rate as steady-state conditions are established in the area of the steel where the concrete is cracked. The corrosion rate of the steel within the HPC/SF is relatively high for the reasons described in Section 6.3.1. However, the corrosion rate decreases over time as the hydration and pozzolanic reactions continue and the formation of dense corrosion products forms a chemical and physical barrier to further ingress of chlorides and oxygen. This decrease is not observed in the industrial standard concrete because its relatively more open pore structure allows easier chloride and oxygen ingress.
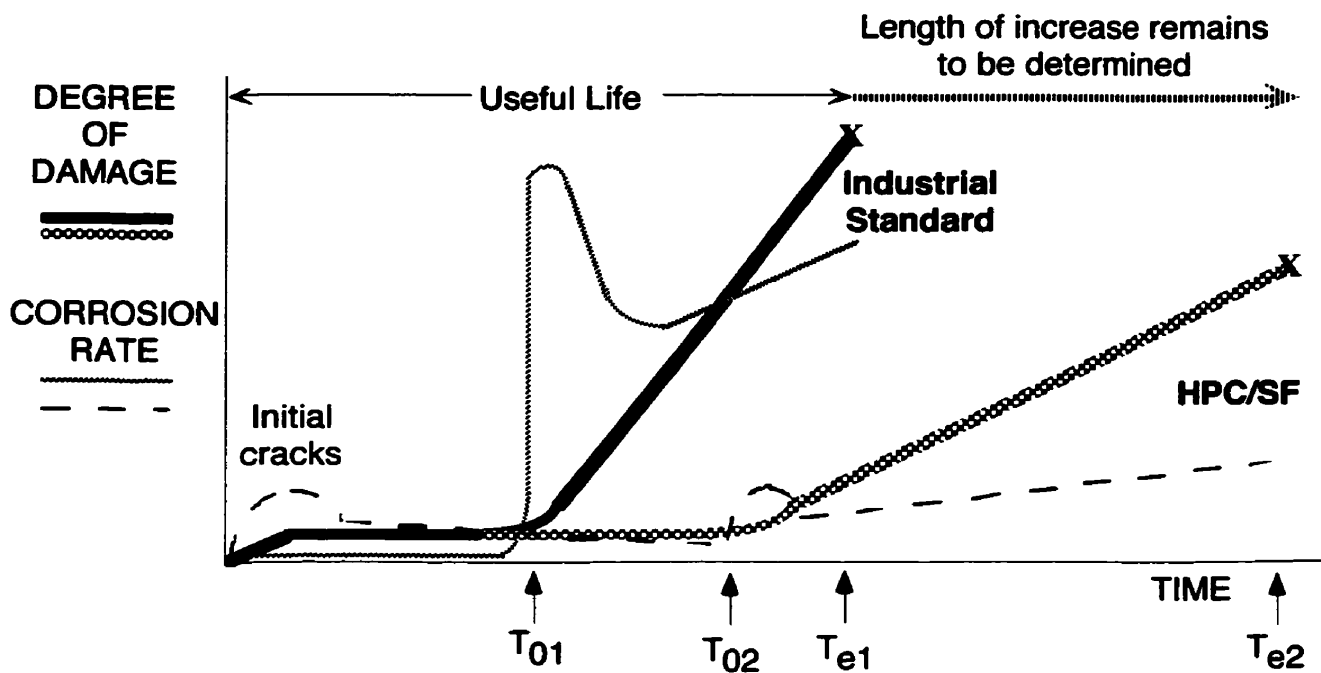
Figure 6.9 Schematic illustration of the relationship between corrosion rate of the embedded steel and degree of concrete damage for structural concrete. $T_{0(x)}$ is the initiation time for the onset of corrosion and $T_{e(x)}$ is the end of practical service life.

Over time, a critical volume of corrosion products forms that cannot be accommodated by the concrete cover. The corresponding tensile stresses crack the cover which allows chlorides and oxygen easier access to the reinforcing steel. This effect can be counteracted again by the formation of more corrosion products but it is unlikely that the former, lower corrosion rate would be restored. This was directly observed in the industrial standard concrete as shown in Figure 6.5(c). The concretes would eventually require repair as the formation of new corrosion products cannot be accommodated indefinitely and the formation of new cracks would accelerate the corrosion process. Overall, it is likely that the high electrical resistivity of the HPC/SF would reduce the corrosion rate for a significantly longer period of time and delay the need for repair. The length of this increase remains to be determined through the evaluation of field structures and long-term laboratory experiments. The conclusions of this thesis have established the relationships amongst the concrete mixes and provide a basis for further investigation.

6.5 CONCLUSIONS

1. In general, the observed behaviour of high performance concrete with respect to industrial standard concrete is not exactly as anticipated. Premature corrosion of steel in HPC had been observed--albeit at a low rate. These rates appeared to be less significant with time, however, as the corrosion rates of the industrial standard and low quality concrete increased. Once all these rates were corrected for the area of steel actually corroding, however, the steel in cracked specimens of both high performance concretes had local corrosion rates that were almost one magnitude higher than their presumably "lower quality" counterparts but the corrosion was confined to highly localized areas. Thus, corrosion occurring in cracked high performance

concretes is potentially more insidious and destructive because corrosion rate measurements will be underestimated by non-destructive techniques such as LPR. On the other hand, corrosion rates may be reduced if any cracks are plugged either by secondary hydration reactions or stable, dense corrosion products such as magnetite (Fe_3O_4).

2. A range of corrosion products was observed to form with estimated specific volumes of 2.2 to 3.5. These values are lower than that usually assumed in theoretical service life models (i.e., 6-7) and these models should be altered to reflect the lower volumes for the experimental conditions studied. However, if the concrete were exposed to different conditions (e.g., longer exposure periods, wet/dry cycling), corrosion products with a larger specific volumes might form. This possibility needs to be determined empirically.

3. Despite the higher compressive strength of the HPC, its lower toughness was illustrated by the inability to produce an intact core and by the cracking observed within the cover from the formation of corrosion products. Concurrently, the presence of silica fume appears to increase the resistance to this sort damage because the corrosion products were only observed in the space of the induced crack and not elsewhere in the concrete cover. Alternatively, it is also possible that a large accumulation of corrosion products at the steel/concrete interface would eventually prise the concrete cover from the steel. Overall it is clear that the most durable structural concrete will limit the formation of corrosion products by restricting access to water and oxygen and limiting any destructive volume expansion, and have a low corrosion rate.

4. Overall, the net effect is an extended life for reinforced high performance concrete relative to normal reinforced concrete and the addition of silica fume adds further benefit provided that any cracks are appropriately repaired as they arise. How much

extra service life this represents remains to be determined. Quantitative information regarding the service life of structures designed from these types of concrete mixes must be collected from field structures and long-term laboratory experiments.

CHAPTER SEVEN

DISCUSSION

As described in the introduction to this thesis, it was the objective of this work to identify the physical and chemical characteristics, and spatial distribution of corrosion products resulting from chloride-induced corrosion of steel in concrete and the role of different types of cementitious materials and the presence of cracks. The following Sections integrate the observations and conclusions of the previous Chapters such that a more thorough understanding is gained into the propagation stage of the corrosion process.

7.1 EFFECT OF A CEMENTITIOUS COVER

7.1.1 Effect of Cement Type

The effect of two different types of cement on the corrosion behaviour of steel was directly compared during the simulated pore solution and modified cement paste experiments presented in Chapters 4 and 5, respectively. The simulated pore solution experiments showed that the lower pH of the white solution permitted corrosion to initiate on steel at lower applied potentials and chloride levels than that observed in the Type 10 solutions. This effect can be expected to be even more pronounced for blended cements, for example, with silica fume, fly ash or slag which would reduce the pH of the pore solution.

This agreed with the results of the modified cement paste experiments which showed that the steel in the white cement paste corroded at a higher rate than the steel in the Type 10 for similar periods of chloride exposure, as shown in Figure 5.3.2. These higher corrosion rates were attributed to the limited chloride binding which could have occurred in the white cement with its relatively lower C_3A and C_4AF contents when compared to that of the Type 10 modified cement paste, as detailed in Table 3.1(b). A

reduced chloride binding capacity would result in a higher chloride concentration in the pore solution of the white modified cement paste and would cause the observed higher corrosion rates.

Although higher corrosion rates were measured for steel in the white modified cement paste, orange stains composed of magnetite and haematite intermixed with the cement paste formed within the Type 10 modified cement paste cover, shown in Figure 5.3.1(b), which were not observed within the white specimens. This difference was attributed to the more open pore structure of the Type 10 cement paste which permitted iron ions to diffuse more easily through the concrete cover. This effect is similar to that observed with the different concrete mixes of Chapter 6 which is related to their different w/cm ratios. Large volumes of corrosion products were observed within the concrete cover for the low quality concrete and the HPC without silica fume. The presence of corrosion products in the low quality concrete was attributed to its more open pore structure while the corrosion products in the HPC without silica fume resulted from the presence of microcracks No similarities between their corresponding corrosion rates were noted which would have predicted this distribution of the products. It can then be concluded that there is not any correlation between the corrosion rate measurements and the types of corrosion products which form or their distribution either at the steel/cementitious material interface or within the concrete cover. The corrosion products clearly depend upon the characteristics of the cementitious cover, such as the cement type as well as on the degree of moisture saturation (i.e., different products were observed above, at, and below the solution line in the cement paste specimens of Chapter 5). This influence of concrete mixture proportions is described in more detail in the next Section.

7.1.2 Effect of Mixture Proportions and Constituents

An examination of all experiments conducted for this thesis indicates that the most

important influence on the types of corrosion products is the composition of the cementitious cover and its pore and microcrack network. While the simulated pore solution experiments of Chapter 4 and the modified cement paste experiments of Chapter 5 showed some minor variations in the corrosion behaviour of any embedded steel, the range of corrosion conditions observed within the different concretes was relatively larger as described in Section 6.3.4.2 and provided considerable insight into the corrosion process once it is initiated.

The presence of a relatively interconnected pore network which can be enhanced by microcracking, permits corrosion species such as chlorides and oxygen to readily diffuse to and from active corrosion sites and results in the formation of corrosion products within the concrete cover. As the size of the pore network increases, a reduction in the corrosion rate due to the blockage of the pore network by corrosion products becomes progressively more difficult because the volume of products required to accomplish this would increase proportionately with the size of the pore network. Thus, concretes with higher w/cm ratios such as the low quality concrete will provide far less protection to its embedded steel than concretes with lower w/cm ratios. In addition, mix constituents which produce a less permeable concrete upon full hydration at similar w/cm ratios would reduce the corrosion rate of steel provided the concrete remained uncracked. If cracked, the chemistry of the cement paste and associated pore solution will determine the resulting corrosion rates. This aspect is illustrated by the observation that less corrosion products were formed in the white modified cement paste than in the Type 10, the white having a lower porosity and denser microstructure as indicated in Chapter 5. Had the white cement paste remained uncracked, the corrosion rate of its embedded steel would have probably been lower than that in the Type 10 as demonstrated by the sealed white specimens in Figure 5.3.2.

The distribution of products away from the steel/cementitious interface is generally thought to be undesirable because iron is thermodynamically metastable and thus, will

259

potentially continue to oxidize and hydrate to form more expansive products which could lead to cracking of the cover. Volume expansions of as high as 7 are commonly asserted as the reason for the deterioration of the concrete cover. However, products which, in their pure state, have specific volumes of only between 2 to 3 were observed in the modified cement paste specimens and not more than 3.5 (i.e., akaganeite, β-FeOOH) in the concretes of Chapter 6. These products were observed as precipitates within the concrete cover, and microcracks resulting from the corrosion product expansion were observed in isolated areas away from the surface of the steel in the HPC without silica fume (Figures 6.7(k) and (l)). These microcracks were assumed to be the cause of the brittle fracture of the cores during coring (Section 6.3.4.1) and indicates that even high performance concrete with low w/cm ratios are susceptible to deterioration from the formation of corrosion products in the cover.

However, even if corrosion products are confined to the steel interface by less permeable concrete, the localized corrosion attack can have considerable destructive impact as shown by the deep macropits which formed on the steel in the HPC/SF. Moreover, the localized accumulation of corrosion products at the steel interface can act as a wedge that prises the cementitious cover from the steel.

However, it has been speculated that once sufficiently dense corrosion products form over the surface of the active sites, the occlusion of the site will prevent continued interaction and the local supply of oxygen and chlorides will be depleted (Ashworth, Boden et al. 1970; Leek 1997). The work of Chapter 5 and 6 showed that, provided the cementitious cover was sufficiently impermeable, corrosion products such as magnetite were observed to partially fill the cracks. A corresponding decrease, or plateau, in the corrosion rates was observed for the corroding steel in the HPC with silica fume but was not observed in the cracked white modified cement paste specimens or the industrial standard concrete. It is possible that the cracks must be completely filled to reduce the increasing corrosion rate such as was observed with the sealed white specimens in Figure

260

5.3.2 but it is more likely that the unusually high electrical resistivity and the reduced capillary porosity of the silica fume mix addition produced this effect in the HPC.

In summary, it is well-understood that uncracked, impermeable concrete provides the best protection for steel in a chloride environment. Should, however, this impermeable concrete become cracked because of structural overloading or inevitable shrinkage, the results of this thesis show that extra precautions must be taken to prevent the more localized and insidious corrosion damage (i.e., little or no rust staining in the cover that would signal a problem) from accumulating until a catastrophic failure occurs. Ideally, all cracks should be injected to completely block the access of the chlorides to the embedded steel before corrosion is initiated.

7.2 EFFECT OF CHLORIDE SOURCE AND EXPOSURE

Two chloride sources, derived from either NaCl for the experiments of Chapters 4 and 5 or from simulated sea water for the experiments of Chapter 6, were studied for the work of this thesis. A comparison of the corrosion behaviour of steel and the types of products formed indicates that the chloride source has no effect. Although a greater range of corrosion products was observed (i.e., lepidocrocite and akaganeite) on the steel in the concrete specimens of Chapter 6, this is more likely a result of the significantly older exposure age of these specimens (at least three years) compared to the modified cement paste specimens (up to 1 year). This conclusion is supported by the similar corrosion rates for the first year of exposure to the chloride solutions measured for both the modified cement paste specimens and the concrete specimens, for the first year of exposure to the chloride solutions as shown in Figures 5.3.2 and 6.5(a), respectively. It is possible that with continued exposure, corrosion products such as akaganeite and lepidocrocite which form at higher chloride levels would have been observed in the modified cement paste

specimens.

7.3 EFFECT OF CRACKS

Similar to field observations of steel-reinforced concrete structures in chloride environments, cracks in the cementitious materials studied in this thesis increased the corrosion of embedded steel relative to uncracked specimens with the exception of the low quality concrete specimens.   For loading cracks, this was shown by the comparison between Figures 6.5(c) with Figure 6.5(b) in Section 6.3.1 where the corrosion rates were approximately an order of magnitude higher for the cracked specimens after at least three years exposure to the simulated sea water. However, it was also concluded that cracks have a less significant effect on concretes with relatively accessible pore networks, as previously described in Section 7.1.1.

The effect of cracks was also studied with the modified cement paste specimens (Chapter 5) but these cracks were generated naturally through drying shrinkage, and, therefore, all specimens contained randomly oriented cracks. The geometry of these cracks differed from the loading cracks induced in the concrete specimens of Chapter 6 in that the former likely stopped once they reached the surface of the steel.

In contrast, the loading cracks in the concrete prisms were induced by three-point bending, may have caused some delamination between the embedded steel and the concrete cover. This would have increased the exposed area of the steel in the concrete specimens to the simulated sea water over that experienced by the modified cement paste specimens. However, this did not appear to affect the type or distribution of the corrosion products which precipitated as magnetite was observed at the root of the cracks (i.e., at the surface of the steel) in all specimens.   This concurs with the conclusions of Génin and others presented in Table 2.3. In addition, magnetite was observed to partially fill most cracks in

the modified cement paste specimens (Section 5.3.6), the industrial standard concrete specimens (Figure 6.7(a), and the HPC with silica fume specimens (Figure 6.7(g)). Other corrosion products such as haematite and goethite were observed to form within the cracks closer to the exposed surface of the steel.

The formation of these products was anticipated to halt the increasing corrosion rate of the underlying steel by reducing the diffusion of ionic species to and from the corrosion pit. This was only observed if the concrete cover was sufficiently dense to minimize the diffusion of reactive species through the cementitious cover, as discussed in the previous Section. Under these circumstances, cracks had a more significant effect on the corrosion of embedded steel in cementitious materials with denser pore structures as shown by the difference in corrosion rates between the cracked and sealed white modified cement paste specimens in Figure 5.3.2 and the concretes of Chapter 6.

7.4 EFFECT OF STEEL SURFACE FINISH

The effect of the surface finish of the steel was studied in Chapters 4 and 5 with the steel immersed in the simulated pore solutions and the steel-reinforced modified cement paste specimens. As described in Section 5.3.1, corrosion was observed to initiate first on the as-received steel surfaces for most of the modified cement paste specimens which suggested that the mill scale provided less protection against chloride-induced corrosion. However, the comparison of the corrosion behaviour of the as-received steel surfaces with the ground steel surfaces in the chloride-contaminated simulated pore solutions indicated that the mill scale provided better protection against corrosion but with some unpredictable variability. It was concluded that there were sufficiently large flaws within the typically porous and discontinuous mill scale which could not be easily occluded by the formation of corrosion products and resulted in localized attack.

263

This apparent discrepancy between the two experiments can be explained by comparing the area of the exposed steel for both types of specimens. The exposed as-received steel area of the specimens used for the modified cement paste specimens was approximately 115 times larger than that used in the simulated pore solution experiments. Similar to the volume effect observed for glasses and ceramics where the presence of a catastrophic flaw becomes more probable with increasing volume, it is reasonable to conclude the larger surface area of the Chapter 5 specimens increased the probability that a critically-sized flaw would be present on the surface of the steel which would facilitate corrosion initiation. Alternatively, it might be the case that because corrosion initiation was favoured above the solution line on the as-received steel surface, the remaining area acted as a good cathodic area, thereby promoting anodic dissolution in any breaks in the mill scale. Since the steel samples used in the simulated pore solution experiments were completely immersed in the pore solution, all perforations in the mill scale would have had equal probabilities for corrosion to initiate.

Regardless of the explanation for the observed results, once corrosion initiated, the corrosion products observed on both of the steel surfaces were similar as described in Sections 4.2.2 and 5.3.6, along with the corrosion current densities as shown in Figures 4.2.3(a) through (d). However, it is not economically practical to remove the mill scale from the steel prior to embedding it in concrete in spite of the advantages offered by delaying the initiation of corrosion. Far more effective would be to improve the quality of the concrete cover such that cracks are avoided for the reasons described in Section 7.1.2.

CHAPTER EIGHT

CONCLUSIONS & RECOMMENDATIONS

8.1 CONCLUSIONS

1. The corrosion products clearly depend upon the characteristics of the cementitious cover, such as the cement type as well as on the degree of moisture saturation, the presence of any cracks in the vicinity and, possibly, on the period of exposure of the structure to the chloride contamination. However, there is not any correlation between the corrosion rate measurements and the types of corrosion products which form or their distribution either at the steel/cementitious material interface or within the concrete cover.

2. Volume expansions of as high as 7 are commonly asserted as the reason for the cracking and spalling of the concrete cover and have been used as the basis for models of deterioration of reinforced concrete. However, products which, in their pure state, have specific volumes of only between 2 to 3 were observed in the modified cement paste specimens and not more than 3.5 (i.e., akaganeite β-FeOOH) in the concretes described in Chapter 6. It is recommended that this revision be incorporated into theoretical service life models while recognising that larger volume expansions may occur under different environmental conditions (e.g., extended dry periods, wet/dry cycling).

3. Although corrosion products such as magnetite were observed to partially fill the cracks in all types of cementitious specimens, a corresponding decrease, or plateau, in the corrosion rates was not observed in any specimens except for the corroding steel in the HPC with silica fume. It is possible that the cracks must be completely filled to reduce the increasing corrosion rate but it is more likely that the unusually high electrical resistivity and the reduced capillary porosity of the silica fume mix

addition produced this effect in the HPC. However, these characteristics generated deeper, more localized pitting on the steel in the HPC/SF which is potentially the most devastating of all corrosion attacks observed.

4.   It is well-understood that uncracked, impermeable concrete provides the best protection for steel in a chloride environment. Should, however, this impermeable concrete become cracked because of structural overloading or shrinkage, extra precautions must be taken to prevent the more localized and insidious corrosion damage (i.e., corrosion accompanied by little or no rust staining in the cover that would signal a problem) from accumulating at the steel/concrete interface until a catastrophic failure occurs.

5.   The chloride source (i.e., as dissolved NaCl or as mixed chlorides in simulated sea water) has no effect on the corrosion behaviour of steel and the types of products formed.

6.   Once corrosion initiated, surface finish (either ground or with the mill scale intact) did not have any effect on the type of corrosion products observed or the measured corrosion current densities.

7.   A higher pH of the cement paste pore solution was observed to provide better protection for steel against chloride-induced corrosion even within the narrow range of pH studied (i.e., 12.9 to 13.4). Specifically, corrosion initiated at lower potentials and chloride levels in the lower pH synthetic pore solution mimicking that expressed from white cement paste than in the Type 10 paste. This effect can be expected to be even more pronounced for blended cements, for example, with silica fume, fly ash or slag.

8.2 RECOMMENDATIONS

1. To fully investigate the propagation stage of corrosion in steel-reinforced concrete structures, cores from field structures should be studied and correlated to their service environment. Cores from both deteriorated and sound concrete areas should be taken to represent the range of conditions. This work would permit the underlying interrelationships between the corrosion process and cementitious materials identified in this thesis to be quantified and provide empirical evidence for theoretical service life models and, hopefully, accurate predictions.

2. The materials characteristics, such as specific volume, of the corrosion products that form within cementitious materials were assumed in this thesis to be approximately similar to their bulk counterparts to simplify analyses. Although there was no evidence to suggest that this was unrealistic, this underlying assumption requires further investigation.

3. In this thesis, the role of both shrinkage and static loading cracks on chloride-induced corrosion was studied. However, dynamic cracks are also common in field structures (cracks in bridge decks or parking garage slabs which open and close under vehicle loads, etc.) and merit investigation. These cracks would be more difficult to repair effectively and could become increasingly destructive with time.

APPENDIX A

FULL POLARIZATION CURVES FROM STEEL

IN SIMULATED PORE SOLUTIONS

Full cyclic polarization curves (i.e., applied potential versus log current density) were collected for the work of Chapter 4 to determine the experimental conditions that cause changes on the surface of steel such as passivation or corrosion exposed to two different simulated pore solutions, Type 10 and White cement, and increasing chloride levels to a maximum level equivalent to a 1 M NaCl solution. Section A.1 presents the results for steel samples whose surfaces were ground until uniform with 240 Grit SiC paper while Section A.2 presents the results for those samples which were left in the as-received condition (i.e., with millscale on the surface). In addition, each figure compares the results of two pairs of duplicate samples (4 samples in total) that had undergone different electrochemical testing. One pair of samples was polarized from the open circuit potential, ramped in the anodic direction to +500 mV SCE, down to -800 mV SCE, and returning to the open circuit potential (henceforth referred to as "Anodic Ramp"). The other pair was polarized from the open circuit potential cathodically to -800 mV SCE, up to +500 mV SCE, and finally returning to the open circuit potential (henceforth referred to as the "Cathodic Ramp"). General theory pertaining to the interpretation of full cyclic polarization curves is presented in Section 2.4.2 and a discussion of these results is presented in Section 4.3.1.

A specific example of the determination of corrosion rate from full polarization curves is shown in Figure A. In general, if active corrosion is occurring and there is no diffusion limitation of oxygen, corrosion rates can be determined by extrapolating the linear portion of the anodic and cathodic curves (between 50 to 200 mV above or below the open circuit potential) to the open circuit potential. Since many of the full polarization curves

studied in this thesis were measured on samples which exhibited passivity and diffusion limitations, only an approximation of the corrosion rate can be obtained. In Figure A, the corrosion rate is estimated from the intersection point of pseudo-Tafel slopes. It should be noted that the errors in this method are no greater than the uncertainties in corrosion rates typically encountered with steel in concrete.
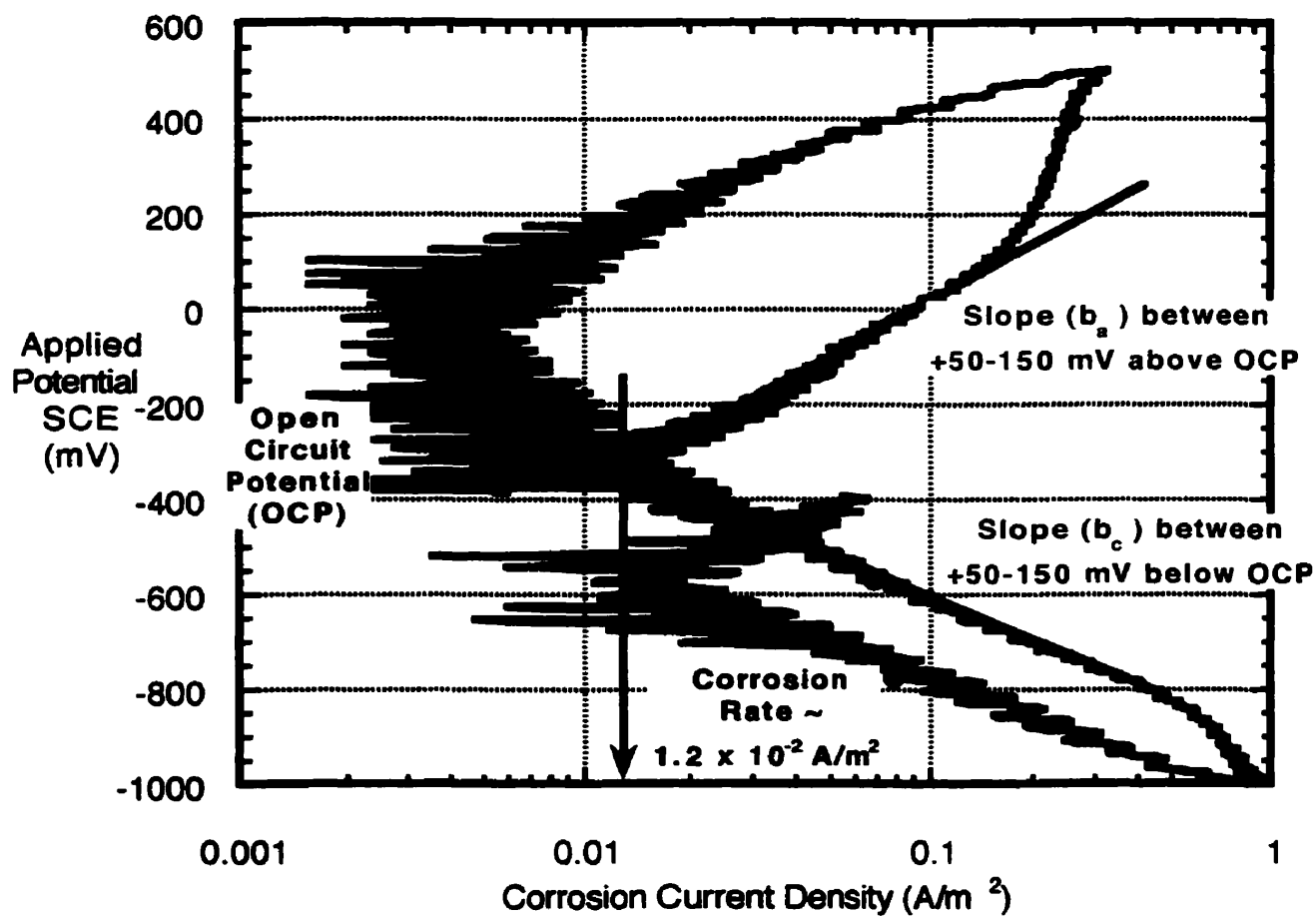
Figure A The estimation of corrosion rates from full polarization curves.

A.1 GROUND STEEL SURFACES

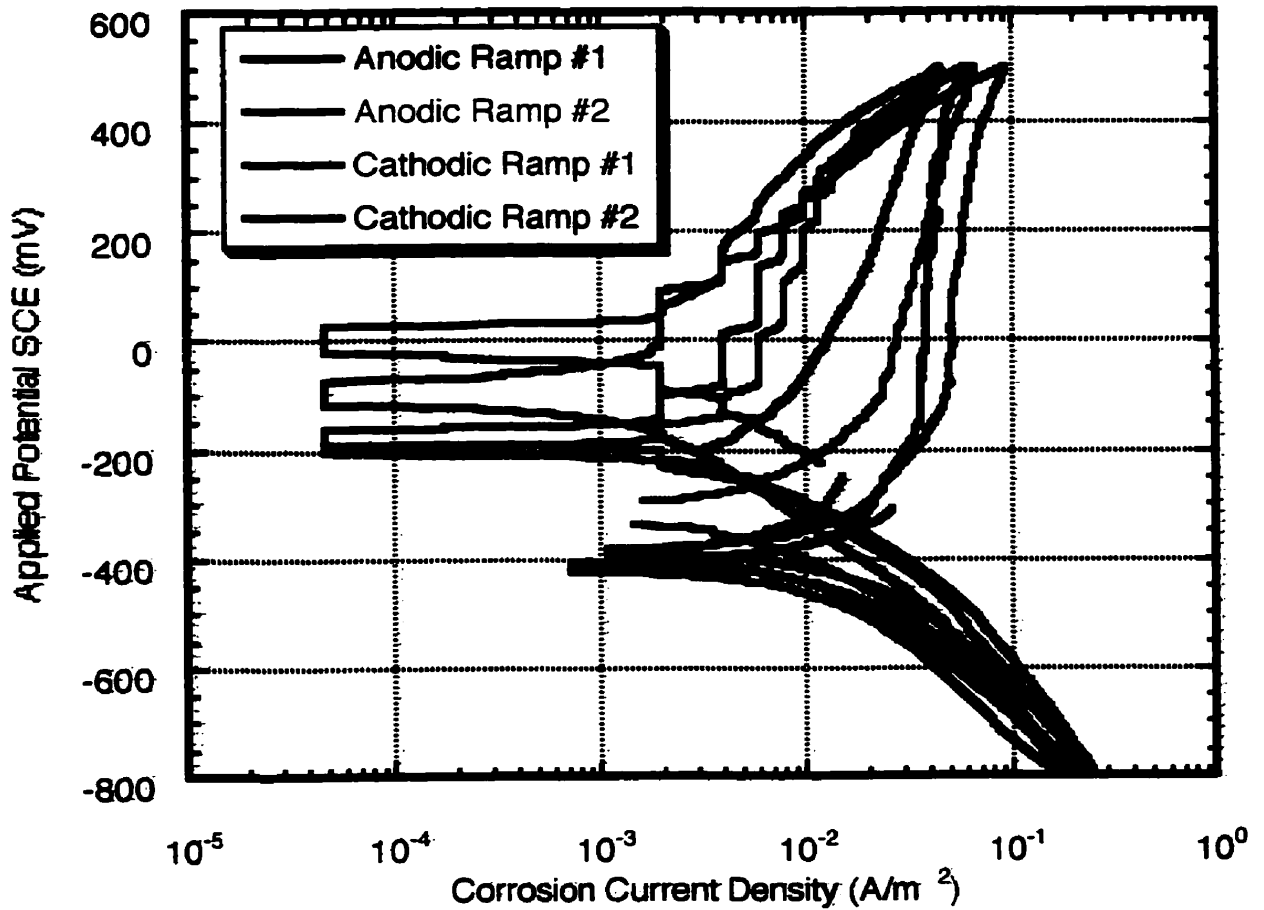### A.1.1 Type 10 Cement Simulated Pore Solution
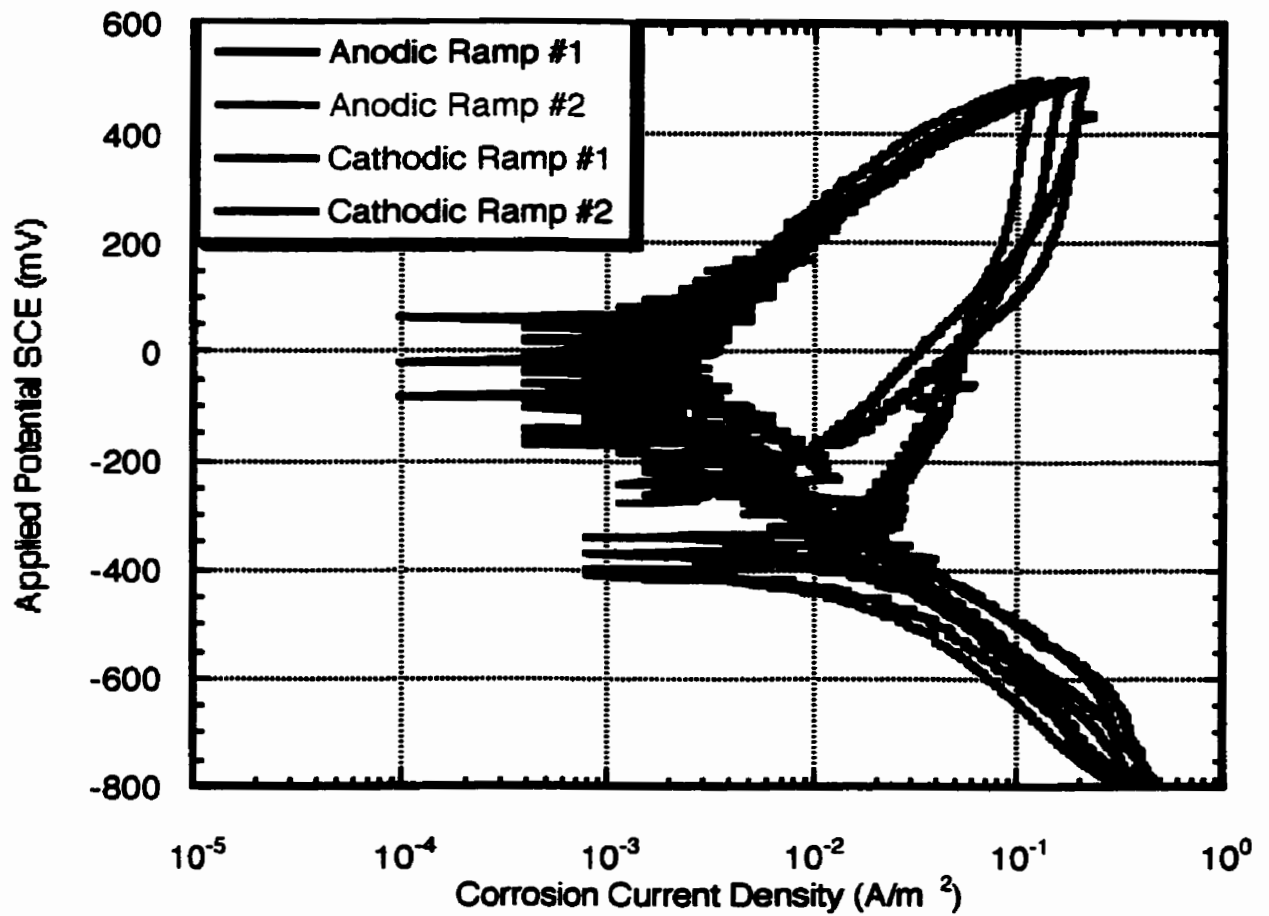
Figure A.1 Comparison of the full polarization curves collected for ground steel samples immersed in a Type 10 cement simulated pore solution that did not contain chlorides.
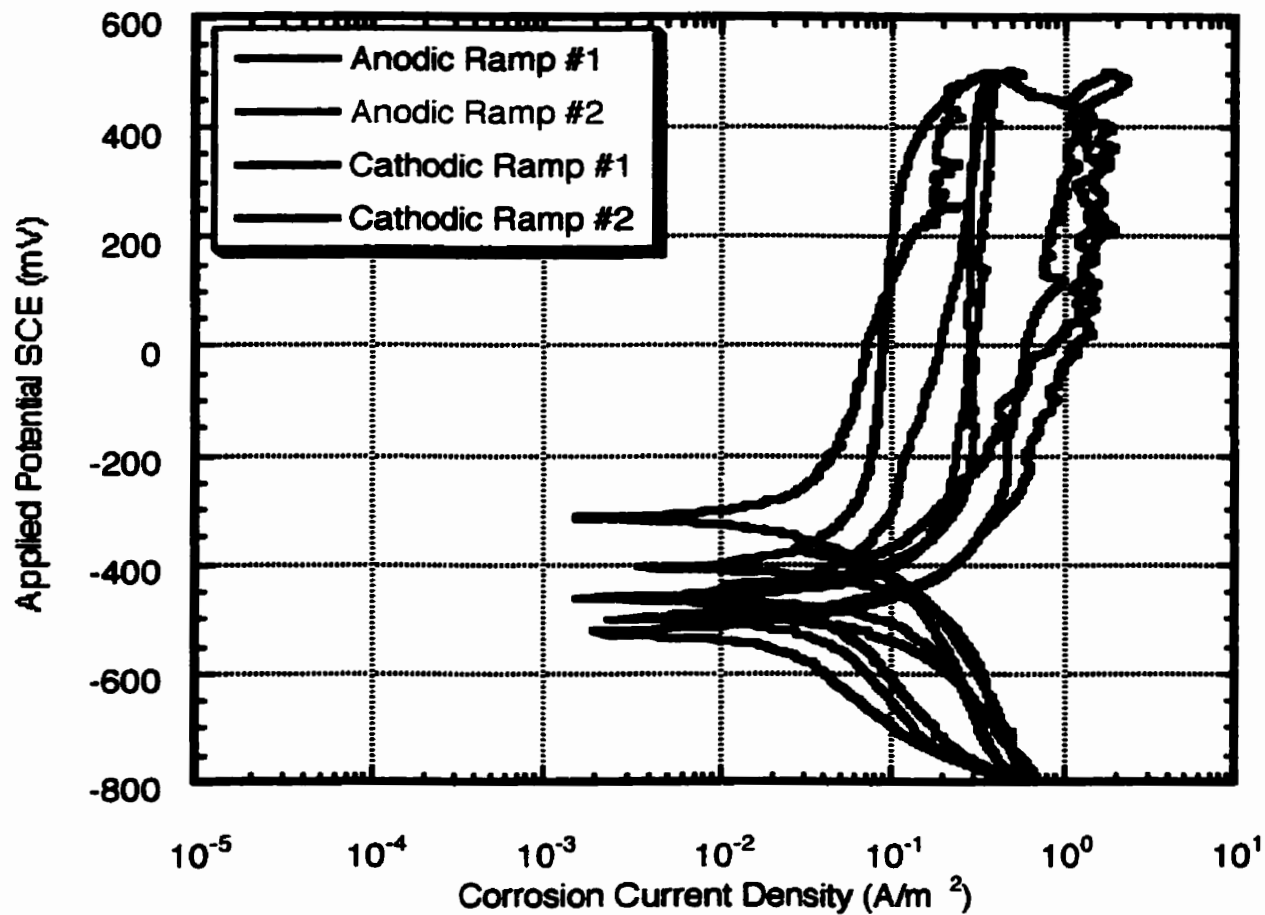
Figure A.2 Comparison of the full polarization curves collected for ground steel samples immersed in a Type 10 cement simulated pore solution that contained sufficient chlorides to make a 0.7 [Cl⁻]/[OH⁻] solution.
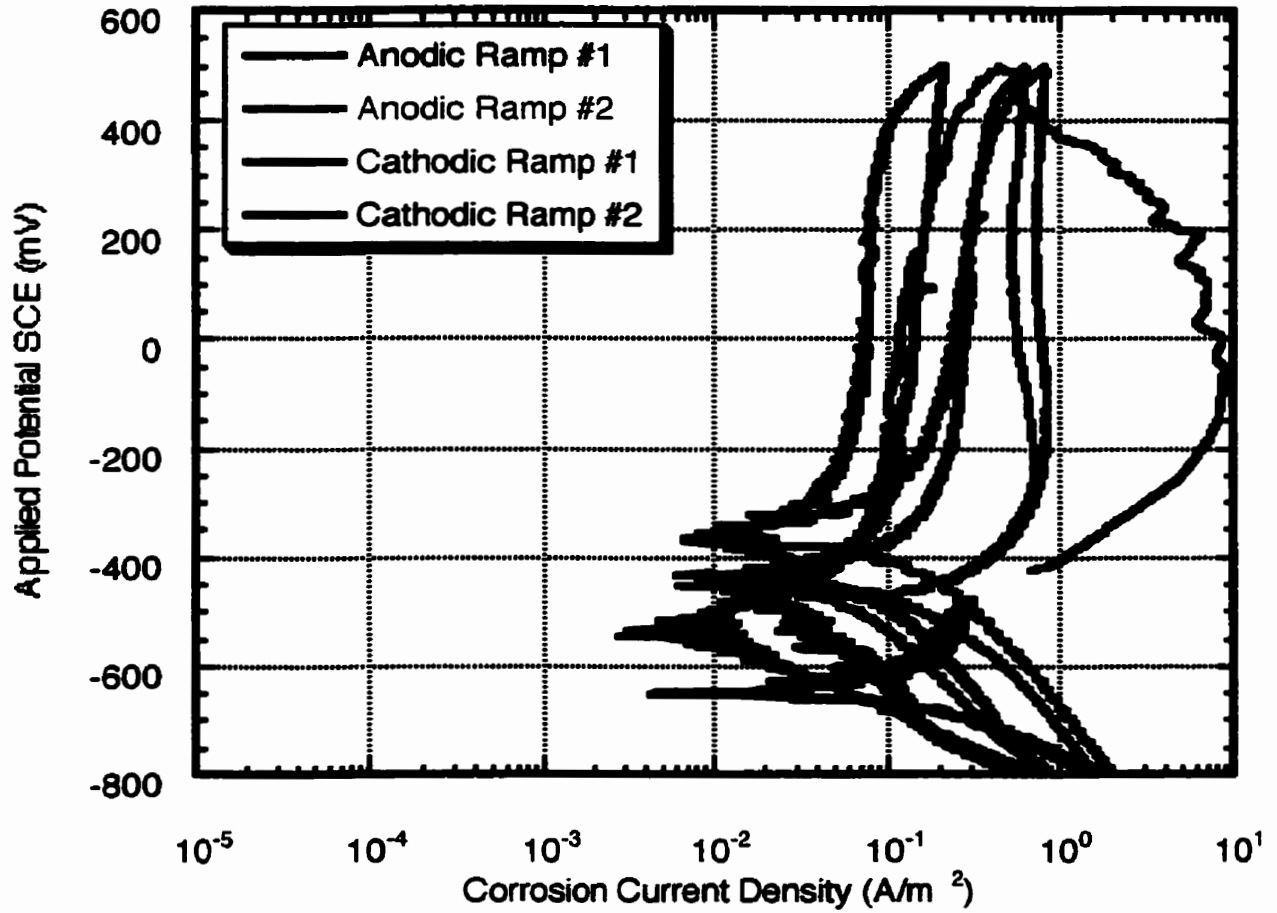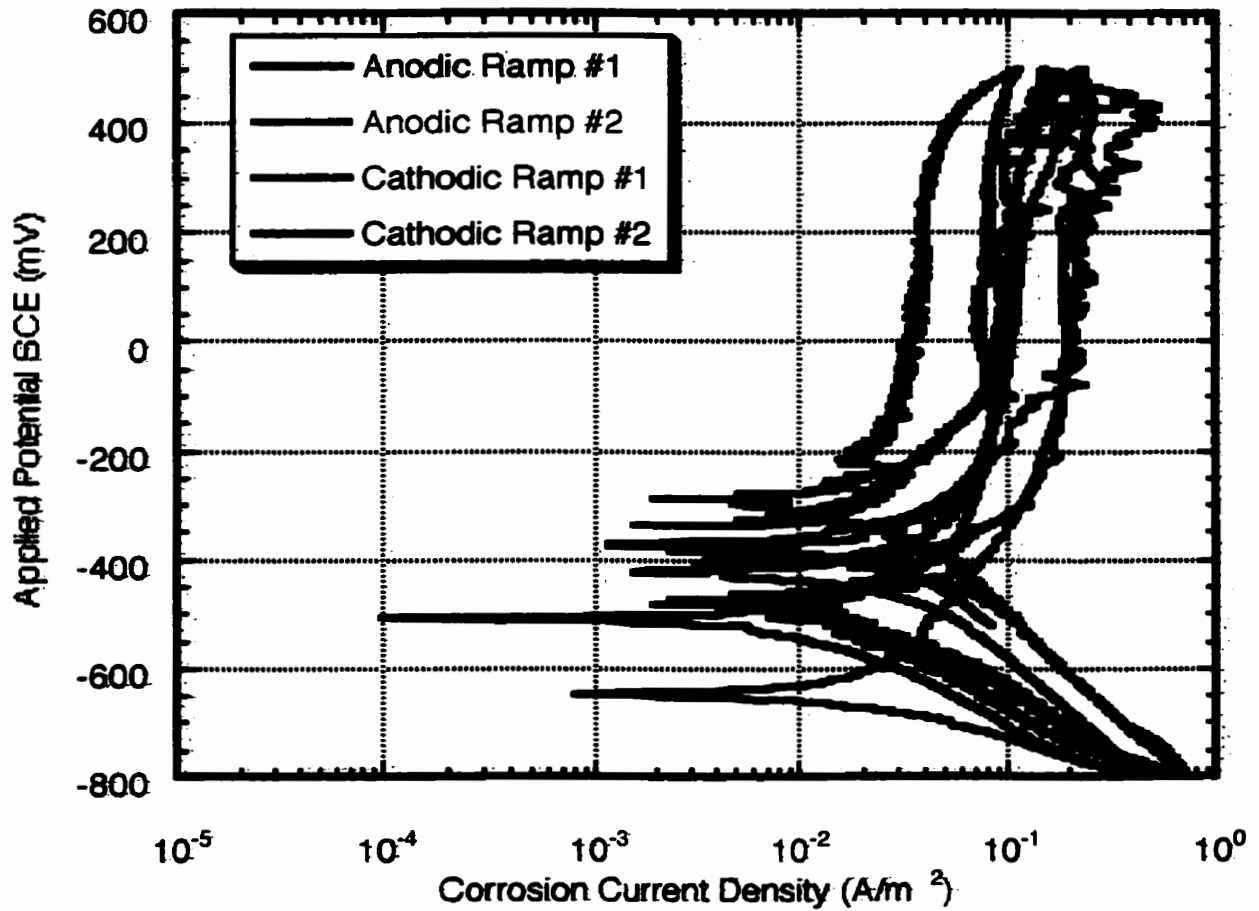
Figure A.3 Comparison of the full polarization curves collected for ground steel samples immersed in a Type 10 cement simulated pore solution that contained sufficient chlorides to make a 1.4 [Cl]/[OH] solution.
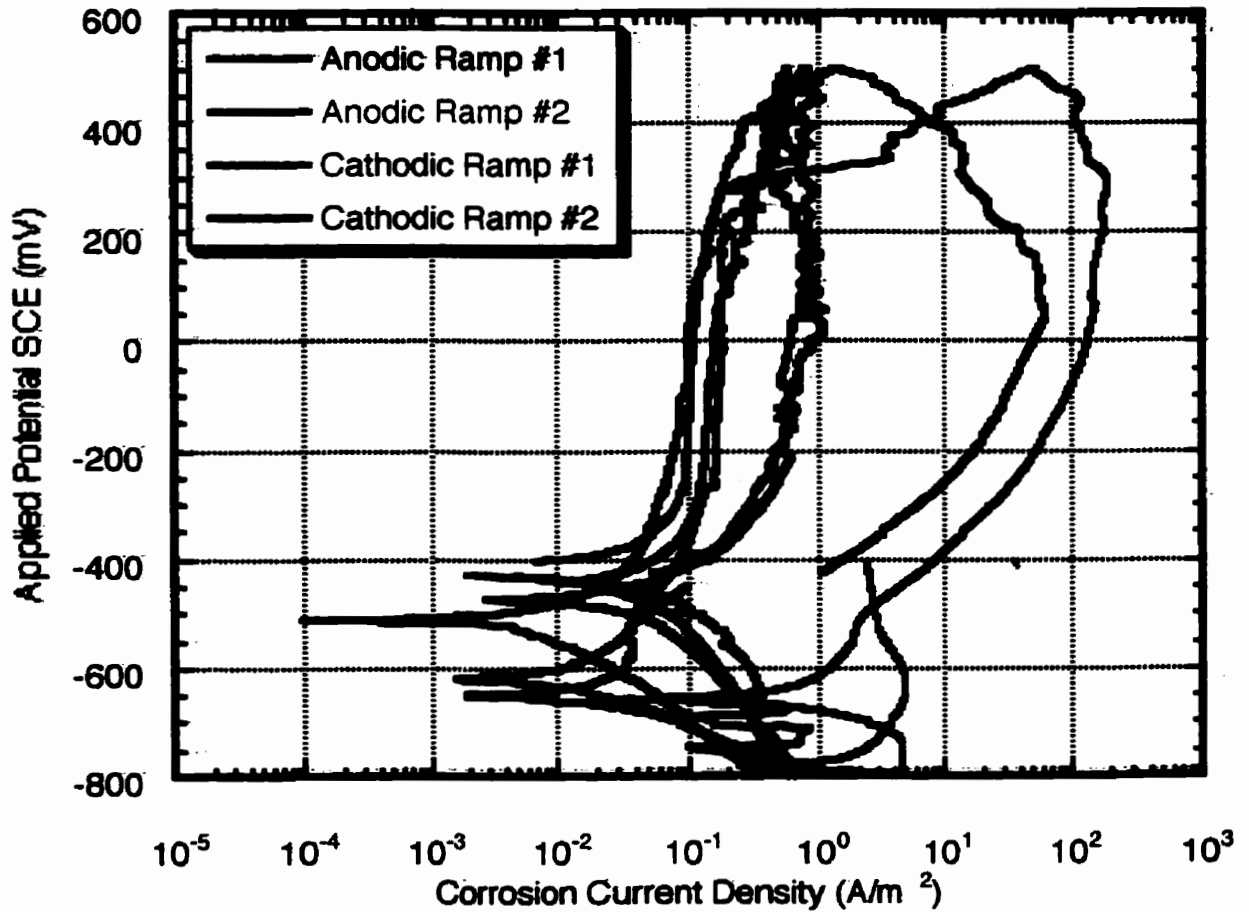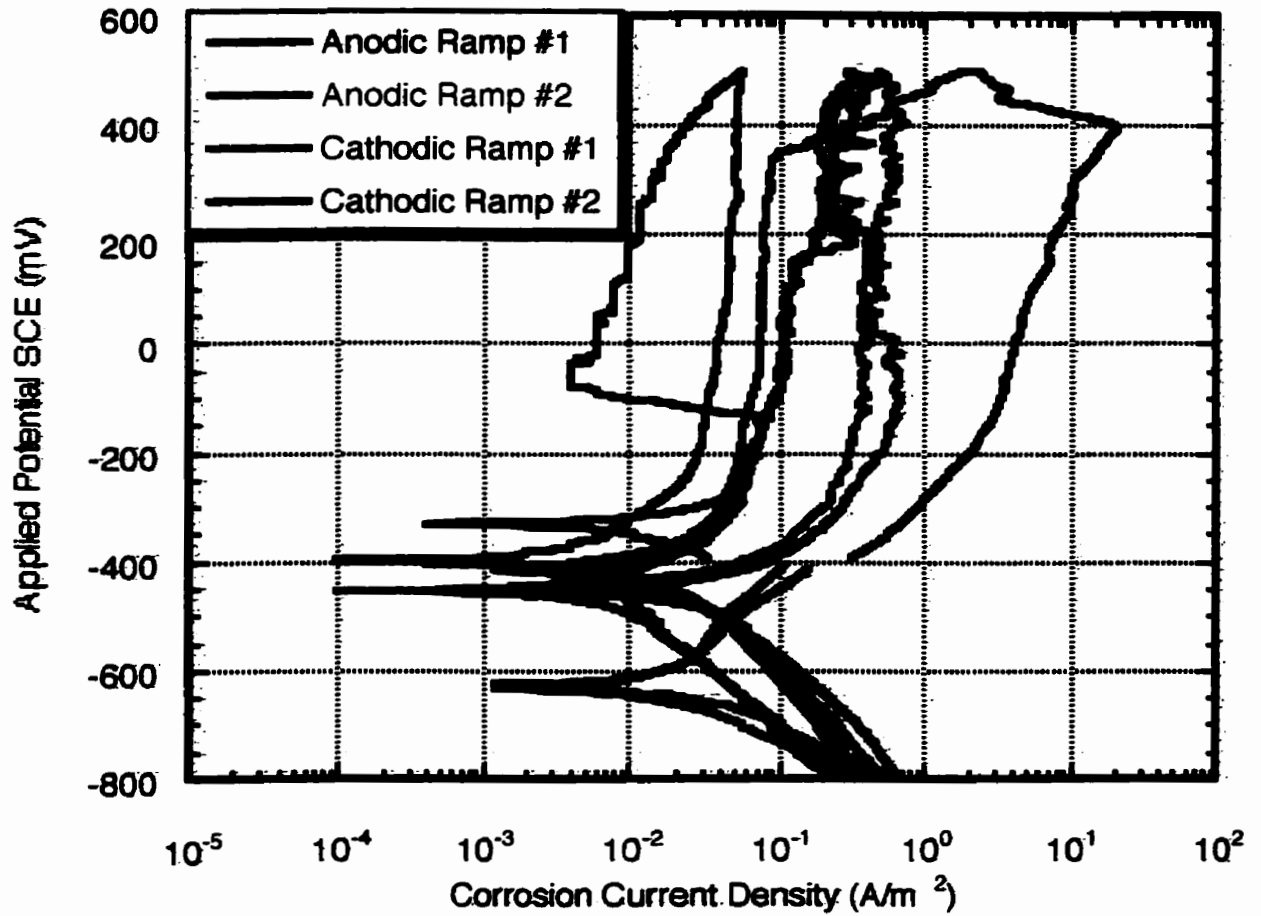
Figure A.4 Comparison of the full polarization curves collected for ground steel samples immersed in a Type 10 cement simulated pore solution that contained sufficient chlorides to make a 2.0 [Cl⁻]/[OH⁻] solution.
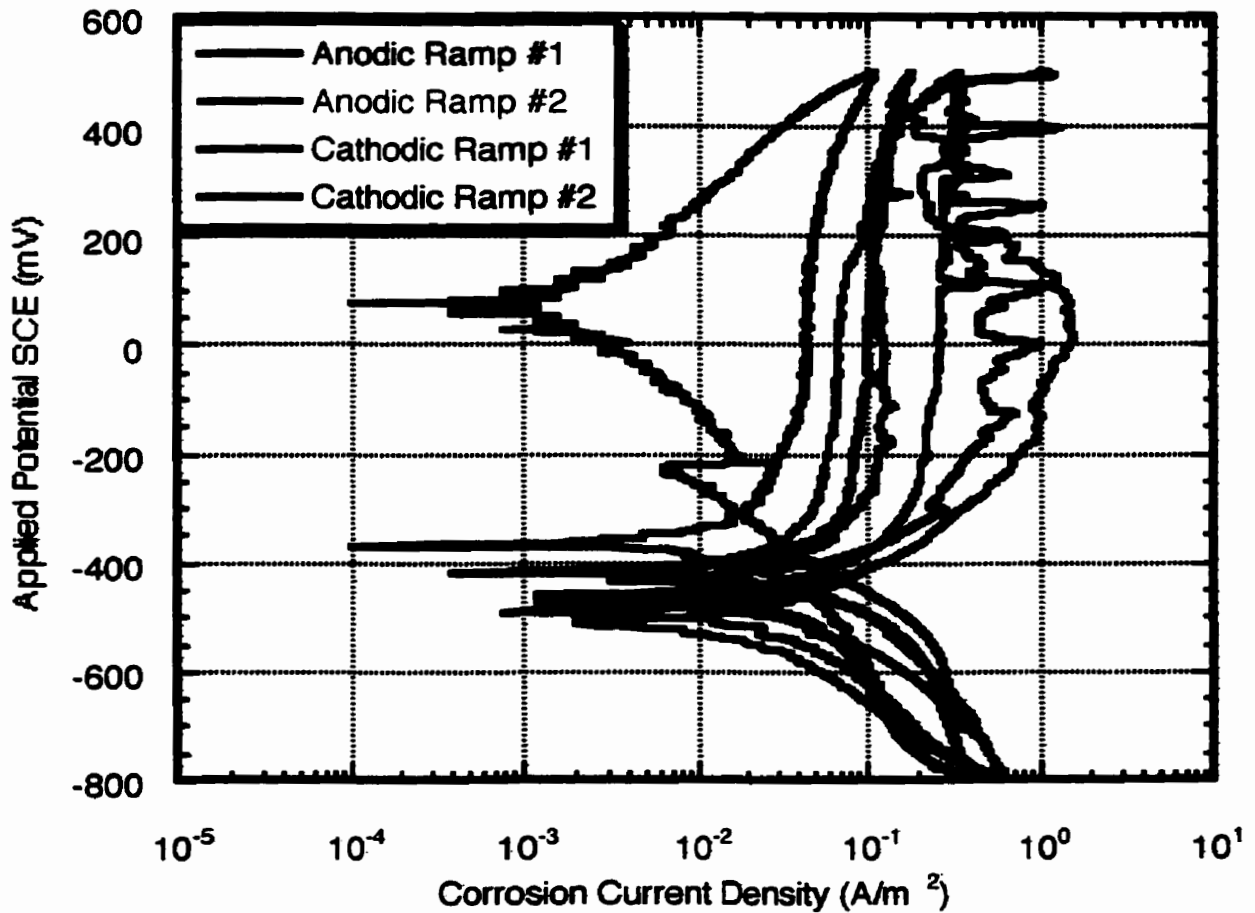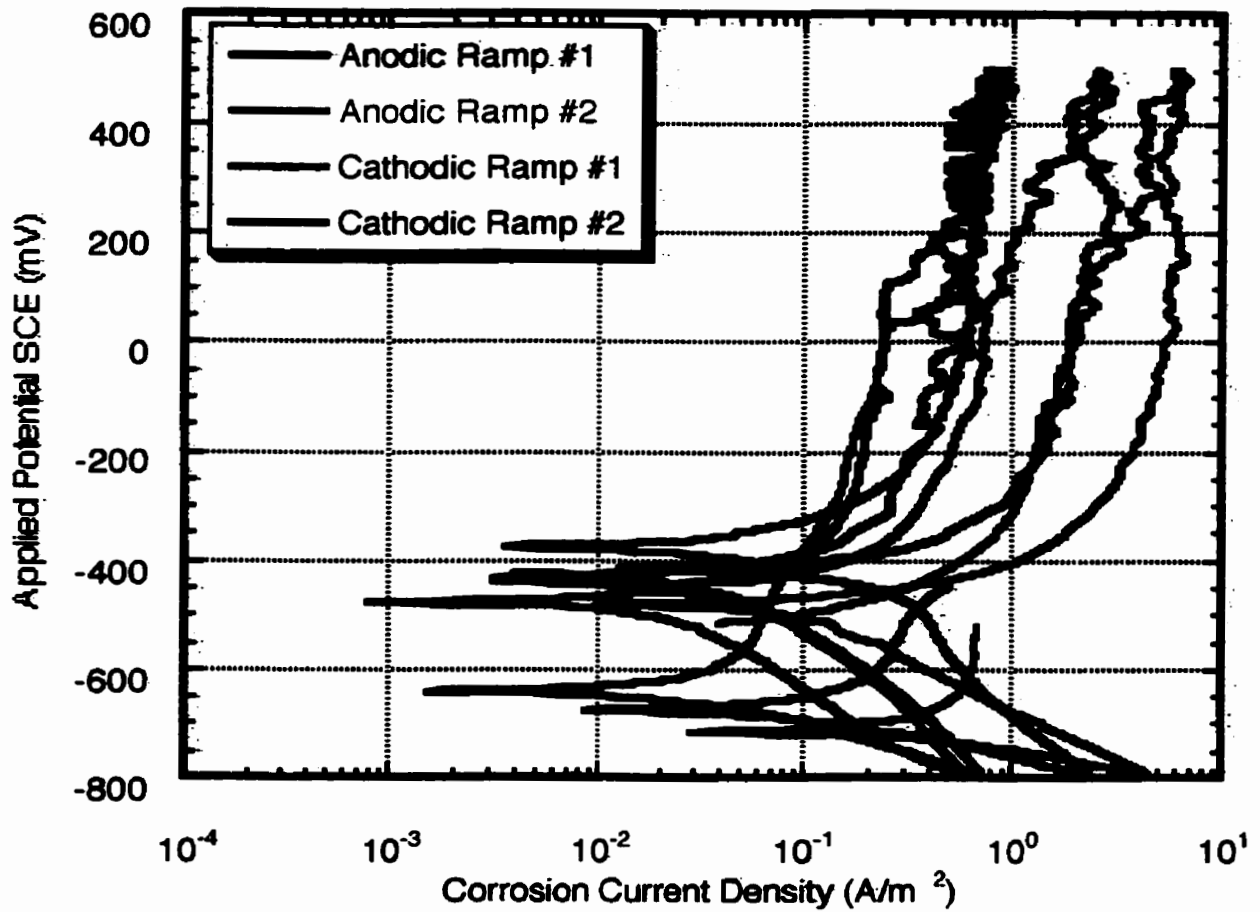
Figure A.5 Comparison of the full polarization curves collected for ground steel samples immersed in a Type 10 cement simulated pore solution that contained sufficient chlorides to make a 4.0 [Cl⁻]/[OH⁻] solution (equivalent to a 1 M NaCl solution for pH 13.3).

A.1.2 White Cement Simulated Pore Solution
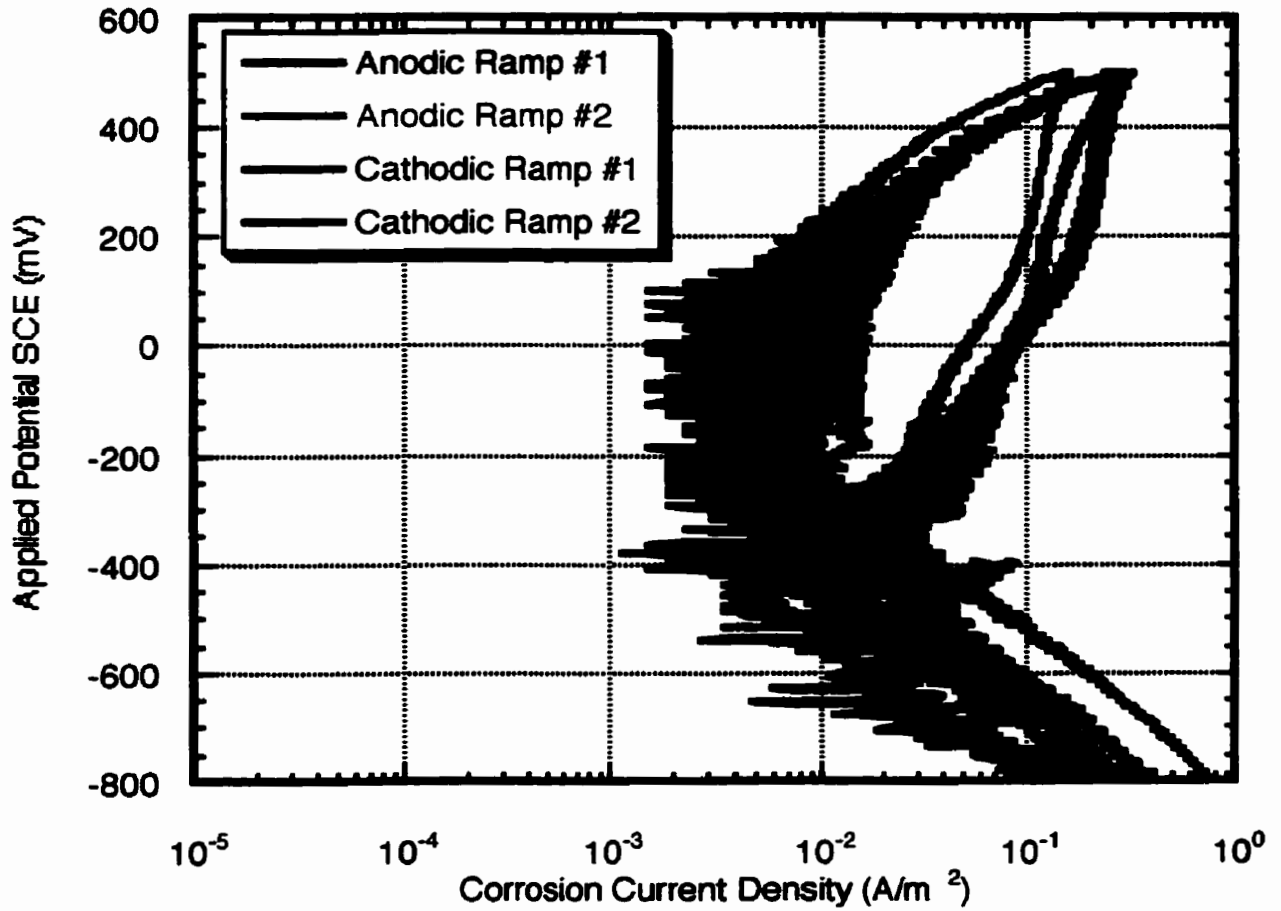
Figure A.6 Comparison of the full polarization curves collected for ground steel samples immersed in a White cement simulated pore solution that did not contain chlorides.
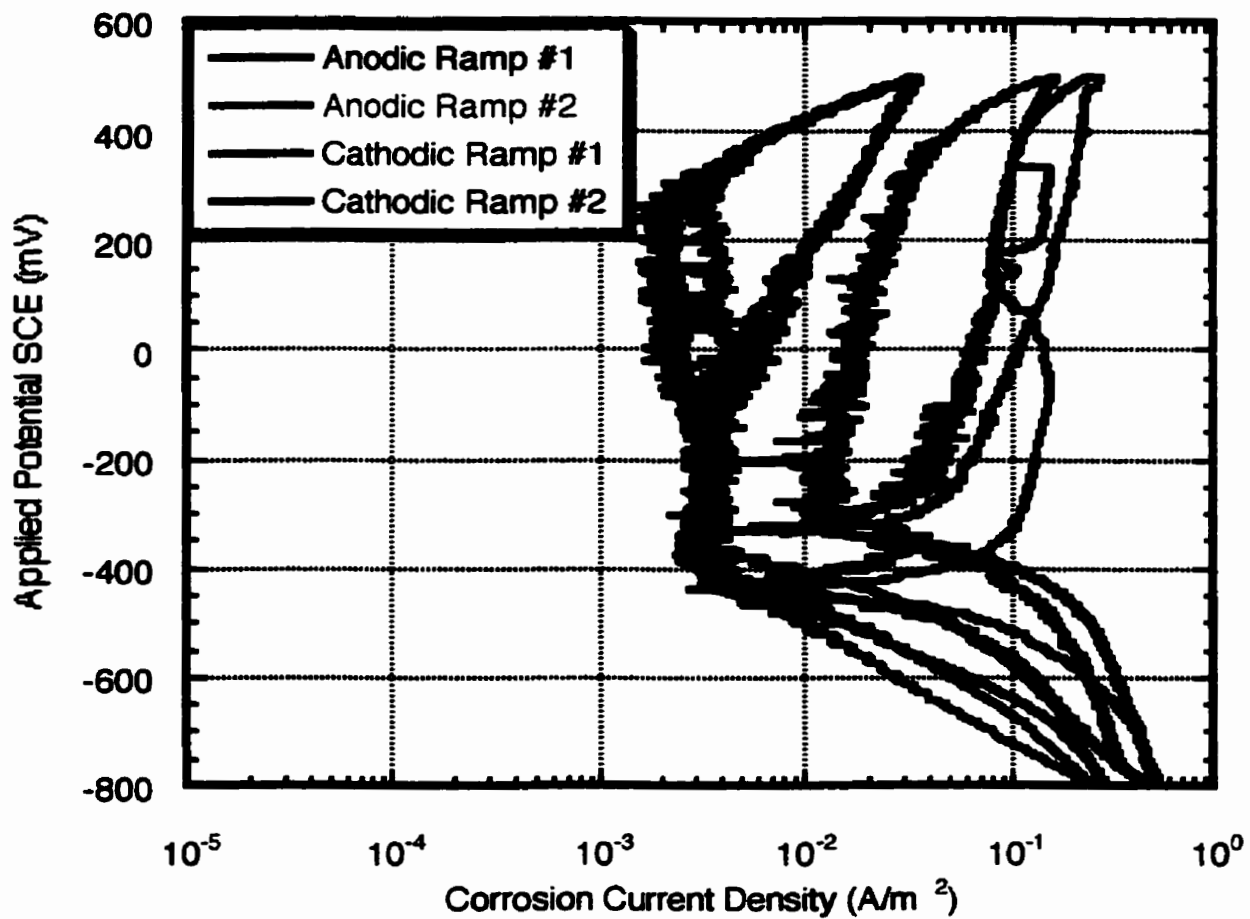
Figure A.7 Comparison of the full polarization curves collected for ground steel samples immersed in a White cement simulated pore solution that contained sufficient chlorides to make a 0.7 [Cl⁻]/[OH⁻] solution.
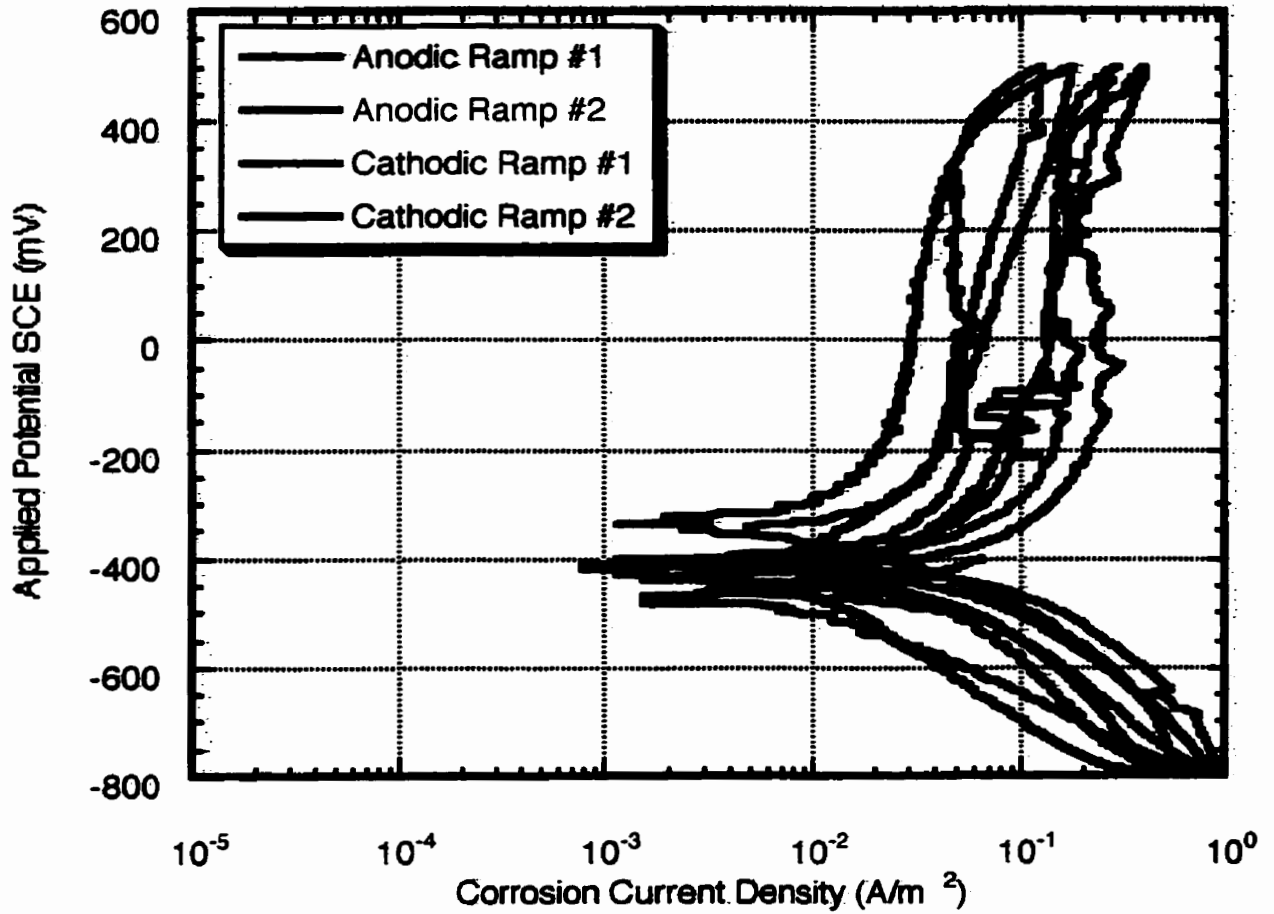
Figure A.8 Comparison of the full polarization curves collected for ground steel samples immersed in a White cement simulated pore solution that contained sufficient chlorides to make a 1.4 [Cl⁻]/[OH⁻] solution.
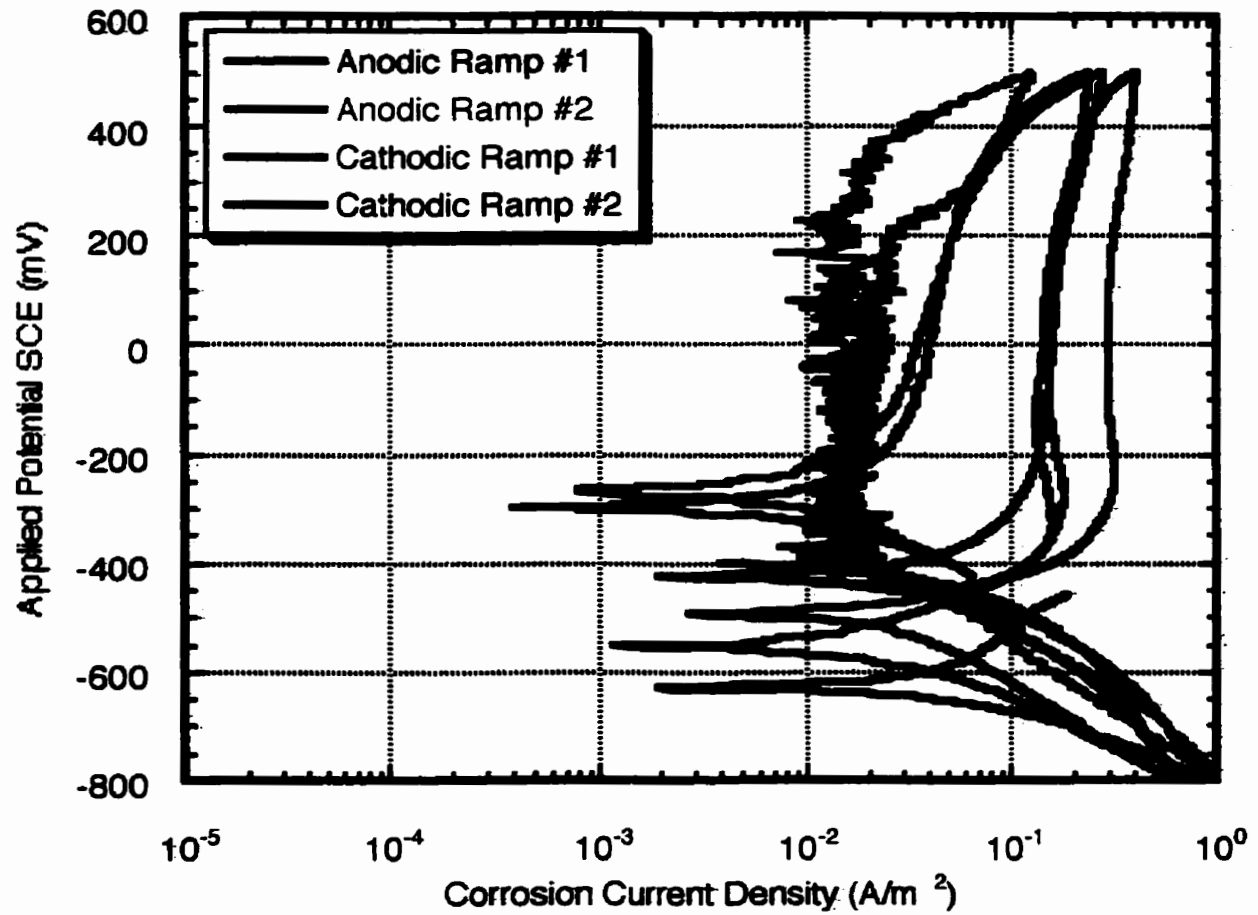
Figure A.9 Comparison of the full polarization curves collected for ground steel samples immersed in a White cement simulated pore solution that contained sufficient chlorides to make a 2.0 [Cl⁻]/[OH⁻] solution.
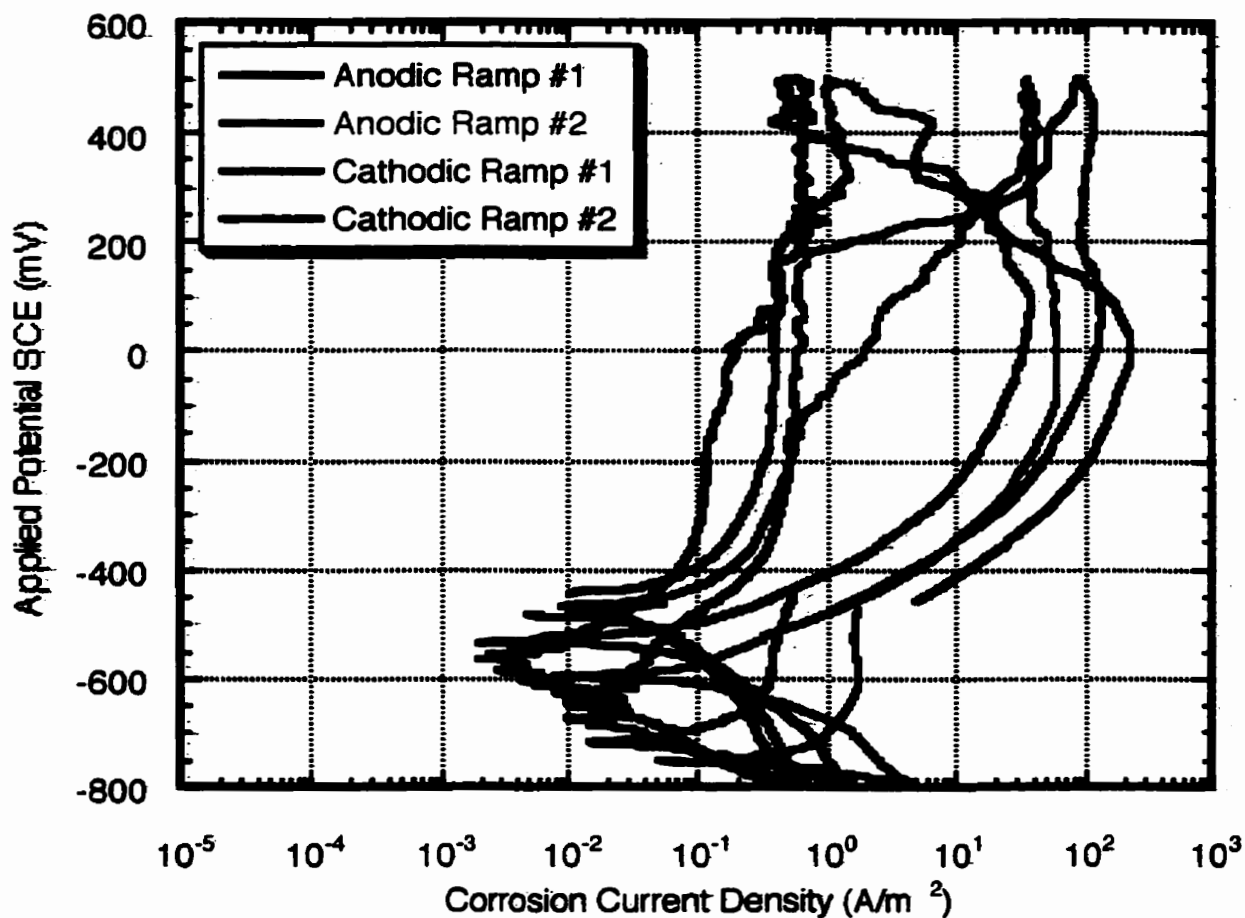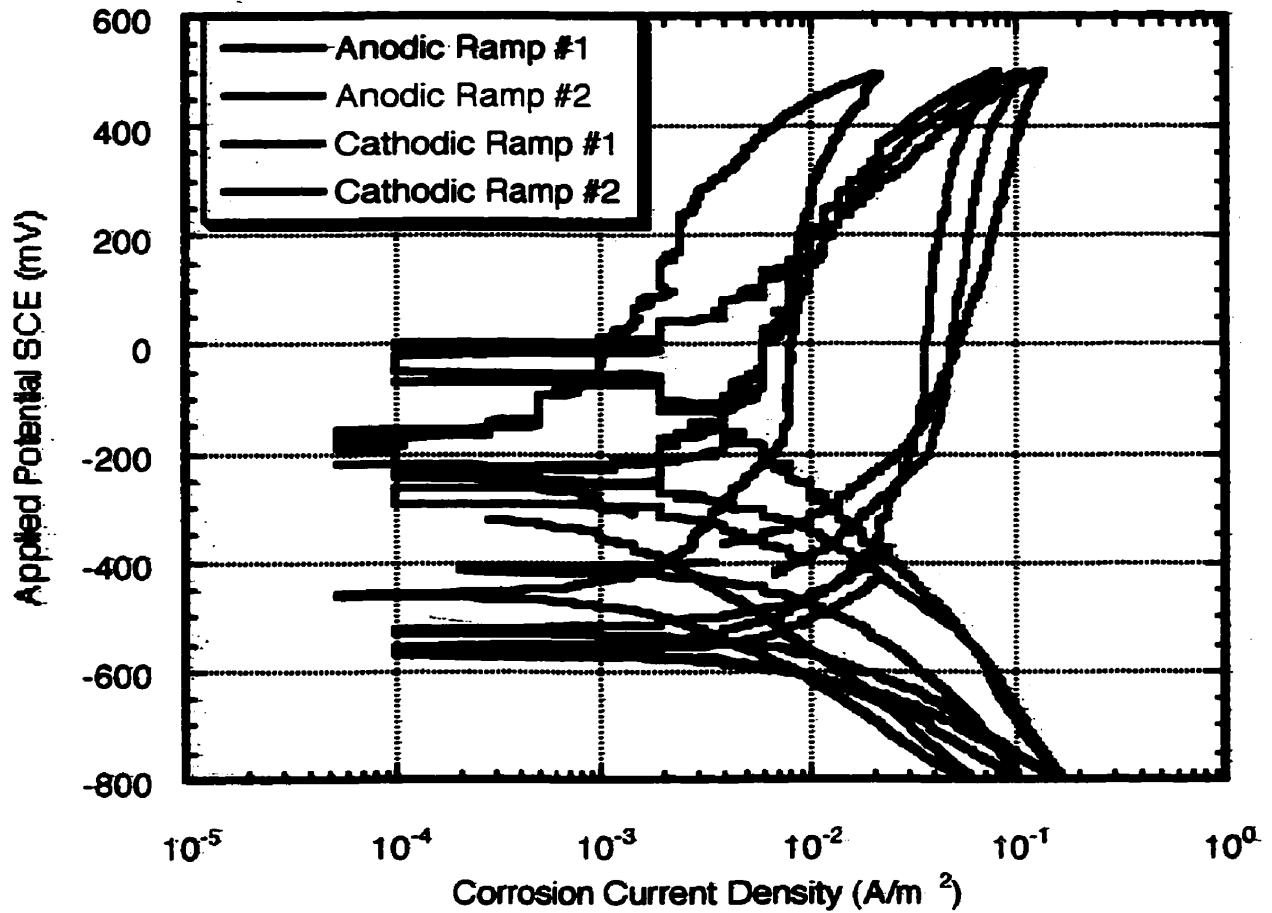
Figure A.10 Comparison of the full polarization curves collected for ground steel samples immersed in a White cement simulated pore solution that contained sufficient chlorides to make a 11.0 $[Cl^-]/[OH^-]$ solution (equivalent to a 1 M NaCl solution for pH 12.9).

A.2 AS-RECEIVED STEEL SURFACE (WITH MILL SCALE)
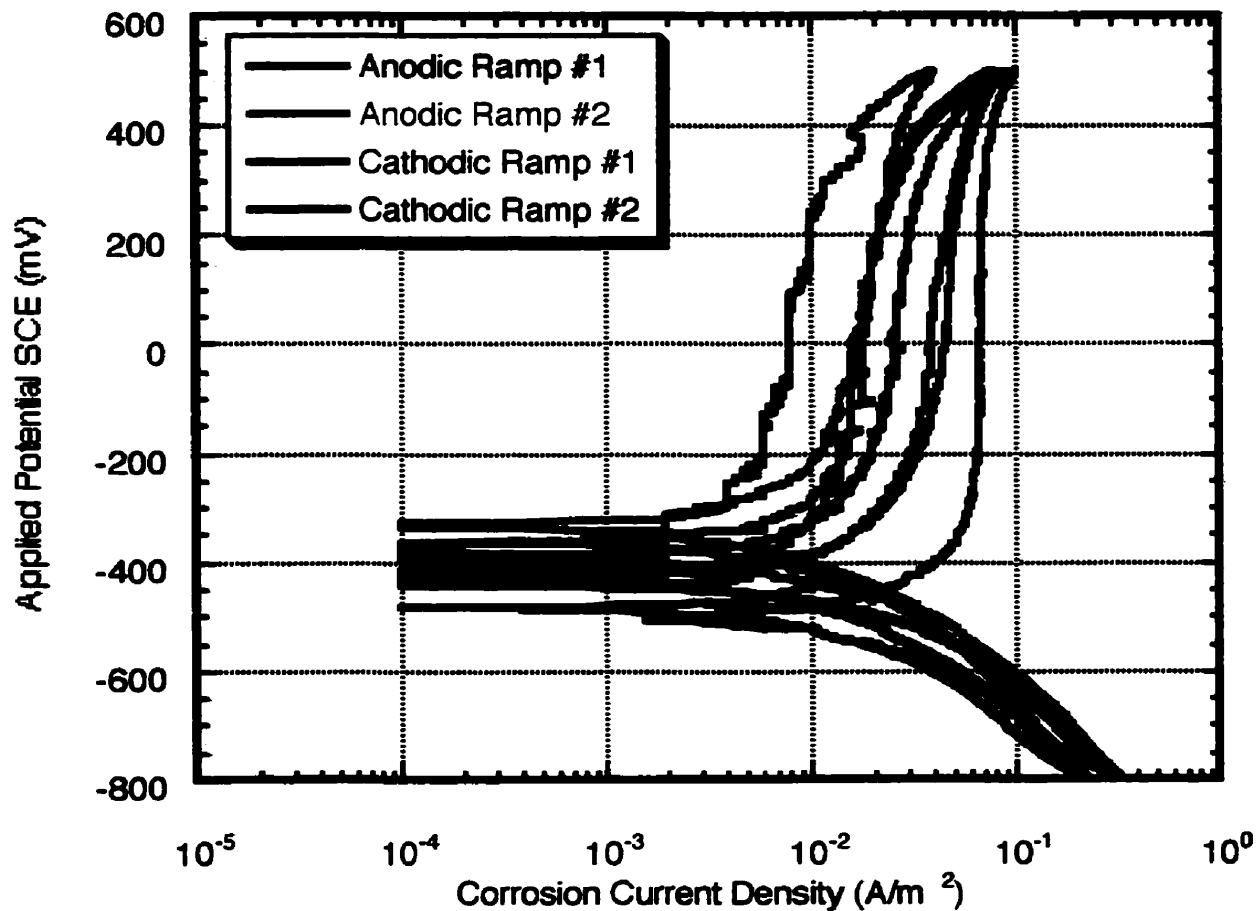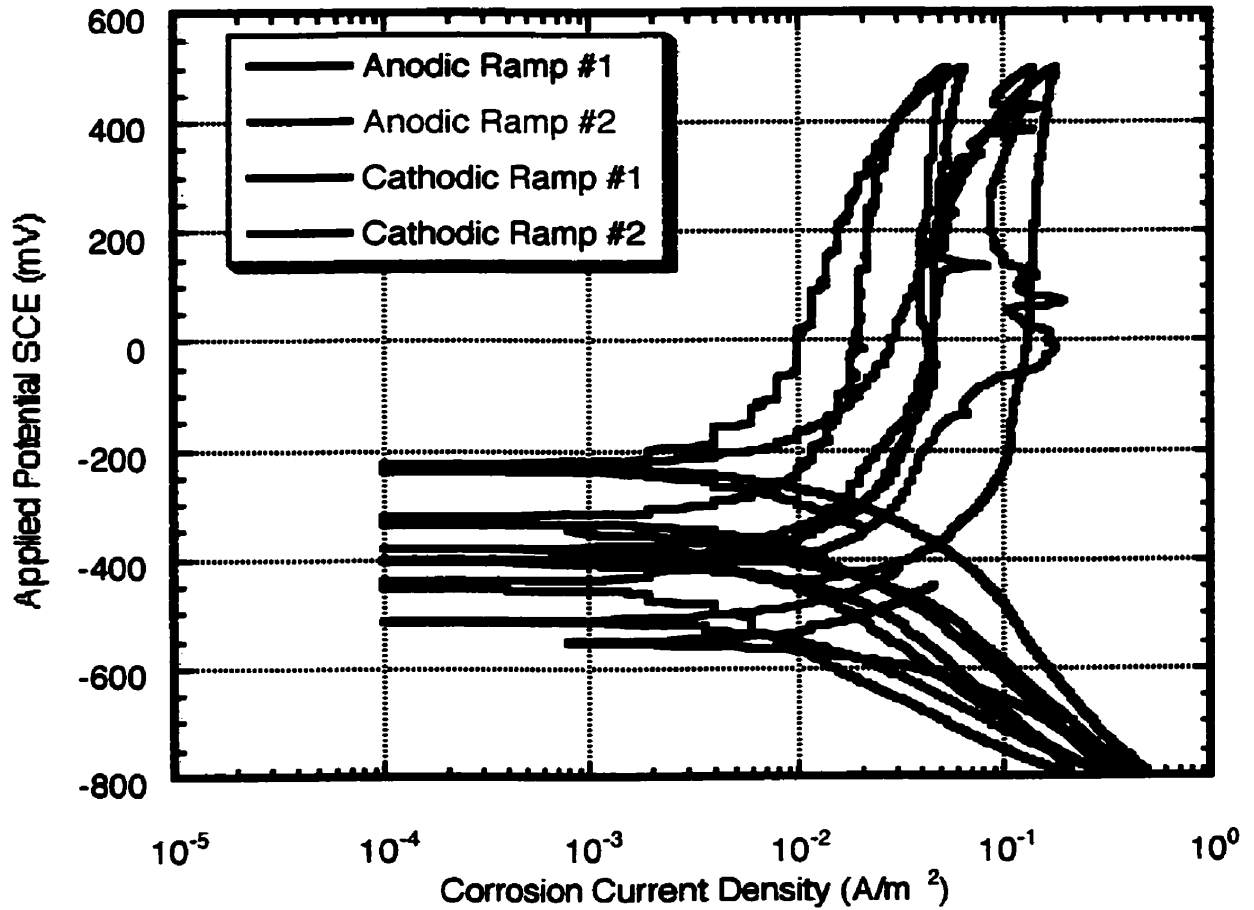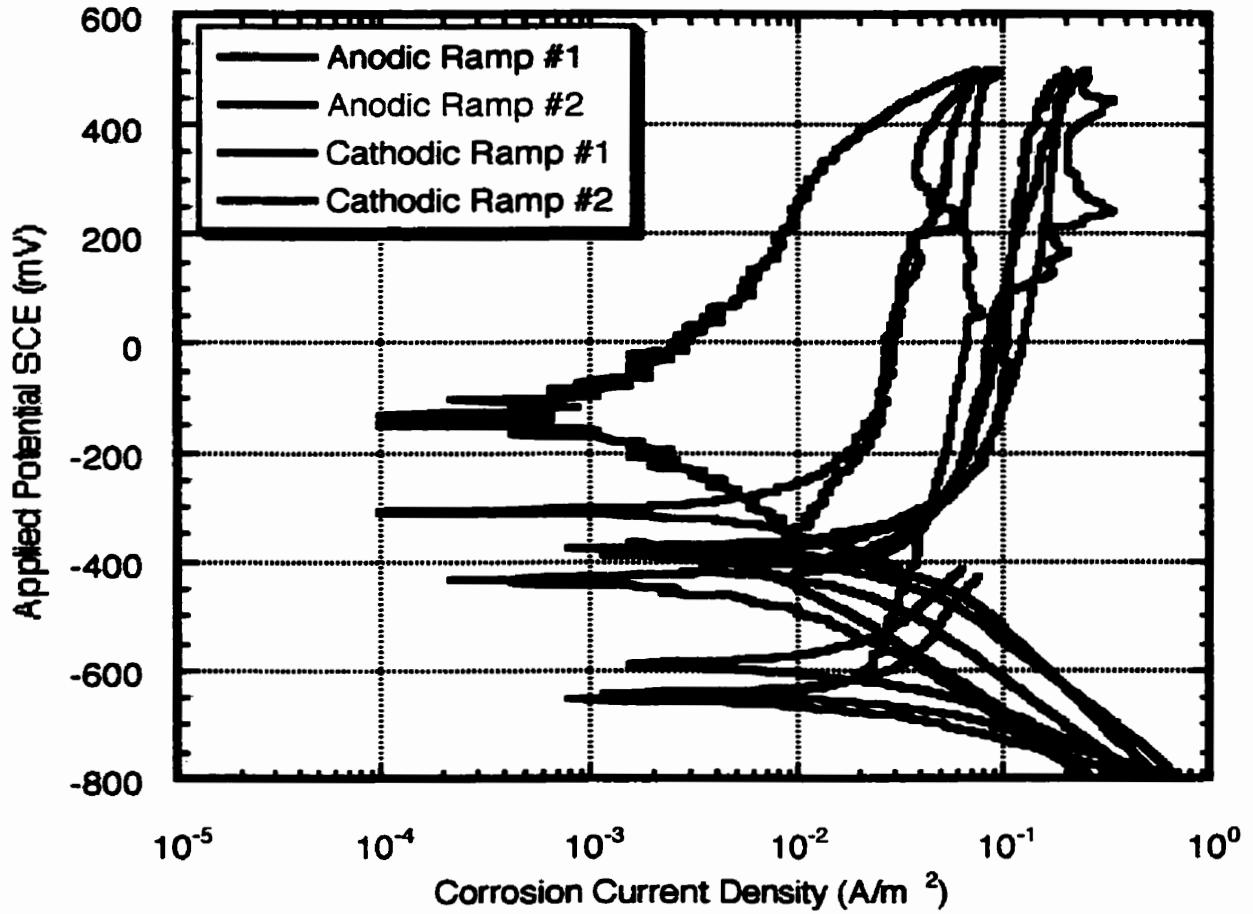
A.2.1 Type 10 Cement Simulated Pore Solution

Figure A.11 Comparison of the full polarization curves collected for the as-received surface of the samples immersed in a Type 10 cement simulated pore solution that did not contain chlorides.

280
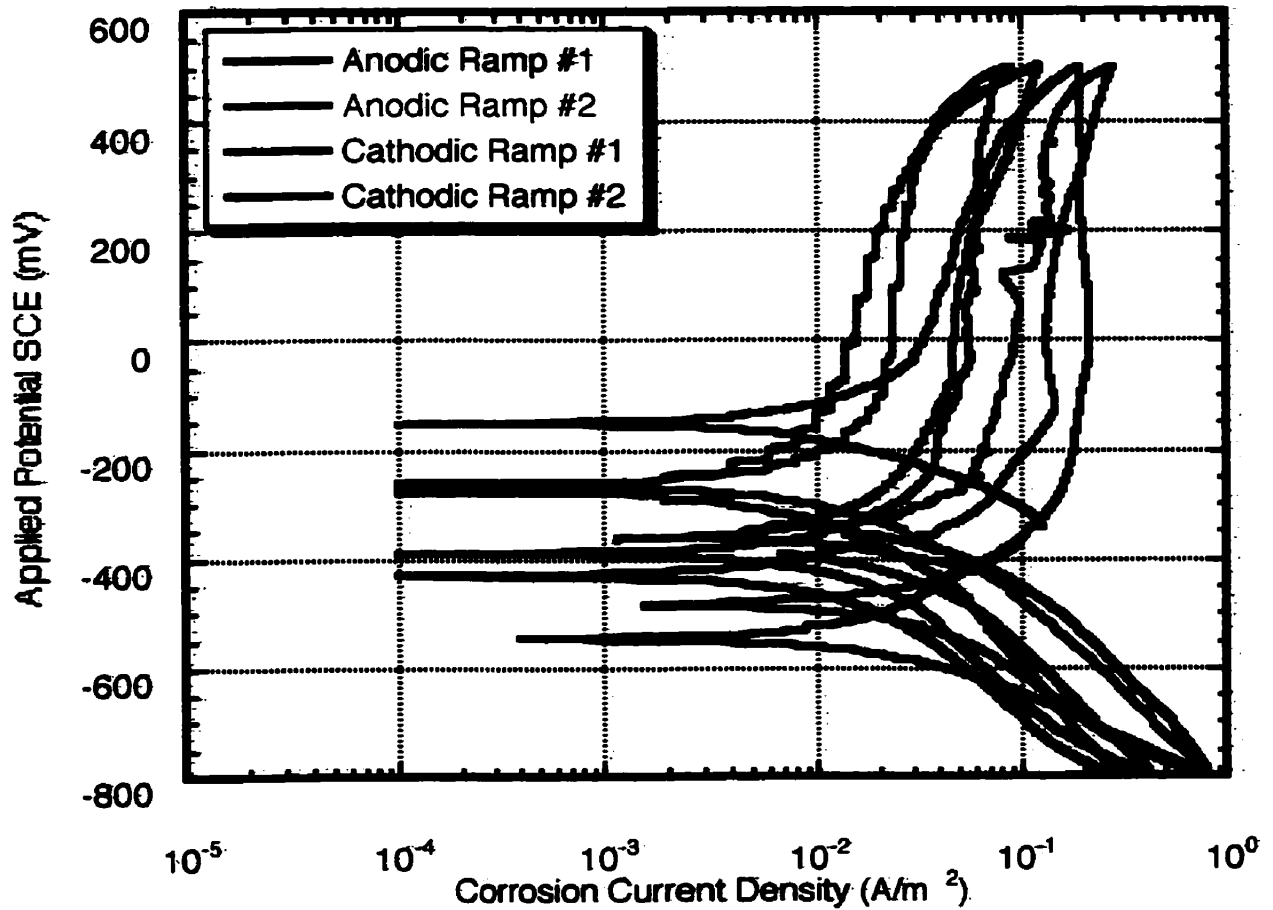
Figure A.12 Comparison of the full polarization curves collected for the as-received surface of the samples immersed in a Type 10 cement simulated pore solution that contained sufficient chlorides to make a 0.7 $[Cl^-]/[OH^-]$ solution.
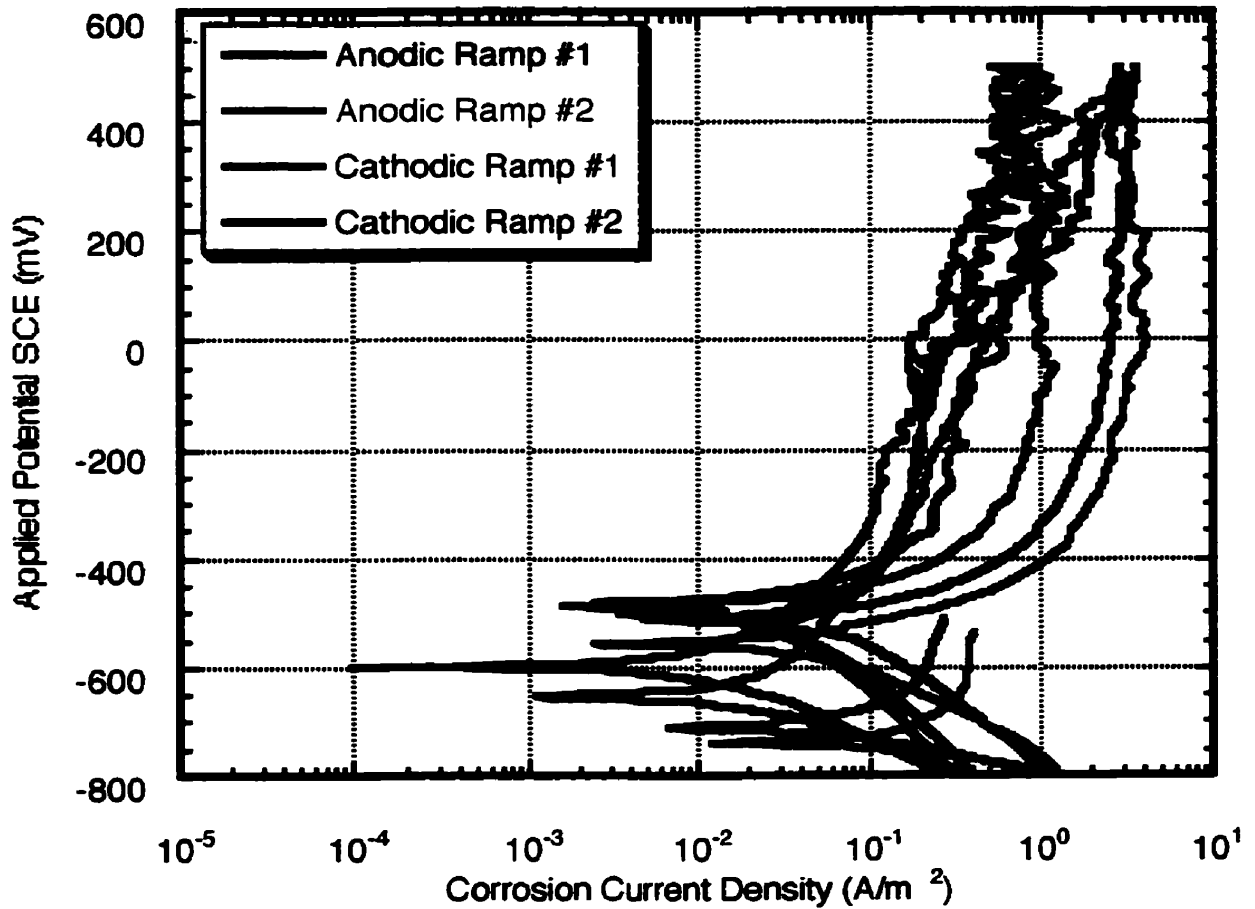
Figure A.13 Comparison of the full polarization curves collected for the as-received surface of the samples immersed in a Type 10 cement simulated pore solution that contained sufficient chlorides to make a 1.4 [Cl⁻]/[OH⁻] solution.

Figure A.14 Comparison of the full polarization curves collected for the as-received surface of the samples immersed in a Type 10 cement simulated pore solution that contained sufficient chlorides to make a 2.0 [Cl⁻]/[OH⁻] solution.

Figure A.15 Comparison of the full polarization curves collected for the as-received surfaces of steel samples immersed in a Type 10 cement simulated pore solution that contained sufficient chlorides to make a 4.0 [Cl⁻]/[OH⁻] solution (equivalent to a 1 M NaCl solution for pH 13.3).

A.2.2 White Cement Simulated Pore Solution

Figure A.16 Comparison of the full polarization curves collected for the as-received surface of the samples immersed in a White cement simulated pore solution that did not contain chlorides.

Figure A.17 Comparison of the full polarization curves collected for the as-received surface of the samples immersed in a White cement simulated pore solution that contained sufficient chlorides to make a 0.7 [Cl⁻]/[OH⁻] solution.

Figure A.18 Comparison of the full polarization curves collected for the as-received surface of the samples immersed in a White cement simulated pore solution that contained sufficient chlorides to make a 1.4 $[Cl^-]/[OH^-]$ solution.

Figure A.19 Comparison of the full polarization curves collected for the as-received surface of the samples immersed in a White cement simulated pore solution that contained sufficient chlorides to make a 2.0 [Cl⁻]/[OH⁻] solution.

Figure A.20 Comparison of the full polarization curves collected for the as-received surfaces of steel samples immersed in a White cement simulated pore solution that contained sufficient chlorides to make a 11.0 [Cl⁻]/[OH⁻] solution (equivalent to a 1 M NaCl solution for pH 12.9).

APPENDIX B

OPEN CIRCUIT POTENTIAL MAPS OF STEEL IN

MODIFIED CEMENT PASTE

B.1 INTRODUCTION

Open circuit potential maps were collected for the work of Chapter 5 to determine the effect of varying experimental conditions, shrinkage cracks, surface finish, and cement type on the changes that occur on the surface of the steel while exposed to simulated pore solutions containing sufficient chlorides to make a 1 M NaCl solution. Section B.2 presents the results for steel in the white modified cement paste after 12, 30, and 160 days exposure to the chloride-containing simulated pore solution. This Section was further subdivided between the cracked (Specimens 2, 3, 4, 6, and 9) and sealed (Specimens 1, 5, 7, 8, and 10) specimens in Sections B.2.1 and B.2.2, respectively. Similarly, Section B.3 presents the results for steel in the Type 10 modified cement paste. All specimens were analyzed after 50 days of exposure to the chloride-containing simulated pore solution but only those that were sectioned were again analyzed after 160 days exposure. Section B.3.1 presents the cracked specimens (Specimens 1, 5, 7, 8, and 10) while B.3.2 presents results for the sealed specimens (Specimens 2, 3, 4, 6, and 9).

The colours used for the potential maps indicate the approximate range of potentials measured, as delineated in Table B.1. In addition, the fine lines of the maps are isopotential lines while the heavier lines indicate the approximate position of any shrinkage cracks over the steel surfaces. Theory pertaining to the interpretation of the open circuit potential maps is presented in Section 2.4.1 and a discussion of these results is presented in Section 5.3.1.

Table B.1 Colours used in potential maps with respect to measured potential ranges.

Open Circuit Potential Range (mV SCE)	Colour	
- 350 to -450	Ruby Red	██
-450 to -550	Olive Green	██
-550 to -650	Rust Red	██
-750 to -850	Purple	██

B.2 STEEL IN WHITE MODIFIED CEMENT PASTE

B.2.1 Cracked Specimens

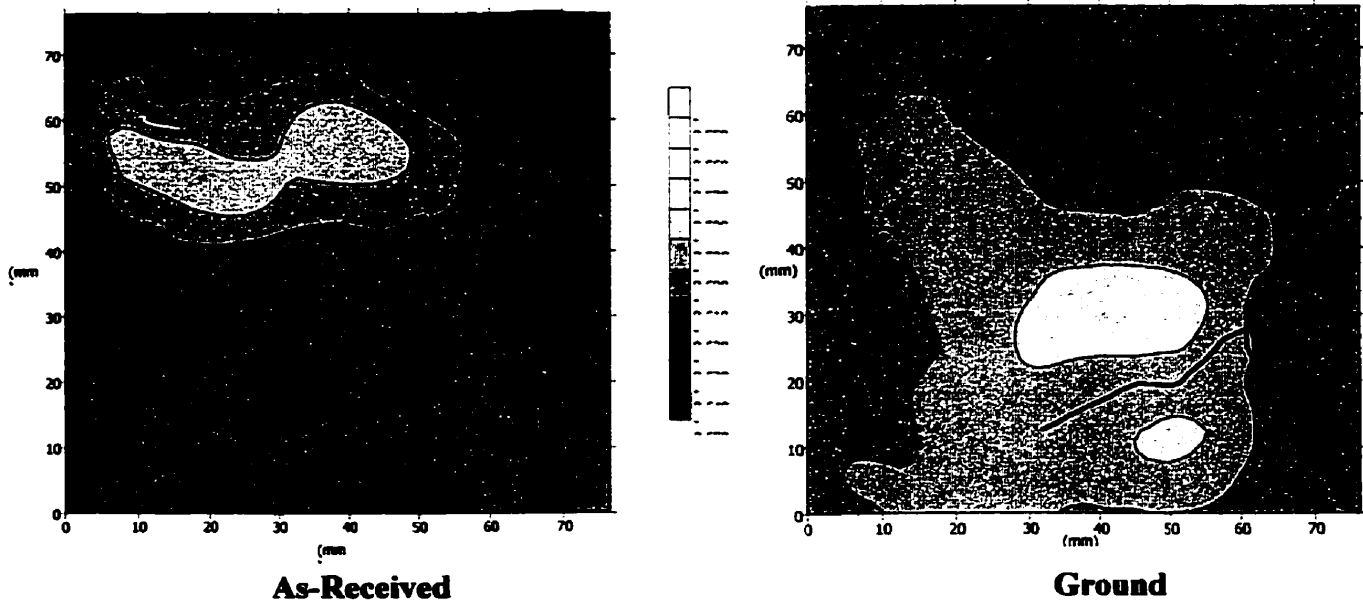**As-Received**   **Ground**

Figure B.2.1(a) Steel embedded in cracked white modified cement paste (Specimen 2) after exposure to the chloride-containing simulated pore solution for approx. 12 days (mV SCE).
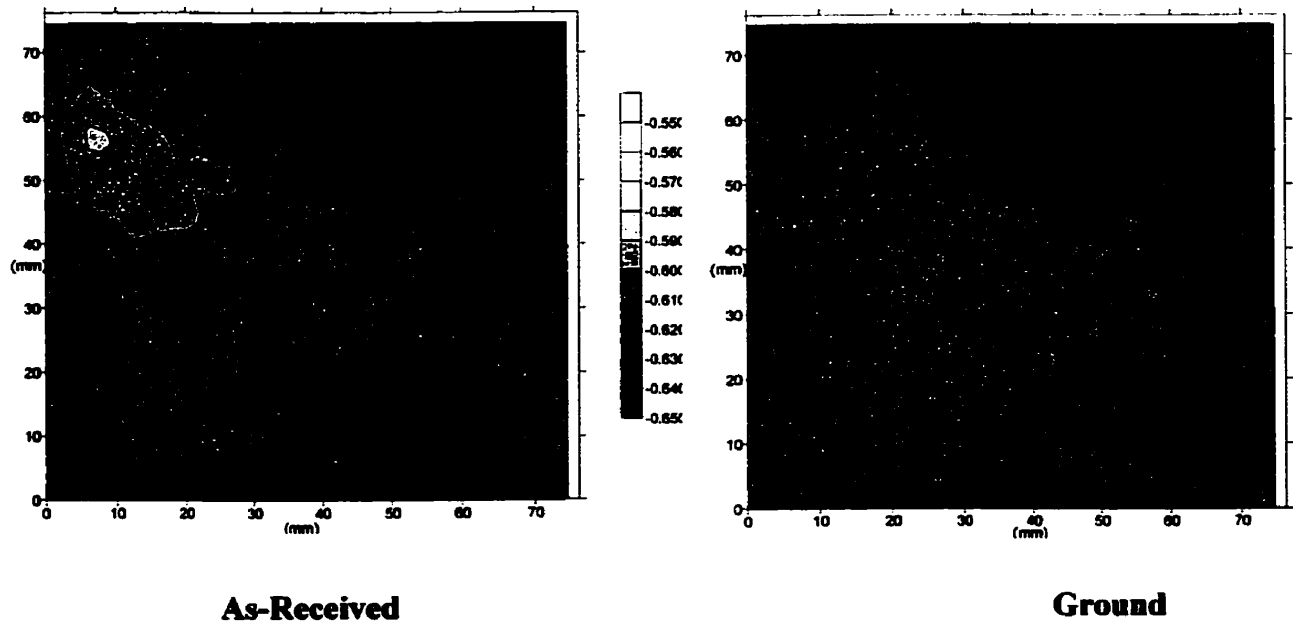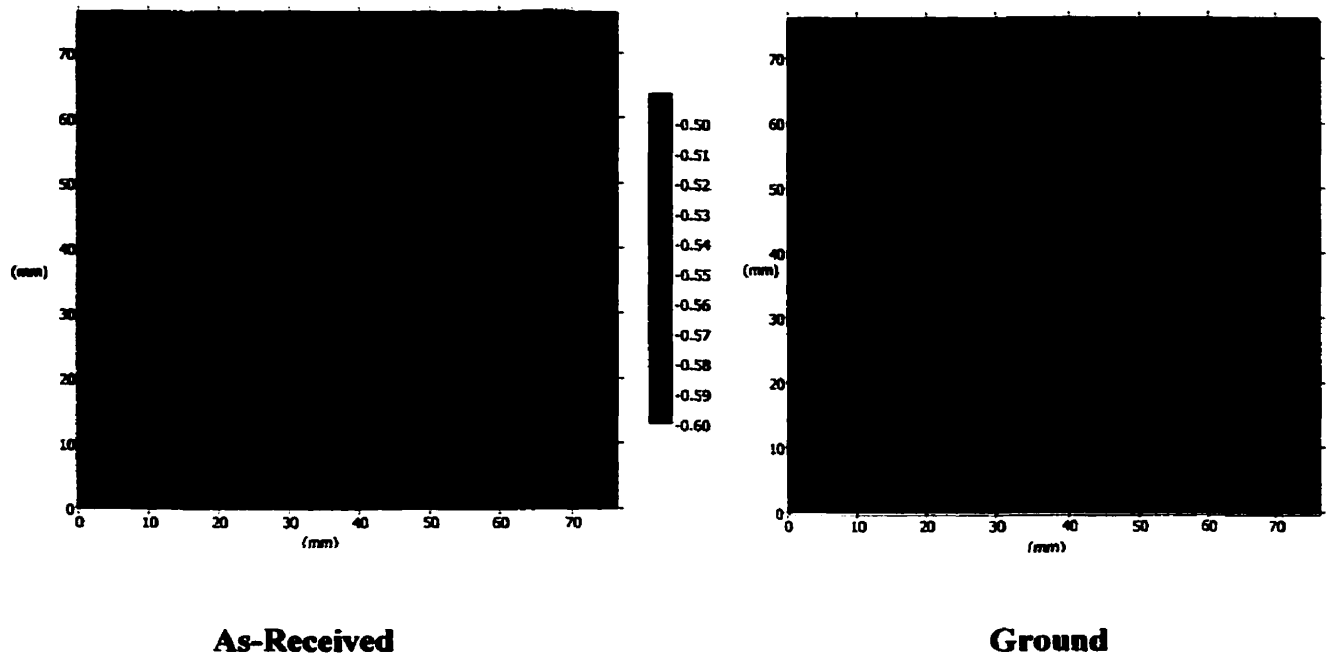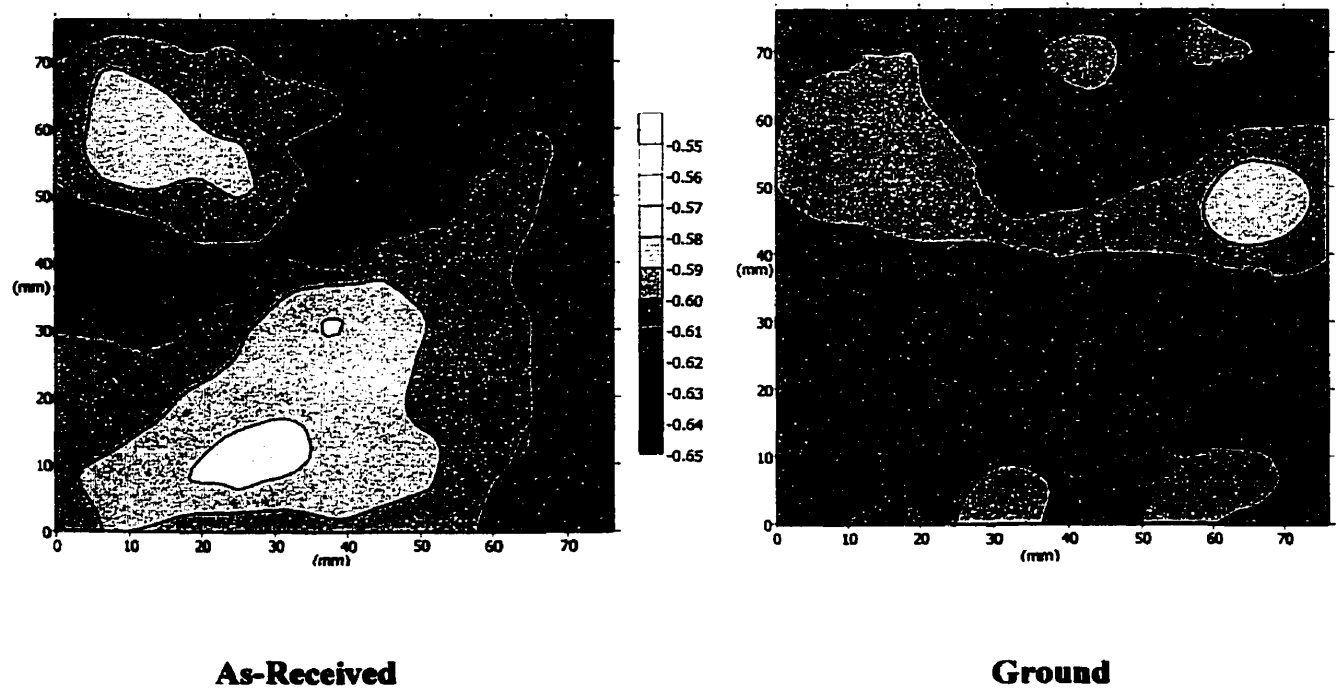

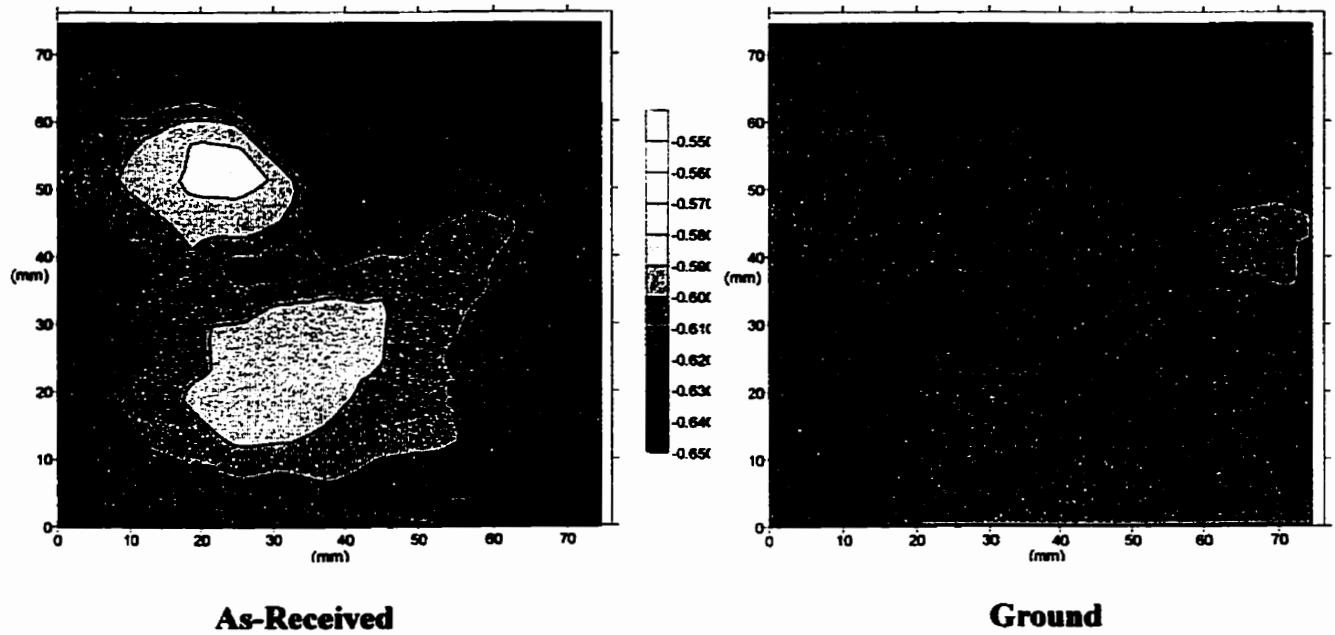**As-Received**   **Ground**

Figure B.2.1(b) Steel embedded in cracked white modified cement paste (Specimen 2) after exposure to the chloride-containing simulated pore solution for approx. 30 days (mV SCE).

291

As-Received   **Ground**

Figure B.2.1(c) Steel embedded in cracked white modified cement paste (Specimen 2) after exposure to the chloride-containing simulated pore solution for approx. 160 days (mV SCE).
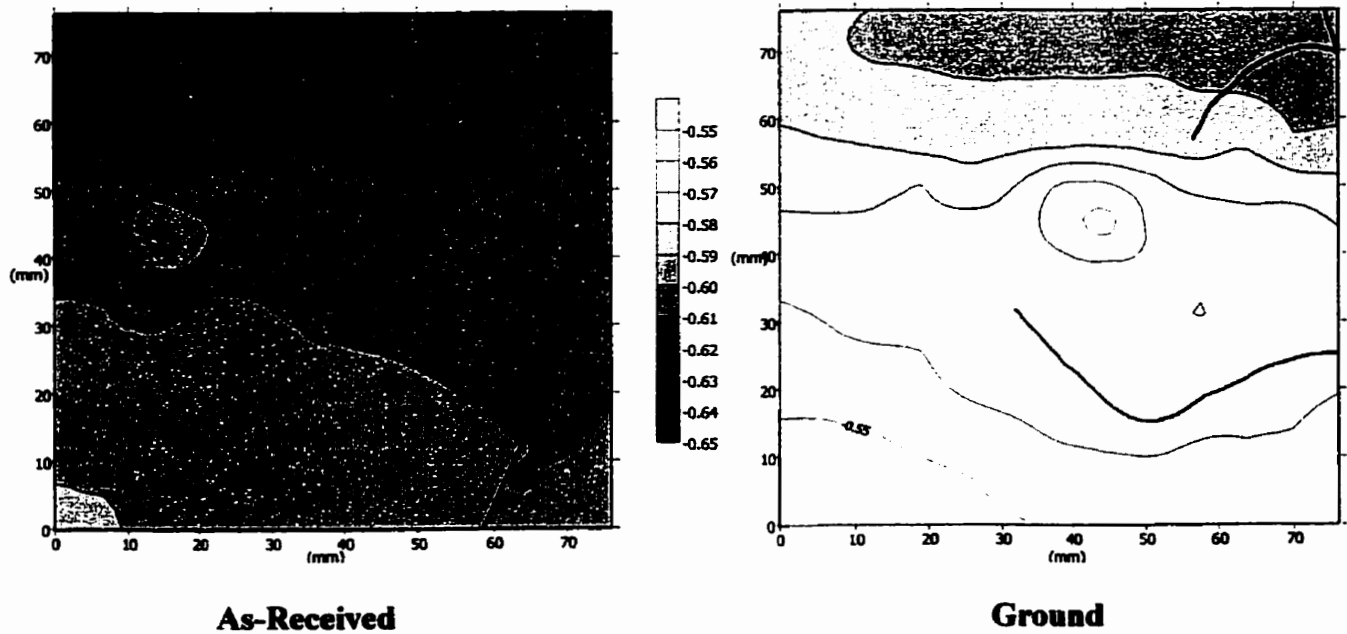

As-Received   **Ground**

Figure B.2.1(d) Steel embedded in cracked white modified cement paste (Specimen 3) after exposure to the chloride-containing simulated pore solution for approx. 12 days (mV SCE).

292

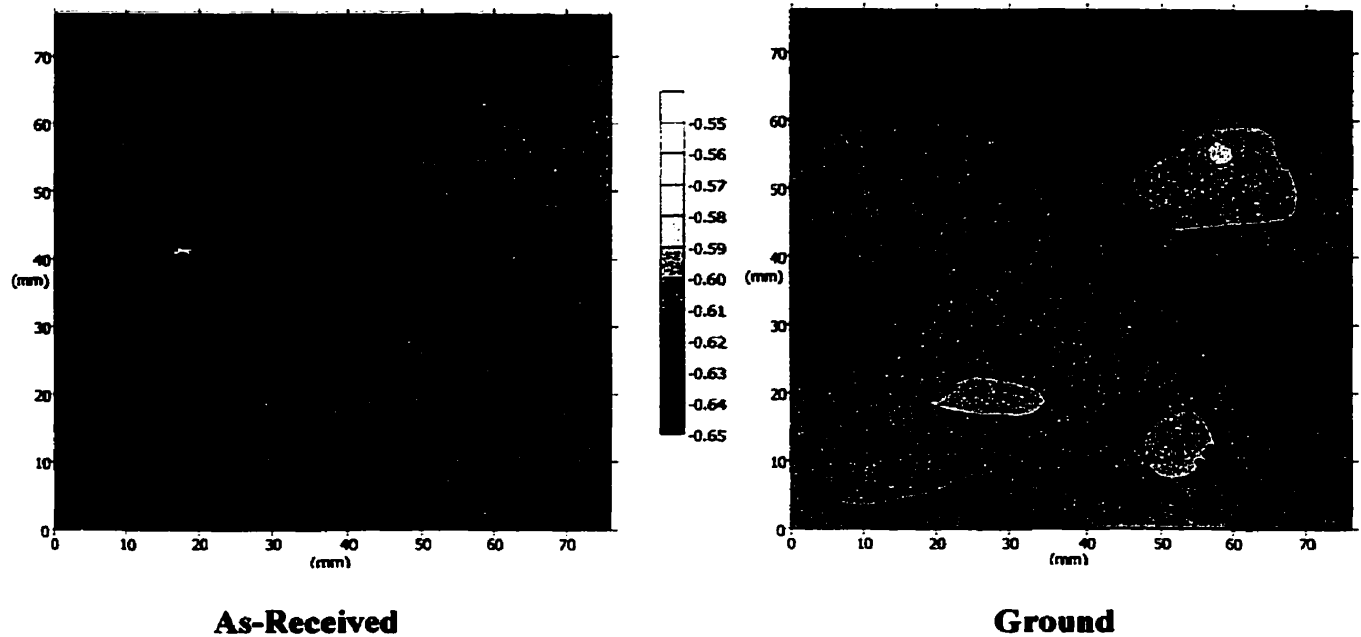**As-Received**   **Ground**

Figure B.2.1(e) Steel embedded in cracked white modified cement paste (Specimen 3) after exposure to the chloride-containing simulated pore solution for approx. 30 days (mV SCE).

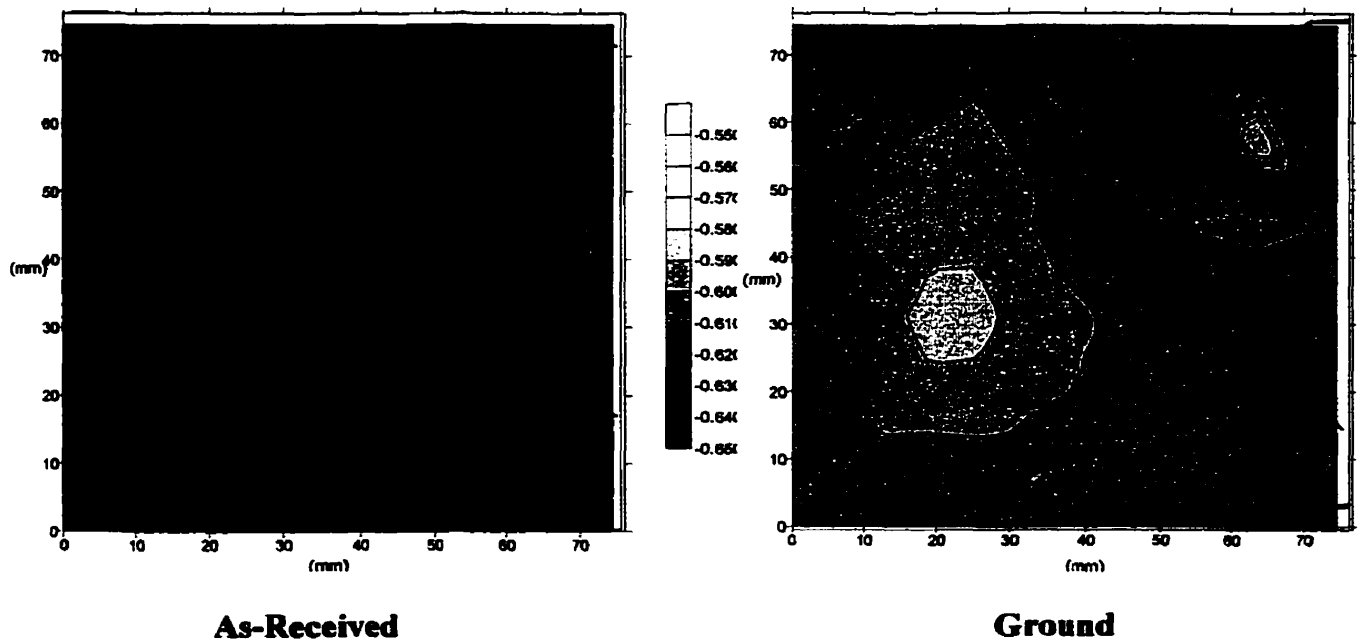**As-Received**   **Ground**

Figure B.2.1(f) Steel embedded in cracked white modified cement paste (Specimen 3) after exposure to the chloride-containing simulated pore solution for approx. 160 days (mV SCE).

293

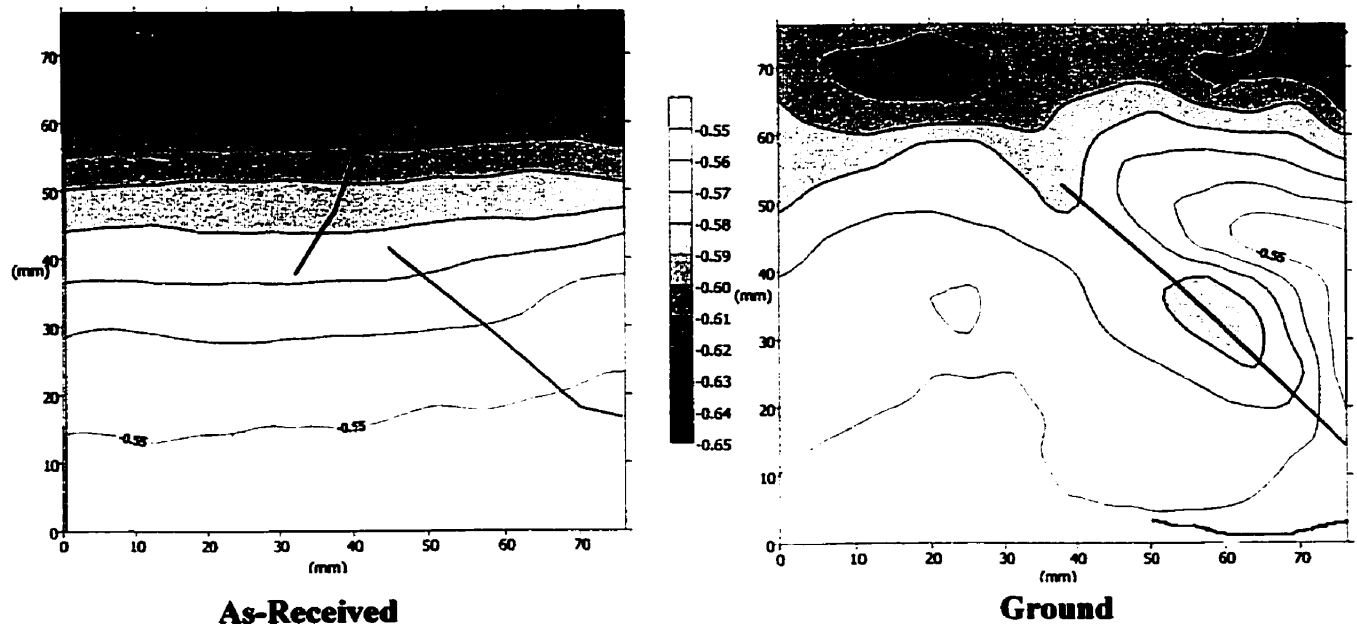**As-Received**   **Ground**

Figure B.2.1(g) Steel embedded in cracked white modified cement paste (Specimen 4) after exposure to the chloride-containing simulated pore solution for approx. 12 days (mV SCE).

As-Received   **Ground**

Figure B.2.1(h) Steel embedded in cracked white modified cement paste (Specimen 4) after exposure to the chloride-containing simulated pore solution for approx. 30 days (mV SCE).
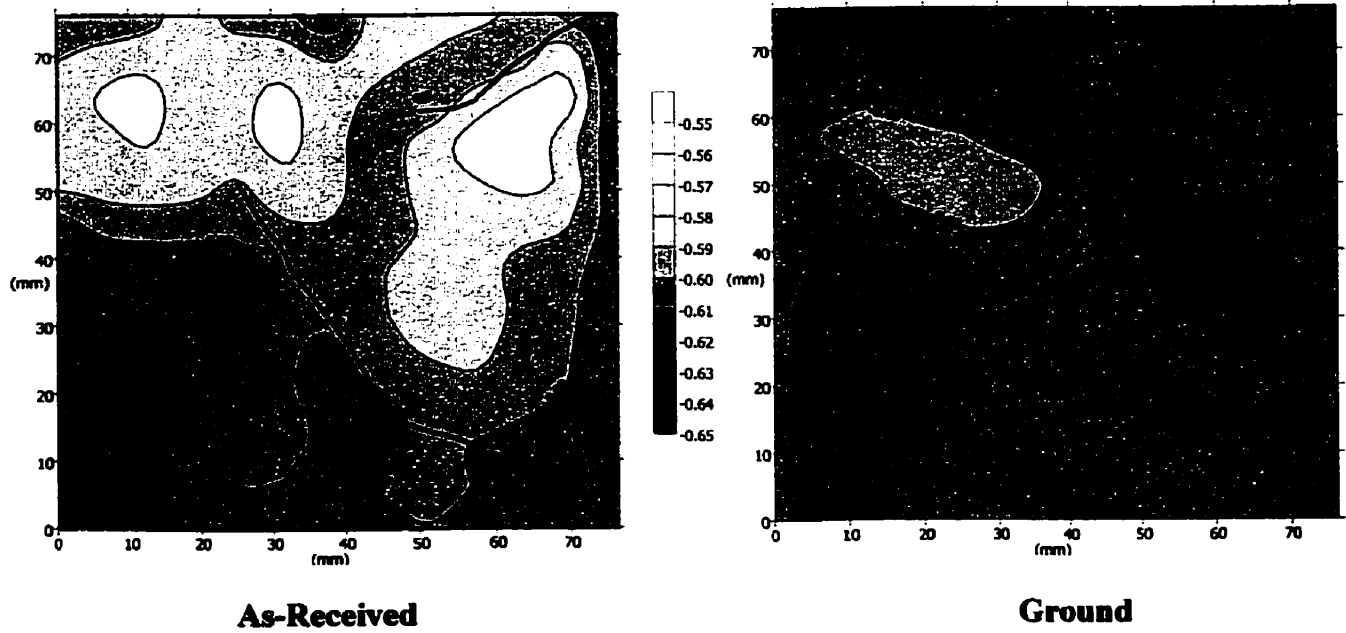
As-Received   **Ground**

Figure B.2.1(i) Steel embedded in cracked white modified cement paste (Specimen 4) after exposure to the chloride-containing simulated pore solution for approx. 160 days (mV SCE).
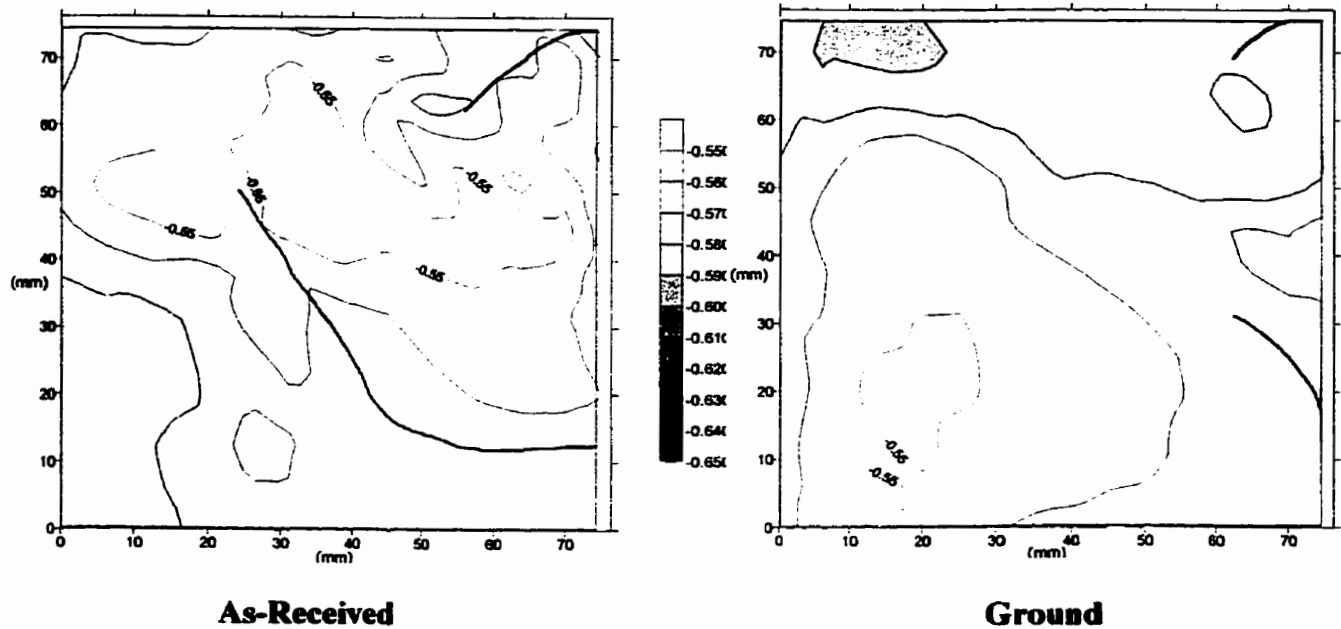

As-Received   **Ground**

Figure B.2.1(j) Steel embedded in cracked white modified cement paste (Specimen 6) after exposure to the chloride-containing simulated pore solution for approx. 12 days (mV SCE).

295

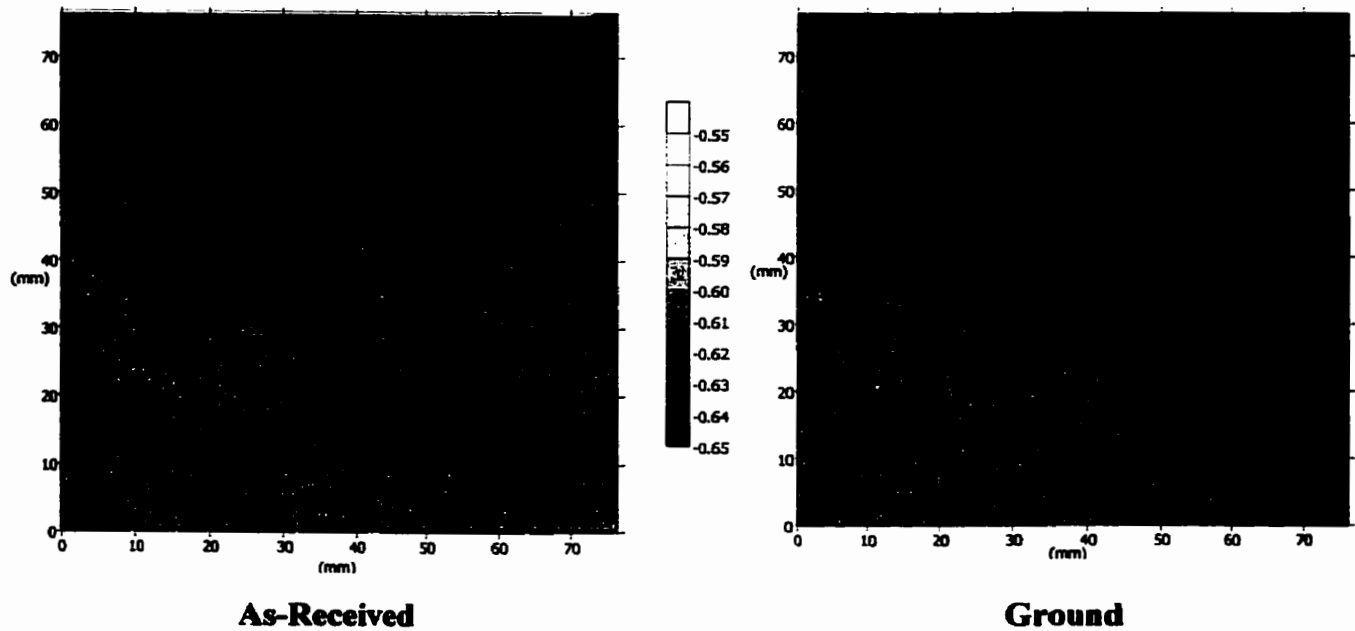**As-Received**   **Ground**

Figure B.2.1(k) Steel embedded in cracked white modified cement paste (Specimen 6) after exposure to the chloride-containing simulated pore solution for approx. 30 days (mV SCE).

As-Received   **Ground**

Figure B.2.1(l) Steel embedded in cracked white modified cement paste (Specimen 6) after exposure to the chloride-containing simulated pore solution for approx. 160 days (mV SCE).

296
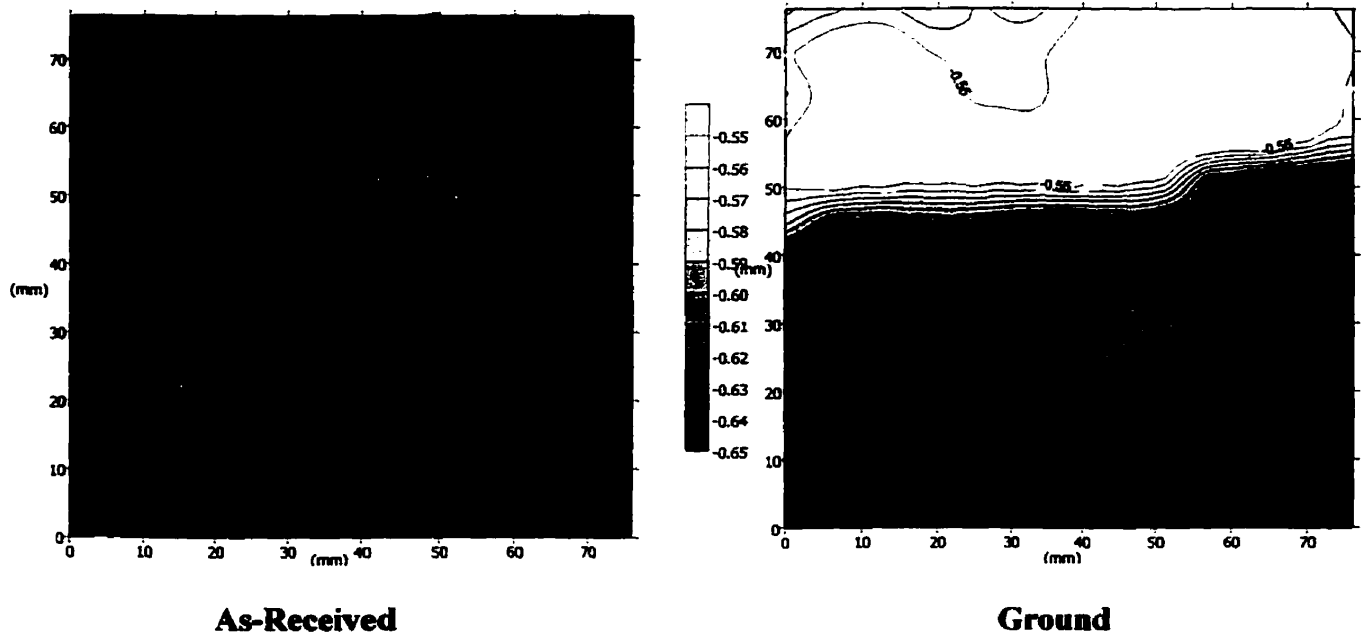
As-Received

Ground

Figure B.2.1(m) Steel embedded in cracked white modified cement paste (Specimen 9) after exposure to the chloride-containing simulated pore solution for approx. 12 days (mV SCE). Note: The white area on the ground steel plot is an artifact resulting from the specimen becoming too dry during the measurement procedure.

As-Received

Ground

Figure B.2.1(n) Steel embedded in cracked white modified cement paste (Specimen 9) after exposure to the chloride-containing simulated pore solution for approx. 30 days (mV SCE).
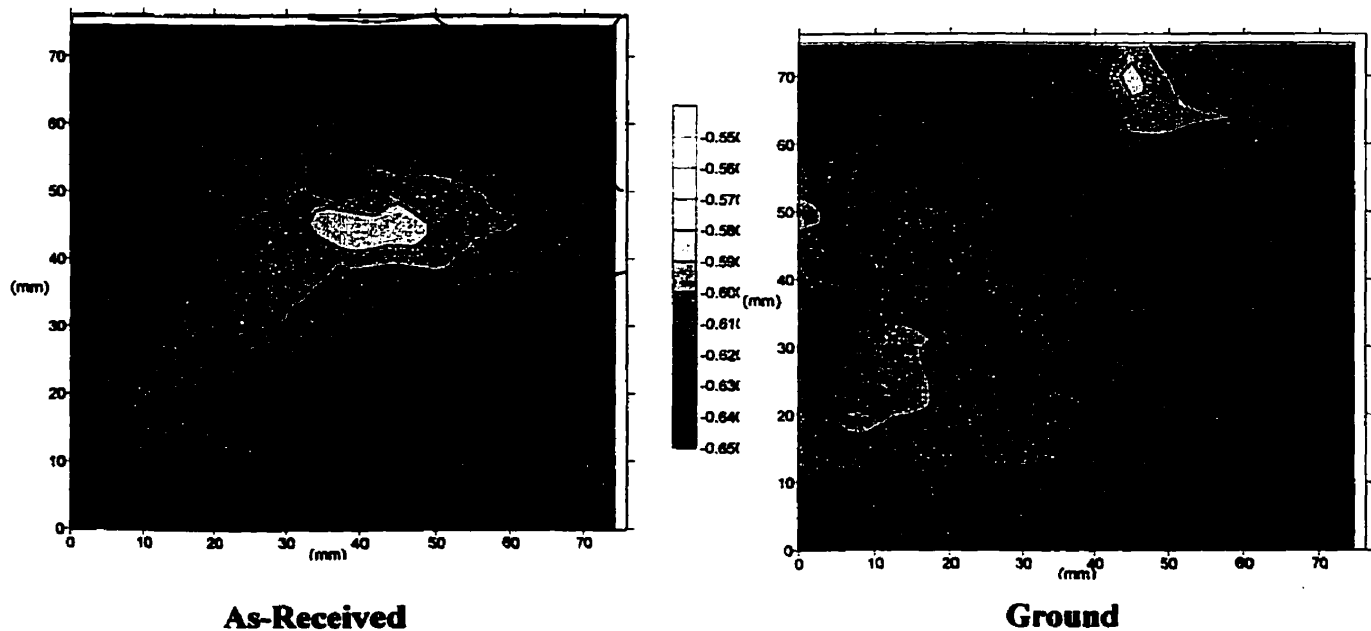
As-Received

Ground

Figure B.2.1(o) Steel embedded in cracked white modified cement paste (Specimen 9) after exposure to the chloride-containing simulated pore solution for approx. 160 days (mV SCE).

B.2.2 Sealed Specimens

As-Received   **Ground**

Figure B.2.2(a) Steel embedded in sealed white modified cement paste (Specimen 1) after exposure to the chloride-containing simulated pore solution for approx. 12 days (mV SCE).
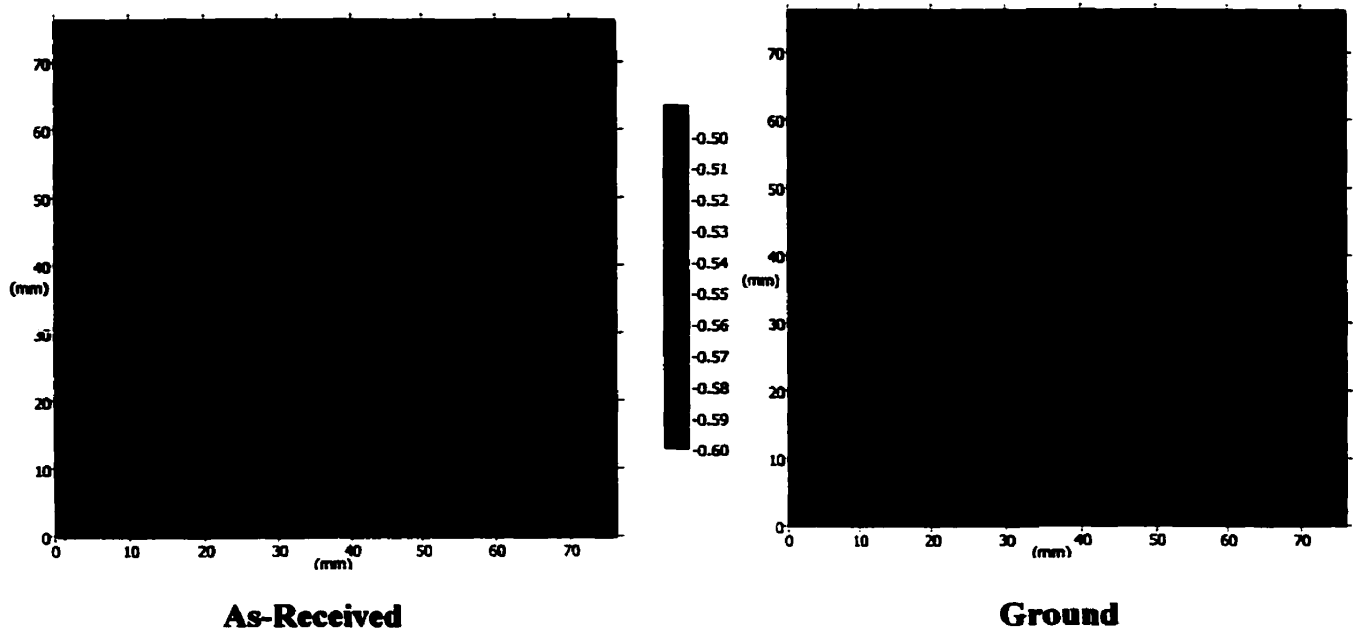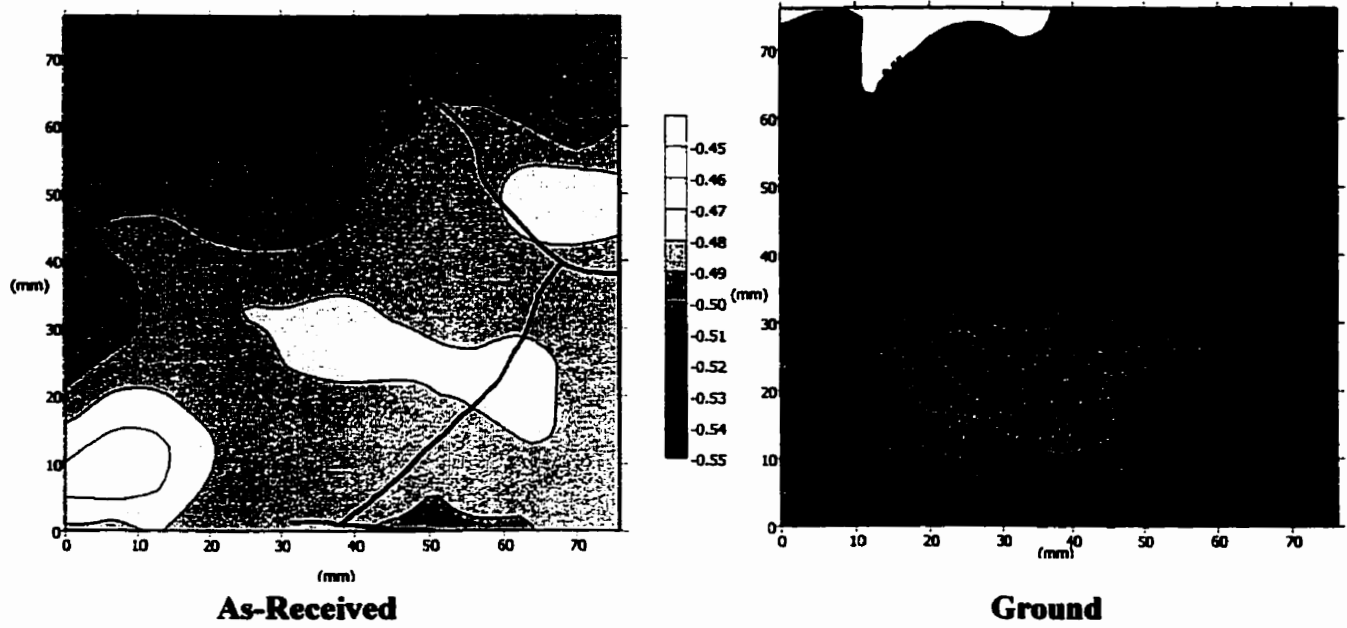

As-Received   **Ground**

Figure B.2.2(b) Steel embedded in sealed white modified cement paste (Specimen 1) after exposure to the chloride-containing simulated pore solution for approx. 30 days (mV SCE).

As-Received   **Ground**

Figure B.2.2(c) Steel embedded in sealed white modified cement paste (Specimen 1) after exposure to the chloride-containing simulated pore solution for approx. 160 days (mV SCE).
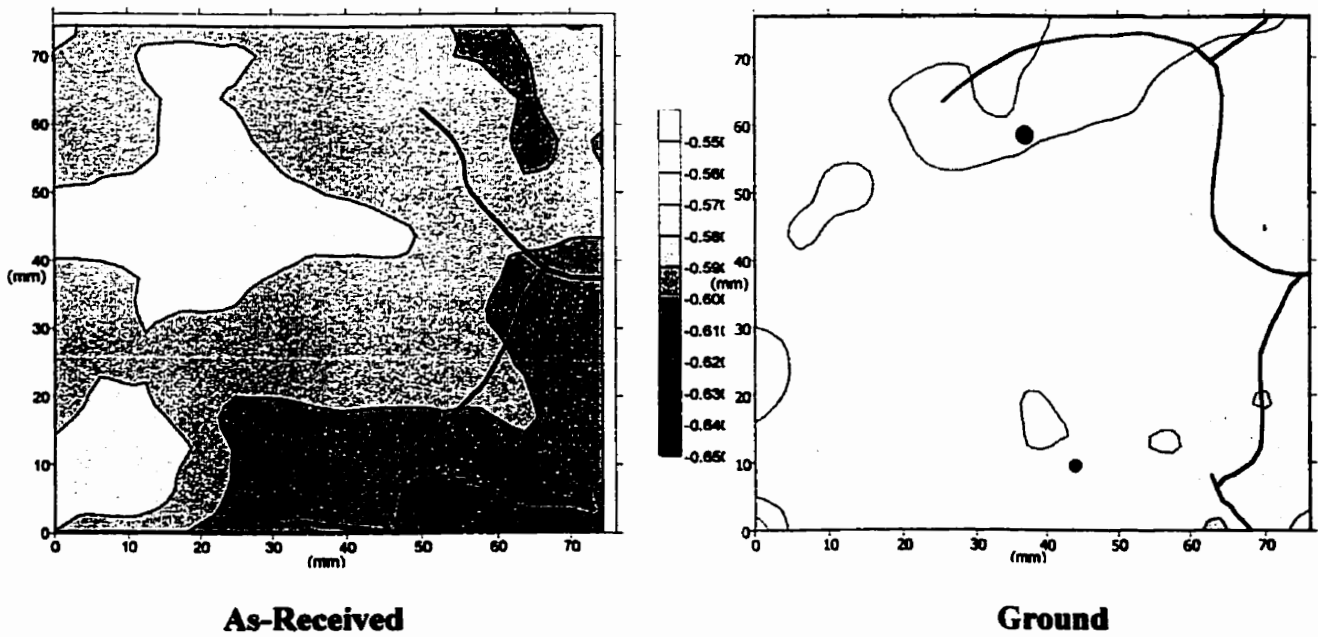

As-Received   **Ground**

Figure B.2.2(d) Steel embedded in sealed white modified cement paste (Specimen 5) after exposure to the chloride-containing simulated pore solution for approx. 12 days (mV SCE).
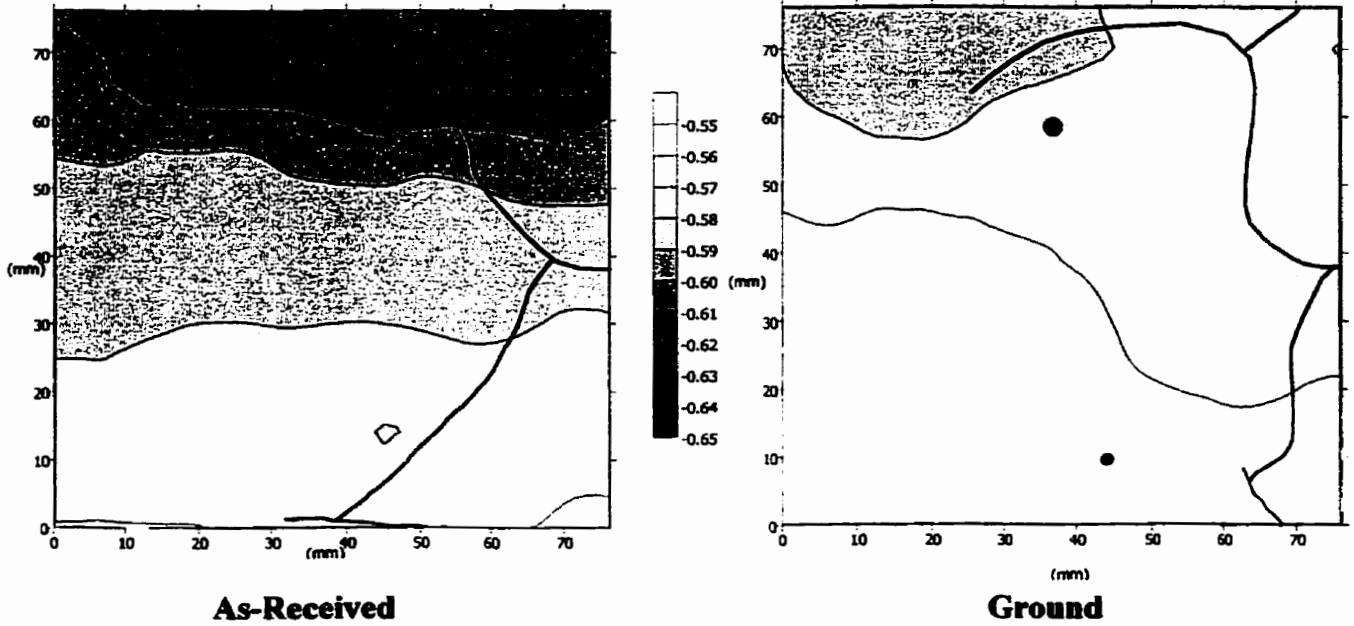
300

Figure B.2.2(e) Steel embedded in sealed white modified cement paste (Specimen 5) after exposure to the chloride-containing simulated pore solution for approx. 30 days (mV SCE).

Figure B.2.2(f) Steel embedded in sealed white modified cement paste (Specimen 5) after exposure to the chloride-containing simulated pore solution for approx. 160 days (mV SCE).

As-Received   Ground

Figure B.2.2(g) Steel embedded in sealed white modified cement paste (Specimen 7) after exposure to the chloride-containing simulated pore solution for approx. 12 days (mV SCE).
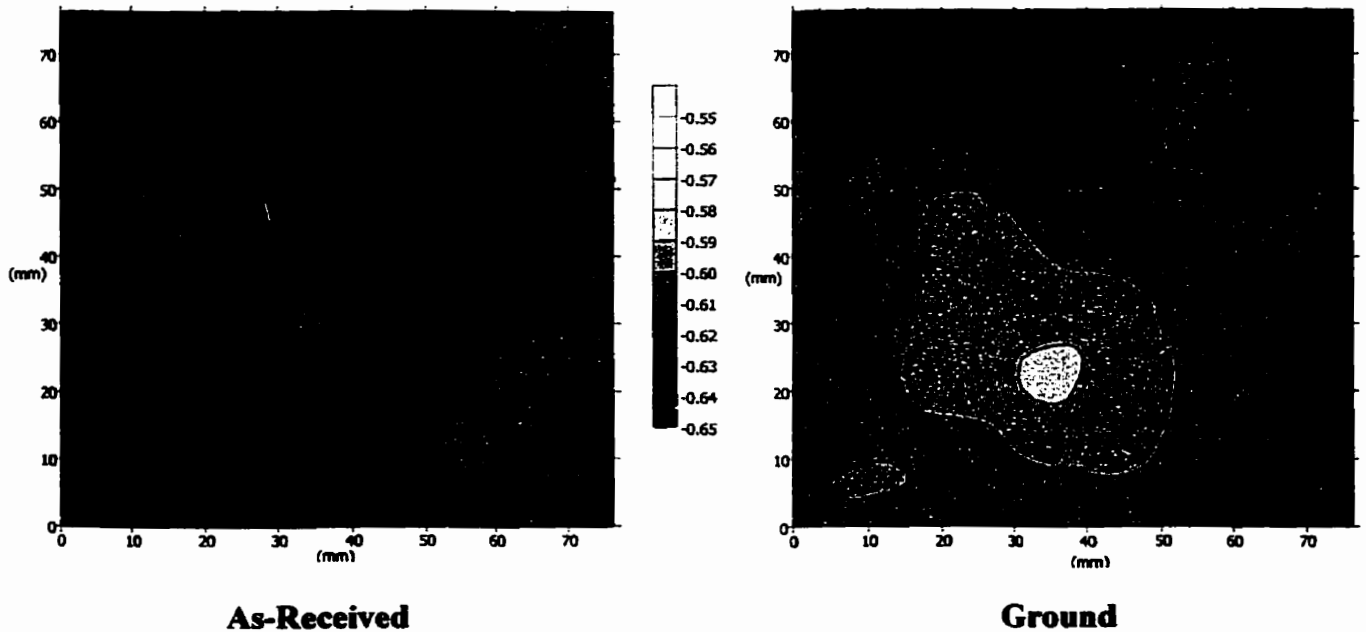

As-Received   Ground

Figure B.2.2(h) Steel embedded in sealed white modified cement paste (Specimen 7) after exposure to the chloride-containing simulated pore solution for approx. 30 days (mV SCE).

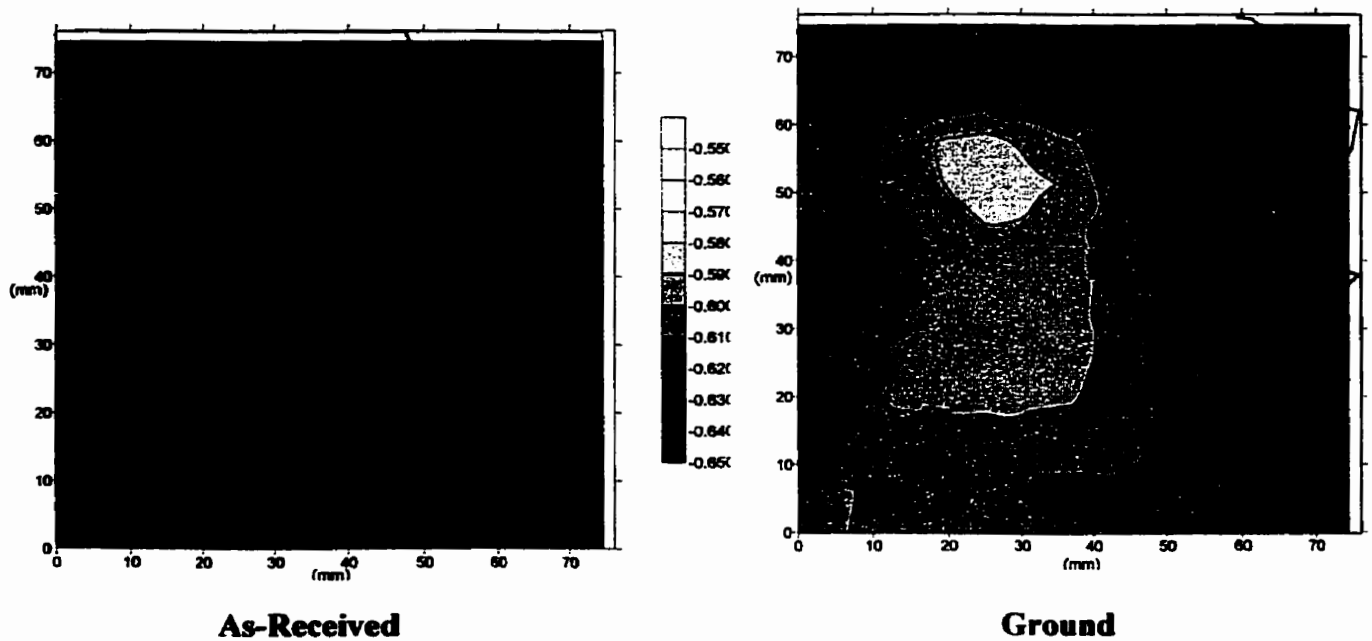**As-Received**   **Ground**

Figure B.2.2(i) Steel embedded in sealed white modified cement paste (Specimen 7) after exposure to the chloride-containing simulated pore solution for approx. 160 days (mV SCE).

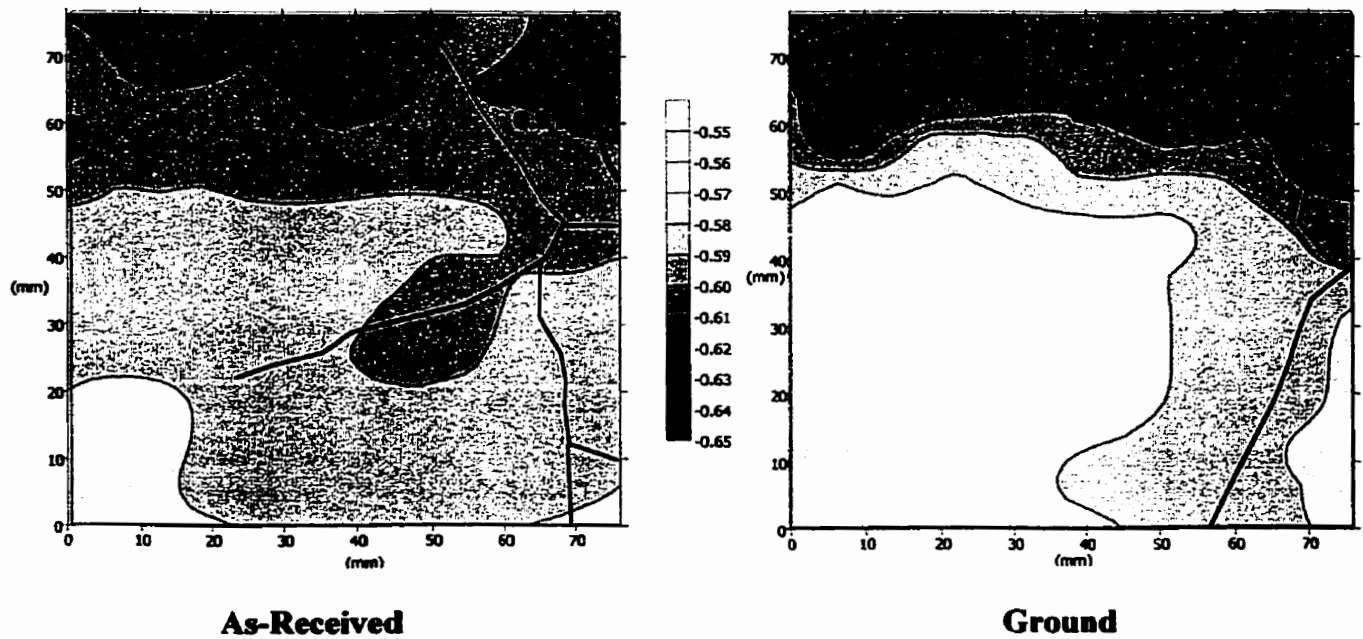**As-Received**   **Ground**

Figure B.2.2(j) Steel embedded in sealed white modified cement paste (Specimen 8) after exposure to the chloride-containing simulated pore solution for approx. 12 days (mV SCE).

303

As-Received

Figure B.2.2(k) Steel embedded in sealed white mo
exposure to the chloride-containing simulated pore s

As-Received

Figure B.2.2(l) Steel embedded in sealed white mod
exposure to the chloride-containing simulated pore s

304

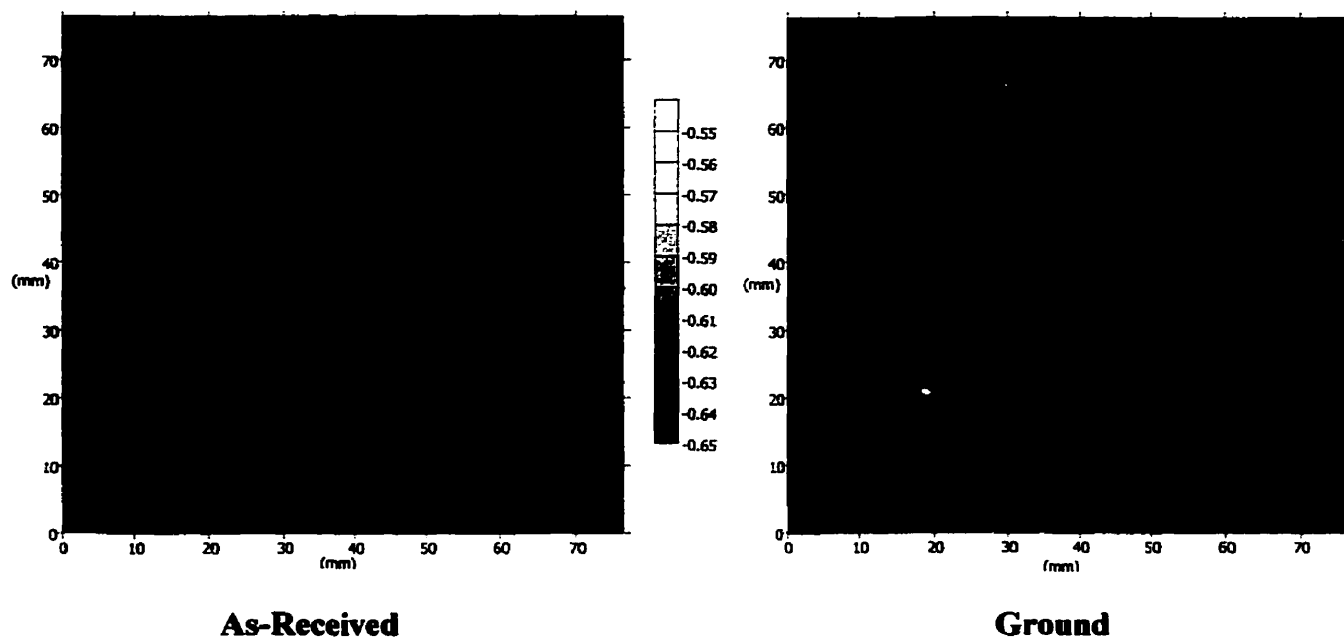**As-Received**   **Ground**
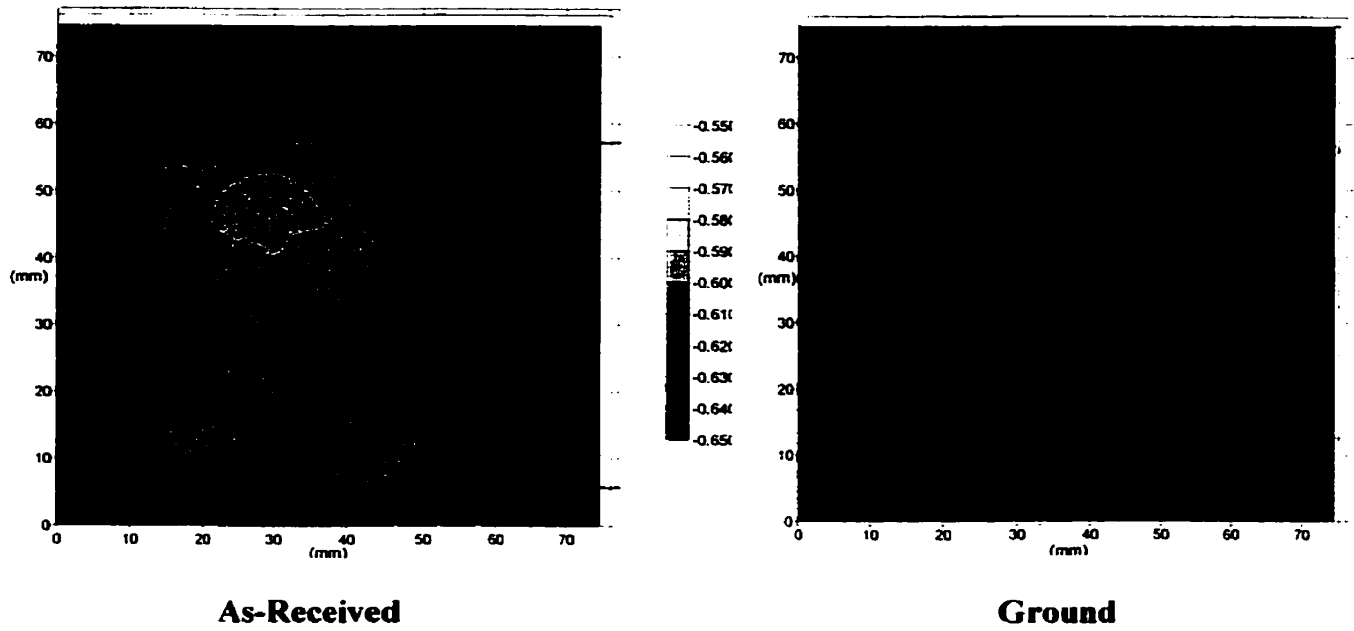
Figure B.2.2(m) Steel embedded in sealed white modified cement paste (Specimen 10) after exposure to the chloride-containing simulated pore solution for approx. 30 days (mV SCE).
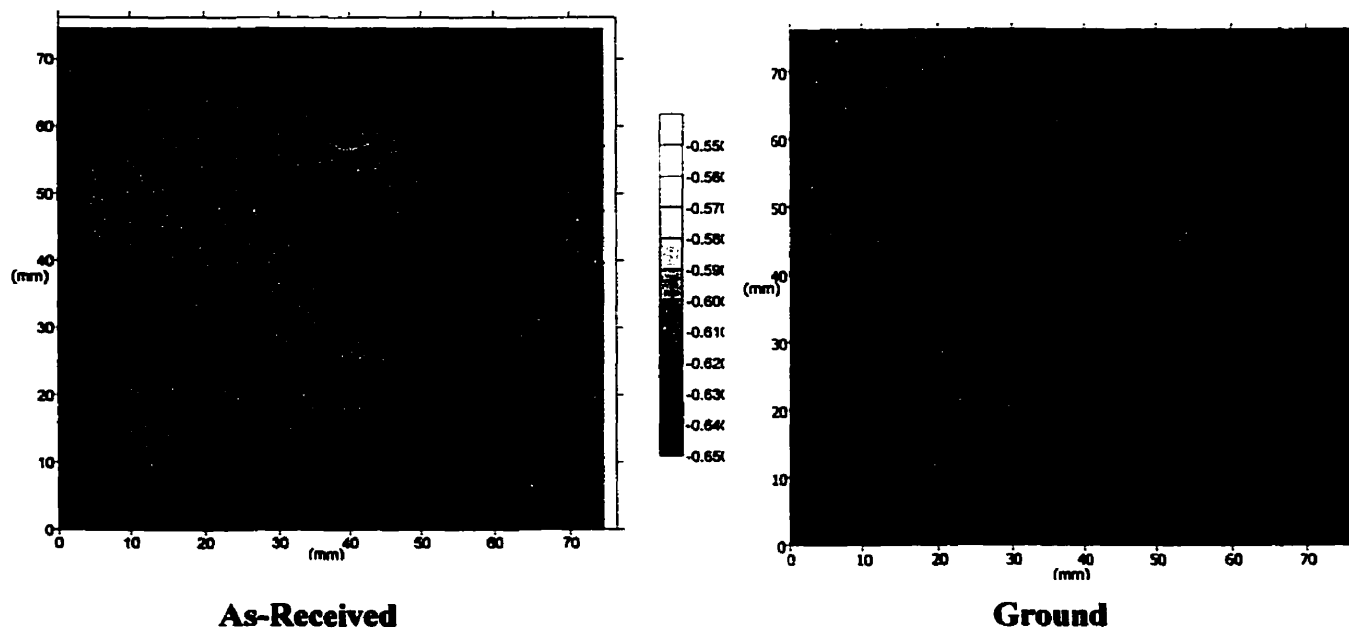

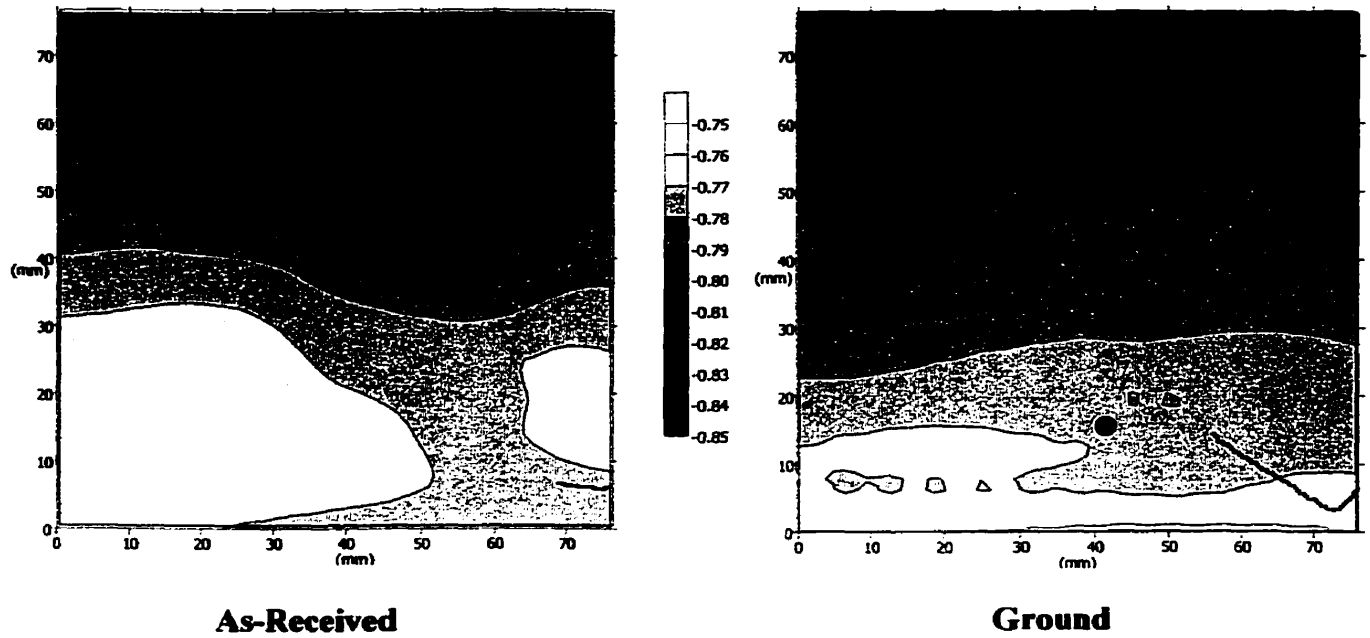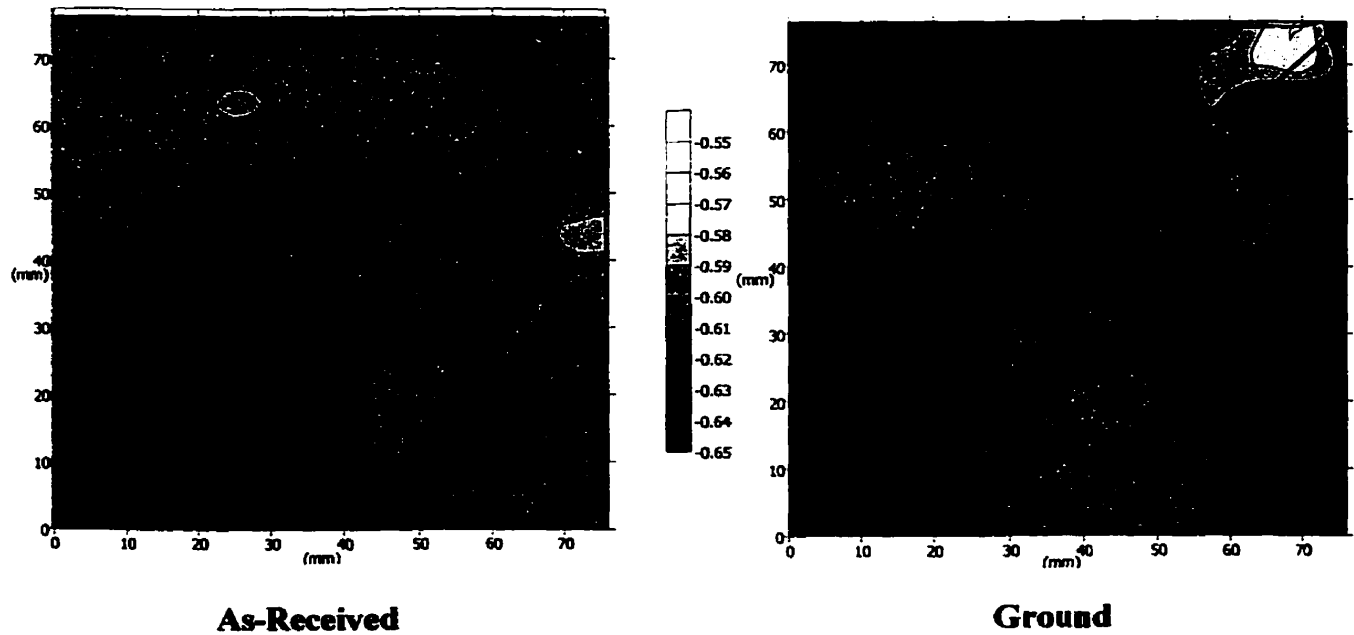**As-Received**   **Ground**
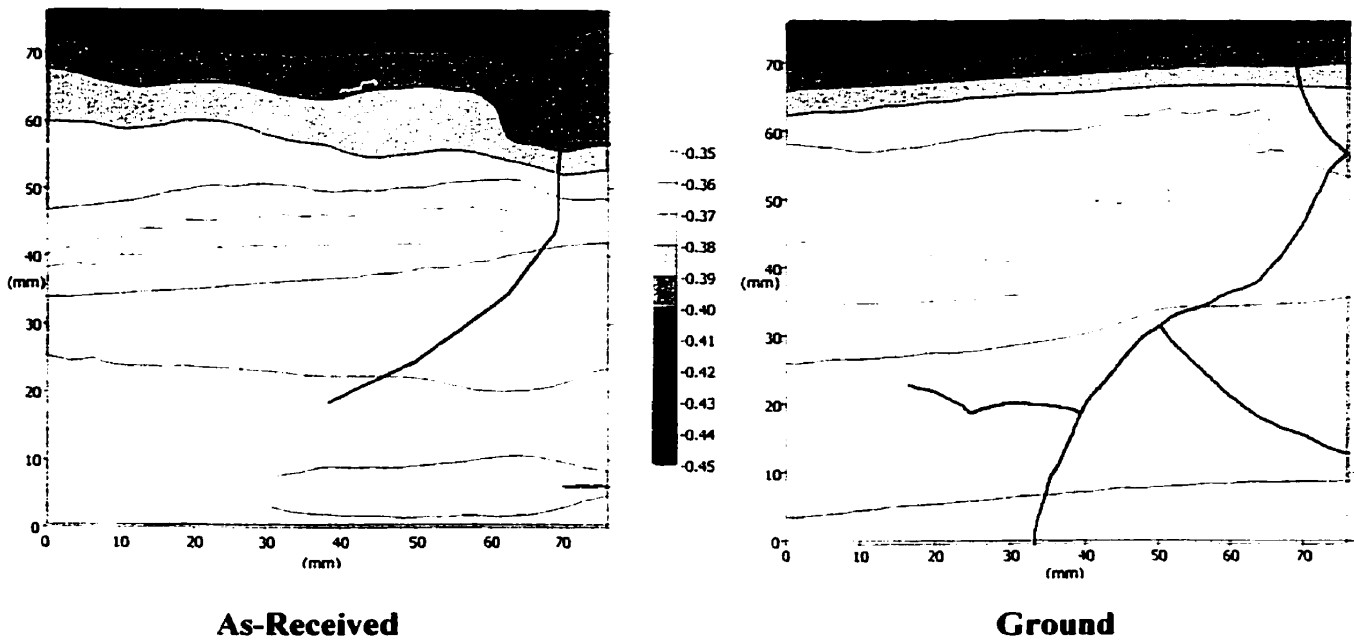
Figure B.2.2(n) Steel embedded in sealed white modified cement paste (Specimen 10) after exposure to the chloride-containing simulated pore solution for approx. 160 days (mV SCE).

305

B.3 STEEL IN TYPE 10 MODIFIED CEMENT PASTE

B.3.1 Cracked Specimens

As-Received

Ground

Figure B.3.1(a) Steel embedded in cracked Type 10 modified cement paste (Specimen 1) after exposure to the chloride-containing simulated pore solution for approx. 50 days (mV SCE).

As-Received   Ground

Figure B.3.1(b) Steel embedded in cracked Type 10 modified cement paste (Specimen 5) after exposure to the chloride-containing simulated pore solution for approx. 50 days (mV SCE).

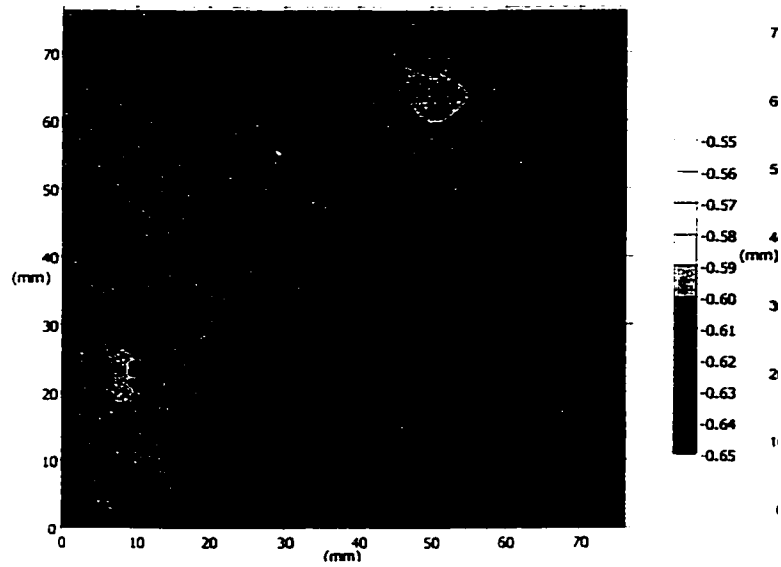As-Received   Ground

Figure B.3.1(c) Steel embedded in cracked Type 10 modified cement paste (Specimen 5) after exposure to the chloride-containing simulated pore solution for approx. 160 days (mV SCE).

307

As-Received   Ground

Figure B.3.1(d) Steel embedded in cracked Type 10 modified cement paste (Specimen 7) after exposure to the chloride-containing simulated pore solution for approx. 50 days (mV SCE).
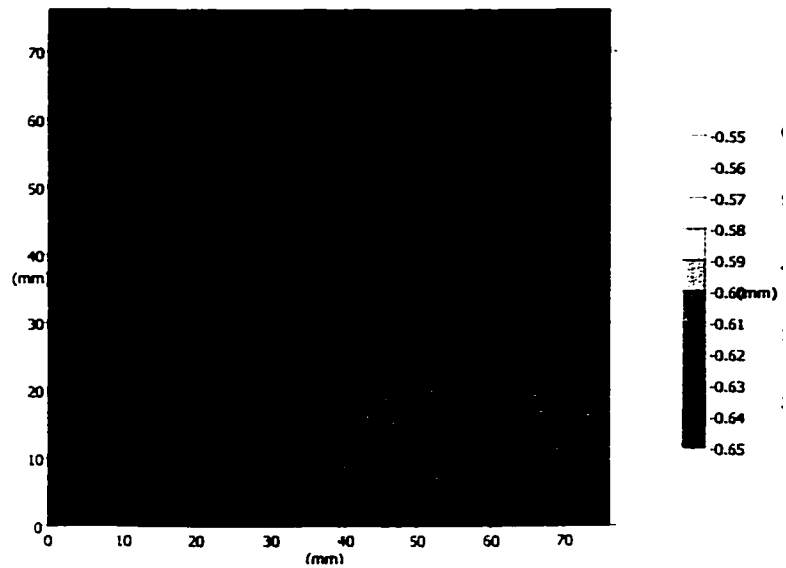

As-Received   Ground

Figure B.3.1(e) Steel embedded in cracked Type 10 modified cement paste (Specimen 7) after exposure to the chloride-containing simulated pore solution for approx. 160 days (mV SCE).

As-Received   Ground

Figure B.3.1(f) Steel embedded in cracked Type 10 modified cement paste (Specimen 8) after exposure to the chloride-containing simulated pore solution for approx. 50 days (mV SCE).

As-Received   Ground

Figure B.3.1(g) Steel embedded in cracked Type 10 modified cement paste (Specimen 8) after exposure to the chloride-containing simulated pore solution for approx. 160 days (mV SCE).

309

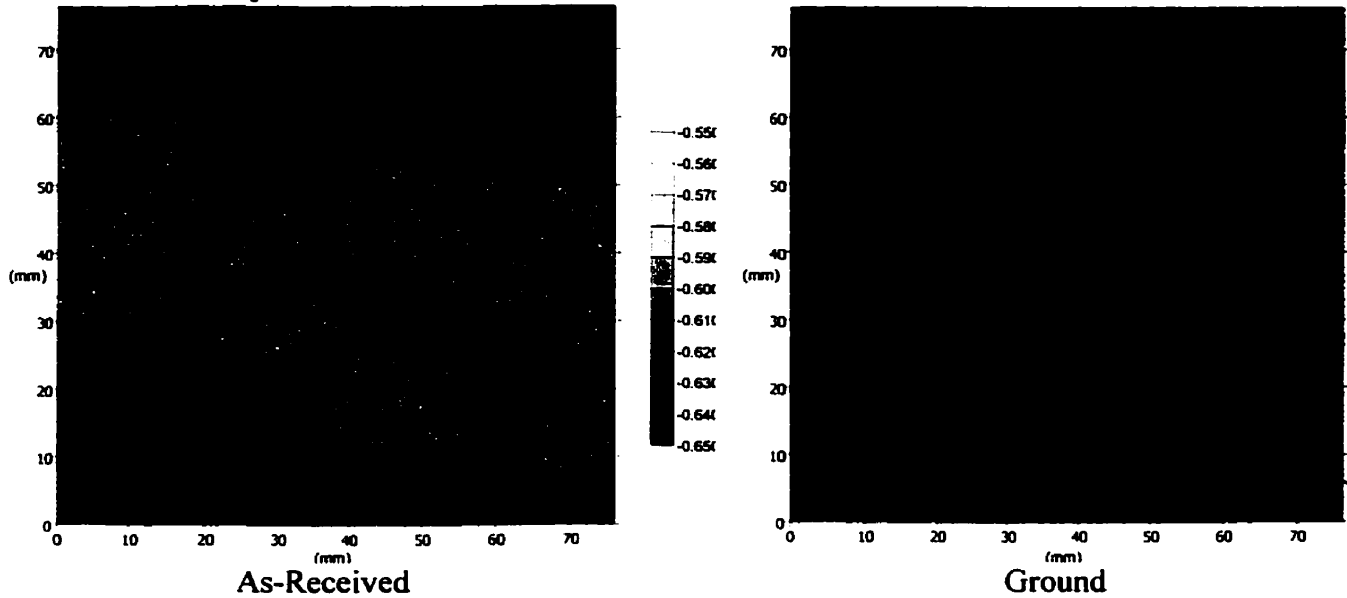As-Received   Ground

Figure B.3.1(h) Steel embedded in cracked Type 10 modified cement paste (Specimen 10) after exposure to the chloride-containing simulated pore solution for approx. 50 days (mV SCE).

B.3.2 Sealed Specimens

As-Received   Ground

Figure B.3.2(a) Steel embedded in sealed Type 10 modified cement paste (Specimen 2) after exposure to the chloride-containing simulated pore solution for approx. 50 days (mV SCE).

As-Received   Ground

Figure B.3.2(b) Steel embedded in sealed Type 10 modified cement paste (Specimen 3) after exposure to the chloride-containing simulated pore solution for approx. 50 days (mV SCE).
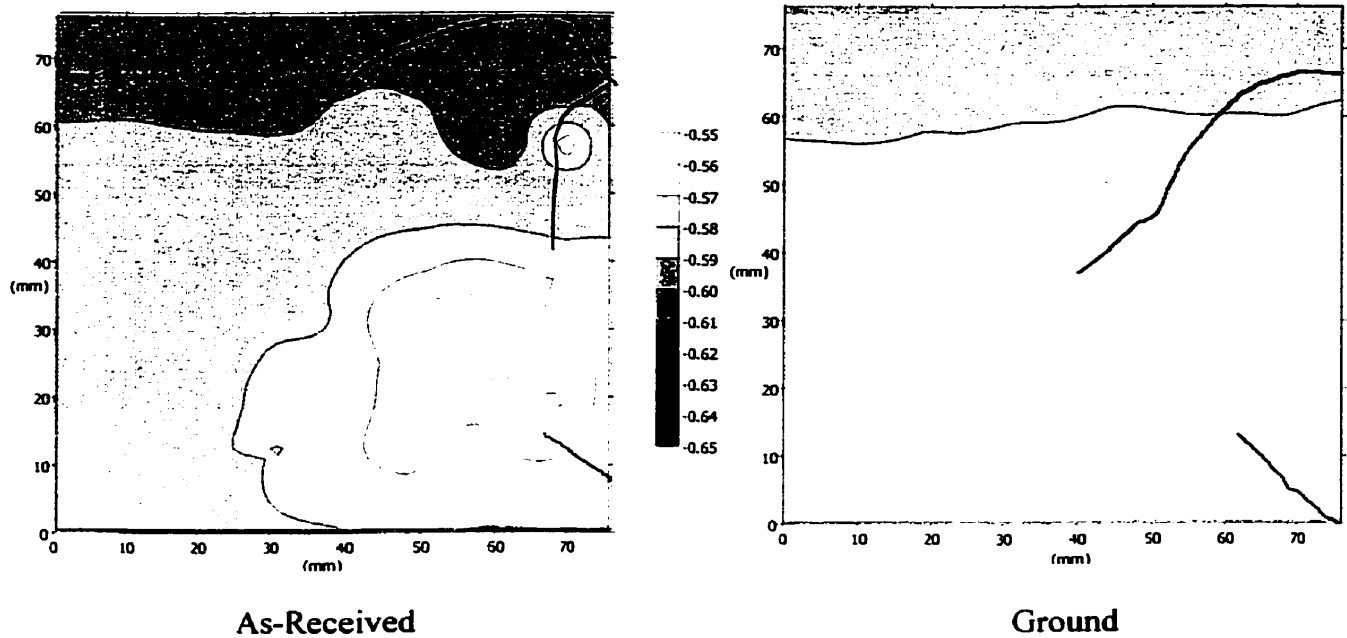

As-Received   Ground
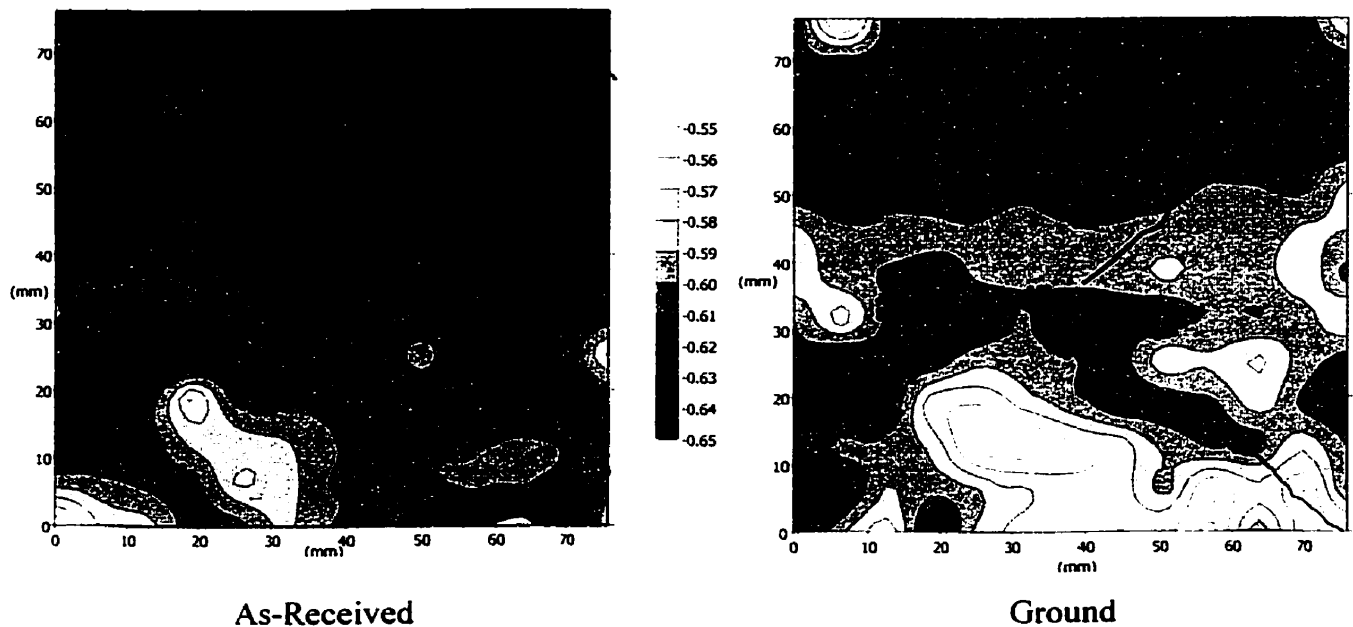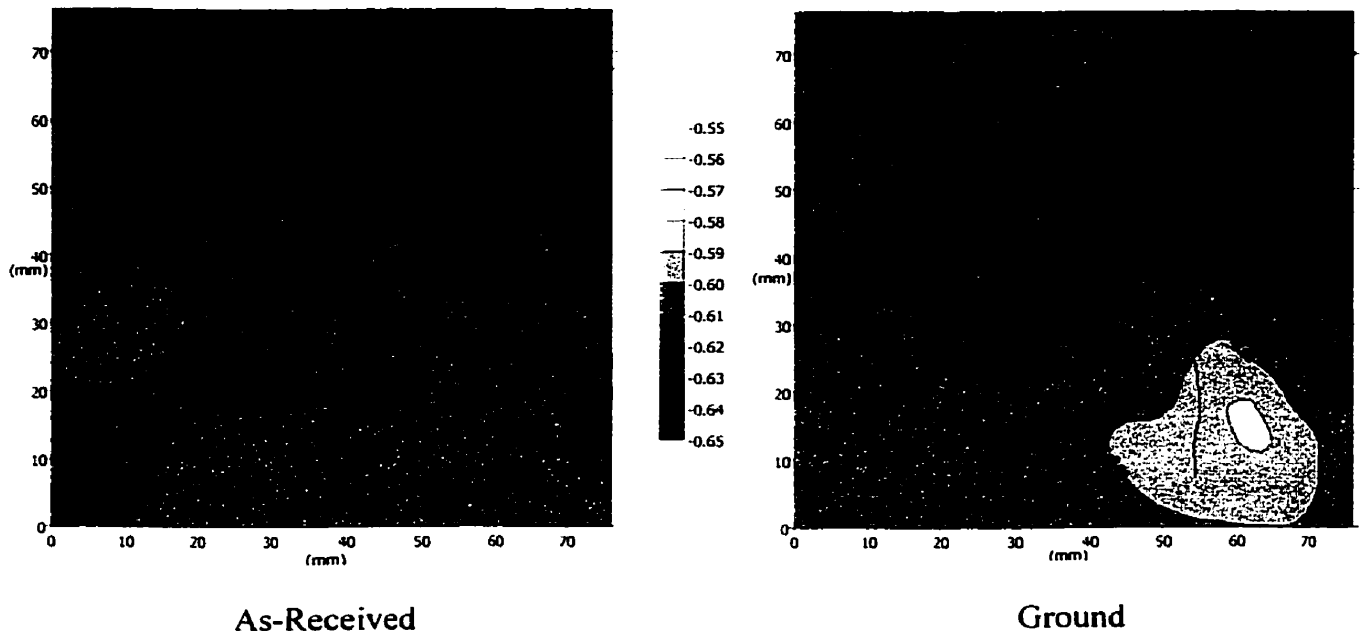
Figure B.3.2(c) Steel embedded in sealed Type 10 modified cement paste (Specimen 3) after exposure to the chloride-containing simulated pore solution for approx. 160 days.

As-Received

Figure B.3.2(d) Steel embedded in sealed Type 10 mo
exposure to the chloride-containing simulated pore so

As-Received

Figure B.3.2(e) Steel embedded in sealed Type 10 mo
exposure to the chloride-containing simulated pore sol
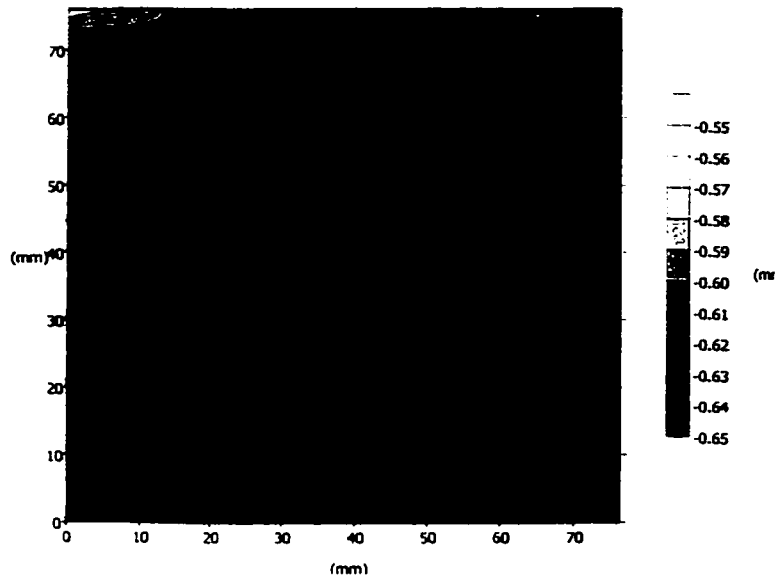
As-Received

Figure B.3.2(f) Steel embedded in sealed Type 10 mc
exposure to the chloride-containing simulated pore sc
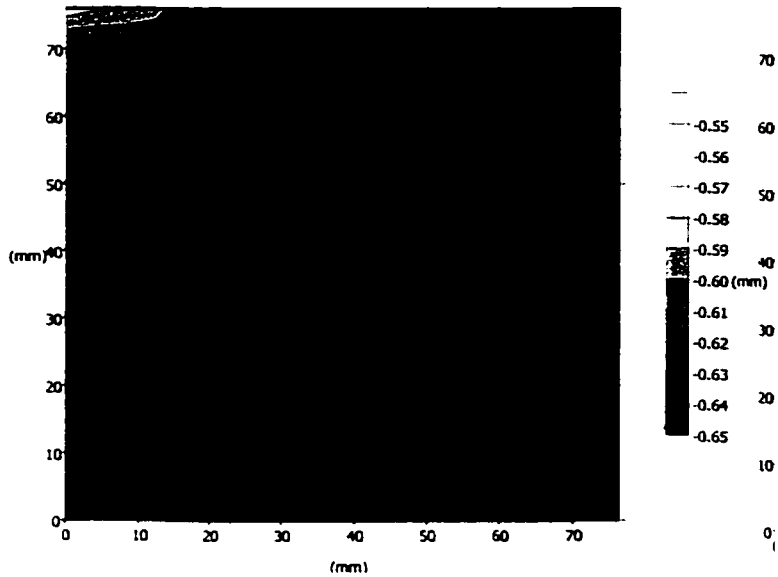
As-Received

Figure B.3.2(g) Steel embedded in sealed Type 10 mc
exposure to the chloride-containing simulated pore so

As-Received   Ground
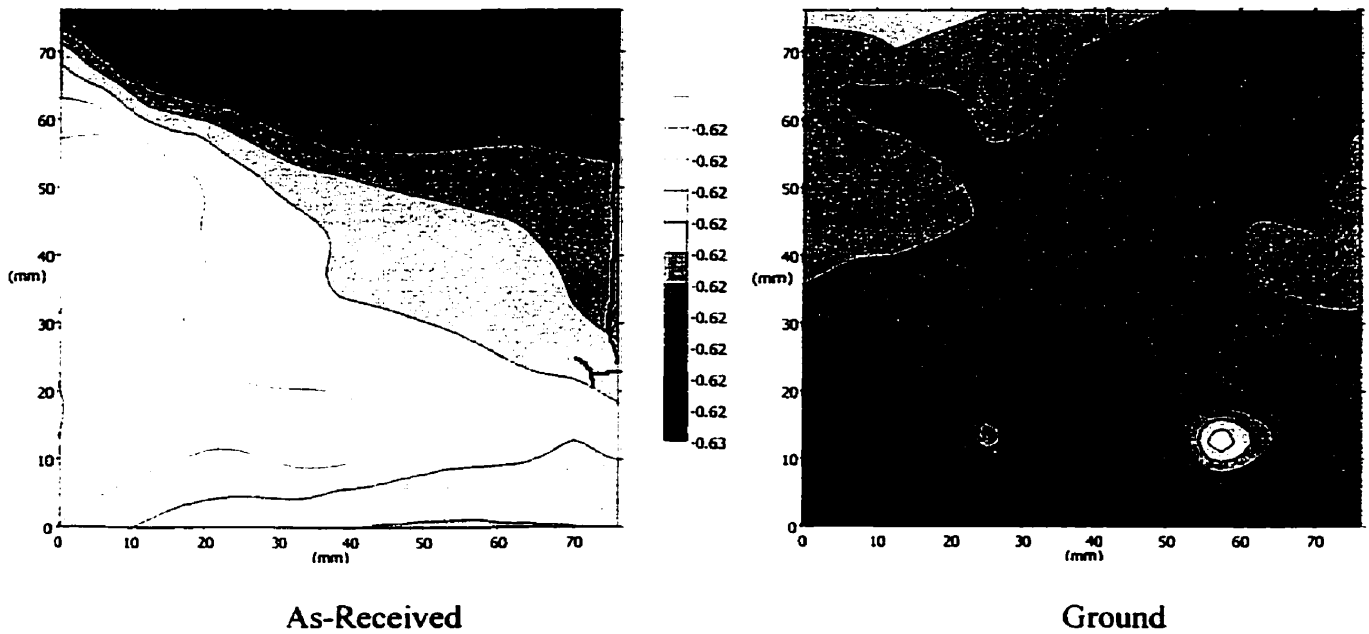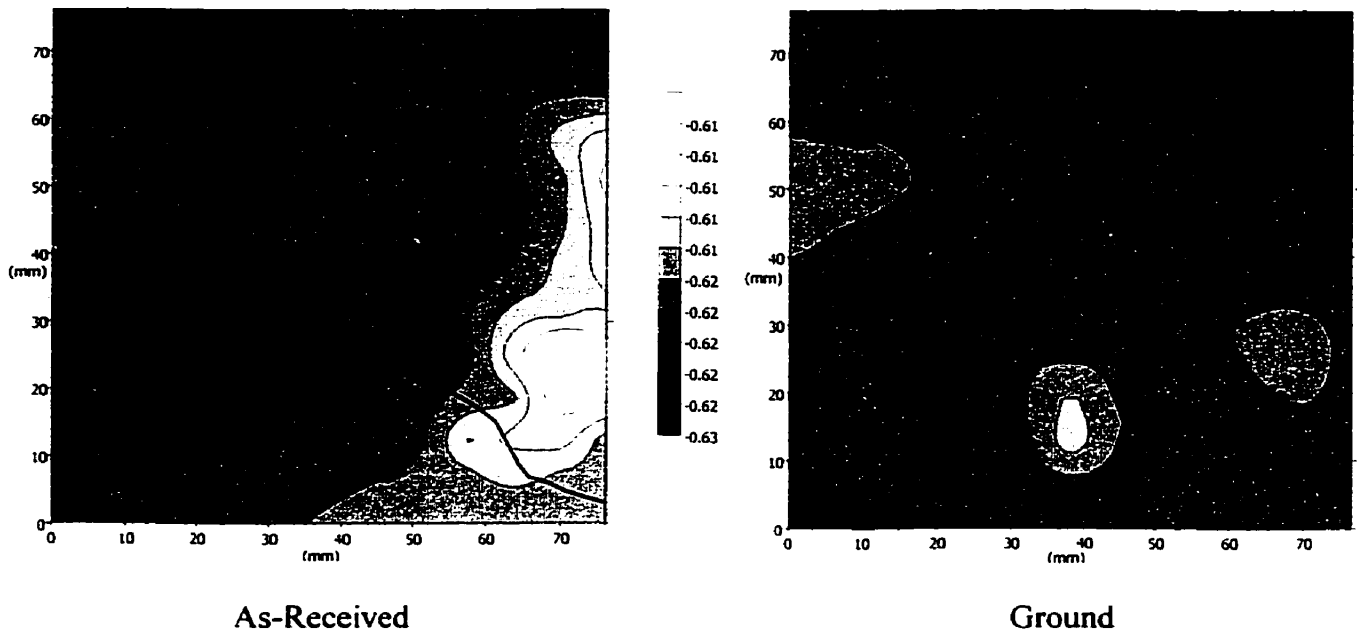
Figure B.3.2(h) Steel embedded in sealed Type 10 modified cement paste (Specimen 9) after exposure to the chloride-containing simulated pore solution for approx. 50 days (mV SCE).
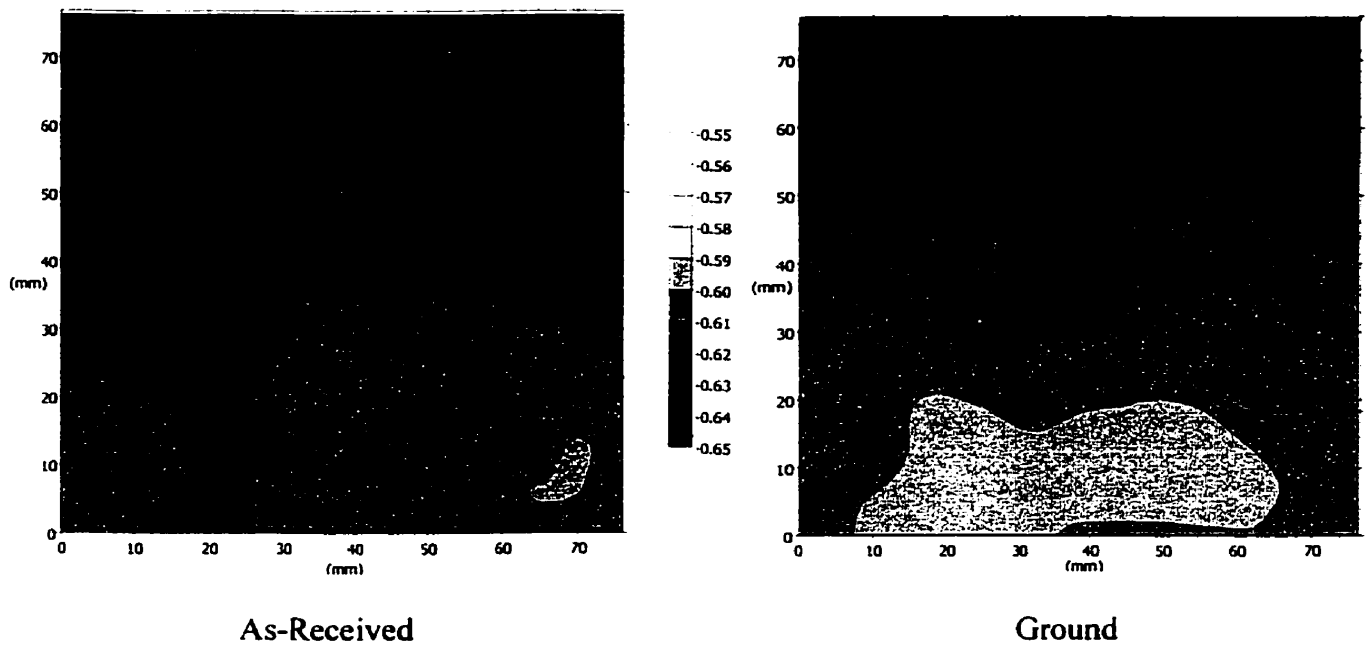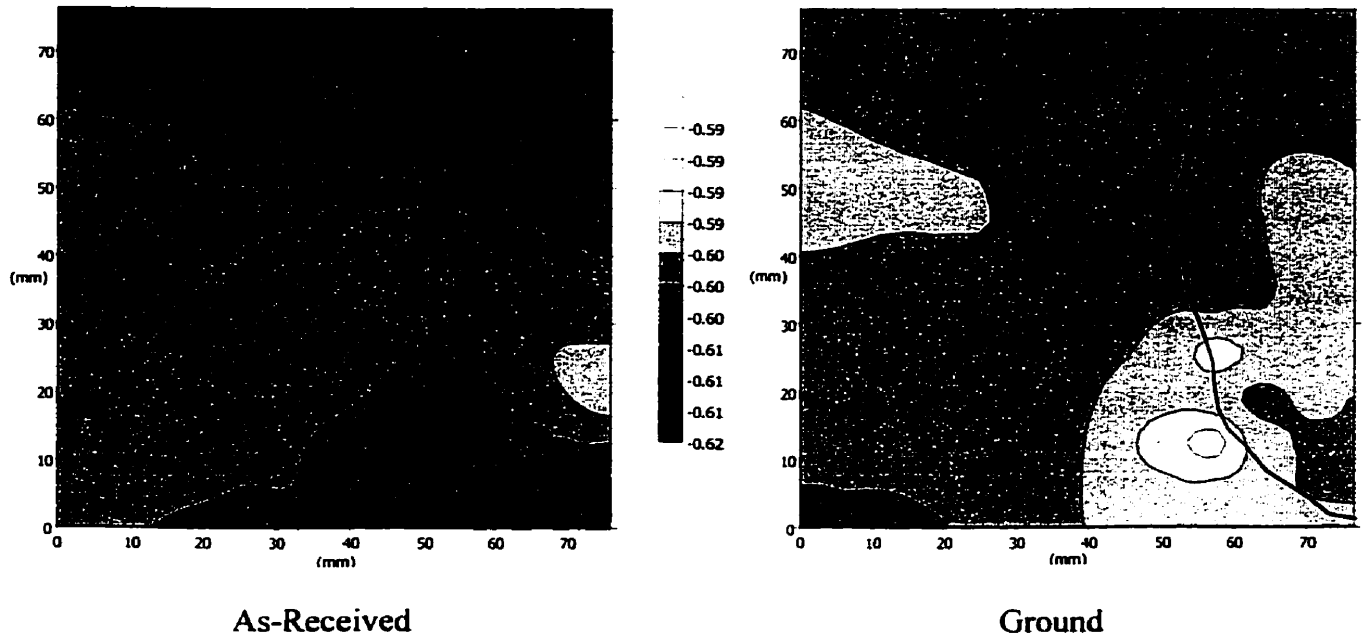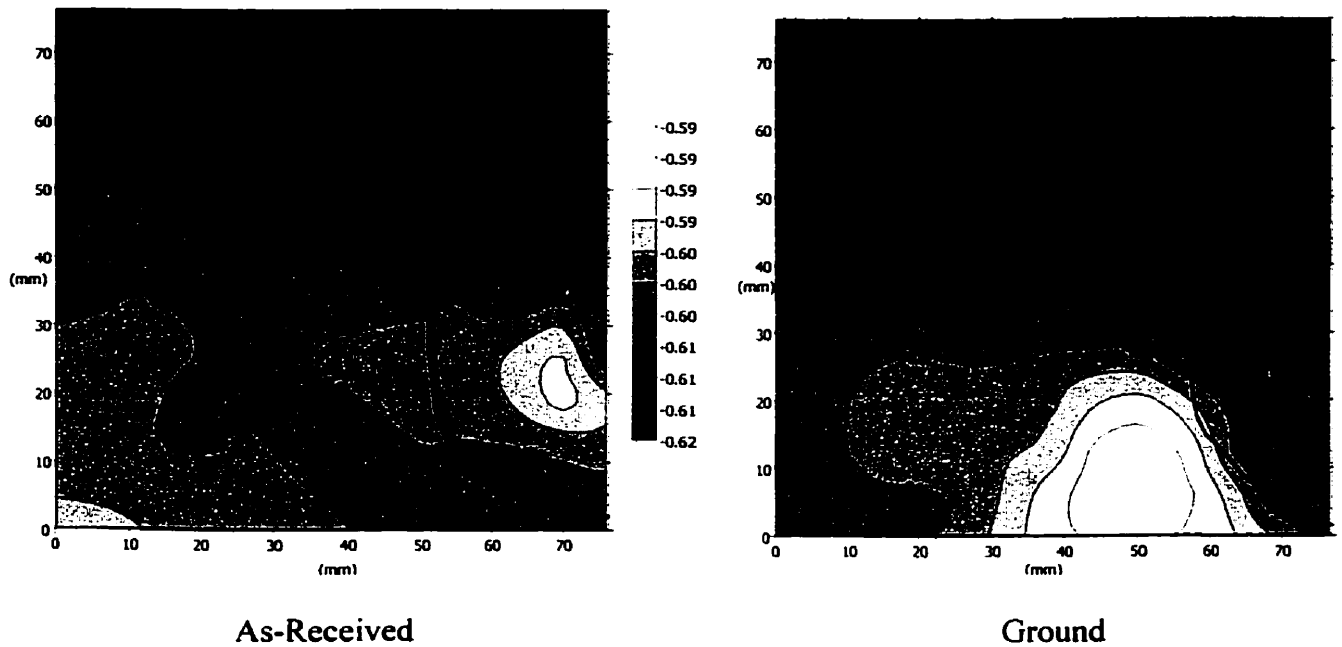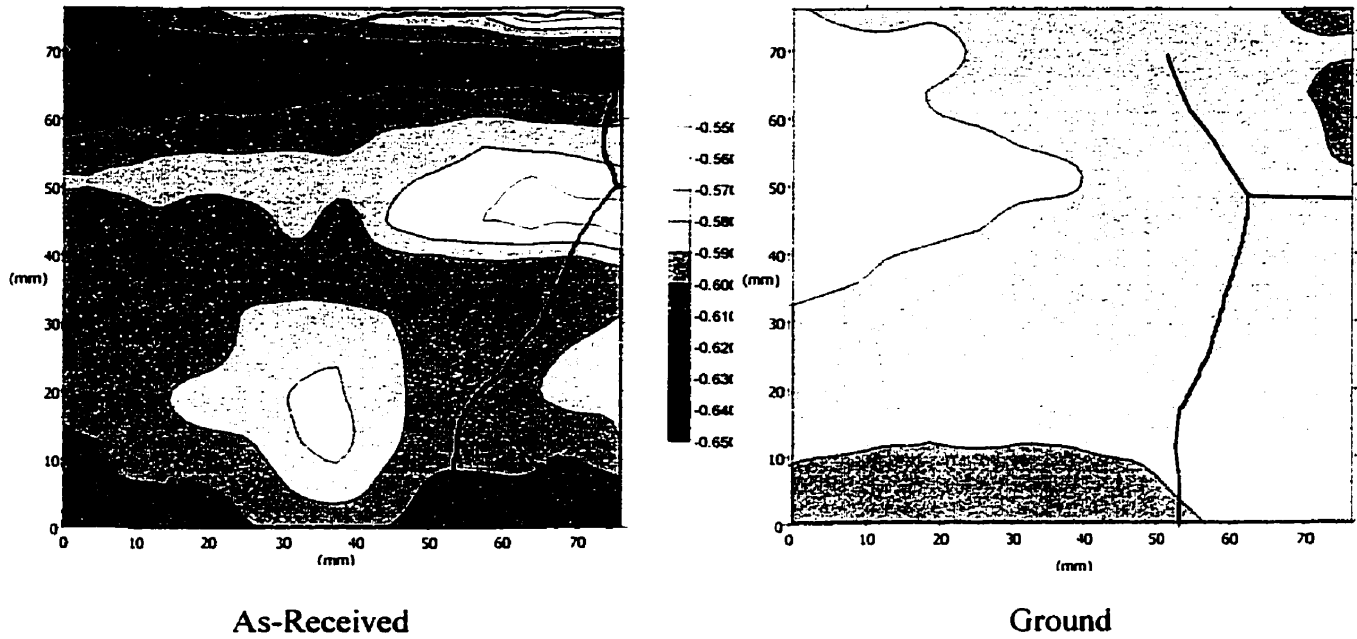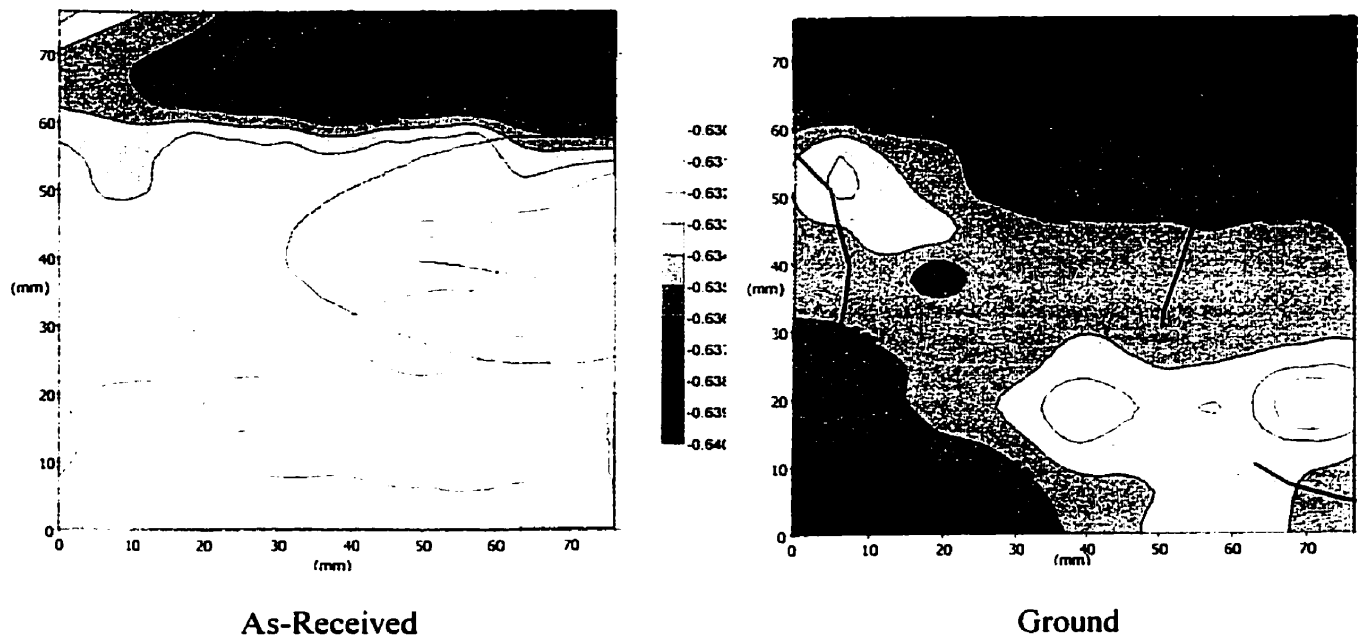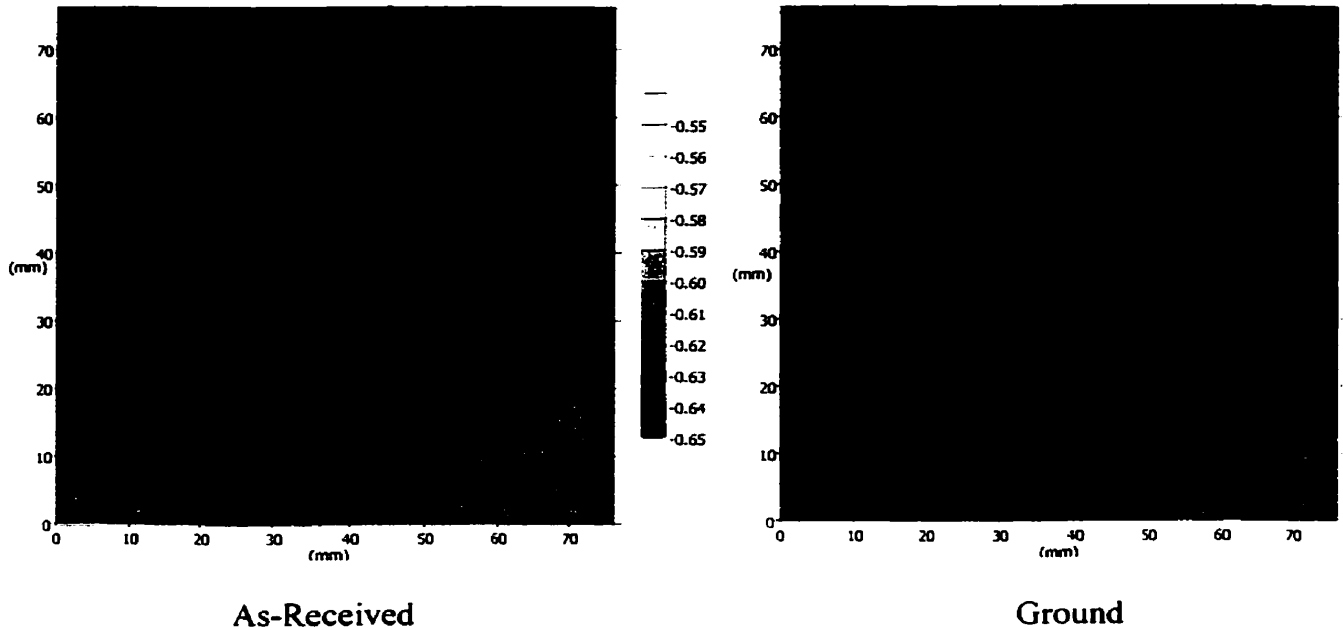
APPENDIX C
MERCURY INTRUSION POROSIMETRY DATA CORRECTION

Corrections to experimental data that account for the compression and thermal expansion of mercury, sample compression and volume changes of glass penetrometer have been detailed by Ioannidis (2001). The mathematical formulae and deductions are described in the following sections.

A. Mercury intrusion porosimetry without sample (i.e., a blank run)

$$\Delta V_b = \Delta V_{Hg,b} - \Delta V_g \tag{C.1}$$

where V_b = the change in volume due to the blank run

$V_{Hg,b}$ = reduction in mercury volume

V_g = reduction in penetrometer volume

$$dV = \left(\frac{\partial V}{\partial P}\right)_T dP + \left(\frac{\partial V}{\partial T}\right)_P dT$$

$$= -\beta V dP + \alpha V dT$$

$$or$$

$$d \ln V = -\beta dP + \alpha dT \tag{C.2}$$

where β = isothermal compressibility coefficient

$$\beta = -\frac{1}{V}\left(\frac{\partial V}{\partial P}\right)_T$$

where α = thermal expansion coefficient

$$\alpha = \frac{1}{V}\left(\frac{\partial V}{\partial T}\right)_P$$

Integration of (C.2) gives:

$$\ln\frac{V_{Hg}(P)}{V_{Hg}(P_a)} = -\int_{P_a}^{P}\beta_{Hg}dP' + \int_{T_a}^{T}\alpha_{Hg}dT'$$

$$\Delta V_{Hg}(P) = V_{Hg}(P_a) - V_{Hg}(P) = V_P\left[1 - \exp\left\{-\int_{P_a}^{P}\beta_{Hg}dP' + \int_{a}^{T}\alpha_{Hg}dT'\right\}\right] \tag{C.3}$$

where $V_p = V_{Hg}(P_a, T_a)$ = penetrometer volume at ambient conditions.

315

Similarly for glass,

$$\Delta V_g(P) = V_g(P_a) - V_g(P) = V_g \left[1 - \exp \left\{ - \int_{P_a}^{P} \beta_g dP' + \int_{T_a}^{T} \alpha_g dT' \right\} \right]$$ (C.4)

where $V_g = V_g(P_a, T_a)$ = glass volume at ambient conditions.

Substitution into of C.3 and C.4 into C.1 gives:

$$\Delta V_b(P) = V_P \left[1 - \exp \left\{ \int_{P_a}^{P} \beta_{Hg} dP' + \int_{T_a}^{T} \alpha_{Hg} dT' \right\} \right] - V_g \left[1 - \exp \left\{ \int_{P_a}^{P} \beta_g dP' + \int_{T_a}^{T} \alpha_g dT' \right\} \right]$$

B. Mercury intrusion porosimetry with non-porous sample of volume V_s

$$\Delta V_{exp}(P) = \Delta V_{Hg}(P) - \Delta V_g(P) + \Delta V_s(P)$$ (C.5)

where $\Delta V_s(P)$ is the reduction in volume of the non-porous sample

$$\Delta V_{Hg}(P) = (V_P - V_s) \left[1 - \exp \left\{ - \int_{P_a}^{P} \beta_{Hg} dP' + \int_{T_a}^{T} \alpha_{Hg} dT' \right\} \right]$$ (C.6)

$$\Delta V_g(P) = V_g \left[1 - \exp \left\{ - \int_{P_a}^{P} \beta_g dP' + \int_{T_a}^{T} \alpha_g dT' \right\} \right]$$ (C.7)

$$\Delta V_s(P) = V_s \left[1 - \exp \left\{ - \int_{P_a}^{P} \beta_s dP' + \int_{T_a}^{T} \alpha_s dT' \right\} \right]$$ (C.8)

Substituting C.6, C.7 and C.8 into C.5 gives:

$$\Delta V_{exp}(P) = (V_p - V_s) \left[1 - \exp \left\{ - \int_{P_a}^{P} \beta_{Hg} dP' + \int_{T_a}^{T} \alpha_{Hg} dT' \right\} \right]$$

$$+ V_s \left[1 - \exp \left\{ - \int_{P_a}^{P} \beta_s dP' + \int_{T_a}^{T} \alpha_s dT' \right\} \right]$$

$$- V_g \left[1 - \exp \left\{ - \int_{P_a}^{P} \beta_g dP' + \int_{T_a}^{T} \alpha_g dT' \right\} \right]$$ (C.9)

Algebraic combination of C.1 and C.9 gives:

$$\frac{\Delta V_{exp}}{V_P - V_s} - \frac{\Delta V_b}{V_P} = \frac{V_s}{V_P - V_s} \left[\begin{array}{l} 1 - \exp\left\{ \int_{P_a}^{P} \beta_s dP' + \int_{T_a}^{T} \alpha_s dT' \right\} + \\ \left(\frac{V_g}{V_P} - \frac{V_g}{V_P - V_s} \right)\left(1 - \exp\left\{ 1 - \int_{P_a}^{P} \beta_g dP' + \int_{T_a}^{T} \alpha_g dT' \right\} \right) \end{array} \right]$$

or

$$\frac{\Delta V_{exp}(P) - \Delta V_b(P)}{V_s} + \frac{\Delta V_b(P)}{V_P} = \Gamma(P)$$

where $\Gamma(P) = 1 - \exp\left\{ -\int_{P_a}^{P} \beta_s dP' + \int_{T_a}^{T} \alpha_s dT' \right\} - \frac{V_g}{V_P}\left[1 - \exp\left\{ -\int_{P_a}^{P} \beta_g dP' + \int_{T_a}^{T} \alpha_g dT' \right\} \right]$

Therefore, correction value at each intruded pressure for cement paste specimens is given by:

$$\Delta V_{cem}(P) = \left(1 - \frac{V_{cem}}{V_P} \right)\Delta V_b(P) + V_{cem}\Gamma(P)$$

Corrected incremental intrusion volume is given by:

$$\Delta V_{uncorrected}(P) - \Delta V_{cem}(P) = \Delta V_{corrected}(P)$$

REFERENCES

ACI Committee 222 (1996). Corrosion of Metals in Concrete, American Concrete Institute.

Addleson, L. and C. Rice (1995). Performance of Materials in Buildings - A Study of the Principles and Agencies of Change. Oxford, UK, Butterworth -Heinemann Ltd.

Aligizaki, K.K., M.R. de Rooij, et al. (2000). "Analysis of Iron Oxides accumulating at the Interface between Aggregates and Cement Paste." Cement and Concrete Research 30: 1941-1945.

Allan, M.L. (1995). "Probability of Corrosion-Induced Cracking in Reinforced Concrete." Cement and Concrete Research 25(6): 1179-1190.

Alonso, C., C. Andrade, et al. (2000). "Chloride Threshold Values to Depassivate Reinforcing Bars Embedded in a Standardized OPC Mortar." Cement and Concrete Research 30: 1047-1055.

Andrade, C. and C. Alonso (1993). "Cover Cracking as a Function of Bar Corrosion Part I - Experimental Test." Materials and Structures 26: 453-464.

Andrade, C. and J.A. González (1978). "Quantitative Measurements of the Corrosion Rate of Reinforcing Steels Embedded in Concrete using Polarization Resistance Measurements." Werkstoffe und Korrosion 29: 515-519.

Arup, H. (1983). The Mechanisms of the Protection of Steel by Concrete in Corrosion of Reinforcement in Concrete Construction. A.P. Crane, Ellis Horwood, Ltd.: 393.

Arya, C., N.R. Buenfeld, et al. (1990). "Factors Influencing Chloride-Binding in Concrete." Cement and Concrete Research 20: 291-300.

Arya, C. and F.K. Ofori-Darko (1996). "Influence of Crack Frequency on Reinforcement Corrosion in Concrete." Cement and Concrete Research 26(3): 345-353.

Ashworth, V., P.J. Boden, et al. (1970). "On the Breakdown of Passive Films on Mild Steel." Corrosion Science 10: 481-488.

ASTM C 114 Test Methods for Chemical Analysis of Hydraulic Cement.

318

Bakker, R.F.M. (1988). Initiation Period. Corrosion of Steel in Concrete, Report of the Technical Committee 60-CSC RILEM. P. Schiessl New York, N.Y., Chapman and Hall. 1: 22-55.

Bale, C.W., A.D. Pelton, et al. (1995). Facility for the Analysis of Chemical Thermodynamics (F*A*C*T). Montréal, Québec, Canada, École Polytechnique.

Barneyback, R.S., Jr. and S. Diamond (1981). "Expression and Analysis of Pore Fluids from Hardened Cement Pastes and Mortars." Cement and Concrete Research 11(2): 279-285.

Bazant, Z.P. (1979). "Physical Model for Steel Corrosion in Concrete Sea Structures." Journal of the Structural Division 105(ST6): 1137-1153.

Bentz, D.P., J.R. Clifton, et al. (1996). "Predicting Service Life of Chloride-Exposed Steel-Reinforced Concrete." Concrete International(December): 42-47.

Borgard, B., C. Warren, et al. (1989). "Correlation between Corrosion of Reinforcing Steel and Voids and Cracks in Concrete Structures." Transportation Research Record 1211: 1-11.

Boucherit, N., A. Hugot-Le Goff, et al. (1991). "Raman Studies of Corrosion Films grown on Fe and Fe-6Mo in Pitting Conditions." Corrosion Science 32(5/6): 497-507.

Browne, R. (1986). "Building Deteriology - The Study and Prediction of Building Life and Performance." Chemistry and Industry(24): 837-844.

Bye, G.C. (1983). Portland Cement Composition, Production and Properties. Toronto, Ontario, Pergamon Press.

Cady, P.D. and R.E. Weyers (1991). Predicting Service Life of Concrete Bridge Decks Subject to Reinforcement Corrosion. Corrosion Forms and Control for Infrastructure, ASTM STP 1137, San Diego, CA, USA, American Society for Testing and Materials.

Canadian Standards Association CAN/CSA-A23.1-M90; CAN/CSA-A23.2-M90 Concrete Materials and Methods of Concrete Construction, Methods of Test for Concrete.

Canadian Standards Association CAN/CSA-G30.18-M92 Billet-Steel Bars for Concrete Reinforcement

Chatterji, S. and A.D. Jensen (1992). Formation and Development of Interfacial Zones Between Aggregates and Portland Cement Pastes in Cement-Based Materials. Interfaces in Cementitious Composites, Toulouse, France, E & FN Spon.

Clifton, J.R. (1993). "Predicting the Service Life of Concrete." ACI Materials Journal 90(6): 611-617.

Concrete Canada. (1997). Meeting the Challenges of the Third Millennium - High Performance Concrete Structures.

Conjeaud, M. (1982). Mecanisme d'Attaque des Ciments Portland par CaCl₂. International Seminary on Calcium Aluminates, Torino, Italy.

Cook, R.A. and K.C. Hover (1993). "Mercury Porosimetry of Cement-Based Materials and Associated Correction Factors." ACI Materials Journal (March-April): 152-161.

Crammond, N.J. (1985). "Quantitative X-ray Diffraction Analysis of Ettringite, Thaumasite and Gypsum in Concretes and Mortars." Cement and Concrete Research 15: 431-441.

Crumbie, A.K. (1994). Characterisation of the Microstructure of Concrete, Ph.D., University of London, Imperial College.

Crumbie, A.K. (1996). Personal Communication.

Csizmadia, J., G. Balázs, et al. (2001). "Chloride Ion Binding Capacity of Aluminoferrites." Cement and Concrete Research 31: 577-588.

Dakhil, F.H., P.D. Cady, et al. (1975). "Cracking of Fresh Concrete as Related to Reinforcement." ACI Journal(August): 421-428.

Danilatos, G.D. (1991). Gas Flow Properties in the Environmental SEM. Microbeam Analysis. D.G. Howitt. San Francisco, CA, U.S.A., San Francisco Press, Inc.: 201-203.

Darwin, D., D.G. Manning, et al. (1985). "Debate: Crack Width, Cover, and Corrosion." Concrete International May: 20-35.

de Faria, D.L.A., S. Venâncio Silva, et al. (1997). "Raman Microspectroscopy of Some Iron Oxides and Oxyhydroxides." Journal of Raman Spectrscopy 28: 873-878.

Delagrave, A., J. Marchand, et al. (1996). Durability of High Performance Cement Pastes in Contact with Chloride Solutions. Fourth International Symposium on the Utilization of High Strength/High Performance Concrete, Paris, France.

Diamond, S. (1989). Methodologies of PSD Measurements in HCP: Postulates, Peculiarities, and Problems. Pore Structure and Permeability of Cementitious Materials, Boston, MA, U.S.A., Materials Research Society.

Diamond, S. (1994). Historical Development of Microstructural Studies in Cement and Concrete Research. Importance of Recent Microstructural Developments in Cement and Concrete: Conference in Tribute to Micheline Moranville Regourd, Sherbrooke, Québec, Canada, Université de Sherbrooke.

Edvardsen, C. (1999). "Water Permeability and Autogenous Healing of Cracks in Concrete." ACI Materials Journal 96(4): 448-454.

EG & G Research (1980). Basics of Corrosion Measurements. Application Note Corr 1. Princeton, N.J., U.S.A.

Eldridge, J. and R.W. Hoffman (1989). "A Mössbauer Spectroscopy Study of the Potential Dependence of Passivated Iron Films." Journal of the Electrochemical Society 136(4): 955-961.

Emmons, P.H. (1993). Concrete Repair and Maintenance Illustrated - Problem Analysis, Repair Strategy, Techniques. Kingston, MA, USA, R.S. Means Company, Inc.

Enevoldsen, J.N. (1993). Factors Controlling the Rate of Corrosion of Steel Embedded in Concrete and Mortar, M.Sc. (Engineering), Queen's University.

Fagerlund, G. (1982). Predicting the Service Life of Concrete Structures. Characterization and Performance Prediction of Cement and Concrete, Henniker, N.H., USA, United Engineering Trustees, Inc.

Farmer, V.C., Ed. (1974). The Infared Spectra of Minerals. London, UK, Mineralogical Society.

Fitch, M.G., R.E. Weyers, et al. (1995). "Determination of End of Functional Service Life for Concrete Bridge Decks." Transportation Research Record 1490.

Funahashi, M. (1990). "Predicting Corrosion-Free Service Life of a Concrete Structure in a Chloride Environment." ACI Materials Journal 87(6): 581-586.

Génin, J.M.R., P. Refait, et al. (1997). Green Rusts, Intermediate Corrosion Products formed on Rebars in Concrete in the Presence of Carbonation or Chloride Ingress. Understanding Corrosion Mechanisms in Concrete: A Key to Improving Infrastructure Durability, M.I.T.,

321

Cambridge, MA.

Génin, J.M.R., D. Rezel, et al. (1986). "Mössbauer Spectroscopy Characterization and Electrochemical Study of the Kinetics of Oxidation of Iron in Chlorinated Aqueous Media: Structure and Equilibrium Diagram of Green Rust One." Materials Science Forum, Electrochemical Methods in Corrosion Research 8: 477-490.

Goetz, R., D.F. Mitchell, et al. (1987). "Stability and Growth of Passive Films on Pure Iron in Borate Buffer as Investigated by ^{18}O/SIMS." Journal of the Electrochemical Society 134(3): 535-539.

Goldstein, J.I. (1981). Scanning Electron Microscopy and X-Ray Microanalysis. New York, NY, Plenum Press.

Grandet, J. and J.P. Ollivier (1980). New Method for the Study of Cement-Aggregate Interfaces (French). The Seventh International Conference on the Chemistry of Cement, Paris, France, Editions Septims.

Grandet, J. and J.P. Ollivier (1980). Orientation of Hydration Products near Aggregate Surfaces (French). The Seventh International Congress on the Chemistry of Cement, Paris, France, Editions Septima.

Grimes, W.D., W.H. Hartt, et al. (1979). "Cracking of Concrete in Sea Water due to Embedded Metal Corrosion." Corrosion 35(7): 309-316.

Guilbaud, J.P., G. Chahbazian, et al. (1994). Electrochemical Behaviour of Steel under Cathodic Protection in Medium Simulating Concrete. Corrosion and Corrosion Protection of Steel in Concrete, University of Sheffield, Sheffield Academic Press.

Guirado, F., S. Galí, et al. (1994). "The Crystallography of $CA_{1-x}F_x$ using X-ray Powder Diffraction Techniques." Cement and Concrete Research 24(5): 923-930.

Gutteridge, W.A. (1979). "On the Dissolution of the Interstitial Phases in Portland Cement." Cement and Concrete Research 9: 319-324.

Hansson, C.M. (1984). "Comments on Electrochemical Measurements of the Rate of Corrosion of Steel in Concrete." Cement and Concrete Research 14: 574-584.

Hansson, C.M. (1986). A Critical Assessment of Methods of Measuring the Rate of Corrosion of Steel in Reinforced Concrete, Research and Development Branch, Ontario Ministry of Transportation and Communications.

Herholdt, A.D., C.F.P. Justesen, et al., Eds. (1985). Beton-Bogen (The Concrete Book - in Danish). Aalborg, Denmark, Aalborg Portland.

Herman, R.G., C.E. Bogdan, et al. (1987). "Discrimination Among Carbonate Minerals by Raman Spectroscopy using the Laser Microprobe." Applied Spectroscopy 41(3): 437-440.

Hwang, C.L., J.C. Chen, et al. (1994). Concrete Cracking and Corrosion of Steel Bar. Corrosion and Corrosion Protection of Steel and Concrete, Sheffield, U.K., Sheffield Academic Press.

Ioannidis, M. (2001) Personal Communication. Professor, Chemical Engineering, University of Waterloo.

Jacobsen, S., J. Marchand, et al. (1998). Concrete Cracks I: Durability and Self-Healing -- A Review. Proceedings of the Second International Conference on Concrete under Severe Conditions (CONSEC '98), Tromsø, Norway, E & FN Spon.

Jennings, H.M., B.J. Dalgleish, et al. (1981). "Morphological Development of Hydrating Tricalcium Silicate as Examined by Electron Microscopy Techniques." Journal of the American Ceramics Society 64(10): 567-572.

Johansen, V. and P.J. Andersen (1991). Particle Packing and Concrete Properties. Materials Science of Concrete. J. Skalny and S. Mindess, American Concrete Society, Inc. 2: 111-147.

John, R. and S.P. Shah (1989). "Fracture Mechanics Anaylsis of High-Strength Concrete." Journal of Materials in Civil Engineering 1(4): 185-198.

Kirkpatrick, R.J., J.L. Yarger, et al. (1997). "Raman Spectroscopy of C-S-H, Tobermorite, and Jennite." Advanced Cement-Based Materials 5: 93-99.

Leek, D.S. (1997). A Study of the effects of Chloride and Sulphate in the Hydration of Portland Cement and the Corrosion of Carbon Steel Reinforcemnt using Electro-optical Techniques and Energy Dispersive X-ray Analysis, Ph.D., University of London (Queen Mary and WestfieldCollege).

Legrand, L., G. Sagon, et al. (2001). "A Raman and Infared Study of a New Carbonate Green Rust obtained by Electrochemical Way." Corrosion Science 43: 1739-1749.

Li, L. and A.A. Sagüés(2001). "Chloride Corrosion Threshold of Reinforcing Steel in Alkaline Solutions--Open-Circuit Immersion Tests." Corrosion 57(1): 19-28.

323

Liang, M.T., K.L. Wang, et al. (1999). "Service life prediction of reinforced concrete structures." Cement and Concrete Research 29: 1411-1418.

Lide, D.R., Ed. (1999). CRC Handbook of Chemistry and Physics. New York, NY, U.S.A., CRC Press.

Mammoliti, L. (1995). Evaluation of Corrosion Inhibitors in Synthetic Concrete Pore Solution, M.Sc., Queen's University, Kingston, Ontario.

Mammoliti, L.T., L.C. Brown, et al. (1996). "The Influence of Surface Finish of Reinforcing Steel and pH of the Test Solution on the Chloride Threshold Concentration for Corrosion Initiation in Synthetic Pore Solutions." Cement and Concrete Research 26(4): 545-550.

Marcotte, T.D. and C.M. Hansson (1998). A Comparison of the Chloride-Induced Corrosion Products from Steel-Reinforced Industrial Standard versus High Performance Concrete Exposed to Simulated Sea Water. High Performance and Reactive Powder Concretes, Sherbrooke, P.Q., Concrete Canada.

Marsh, B.K., R.L. Day, et al. (1985). Principles and Applications of Pore Structural Characterization. RILEM/CNR International Symposium, Bristol, U.K.

Mehta, P.K. (1993). Concrete Structure, Properties and Materials. Englewood Cliffs, N.J., U.S.A., Prentice-Hall, Inc.

Mehta, P.K. and D. Manmohan (1980). Pore Size Distribution and Permeability of Hardened Cement Pastes. 7th International Congress on the Chemistry of Cement, Paris, France, Editions Septima.

Melendres, C.A., M. Pankuch, et al. (1992). "Surface Enhanced Raman SpectroelectrochemicalStudies of the Corrosion Films on Iron and Chromium in Aqueous Solution Environments." Electrochemica Acta 37: 2747-2754.

Misawa, T., K. Hashimoto, et al. (1974). "The Mechanism of Formation of Iron Oxide and Oxyhydroxides in Aqueous Solutions at Room Temperature." Corrosion Science 14: 131-149.

Molina, F.J., C. Alonso, et al. (1993). "Cover Cracking as a Function of Rebar Corrosion Part 2 - Numerical Model." Materials and Structures 26: 532-548.

Monteiro, P.J.M., O.E. Gjørv, et al. (1985). "Microstructure of the Steel-Cement Paste Interface in the Presence of Chloride." Cement and Concrete Research 15: 781-784.

Morinaga, S. (1988). Prediction of Service Life of Reinforced Concrete Buildings Based in Rate of Corrosion of Reinforcing Steel, Institute of Technology, Shimizu Corporation.

Neville, A.M. (1973). Properties of Concrete. New York, N.Y., John Wiley and Sons.

Nilsen, N. and B. Espelid (1985). Corrosion Behaviour of Reinforced Concrete under Dynamic Loading. Corrosion/85, Boston, MA, USA, National Association of Corrosion Engineers.

Oblonsky, L.J. and T.M. Devine (1997). "Corrosion of Carbon Steels in CO_2-Saturated Brine, A Surface Enhanced Raman Spectroscopic Study." Journal of the Electrochemical Society 144(4): 1252-1260.

Okada, K., K. Kobayashi, et al. (1988). "Influence of Longitudinal Cracking Due to Reinforcement Corrosion on Characteristics of Reinforced Concrete Members." ACI Structural Journal(March-April): 134-140.

Poulsen, E. (1996). Estimation of Chloride Ingress into Concrete and Prediction of Service Lifetime with Reference to Marine RC Structures. Durability of Concrete in Saline Environment, Almqvist & Wiksell Tryckeri.

Pourbaix, M. (1966). Atlas of Electrochemical Equilibria in Aqueous Solutions. Toronto, Pergamon Press.

Powers, T.C. (1949). "The Air-Requirement of Frost Resistant Concrete." Proceedings, Highway Research Board, Portland Cement Association 29(Bulletin No. 33): 184-202.

Raharinaivo, A. and J.-M.R. Génin (1986). "On the Corrosion of Reinforcing Steels in Concrete in the Presence of Chlorides." Materiales de Construccion 36(204): 5-16.

Raharinaivo, A., J.-P. Guilbaud, et al. (1992). "The Electrochemical Behaviour of Steel under Polarization in Porous Media Simulating Concrete." Corrosion Science 33(10): 1607-1616.

Ramachandran, V.S. (1976). "Calcium Chloride in Concrete." Science and Technology: 107.

Rasheeduzzafar, S.S. Al-Saadoun, et al. (1992). "Corrosion Cracking in Relation to Bar Diameter, Cover, and Concrete Quality." Journal of Materials in Civil Engineering 4(4): 327-342.

Rasheeduzzafar, S.S. Al-Saadoun, et al. (1990). "Effect of Tricalcium Aluminate Content of Cement on Corrosion of Reinforcing Steel in Concrete." Cement and Concrete Research 20: 723-738.

Refait, P. and J.-M.R. Génin (1993). "The Oxidation of Ferrous Hydroxide in Chloride-Containing Aqueous Media and Pourbaix Diagrams of Green Rust One." Corrosion Science 34(5): 797-819.

Rodríguez, P., E. Ramírez, et al. (1994). "Methods for Studying Corrosion in Reinforced Concrete." Magazine of Concrete Research 46(167): 81-90.

Scrivener, K.L. (1984). The Development of Microstructure During the Hydration of Portland Cement, Ph.D., University of London, Imperial College.

Scrivener, K.L. (1989). The Microstructure of Concrete. Materials Science of Concrete. J. Skalny. Westerville, OH, U.S.A., American Ceramic Society, Inc. 1: 127-161.

Sellevold, E.J., D.H. Bager, et al. (1982). Silica Fume - Cement Pastes: Hydration and Pore Structure, Division of Building Materials, Norwegian Institute of Technology, NTH, Trondheim, Norway: 19-50.

Shibata, T. (1996). "1996 W.R. Whitney Award Lecture: Statistical and Stochastic Approaches to Localized Corrosion." Corrosion Science 52(11): 813-830.

Shreir, L.L., R.A. Jarman, et al., Eds. (1994). Corrosion. Toronto, Butterworth-Heinemann Ltd.

Simmons, G.W. and H. Leidheiser, Jr. (1976). Corrosion and Interfacial Reactions. Applications of Mössbauer Spectroscopy. R.L. Cohen. New York, NY, USA, Academic Press. 1: 85-125.

Simpson, L.J. and C.A. Melendres (1996). "Temperature Dependence of the Surface Enhanced Raman Spectroelectrochemistry of Iron in Aqueous Solutions." Electrochemica Acta 41: 1727-1730.

Stern, M. and A.L. Geary (1957). "Electrochemical Polarization I. A Theoretical Analysis of the Shape of Polarization Curves." Journal of the Electrochemical Society 104(1): 56-62.

Suda, K., S. Misra, et al. (1993). "Corrosion Products of Reinforcing Bars Embedded in Concrete." Corrosion Science 35(5-8): 1543-1549.

Suryavanshi, A.K., J.D. Scantlebury, et al. (1996). "Mechanism of Friedel's Salt Formation in Cements Rich in Tri-Calcium Aluminate." Cement and Concrete Research 26(5): 717-727.

Tarrida, M., M. Madon, et al. (1995). "An In-Situ Raman Spectroscopy Study of the Hydration of Tricalcium Silicate." Advanced Cement-Based Materials 2: 15-20.

Taylor, H.F.W. (1990). Cement Chemistry. New York, Academic Press.

Thierry, D., D. Persson, et al. (1991). "Raman Spectroscopy and XPS Investigations of Anodic Corrosion Films formed on Fe-Mo Alloys in Alkaline Solutions." CorrosionScience 32(3): 273-284.

Torres-Acosta, A.A. and A.A. Sagüés (2000). Concrete Cover Cracking with Localized Corrosion of Reinforcing Stee;. Durability of Concrete, Barcelona, Spain, American Concrete Institute.

Trolard, F., J.-M.R. Génin, et al. (1997). "Identification of a Green Rust Mineral in a Reductomorphic Soil by Mössbauer and Raman Spectroscopies." Geochimicaet CosmochimicaActa 61(5): 1107-1111.

Tuutti, K. (1980). Service Life of Structures with Regard to Corrosion of Embedded Steel. International Conference on Performance of Concrete in Marine Environment, St. Andrews by-the-Sea, Canada, American Concrete Institute.

Uhlig, H.H. and R.W. Revie (1985). Corrosion and Corrosion Control. Toronto, John Wiley & Sons.

Vesikari, E. (1988). Service Life of Concrete Structures With Regard to Corrosion of Reinforcement, Technical Research Centre of Finland.

Wang, K. and P.J.M. Monteiro (1996). Corrosion Products of Reinforcing Steel and Their Effects on the Concrete Deterioration. Third CANMET/ACI International Conference on the Performance of Concrete in Marine Environment, St. Andrews-By-The Sea, N.B., Canada.

Weiermair, R. (1996). An Electrochemical Analysis of the Influence of Concrete Quality on the Corrosion of Reinforcing Steel in a Marine Environment, M.Sc., Queen's University.

Weiermair, R., C.M. Hansson, et al. (1995). Corrosion Measurements on Steel Embedded in High Performance Concrete Exposed to a Marine Environment. Third CANMET/ACI International   Conference on the Performance of Concrete in a Marine Environment, St. Andrews-by-The Sea, N.B., Canada.

Winslow, D. (1989). <u>Some Experimental Possibilities with Mercury Intrusion Porosimetry.</u> Pore Structure and Permeability of Cementitious Materials, Boston, MA, U.S.A., Materials Research Society.

Winslow, D. and D. Liu (1990). <u>Cement and Concrete Research</u> **20**: 227.

Wolski, W. (1990). "Ordered Maghemite in Rust." <u>Corrosion</u> **46**(9): 743-745.

Wranglén, G. (1985). <u>An Introduction to Corrosion and Protection of Metals.</u> New York, NY, Chapman and Hall.

GLOSSARY OF TERMS

Various compounds present in cement are often abbreviated for simplicity: C represents CaO, S represents SiO_2, A represents Al_2O_3, F represents Fe_2O_3, and H represents H_2O. In the case of SO_3 and CO_2, $\overline{S}$ and $\overline{C}$ are used to distinguish them from SiO_2 and CaO, respectively.

AFm, monosulphate	calcium monosulphate hydrate ($C_4A \overline{S} H_{18}$), a hydration product of C_3A
AFt, ettringite	calcium trisulphate hydrate ($C_6A \overline{S}_3 H_{32}$), a hydration product of C_3A
akaganeite	β-FeOOH
BEI	backscattered electron imaging
C_2S, belite	dicalcium silicate, the belite phase in cement powder
C_3S, alite	tricalcium silicate, the alite phase in cement powder
C_3A, aluminate	tricalcium aluminate, the aluminate phase in cement powder
C_4AF, ferrite	tetracalcium aluminoferrite, the ferrite phase in cement powder
C-S-H	calcium silicate hydrate, the primary hydration product of Portland cement
CH	calcium hydroxide, a hydration product of C_3S and C_2S
EDS	energy dispersive X-ray spectroscopy
ESEM (SEM)	environmental scanning electron microscopy
feroxyhite	δ-FeOOH
goethite	α-FeOOH

hæmatite	$\alpha\text{-}Fe_2O_3$
lepidocrocite	$\gamma\text{-}FeOOH$
LPR	linear polarization resistance
maghemite	$\gamma\text{-}Fe_2O_3$
magnetite	Fe_3O_4, may be non-stoichiometric with $Fe_{3-x}O_4$ and $x = 0$ to $1/3$
MIP	mercury intrusion porosimetry
OPC	ordinary Portland cement
SEI	secondary electron imaging
SHE	standard hydrogen electrode
SCE	saturated calomel electrode ($+ 242$ mV SHE)
w/c	water/cement ratio by mass
w/cm	water/cementitious materials ratio by mass (for mixes that include supplementary cementitious materials)
XRD	X-ray diffraction